

" Sixth Workshop on Non-Linear Dynamics and  
Earthquake Prediction"

15 - 27 October 2001

**Self-Affine Time Series:  
I. Generation and Analyses**

*Bruce D. Malamud\* and D. L. Turcotte*

Department of Geological Sciences, Cornell University  
Ithaca, New York, U.S.A.

\* Now at: Department of Geography  
King's College London, U.K.



## PREFACE

Two contrasting approaches to problems in geophysics have been pursued. The first approach has been to use solutions of the classical equations of continuum mechanics. Examples of this approach include LaPlace's equation for gravity and static geomagnetic problems, the wave equation for seismology and electromagnetic wave propagation, and the heat equation for the thermal structure of the earth. The second approach has been the use of stochastic variability or noise. In this volume of *Advances in Geophysics*, we explore in detail one of the main components of noise, that of long-range persistence or memory. The first article in this volume is a broad summary of theory and techniques of long-range persistence in time series; the second article is the application of long-range persistence to a variety of geophysical time series.

Time series can be found in many areas of geophysics. Examples of time series in which one variable changes with time at a given location on the earth include temperature, the geomagnetic field, and sedimentation rates. Some spatial data sets, such as the earth's topography along a linear track, can also be considered the equivalent of a time series. The main attributes of a time series include the statistical distribution of values in the signal and the correlations (the memory or persistence) between values. For the first attribute, the standard approach in the literature is to assume a time series has a Gaussian statistical distribution of values. In many cases, this assumption is appropriate and provides the correct statistical distributions. In other cases, it is appropriate to choose a log-normal distribution of values. We consider both in our discussion of theory and techniques in the first article.

The other main attribute of a time series is persistence. If each value in a time series is chosen randomly from a Gaussian distribution, the series is a Gaussian white noise. All values in a white noise are independent of other values; there are no correlations and the persistence is zero. The running sum of a Gaussian white noise results in a Brownian motion. Brownian motions have been studied for more than a hundred years. In Brownian motions, correlations (the persistence) play an essential role. A Brownian motion is a nonstationary time series where the mean of the signal increases as the length of the time series increases. The persistence is positive: each value in the time series has a positive correlation with the other values. In a Brownian motion, if one value is larger than the average of the entire time series, the next value will also have a strong likelihood of being larger than the mean. Brownian motions have many applications, including topography and the diffusion of species in a gas.

A Brownian motion is an example of a time series that exhibits long-range persistence; each value in the time series has a correlation with all other values. The pioneering work of Mandelbrot and co-workers recognized that there is an entire class of fractional noises and motions, all with the property of long-range

persistence, that bridge the gap between Gaussian white noises and Brownian motions. There are also empirical techniques for studying short-range correlations between neighboring values. This approach generally limits in an arbitrary way the number of preceding values that influence the next value. Examples of short-range persistence techniques include the autoregressive (AR) model, the moving average (MA) model, and the ARMA combined model.

In studying long-range persistence, there are fundamental problems of analysis and a wide range of applications. In the first article in this volume, we provides a comprehensive introduction and framework for the theory of long-range persistence in time series, followed by a discussion and comparison of four techniques: semivariograms, rescaled-range, Fourier spectral analysis, and wavelet variance analysis. Wavelet variance analysis is particularly useful for nonstationary time series, such as Brownian motions. The theory of each technique is discussed at a level understandable to advanced undergraduate students, graduate students, and researchers. Strengths and weakness of each technique are then compared by applying each to a broad range of synthetic time series (fractional noises an motions).

In the second article of this volume, we apply techniques of long-range persistence to climate variability, the earth's magnetic field and sediment deposition. Each application is an in-depth and innovative way of examining these parameters. The treatment of climate variability includes the first comprehensive examination of the stochastic component of temperature, and provides fundamental new insights into how the global ocean-atmosphere system operates. The variability of climate is quantified in terms of fractional noises and motions. Numerical studies of climate should be able to reproduce this variability. The treatment of the Earth's magnetic field provides new insights into the behavior of the Earth's geodynamo. We follow these three detailed applications with a summary of long-range persistence applications by other scientists. Both articles in this volume include extensive bibliographies.

The first article in this volume benefited from the detailed comments of Teresa Jordan, Peter Thomas and Wilfried Brutsaert. We also acknowledge a very comprehensive and useful review of this volume by Alberto Malinverno, whose detailed comments allowed us to substantially improve our contributions.

Donald L. Turcotte  
Jon D. Pelletier  
Bruce D. Malamud

# SELF-AFFINE TIME SERIES: I. GENERATION AND ANALYSES

BRUCE D. MALAMUD AND DONALD L. TURCOTTE

*Department of Geological Sciences  
Cornell University  
Ithaca, New York 14853-1504*

## 1. INTRODUCTION

### 1.1. Brief Overview of Article

Mandelbrot (1967) introduced the concept of fractals in terms of statistical self-similarity or scale invariance, the idea that the shape of an object does not define its size. The original example was the length of a rocky coastline; a map of a rocky coastline gives no indication of its scale. Subsequently, many natural phenomena have been shown to exhibit statistical self-similarity. Examples include earthquakes, fragments, river networks, and mineral deposits (Turcotte, 1997). For real applications, scale invariance is valid only over a limited range; for example, in terms of fragments, there will always be a largest fragment and a smallest fragment.

Mandelbrot and Van Ness (1968) extended the concept of statistical self-similarity to time series. This was done within the context of the self-affine time series. A two-dimensional object is self-affine if it is statistically self-similar when the two axes are scaled differently. The classic example of a self-affine time series is a Brownian motion. In this article, we consider, in detail, methods of generating synthetic self-affine time series and methods for their analysis. Our basic definition of a self-affine time series is that the power-spectral density of the time series has a power-law dependence on frequency. The concepts of persistence and stationarity are examined in detail.

Examples of time series in geophysics include global temperature, the strength of the Earth's magnetic field, and the flow in a river. After obvious periodicities and trends in a time series have been removed, the remaining values are the stochastic component. The stochastic component of a time series has two main aspects, its statistical distribution of values and its persistence. Typical statistical distributions are Gaussian (normal) and log-normal. The persistence measures the correlations between adjacent values within the time series. The persistence of values with respect to each other can be strong, weak, or nonexistent (white noise). A strong correlation implies a "memory" of previous values in the time series.

Values of a time series can affect other values in the time series that are not only nearby in time (short-range) but also far away in time (long-range). Since self-affine time series have a power-law dependence of the power-spectral density function on frequency, they exhibit long-range persistence.

There are many statistical approaches currently in use for the purpose of quantifying geophysical data sets. The purpose of this paper is to systematically compare many of these statistical approaches and to illustrate their robustness and utility through applications to synthetic data sets whose properties are known. To achieve this purpose, we generate self-affine synthetic fractional noises and motions with a wide range of persistence strengths and two different statistical distributions, Gaussian and log-normal. These synthetic noises and motions have similar properties to many time series found in geophysics and other fields. The persistence analyses we use to quantify these time series are semivariogram analysis, rescaled-range analysis, average extreme-value analysis, Fourier power-spectral analysis, and wavelet variance analysis. The last two techniques measure the strength of persistence over a broad range of self-affine time series, whereas the others measure the strength only over specific subsets. We discuss the theory behind each technique and its use in measuring the strength of persistence for self-affine time series.

## 1.2. What Is a Time Series?

A time series is the set of numerical values of any variable that changes with time. A time series is generally either continuous or discrete. A continuous time series  $y(t)$  is a set of values that are continuous in time over the interval  $T$ . Examples include the continuous record of the atmospheric temperature at a specified point in space and the discharge down a river measured at a gauging station. A discrete time series consists of a set of values that are not continuous. The values in a discrete time series,  $y_n$ , are often specified at equal increments of time,  $\delta$ . Values of  $y_n$  are then given at times  $t_n = n\delta$ ,  $n = 1, 2, 3, \dots, N$  with interval  $T = N\delta$ . Although the time between successive  $n$  is a constant  $\delta$ , the values of  $y_n$  may occur arbitrarily during each  $\delta$  interval (e.g., floods), they may occur at exactly every  $\delta$  interval (e.g., hourly temperature readings), or they can be the integral of the continuous time series taken over each  $\delta$  (e.g., a yearly time series of lake sediment accumulation). Note that in this article, we connect individual points in a discrete time series by straight lines; this can give the false impression of continuous observation, but aids the eye in following the time series.

Time series are generally sets of values given as a function of time,  $t$ ; for instance, current as a function of time can be represented as  $I(t)$ . However, time series are also good representations of other kinds of data sets. For example, topographic elevations along linear transects,  $h(x)$ , are essentially equivalent to continuous time series. Here, the topographic elevation,  $h$ , is a function of the horizontal coordinate,  $x$ . Another example is the concentration of a mineral as a function of depth in a drill core. The actual concentrations are continuous, with possibly a few exceptions, but from practical considerations, measurements of concentrations are carried out at discrete intervals, giving a discrete time series. Well logs are an example of a time series in a geological context; digitized measurements of density, porosity, and/or permeability at prescribed depth intervals represent discrete time series. Three examples of geophysical time series are given in Fig. 1.

Although time series are defined to be sets of values as a function of a single variable, i.e.,  $y(t)$ , time series can be extended to functions of more variables. An example is topography,  $h(x, y)$ , where the elevation  $h$  is a function of two horizontal coordinates,  $x$  and  $y$ . In this article, we will only examine time series that are functions of one variable and can be plotted in two dimensions (two coordinates).

A time series may be characterized by any combination of the following: a trend component, one or more periodic components, and a stochastic component. The trend component is a long-term increase or decrease in the series; for example, trends in stream-flow series often result from gradual human-induced changes to the land. Many time series have periodic components; for example, an atmospheric temperature time series will have strong daily and yearly periodicities. The stochastic component is the fluctuations not included in either the trend or periodic components.

### 1.3. How Is a Time Series Quantified?

In order to quantify the stochastic component of a time series it is necessary to specify: (1) the statistical distribution of values, and (2) the persistence (or antipersistence).

The values of the variable in a natural time series may take on any statistical distribution of values. The most commonly used distributions may be divided into four families: the normal family (normal, log-normal, log-normal type 3), the general extreme-value (GEV) family (GEV, Gumbel, log-Gumbel, Weibull), the Pearson type 3 family (Pearson type 3, log-Pearson type 3), and the generalized Pareto distribution. Stedinger *et al.*

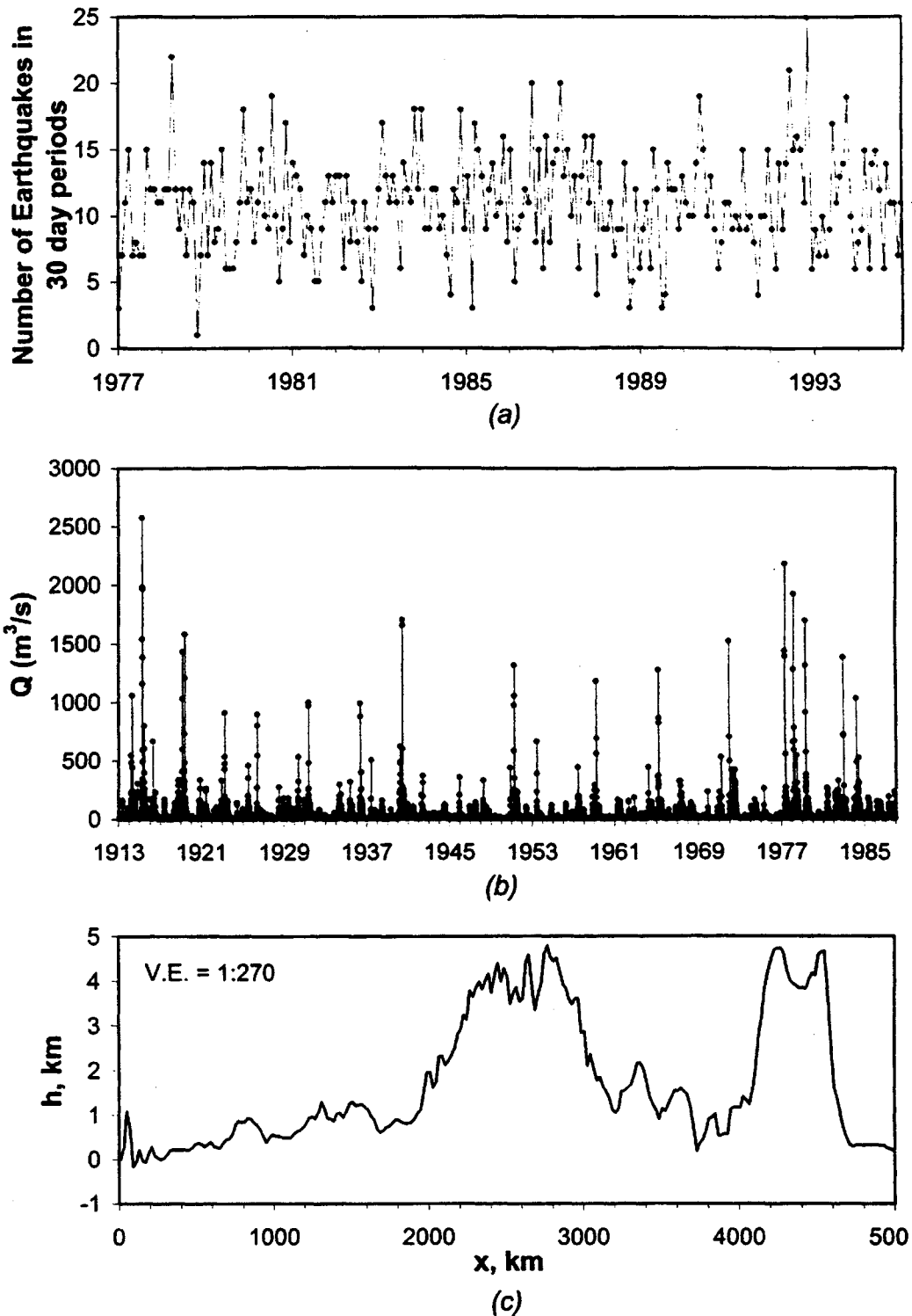


FIG. 1. Three examples of time series. (a) The number of worldwide earthquakes with seismic moments  $M_0 > 10^{25}$  N · m in successive 30-day intervals, 1977–1995 (Harvard Centroid–Moment Tensor Database, 1997). (b) Average daily river discharges (Slack and Landwehr, 1992) for the hydrologic gauging station at Salt River near Roosevelt, AZ, Oct. 1, 1913 to Sept. 30, 1988, drainage area 11,200 km<sup>2</sup>. (c) Elevation  $h$  as a function of position  $x$ . Earth's topography from 70W, 55S (southern tip of South America) to 70W, 10S (intersection of Bolivia, Peru, and Brazil). Both (a) and (b) are examples of discrete time series and (c) is an example of a continuous time series. In (a), the values are independent of one another; this is an example of an uncorrelated time series. In both (b) and (c), the values in each time series are positively correlated with one another; these are examples of persistent time series.

(1993) provide an excellent discussion and review of these different distributions.

In many cases, the distribution of values is well approximated by a Gaussian (normal) distribution. For example, the discrete time series of the number of worldwide earthquakes occurring during successive 30-day periods (Fig. 1a) is closely approximated by a Gaussian distribution. In other cases, the distribution may be strongly skewed with only positive values possible and it is appropriate to consider log-normal distributions. An example is the discrete time series of daily river discharges illustrated in Fig. 1b. Hydrologic time-series studies have been considered in detail by Bras and Rodriguez-Iturbe (1993) and Salas (1993).

In addition to the statistical distribution of values, it is also necessary to specify whether a time series is persistent, uncorrelated, or antipersistent. The stochastic component of a time series is persistent if adjacent values are positively correlated; i.e., adjacent values are on average closer to each other than for an uncorrelated time series. It is antipersistent if adjacent values are anticorrelated; i.e., adjacent values are on average further apart than for an uncorrelated time series. Beran (1992, 1994) and Bassingthwaite *et al.* (1994) give good overviews of statistical methods for treating data with persistence, and consider a variety of applications. Persistence is also known as the “memory” or internal correlation of a process.

An example of a persistent time series is the discrete time series of average daily river discharges given in Fig. 1b. Adjacent values of the average daily river discharges are positively correlated with one another. If a value for an average daily discharge is greater than the mean of the average daily discharges, then the next successive average daily discharge will have a high probability of also being greater; big values have a tendency to follow other big values, and small ones tend to follow small. An example of a continuous time series is the topography profile given in Fig. 1c. Topography as a time series has been considered in detail by Malinverno (1995). Topography clearly has horizontal persistence; adjacent values of topography are correlated. If adjacent values in the time series are independent of one another, then the stochastic component is uncorrelated. For example, the number of worldwide earthquakes occurring during successive 30-day periods (Fig. 1a) is a sequence of independent measurements and the values in the time series are uncorrelated.

Persistence can be either weak or strong, short-range or long-range. The terms weak and strong are taken here to mean how strongly time-series values that are separated by a given number of points (the lag) are correlated with one another. Short-range vs long-range persistence specifies whether there is persistence for only short lags, or also for much

longer lags. For instance, if values have a strong correlation with one another, but only for short lags, this is strong persistence over a short range. Topography is an example of a process that exhibits strong persistence over a long range.

There is a large literature on models containing short-range persistence; examples include autoregressive (AR) processes, moving average (MA) processes, and combinations of the two (ARMA) (e.g., Salas, 1993; Box *et al.*, 1994). A number of fields, for example hydrology, use models based on short-range persistence. In this article, we examine time-series models that exhibit long-range persistence. We create synthetic self-affine time series with long-range persistence and systematic variations in the strengths of persistence, similar to many time series found in geophysics and other fields. We examine a variety of techniques that quantify the strengths of persistence in self-affine time series, and discuss the relative merits of each technique.

#### 1.4. Autocorrelations and Semivariograms

In many cases the persistence (or antipersistence) of a time series can be quantified by using the autocorrelation function. Many books and papers discuss this function. A very readable and comprehensive review of the use of the autocorrelation function for time-series analysis is given by Box *et al.* (1994).

The autocorrelation function,  $r(s)$ , at lag  $s$ , measures the correlation of a time series with itself,  $y(t + s)$  compared with  $y(t)$ , at increasing values of  $s$ . This is given by

$$r(s) = \frac{c(s)}{c(0)}, \quad (1)$$

with the autocovariance function,  $c(s)$ , given by

$$c(s) = \frac{1}{(T - s)} \int_0^{T-s} [y(t + s) - \bar{y}][y(t) - \bar{y}] dt \quad (2)$$

and the autocovariance function at 0 lag,  $c(0)$ , given by

$$c(0) = \frac{1}{T} \int_0^T [y(t) - \bar{y}]^2 dt = V. \quad (3)$$

The time series,  $y(t)$ , is prescribed over the interval  $0 \leq t \leq T$ . The average and variance of  $y(t)$  over the interval  $T$  are  $\bar{y}$  and  $V$ . The autocorrelation function,  $r(s)$ , is dimensionless and does not depend on the units of  $y(t)$  or  $t$ . With  $s = 0$  we have  $c(s) = c(0) = V$ , the variance of

the time series over the period  $T$ , resulting in  $r(s) = 1$ . The time series when compared with itself (0 lag) has a correlation of 1, the most positive that  $r(s)$  can be. With increasing lag,  $s$ , the values of  $r(s)$  become smaller as the statistical correlations of  $y(t + s)$  with  $y(t)$  decrease. The plot of  $r(s)$  versus  $s$  is known as a correlogram. Although the autocorrelation, Eq. (1), at a particular lag,  $s$ , can give insight into the data, one is generally more interested in the overall structure of the autocorrelation function taken over a range of lags. Large values of  $r(s)$  indicate a strong correlation between those points in the time series that are separated by lag  $s$ , small values of  $r(s)$  indicate weak correlation, and values of  $r(s) = 0$  indicate no correlation (white noise). Persistence here can be defined as a sequence of  $r(s)$  that have positive values. If the values of  $r(s)$  are large, but then quickly drop to  $r(s) = 0$ , we have an example of strong persistence over a short range of values. If the values of  $r(s)$  are small (nonzero) and continue to stay small for very large lags, then the persistence is weak and long-range.

For a discrete time series, the autocorrelation function,  $r_k$ , is given by

$$r_k = \frac{c_k}{c_0}, \quad (4)$$

with the autocovariance,  $c_k$ , given by

$$c_k = \frac{1}{(N - k)} \sum_{n=1}^{N-k} (y_{n+k} - \bar{y})(y_n - \bar{y}) \quad (5)$$

and the autocovariance at 0 lag (the variance) given by

$$c_0 = \frac{1}{N} \sum_{n=1}^N (y_n - \bar{y})^2 = V. \quad (6)$$

Increasing values of  $k$  correspond to increasing lag. The variance,  $V$ , is taken over the  $N$  values of  $y_n$ . For an uncorrelated stochastic time series (white noise), the values of  $r_k$  will be near zero. Positive values of  $r_k$  indicate persistence while negative values indicate antipersistence. The power spectrum of a time series is the Fourier transform of the autocorrelation function. The power spectrum, a measure of long-range persistence and antipersistence, is used frequently in the analysis of geophysical time series and will be discussed in detail in Sections 2 and 3.

Note that in Eqs. (2) and (5), some authors use  $T$  and  $N$  instead of  $(T - s)$  and  $(N - k)$ ; there is little difference for values of  $k$  less than about  $N/4$ . For a discussion of the two different quantities, see Jenkins and Watts (1968) and Section 6.2 in Percival and Walden (1993). We use

$(T - s)$  and  $(N - k)$  to maintain the same nomenclature that is used with the definition of semivariograms introduced later in this section.

One important aspect of time series is the question of stationarity. Broadly speaking, a time series is said to be stationary if there are no systematic changes in the mean (i.e., no trend), no systematic changes in variance, and if periodic components have been removed (Chatfield, 1996). For this article, we use the concept of weak stationarity, where the mean and the variance must be independent of the length of the interval considered. In weak stationarity, higher moments are not considered. If the mean or the variance vary with the length of the interval considered, then the time series is nonstationary.

It is inappropriate to use correlograms for nonstationary time series, because the autocorrelation function,  $r$ , has the mean,  $\bar{y}$ , in its definition. An alternative way to measure long-range correlations, which is valid for both stationary and nonstationary time series, is the semivariogram  $\gamma$ . Like the autocorrelation function, the semivariogram measures the dependence of values in a time series that are separated by a lag,  $s$ . The variogram was developed by a French professor of mining and engineering, Matheron (1962, 1963a, b), for the analysis of ore reserves and their distribution. The variogram is a quantification of the mean-square successive differences within a time series taken at increasing lag,  $s$ ; i.e., how much the values on average vary from one another, hence the term "variogram." Note that the variogram is not a measure of the variance (second moment),  $V$ , of a time series, but rather the variance of increments within the time series. Geostatisticians (e.g., Journel and Huijbregts, 1978) generally use half of the variogram, called the semivariogram. There are many examples of the use of the semivariogram in geology and geophysics; for example, Oliver and Webster (1986) have applied semivariograms to landforms and soil properties, and Hewett (1986), along with a review of many other fractal techniques, uses semivariograms for the analysis of fluid transport.

For a continuous time series, the semivariogram,  $\gamma(s)$ , is given by

$$\gamma(s) = \frac{1}{2(T-s)} \int_0^{T-s} [y(t+s) - y(t)]^2 dt. \quad (7)$$

Note that neither the mean,  $\bar{y}$ , nor the variance,  $V$ , is used in this definition. For a discrete time series we have

$$\gamma_k = \frac{1}{2(N-k)} \sum_{n=1}^{N-k} (y_{n+k} - y_n)^2. \quad (8)$$

Increasing values of  $s$  or  $k$  correspond to increasing lag. The plot of  $\gamma_s$  vs  $s$  or  $\gamma_k$  vs  $k$  is known as a semivariogram. For a stationary time series, the

semivariogram,  $\gamma_k$ , and the autocorrelation function,  $r_k$ , are related. The mean of the time series,  $\bar{y}$ , can be added and subtracted within the summation in Eq. (8) to give

$$\gamma_k = \frac{1}{2(N-k)} \sum_{n=1}^{N-k} [(y_{n+k} - \bar{y}) - (y_n - \bar{y})]^2. \quad (9)$$

When expanded this gives

$$\gamma_k = \frac{1}{2(N-k)} \left[ \sum_{n=1}^{N-k} (y_{n+k} - \bar{y})^2 + \sum_{n=1}^{N-k} (y_n - \bar{y})^2 - \sum_{n=1}^{N-k} 2(y_{n+k} - \bar{y})(y_n - \bar{y}) \right]. \quad (10)$$

Provided the time series is stationary, two of the terms in Eq. (10) are equivalent to the variance in Eq. (6), giving

$$\gamma_k = V - \frac{1}{(N-k)} \sum_{n=1}^{N-k} (y_{n+k} - \bar{y})(y_n - \bar{y}). \quad (11)$$

Substituting the definition for  $c_k$  from Eq. (5) into Eq. (11) and using the definitions of  $c_0$  from Eq. (6) and  $r_k$  from Eq. (4), we find

$$\gamma_k = (V - c_k) = \left( V - V \frac{c_k}{c_0} \right) = V(1 - r_k). \quad (12)$$

For an uncorrelated time series we have  $r_k = 0$  and  $\gamma_k = V$ . In Section 3.4, we use semivariograms to quantify some nonstationary time series that exhibit long-range persistence; the quantification will give us a measure of the strength of the persistence.

Both the autocorrelation function and semivariograms have been applied by a number of authors to synthetic time series that exhibit long-range persistence, similar to the synthetic time series used in this paper. Schepers *et al.* (1992) applied the autocorrelation function to synthetic stationary time series. Gallant *et al.* (1994) applied the semivariogram to both stationary and nonstationary synthetic time series. Beran (1992, 1994) has an extensive discussion of the relationship between the autocorrelation function and long-range persistence; in addition, he gives extensive references to applications.

### 1.5. Self-Affine Fractals

Before continuing our discussion of time series, we introduce the concept of the self-affine fractal and the Hausdorff exponent. Extensive work has been done in this area over the last two decades (Mandelbrot, 1982, 1985, 1986; Feder, 1988; Meakin, 1988; Korvin, 1992; Hastings and Sugihara, 1993; Schmittbuhl *et al.*, 1995; Turcotte, 1997).

The concept of fractals finds its origins in the concept of scale invariance. In the geological sciences, there are many examples of scale invariance. For example, a photograph of a geological outcrop requires a scale, such as a person or a rock hammer, in order for the viewer to have an idea of how big or how small the folds, layers of rocks, and other structures are in the outcrop. Mandelbrot (1967) introduced the concept of fractals by examining the length of the coastline of Britain with different-sized measuring rods, and found a power-law dependence (scale invariance) of the total length of the coastline on the length of the measuring rod. In addition, a distribution of objects is fractal if the frequency-size distribution satisfies a power law. Examples include the frequency-size distributions of faults, earthquakes, volcanic eruptions, mineral deposits, and oil fields. We examine first the concept of self-similar fractals and then the more general case of self-affine fractals.

A statistically self-similar fractal is by definition isotropic. In two dimensions defined by  $x$ - and  $y$ -coordinates, the results do not depend on the geometrical orientation of the  $x$ - and  $y$ -axes. A formal definition of a self-similar fractal in two-dimensional  $xy$ -space is that  $f(rx, ry)$  is statistically similar to  $f(x, y)$ , where  $r$  is a scaling factor. This result is quantified by the fractal relation (Turcotte, 1997)

$$N_i \sim r_i^{-D}, \quad (13)$$

where the number of objects,  $N_i$ , and the characteristic linear dimension,  $r_i$ , are related by a power law, and the constant exponent,  $D$ , is the fractal dimension. There are also formal limits on the acceptable values of  $D$ . Fractals on a line have  $0 \leq D \leq 1$ , fractals on a surface have  $0 \leq D \leq 2$ , and fractals in a volume have  $0 \leq D \leq 3$ .

One method for determining the fractal dimension of a rocky coastline is to determine the number of boxes required to cover a map of the coastline. If the number of boxes with dimension  $r_1$  required to cover the rocky coastline is  $N_1$  and if the number of boxes with dimension  $r_2$  required to cover the rocky coastline is  $N_2$ , then the rocky coastline is a self-similar fractal if  $N_1$  and  $N_2$  satisfy Eq. (13), i.e.,  $(N_1/N_2) \sim (r_1/r_2)^{-D}$ .

A statistically self-affine fractal is generally not isotropic; the  $x$ - and  $y$ -coordinates can scale differently. The boxes used to quantify self-affine fractal are rectangular instead of square. A definition of a self-affine fractal (Mandelbrot, 1982; Voss, 1985c) in a two-dimensional  $xy$ -space is

$$f(rx, r^{Ha}y) \text{ is statistically similar to } f(x, y), \quad (14)$$

where  $x$  and  $y$  are variables,  $r$  is a scaling factor, and  $Ha$ , the Hausdorff exponent, is a constant.

For the special case where  $Ha = 1$ , the self-affine fractal is also self-similar. Topography along a linear track is usually an example of a naturally occurring, self-affine fractal. Consider the mean of many  $\Delta h$ , where  $\Delta h$  is the difference in elevation between pairs of points separated by a horizontal distance  $L$ . Self-affinity of topography implies that

$$\Delta h(L) \sim L^{Ha}, \quad (15)$$

where  $Ha$  is again the Hausdorff exponent. Ahnert (1984) found that actual topography is in very good agreement with Eq. (15) taking  $Ha = 0.6 \pm 0.1$ .

A deterministic construction of a self-affine fractal is illustrated in Fig. 2 (Mandelbrot, 1985; Section 3.3 of Barabási and Stanley, 1995). In this deterministic construction, a rectangular region with width  $r_0$  and arbitrary height  $h_0$  is considered. Note that the aspect ratio of this rectangle is irrelevant since the units of  $r_0$  and  $h_0$  are arbitrary. At all orders this fractal construction will begin at  $(0, 0)$  and end at  $(r_0, h_0)$ . At zero order, Fig. 2a, a straight line is drawn between  $(0, 0)$  and  $(r_0, h_0)$ . At first order, Fig. 2b, the self-affine fractal is defined by dividing the horizontal coordinate into four equal parts so that  $r_1 = r_0/4$  and dividing the vertical coordinate into two equal parts so that  $h_1 = h_0/2$ . Connecting the points  $(0, 0)$ ,  $(r_0/4, h_0/2)$ ,  $(r_0/2, 0)$ , and  $(r_0, h_0)$  gives the generator that will be used for second and higher orders in this fractal construction, where the generator will replace each straight-line segment of preceding orders.

In the second-order fractal illustrated in Fig. 2c, the generator has replaced each straight-line segment in the first-order fractal. At second order, the horizontal coordinate has been divided into sixteen equal parts so that  $r_2 = r_0/16$ , and the vertical coordinate has been divided into four equal parts so that  $h_2 = h_0/4$ . In terms of the formal definition of a self-affine fractal given in Eq. (14),  $f(x/4, y/2)$  is statistically similar to  $f(x, y)$ ; at each step the horizontal coordinate has been divided into four equal parts and the vertical coordinate into two equal parts. Thus the Hausdorff exponent can be obtained from  $r = \frac{1}{4}$  and  $r^{Ha} = \frac{1}{2}$ . This gives  $(\frac{1}{4})^{Ha} = \frac{1}{2}$  with the result  $Ha = \frac{1}{2}$ . This construction of a self-affine fractal

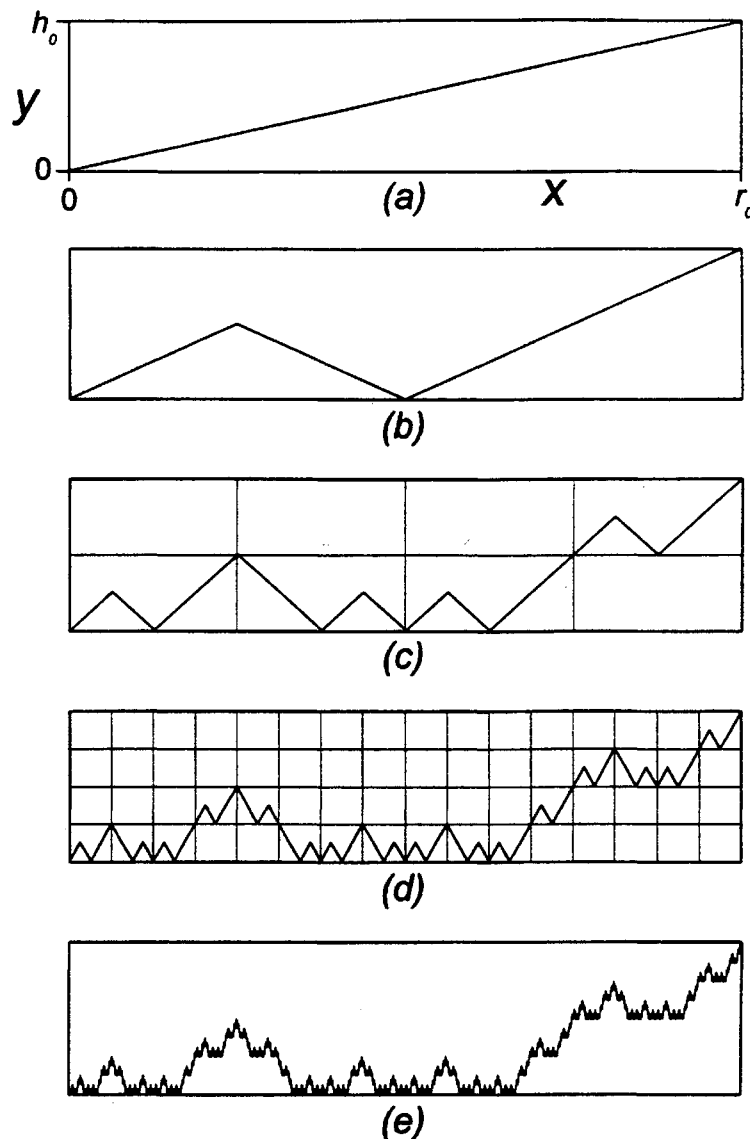


FIG. 2. Illustration of a deterministic self-affine fractal. (a) At zero order, a rectangular region of width  $r_0$  and height  $h_0$  is considered. A straight-line segment extends from  $(0, 0)$  to  $(r_0, h_0)$ . (b) The first-order self-affine fractal is given. This construction also serves as the generator for higher-order fractals. (c) Each first-order straight-line segment in Fig. 2b is replaced by the rescaled generator from Fig. 2b to give the second-order fractal construction. (d) Each second-order straight-line segment in Fig. 2c is replaced by the rescaled generator from Fig. 2b to give the third order fractal. (e) The construction is carried out to sixth order.

is extended to third order in Fig. 2d, where the generator has replaced each straight-line segment in the second-order fractal. In Fig. 2e, we extend this construction to sixth order. Note that this sixth-order construction looks very similar to a profile of topography. As we see later, this deterministic self-affine fractal construction has the same long-range persistence characteristics as both topography and Brownian motions.

To determine the fractal dimension of this self-affine fractal we use the box-counting method (Voss, 1988). For self-similar fractals we use square boxes, but for self-affine fractals it is necessary to use rectangular boxes. At zero order consider the single rectangular box with width  $r_0$  and height  $h_0$ ; thus  $N_0 = 1$ . At first order we have  $r_1 = r_0/4$ , so we will use rescaled rectangular boxes with width  $r_0/4$  and height  $h_0/4$ . The rescaled box has the same aspect ratio as the original box. We wish to determine how many of these boxes are required to cover the first-order fractal illustrated in Fig. 2b. This is illustrated in Fig. 3, where we find  $N_1 = 8$ . Using Eq. (13), we find

$$D = \frac{\log(N_1/N_0)}{\log(r_0/r_1)} = \frac{\log(8)}{\log(4)} = \frac{3 \log(2)}{2 \log(2)} = \frac{3}{2} = 1.5. \quad (16)$$

The fractal dimension,  $D$ , can be an integer, in which case it is equivalent to a Euclidean dimension. Euclidean dimensions of a point, line, square, and cube are, respectively, 0, 1, 2, and 3. In general,  $D$  is not integer, but some fraction between integers; this is the origin of the word fractal. The fractal dimension  $D = 1.5$  from Eq. (16) is intermediate between  $D = 1.0$  for a straight line and  $D = 2.0$  for a square.

### 1.6. Gaussian White Noises and Brownian Motions

The classic example of a stationary, discrete time series is a Gaussian white noise. Consider a variable  $\varepsilon_n$ ,  $n = 1, 2, 3, \dots, N$ , with a Gaussian

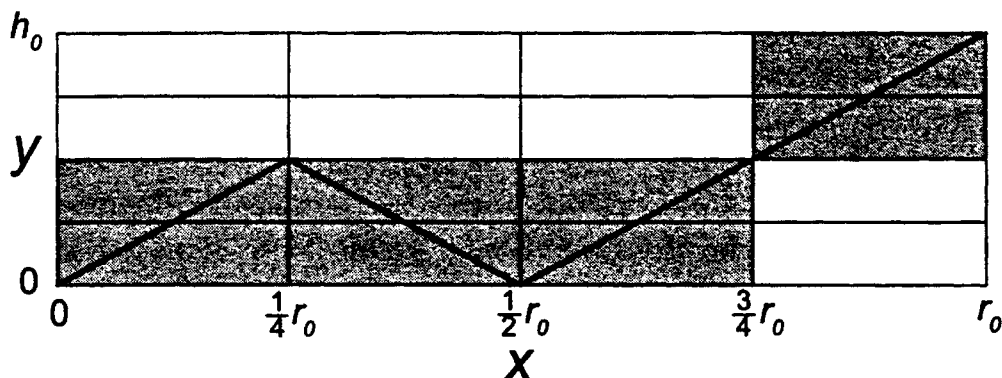


FIG. 3. Box-counting technique applied to the first-order self-affine fractal given in Fig. 2b. To determine its fractal dimension, rectangular boxes with width  $r_1 = r_0/4$  and height  $h_1 = h_0/4$  are used. This results in  $N_1 = 8$  shaded boxes (out of 16) covering the fractal construction. Noting that  $N_0 = 1$  box for the single box of width  $r_0$  and height  $h_0$ , we find the fractal dimension  $D = 1.5$ .

distribution of values that are uncorrelated and random; the distribution has zero mean and variance  $V_\varepsilon = \sigma_\varepsilon^2$ , where  $\sigma_\varepsilon$  is the standard deviation of the  $\varepsilon_n$ . The time series is stationary, so the variance does not vary for different subintervals. A white noise is a time series constructed with a set of  $y_n = \varepsilon_n$ . Four examples of synthetic Gaussian white noises are given in Fig. 4a. In each case,  $V_\varepsilon = 1$  and a different set of random numbers has been used.

The classic example of a nonstationary time series is a Brownian motion, obtained by summing a Gaussian white-noise sequence. For an excellent review of the theory and history of the Brownian motion, see Wang and Uhlenbeck (1945). The values in a Brownian-motion time series  $y'_n$  are given by

$$y'_n = \sum_{i=1}^n \varepsilon_i. \quad (17)$$

The white-noise sequences shown in Fig. 4a have been summed to give the four Brownian motions illustrated in Fig. 4b.

The variance of a Brownian motion, after  $n$  values of the white noise have been summed, is given by

$$V'_n = \sigma_\varepsilon^2 n, \quad (18)$$

where  $\sigma_\varepsilon^2 = V_\varepsilon$  is the variance of the white-noise sequence. The corresponding standard deviation of the motion is given by

$$\sigma'_n = \sigma_\varepsilon n^{1/2}. \quad (19)$$

This result is compared with each of the four Brownian motions illustrated in Fig. 4b.

In Eq. (14), the Hausdorff exponent,  $Ha$ , was introduced in the context of the self-affine scaling relation, where  $f(rx, r^{Ha}y)$  is statistically similar to  $f(x, y)$ , and the vertical and horizontal coordinates can scale differently. The standard deviation of a self-affine time series taken over  $n$  values is given by  $\sigma_n$ . We can associate  $\sigma_n$  with the  $y$ -coordinate of the self-affine relation, and the variable  $n$  with the  $x$ -coordinate. Then the dependence of the standard deviation,  $\sigma_n$ , on  $n$  can be expressed in terms of the Hausdorff exponent,  $Ha$ , (Mandelbrot and Van Ness, 1968), according to

$$\sigma_n \sim n^{Ha}, \quad (20)$$

with the corresponding variance given by

$$V_n \sim n^{2Ha}. \quad (21)$$

For a white noise,  $\sigma_n$  is independent of  $n$ ; thus  $Ha = 0$ . For any stationary time series,  $\sigma_n$  must be independent of  $n$ , by definition; thus again

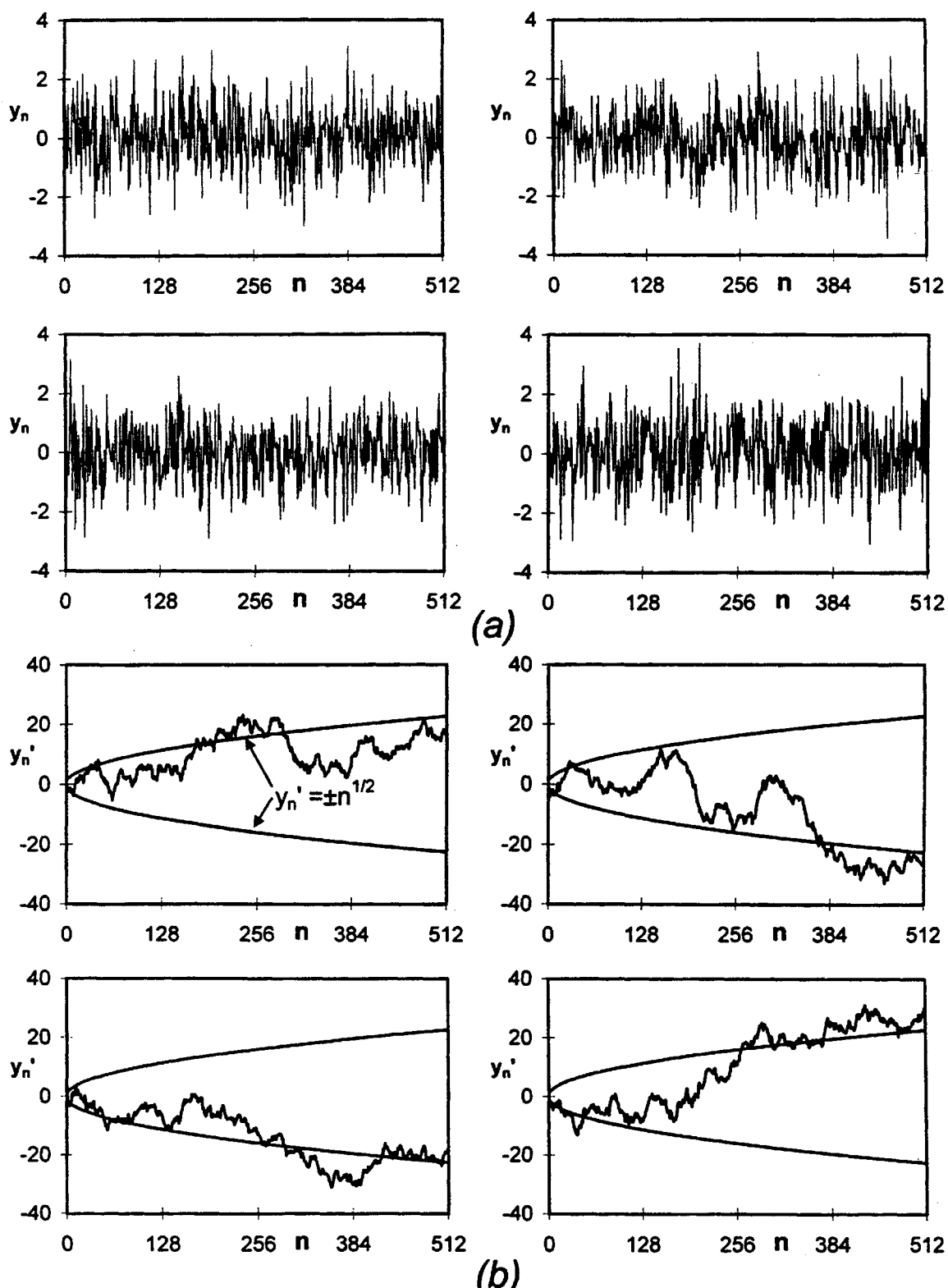


FIG. 4. (a) Four examples of Gaussian white noises. Successive values are chosen randomly from a Gaussian distribution with zero mean ( $\bar{y} = 0$ ) and unit variance ( $V = 1$ ). Adjacent values are not correlated. (b) The four white noises in (a) are summed using Eq. (17) to give four Brownian motions. In each case, the envelope given by the standard deviation after  $n$  steps, Eq. (19), is included.

$Ha = 0$ . From Eqs. (19) and (20) we find  $Ha = \frac{1}{2}$  for a Brownian motion. We also obtained  $Ha = \frac{1}{2}$  for the deterministic self-affine fractal illustrated in Fig. 2.

In Section 1.5, we gave an example of a deterministic fractal construction with a Hausdorff exponent of  $Ha = 0.5$  and calculated this construction to have a self-affine fractal dimension of  $D = 1.5$ . We now obtain a general relation (Voss, 1988), one that can be applied to self-affine time series, between the Hausdorff exponent,  $Ha$ , and the self-affine fractal dimension,  $D$ . A derivation of the fractal dimension of a self-affine time series can be obtained by using the box-counting method. We first introduce a rectangular reference “box” with a width  $T$ ; the height of the reference “box” is  $\sigma_T \equiv \sigma(T)$ , where  $\sigma(T)$  is the standard deviation of the signal  $y$  over the interval  $T$ . Since  $\sigma(T)$  is in general a function of  $T$ , we are studying, by definition, nonstationary processes (see Section 1.4); the standard deviation changes with the interval considered. The units of the signal  $y$ , and therefore the units of the signal’s standard deviation  $\sigma_T$ , can differ from the units of the interval  $T$ . Therefore, the aspect ratio (width to height =  $T/\sigma_T$ ) of the box can have arbitrary units. As an example, we consider the sixth-order deterministic self-affine fractal construction illustrated in Fig. 2e. This is analogous to a time series, with  $y$  varying from 0 to  $h_0$  over the interval 0 to  $r_0$ . The standard deviation of this series of data (Fig. 5a) over the interval  $T = r_0$  is calculated to be  $\sigma_T = h_0/4$ . The reference “box” for this example (Fig. 5b) has a width of  $T = r_0$  and a height of  $\sigma_T = h_0/4$ .

We next divide the interval  $T$  into  $N$  equal-sized smaller intervals with length  $\tau = T/N$ . The standard deviation of the signal  $y$  over each of these smaller intervals will be approximately the same, and is given by  $\sigma_\tau \equiv \sigma(\tau)$ . In our example (Fig. 5a), we let  $\tau = T/4 = r_0/4$ ; the standard deviation of the signal  $y$  over each of the smaller intervals  $\tau$  is calculated to be  $\sigma_\tau = h_0/8$ . We then introduce smaller rescaled boxes of width  $\tau = T/N$  and height  $\sigma_N = \sigma_T/N$ . These boxes have the same aspect ratio as the reference box. However, the standard deviation of the signal  $y$  over the interval  $\tau$ ,  $\sigma_\tau = \sigma(\tau)$ , is not necessarily equal to  $\sigma_N = \sigma_T/N$ . In our example (Fig. 5b), we divide our reference box into scaled smaller boxes with width  $\tau = T/4 = r_0/4$  and height  $\sigma_N = \sigma_T/4 = h_0/16$ .

We determine the number of scaled smaller boxes  $N_b$  of size  $\tau$  by  $\sigma_N$  that are required to cover the area of width  $T$  and height  $\sigma_\tau$ . In our example (Fig. 5b), we find  $N_b = 8$  boxes. This construction is generalized by writing

$$N_b = \frac{T\sigma_\tau}{\tau\sigma_N} = N\frac{\sigma_\tau}{\sigma_N} = N^2\frac{\sigma_\tau}{\sigma_T}. \quad (22)$$

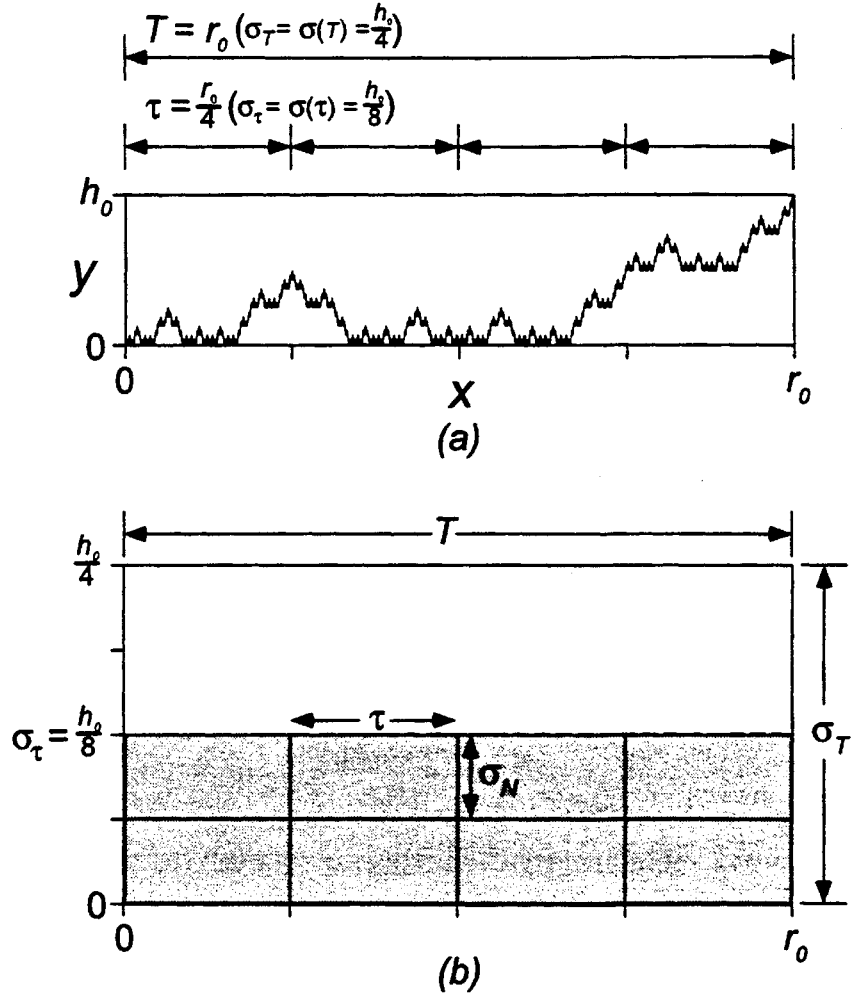


FIG. 5. (a) The sixth-order deterministic self-affine fractal construction from Fig. 2e is shown with the standard deviations calculated for the entire series ( $T = r_0$ ) and for four equal smaller subdivisions of the series ( $\tau = r_0/4$ ). (b) Box counting for the standard deviations. The reference “box” has width  $T$ , the length of the original series, and height  $\sigma_T$ , the standard deviation for the entire series. The reference box is scaled by 4 in width and height, giving smaller boxes with width  $\tau = T/4$  and height  $\sigma_N = \sigma_T/4$ . The number of smaller scaled boxes ( $\tau$  by  $\sigma_N$ ) required to cover an area  $T$  by  $\sigma_\tau$ , where  $\sigma_\tau$  is the standard deviation of the series over each smaller subinterval  $\tau$ , is  $N_b = 8$ .

However, from Eq. (20) we have

$$\sigma(T) \sim T^{Ha}, \quad (23)$$

so we can write

$$\frac{\sigma_\tau}{\sigma_T} = \frac{\sigma(\tau)}{\sigma(T)} = \frac{\sigma(T/N)}{\sigma(T)} = \left(\frac{T/N}{T}\right)^{Ha} = \frac{1}{N^{Ha}}, \quad (24)$$

and combining Eqs. (22) and (24) gives

$$N_b = N^2 \left( \frac{1}{N^{Ha}} \right) = N^{2-Ha} = \left( \frac{T}{\tau} \right)^{2-Ha}. \quad (25)$$

In our example (Fig. 5),  $N_b = 8$ , and  $T/\tau = 4$ , i.e.,  $(8) = (4)^{2-Ha}$  giving  $(2 - Ha) = 1.5$ , thus  $Ha = 0.5$ . Equation (25) is a fractal relation: the number of boxes,  $N_b$ , is inversely proportional to the size of the subinterval considered, raised to a constant power  $(2 - Ha)$ . The interval over which the signal  $y$  is considered,  $T$ , is a constant. We can extend this analysis to smaller intervals of  $\tau$ , and at each different subinterval considered,  $\tau_i$ , there will be a corresponding  $N_{bi}$  boxes. Equation (25) becomes

$$N_{bi} = \left( \frac{T}{\tau_i} \right)^{2-Ha}. \quad (26)$$

If we compare this to the power-law relation from Eq. (13) and associate  $\tau_i$  with  $r_i$  and  $N_{bi}$  with  $N_i$ , then

$$Ha = 2 - D. \quad (27)$$

For a Brownian motion,  $Ha = \frac{1}{2}$  and we have  $D = \frac{3}{2}$ . We obtained the same result for our deterministic self-affine fractal example illustrated in Fig. 2:  $Ha = \frac{1}{2}$  and  $D = \frac{3}{2}$ . Since for the self-affine fractals illustrated here, the value for  $D$  is always between 1 (a line) and 2 (a square),  $Ha$  for a self-affine fractal is between 0 and 1. We have derived here a general equation for  $Ha$  as a function of  $D$ . Self-affine fractal time series,  $1 \leq D \leq 2$ , are a subset of self-affine time series. A smooth time series (low frequencies dominate over high frequencies) approaches a straight line so that it has a fractal dimension near 1. A very rough time series (with a large high-frequency component) becomes area filling and has a fractal dimension near 2.

An alternative measure of a self-affine time series is that the semivariogram,  $\gamma(s)$  or  $\gamma_k$  from Eqs. (7) or (8), scales with  $s$  or  $k$ , the lag, such that (Mandelbrot and Van Ness, 1968)

$$\gamma(s) \sim s^{2Ha} \quad (28)$$

and

$$\gamma_k \sim k^{2Ha}, \quad (29)$$

where, again,  $Ha$  is the Hausdorff exponent. The dependence of the semivariogram on the lag is directly analogous to the dependence of the variance of a time series,  $V_n$ , on the length of the time series,  $n$ , as given in Eq. (21). We verify Eqs. (28) and (29) when we determine the semivariograms of synthetic fractional motions in Section 3.4.

The Hausdorff exponent,  $Ha$ , and the fractal dimension,  $D$ , are both measures of the strength of persistence for a subclass of self-affine time series, for which  $0 \leq Ha \leq 1$  ( $1 \leq D \leq 2$ ). There are a number of other measures for the strength of persistence, discussed in this paper, which can be used to calculate the strength of persistence for self-affine time series that do not fall in the range where  $Ha$  and  $D$  are useful. General discussions of methods used to estimate  $Ha$ ,  $D$ , and other measures of the persistence of time series have been given by Korvin (1992), Schepers *et al.* (1992), Schmittbuhl *et al.* (1995), and Hall (1997).

## 2. SPECTRAL ANALYSIS

### 2.1. The Fourier Transform

Spectral analysis is a technique that estimates the spectral density function, or spectrum, of a time series. In the past, most spectral analyses were concerned with finding periodicities in data; today, they are widely used to obtain a complete spectrum over a wide range of frequencies. One standard approach is to carry out a Fourier transform on a time series. Fourier analysis is essentially concerned with approximating a function by a sum of sine and cosine terms. A large body of literature has been written on Fourier analysis and spectral analysis in general; comprehensive summaries have been given by Priestley (1981) and Percival and Walden (1993). Press *et al.* (1994) provide an easy to understand basic theory and computational implementation of most techniques found in spectral analysis.

A time series can be prescribed either in the time domain as  $y(t)$  or in the frequency domain in terms of the Fourier transform,  $Y(f)$ , where  $f$  is the frequency. The quantity  $Y(f)$  is generally a complex number indicating both the amplitude and the phase of the signal. We first begin with the general case where  $g(t)$  is a continuous function that satisfies  $g(t) = g(t + kT)$ ,  $k = 0, \pm 1, \pm 2, \pm 3, \dots$ , and the function  $g(t)$  is defined for all  $t$ ,  $-\infty < t < +\infty$ . If  $T$  is the smallest number that satisfies  $g(t) = g(t + kT)$ , then the function  $g(t)$  is periodic with a period  $T$ . If there is no value of  $k$  (other than  $k = 0$ ) for which  $g(t) = g(t + kT)$  holds, then  $g(t)$  is nonperiodic. The Fourier transform,  $G(f)$ , of the periodic continuous function,  $g(t)$ , is defined as

$$G(f) = \int_{-\infty}^{\infty} g(t)e^{2\pi ift} dt. \quad (30)$$

The complementary inverse Fourier transform is then given by

$$g(t) = \int_{-\infty}^{\infty} G(f)e^{-2\pi ift} df. \quad (31)$$

The exponents in Eqs. (30) and (31) represent an infinite number of sine and cosine functions, with  $e^{-2\pi ift} = \cos(2\pi ft) + i \sin(2\pi ft)$ . The  $i$  in the exponents is the square root of  $-1$ . One goes between  $g(t)$  and  $G(f)$  by the use of the Fourier transform equations given in Eqs. (30) and (31). The Fourier transform,  $G(f)$ , of the time series represents the contribution of each sine and cosine function at each frequency, and is commonly called the Fourier spectrum of  $g(t)$ .

A time series with three periodic components at periods  $T$ ,  $T/2$ , and  $T/5$ , will have spikes in its Fourier spectrum at the frequencies  $f = 1/T$ ,  $2/T$ , and  $5/T$ . If  $T$  has the units of seconds, then  $f$  will have the units of cycles per second. A white noise has no embedded frequencies and its Fourier spectrum is approximately flat. We use frequency,  $f$ , instead of the alternative angular frequency,  $\omega = 2\pi f$ , because  $f$  is more informative for the time series we consider in this article.

For this article, we are interested in stochastic time series that are nonperiodic and defined over a finite interval,  $0 \leq t \leq T$ . For  $t$  outside this interval ( $t < 0$  and  $t > T$ ), we require  $y(t) = 0$ . A periodic time series is normally composed of a finite number of subperiods, corresponding to a finite number of spikes at discrete frequencies in the resulting Fourier spectrum. A nonperiodic function has no fixed period or subperiods and instead can be viewed as being composed of an infinite number of subperiods in the time domain or a continuous and infinite range of frequencies in the Fourier frequency domain. We use the notation  $Y(f, T)$  when taking the Fourier transform of  $y(t)$  over the interval  $0 \leq t \leq T$ . For a stochastic nonperiodic time series, the Fourier transform pair given by Eqs. (30) and (31) becomes (Priestley, 1981)

$$Y(f, T) = \int_0^T y(t)e^{2\pi ift} dt \quad (32)$$

and

$$y(t) = \int_{-\infty}^{\infty} Y(f, T)e^{-2\pi ift} df. \quad (33)$$

In the time domain, Eq. (32), the integral is from  $0 \leq t \leq T$ , since  $y(t) = 0$  outside this range; however, in the frequency domain, Eq. (33), there is a continuous range of frequencies possible,  $-\infty < f < +\infty$ , since we are dealing with a nonperiodic function. In Eq. (32) we could have defined  $y(t)$  to range from  $-T/2 \leq t \leq T/2$  (commonly done in many texts) instead of

$0 \leq t \leq T$ ; however, the result in Eq. (32) would be the same except that the integral would be  $-T/2$  to  $T/2$  instead of  $0$  to  $T$ . The units of the Fourier transform depend on the units of the time series  $y(t)$ . For example, if the units for  $y(t)$  are in amperes and the units for  $t$  in seconds, then the Fourier transform,  $Y(f, T)$ , has the units of ampere-second, and the frequency,  $f$ , has the units of second<sup>-1</sup>.

The concepts described above are easily modified for discrete time series. Consider the discrete time series,  $y_n$ ,  $n = 1, 2, 3, \dots, N$ , where the total time interval,  $T$ , has been divided into  $N$  equal intervals of length  $\delta$ , i.e.,  $\delta = T/N$ . The units of  $\delta$  are those of  $T$ ;  $N$  is dimensionless. Many authors do not include  $\delta$  in their studies of discrete time series; they assume  $\delta = 1$  time unit. We include  $\delta$  in the equations that follow so that the units will be analogous to the equations given for continuous time series. If we approximate the integrals given in Eqs. (32) and (33), then the discrete Fourier transform (DFT) applied to the discrete time series,  $y_n$ , is (Priestley, 1981)

$$Y_m = \delta \sum_{n=1}^N y_n e^{2\pi i n m / N}, \quad m = 1, 2, 3, \dots, N, \quad (34)$$

and the inverse DFT is

$$y_n = \frac{1}{N\delta} \sum_{m=1}^N Y_m e^{-2\pi i n m / N}, \quad m = 1, 2, 3, \dots, N. \quad (35)$$

There are now discrete values in both the time and frequency domains. Many variations on the DFT pairs exist (see, e.g., Percival and Walden, 1993, for a complete discussion). Some authors let the running variable in Eqs. (34) and (35) vary from  $0$  to  $(N - 1)$ . For consistency with the rest of this article, we allow the index to run from  $1$  to  $N$ ; the Fourier pairs are equivalent for the two different running indices (Priestley, 1981). The Fourier coefficients,  $Y_m$ ,  $m = 1, 2, 3, \dots, N$ , are associated with frequencies  $f_m = m/(N\delta)$ . As before, the Fourier coefficients,  $Y_m$ , are complex numbers with real and imaginary parts,  $Y_m = a_m + ib_m$ . The complex modulus of  $Y_m$  is

$$|Y_m| = \sqrt{(a_m^2 + b_m^2)}. \quad (36)$$

The Fourier coefficients are symmetric such that

$$|Y_m| = |Y_{N-m}|. \quad (37)$$

For example, if  $N = 4096$ , then  $|Y_1| = |Y_{4095}|$ ,  $|Y_2| = |Y_{4094}|$ , etc. The highest frequency resolvable using Fourier analysis of a discrete time series,  $y_n$ ,

$n = 1, 2, 3, \dots, N$ , is the frequency with a period of 2 time units,  $2\delta$ . Any spectral components of a higher frequency cannot be distinguished from lower-frequency components; this is aliasing. Consequently, the highest frequency that we can resolve in Fourier space will be  $f_m = 0.5$ , where  $f_m = m/(N\delta)$ ; the unique Fourier coefficients will be given by  $Y_m$ ,  $m = 1, 2, 3, \dots, N/2$ .

## 2.2. The Power-Spectral Density

The modulus of the complex number  $Y(f) = (a + bi)$  is given by  $|Y(f)| = (a^2 + b^2)^{1/2}$ . In the frequency domain, a measure of the energy distribution of a signal as a function of frequency is  $|Y(f, T)|^2$ . As  $T$  approaches infinity, the total energy diverges and also approaches infinity. Thus it is standard practice to convert the energy to power; that is, we divide  $|Y(f, T)|^2$  by  $T$ . The power-spectral density function of  $y(t)$  is defined (Priestley, 1981) as

$$S(f) = \lim_{T \rightarrow \infty} \left\{ \frac{|Y(f, T)|^2}{T} \right\}. \quad (38)$$

The function  $S(f)$  in Eq. (38) is for the limit as  $T$  goes to infinity. For a discrete time series, one calculates an estimate of  $S(f)$ . A plot of this estimate of  $S(f)$  against  $f$  is known as a periodogram. In terms of units, if  $y(t)$  is in amperes,  $t$  (and  $T$ ) in seconds, and  $Y(f, T)$  in ampere-seconds, then  $|Y(f, T)|^2$  has the units of ampere<sup>2</sup>-second<sup>2</sup>, and the power-spectral distribution function,  $S(f)$ , has the units of ampere<sup>2</sup>-second.

The quantity  $S(f) df$  in a periodogram represents the contribution to the total power from those components in the time series,  $y(t)$ , whose frequencies lie in the interval between  $f$  and  $f + df$ . For a time series that is self-affine, the power-spectral density is defined (e.g., Voss, 1985a) to have a power-law dependence on frequency

$$S(f) \sim f^{-\beta}. \quad (39)$$

This relation also defines a self-affine fractal in the same way that  $N_i \sim r_i^{-D}$ , Eq. (13), defines a self-similar fractal. The implications of Eq. (39) will be a major focus of this article. Because of the power-law dependence of  $S(f)$  on  $f$ , self-affine time series with  $\beta > 0$  exhibit long-range persistence, and self-affine time series with  $\beta < 0$  exhibit long-range antipersistence. The value of  $\beta$ , the slope of the best-fit straight line to  $\log(S(f))$  vs  $\log(f)$ , is a measure of the strength of persistence or antipersistence in a time series.

The power-spectral density function,  $S_m$ , for a discrete time series,  $y_n$ , can be written as

$$S_m = \lim_{N \rightarrow \infty} \left\{ \frac{2|Y_m|^2}{N\delta} \right\}, \quad m = 1, 2, 3, \dots, \frac{N}{2}. \quad (40)$$

The factor of 2 in Eq. (40) is a result of summing  $Y_m$  from  $m = 1$  to  $N/2$  instead of  $N$ . For a discrete self-affine time series, the power-spectral density,  $S_m$ , again has a power-law dependence on frequency

$$S_m \sim \left( \frac{m}{N\delta} \right)^{-\beta}, \quad m = 1, 2, 3, \dots, \frac{N}{2}. \quad (41)$$

This is equivalent to

$$S_m \sim f_m^{-\beta}, \quad m = 1, 2, 3, \dots, \frac{N}{2}. \quad (42)$$

As an example, we obtain the discrete power-spectral density for two discrete time series. We use the fast Fourier transform (e.g., Press *et al.*, 1994), an algorithm that is commonly used to speed up the computation of the discrete Fourier transform. The first time series is a white noise (Fig. 6a), where the values are randomly chosen from a Gaussian (normal) distribution with mean  $\bar{y} = 0$  and variance  $V = 1$ . The second time series is the corresponding Brownian motion (Fig. 6c) obtained by summing the white noise given in Fig. 6a using Eq. (17). The Brownian motion has a mean  $\bar{y} = -23$  and variance  $V = 950$ . Both time series have  $N = 4096$  points.

The two resulting periodograms,  $S_m$  plotted as a function of  $f_m$  with log-log scaling, are shown in Figs. 6b, d. Plotted on log-log axes, there are many more values of  $S_m$  at the high frequencies ( $f_m$  large) than at low frequencies. Therefore, to obtain the best-fit straight line to  $\log(S_m)$  vs  $\log(f_m)$ , we bin the data. We first divide the  $f_m$  axis into equal log-increments, then for each  $\log(f_m)$  bin calculate the average of all the  $\log(S_m)$  that are in that bin. The best-fit least-squares straight line is then calculated for the resulting average( $\log(S_m)$ ) as a function of the center of each  $\log(f_m)$  bin; these values are plotted as circles in Figs. 6b, d, with the best-fit straight line to these circles shown.

We use  $\beta_{PS}$  to indicate the negative of the slope of the best-fit straight line when applying power-spectral analysis, Eq. (42). Because the white noise is a stationary uncorrelated time series, we expect the power spectrum to be essentially flat; i.e., all frequencies are present in equal amounts. For the example given in Fig. 6b we find  $\beta_{PS} = -0.03$ , close to the theoretical value of  $\beta = 0$ . The Brownian motion (Fig. 6c) is a non-stationary signal that is much ‘‘smoother’’ than the white noise (Fig. 6a).

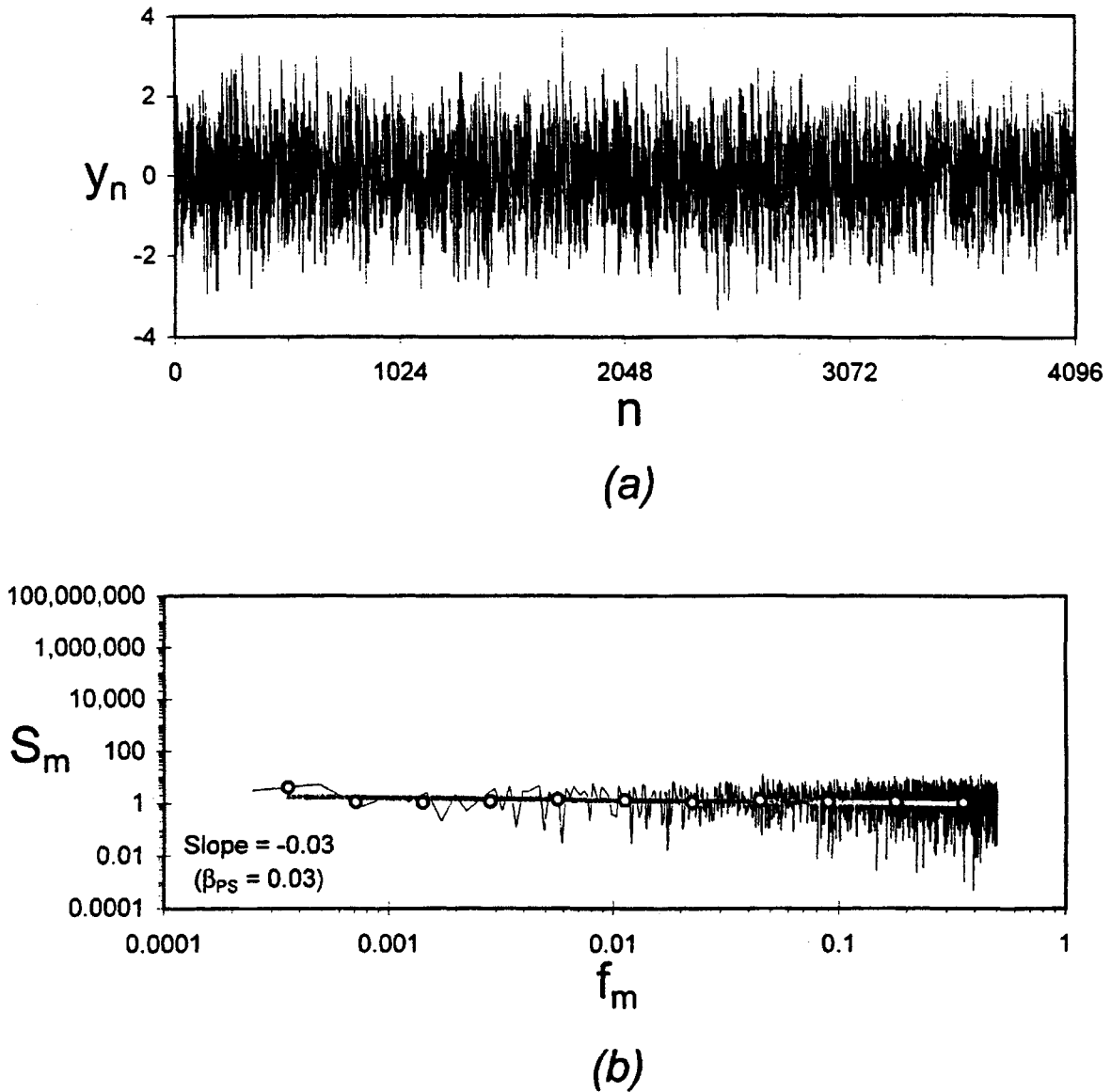


FIG. 6. Two examples of power-spectral analysis. Two time series are given in (a) and (c) with their respective periodograms given in (b) and (d). The first time series (a) is a white noise with  $N = 4096$  points, and was obtained by randomly choosing values from a Gaussian distribution of values with a mean,  $\bar{y} = 0$ , and a variance,  $V = 1$ . The second time series (c) is a Brownian motion obtained by summing the white noise in (a); it has a mean,  $\bar{y} = -23$ , and a variance,  $V = 950$ . The Fourier power spectrum (periodograms) for the white noise and Brownian motion are shown, respectively, in (b) and (d). In both periodograms, the power spectral-density function,  $S_m$ , from Eq. (40) is given as a function of frequency  $f_m = m/N$ , where  $m = 1, 2, 3, \dots, N/2$ . The circles are obtained by averaging the  $\log(S_m)$  into equal  $\log(f_m)$  bins. In the log-log plots, the value of  $\beta_{PS}$  is the negative of the slope of the best-fit least-squares straight line to the circles. The white noise has  $\beta_{PS} \approx 0$ , and the Brownian motion has  $\beta_{PS} \approx 2$ .

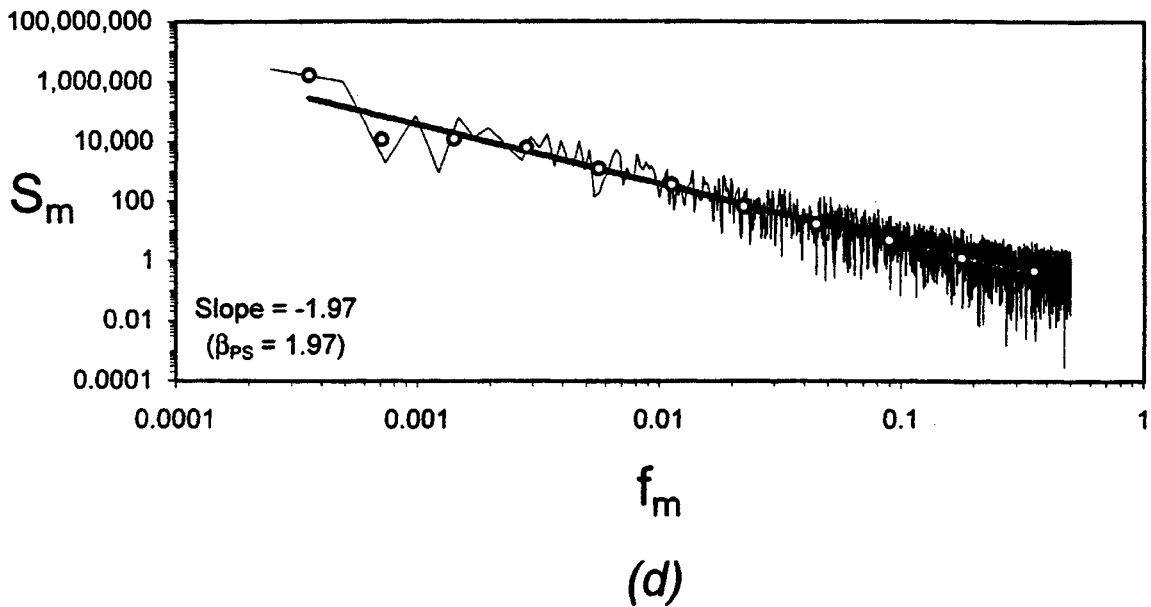
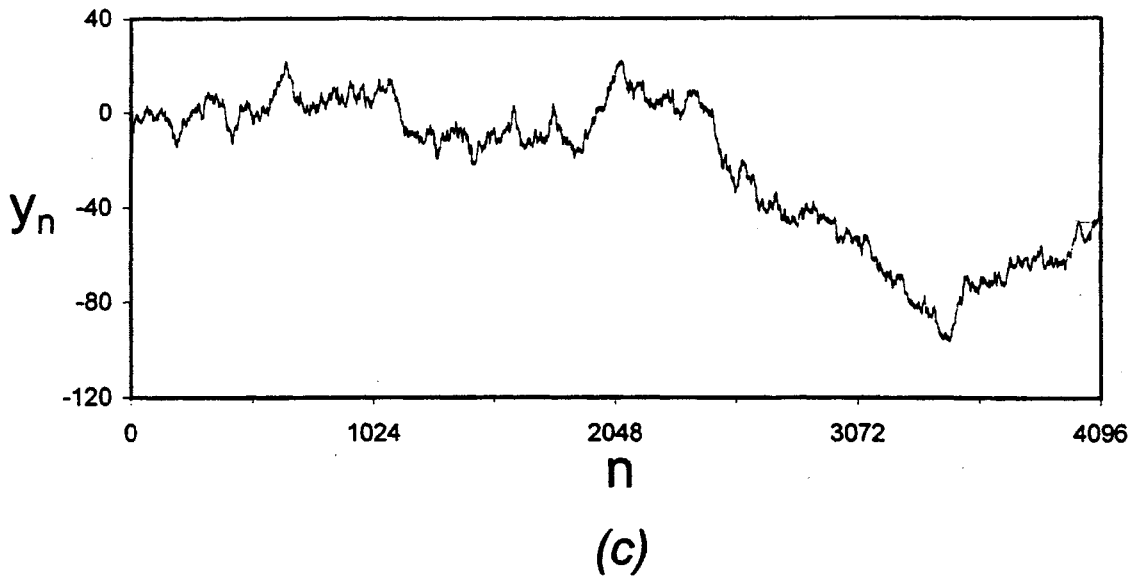


FIG. 6. *Continued.*

Thus, we expect that the low frequencies ( $f_m$  small) will be dominant over the high frequencies ( $f_m$  large), and that the slope of the best-fit straight line will be negative and  $\beta$  positive. This is found to be true; the Brownian motion has a slope  $-1.97$ , i.e.,  $\beta_{PS} = 1.97$ .

We found that a Brownian motion (a summed white noise) has  $\beta_{PS} \approx 2$  and a white noise has  $\beta_{PS} \approx 0$ ; the summed time series has a  $\beta_{PS}$  that is approximately  $+2$  larger than the nonsummed time series. This can be generalized to all self-affine time series: summing a self-affine time series shifts the theoretical power-spectral density exponent,  $\beta$ , by  $+2$ . We can

also reverse the process; the differences in adjacent values (the first differences) of a Brownian motion result in a white noise. This can also be generalized to all self-affine time series: taking the first differences shifts the theoretical power-spectral density exponent,  $\beta$ , by  $-2$ . We will now show that this is true by considering the derivative (first difference) of a self-affine time series.

The self-affine time series,  $y(t)$ , has a corresponding Fourier transform,  $Y(f, T)$ , defined by Eq. (32) and a power-spectral density function,  $S(f)$ , defined by Eq. (38). The derivative of  $y(t)$ ,  $y'(t)$ , with its corresponding inverse Fourier transform from Eq. (33), is given by

$$y'(t) = \frac{dy(t)}{dt} = \int_{-\infty}^{\infty} Y'(f, T) e^{-2\pi ift} df. \quad (43)$$

The corresponding Fourier transform from Eq. (32) of  $y'(t)$  is

$$Y'(f, T) = \int_0^T y'(t) e^{2\pi ift} dt. \quad (44)$$

Taking the derivative of both sides of Eq. (33) gives

$$\begin{aligned} y'(t) &= \frac{dy(t)}{dt} = \frac{d}{dt} \left[ \int_{-\infty}^{\infty} Y(f, T) e^{-2\pi ift} df \right] \\ &= \int_{-\infty}^{\infty} (-2\pi if) Y(f, T) e^{-2\pi ift} df. \end{aligned} \quad (45)$$

Comparing the right-hand sides of Eqs. (43) and (45), the integrands must be equal; therefore,

$$Y'(f, T) = (-2\pi if) Y(f, T). \quad (46)$$

Using Eq. (38), the power-spectral density function,  $S'(f)$ , corresponding to  $y'(t)$  is

$$S'(f) = \lim_{T \rightarrow \infty} \left\{ \frac{|(-2\pi if) Y(f, T)|^2}{T} \right\} = (4\pi^2 f^2) S(f), \quad (47)$$

where  $S(f)$  is the power-spectral density function, Eq. (38), of  $y(t)$ . Finally, from Eq. (39), where the power-spectral density function has a power-law dependence on frequency, we can write

$$f^{-\beta'} \sim (4\pi^2 f^2) f^{-\beta}, \quad (48)$$

which simplifies to

$$f^{-\beta'} \sim f^{-\beta+2} \quad (49)$$

and

$$\beta' = \beta - 2. \quad (50)$$

If the self-affine time series,  $y(t)$ , is characterized by a power-spectral exponent,  $\beta$ , then the first difference (derivative) of that time series is characterized by a power-spectral exponent of  $\beta - 2$ . We can use the same logic as that shown in Eqs. (43) through (50) to show that if  $y(t)$  has a characteristic  $\beta$ , then the running sum (integral) of  $y(t)$  is characterized by a power-spectral exponent of  $\beta + 2$ . Thus since  $\beta = 0$  for a white noise, we expect  $\beta = 2$  for a Brownian motion, close to the value found. In subsequent sections, we will use this summing and differencing property as part of the construction of a variety of synthetic self-affine time series.

The power-spectral density function can also be related to other statistical measures of time series. We introduced the autocorrelation function  $r_k = c_k/c_0$  in Eq. (4), with  $c_k$  given by Eq. (5) and  $c_0$  (the variance) by Eq. (6). The autocorrelation function is directly related to the power-spectral density (Box *et al.*, 1994) by

$$S_m = 2 \left\{ c_0 + 2 \sum_{k=1}^{N-1} \left[ \left( 1 - \frac{k}{N} \right) c_k \cos \left( \frac{2\pi mk}{N} \right) \right] \right\}, \quad m = 1, 2, 3, \dots, \frac{N}{2}. \quad (51)$$

The power-spectral density is the Fourier transform of  $c_k$ . There are no sine components in Eq. (51) because the autocorrelation function is an even function (symmetric around the  $y$  axis). There is a  $(1 - (k/N))$  in Eq. (51) because of the way we defined the autocorrelation function in Eq. (5); note that in many texts this factor would not be included in Eq. (51). The autocorrelation function and the power-spectral density are equivalent ways of describing a stochastic process; both contain the same information but express it in different ways. In this article, we use the power-spectral density in order to quantify the persistence in time series.

We next relate the power-spectral density function,  $S_m$ , to the variance,  $V_N$ , of a discrete time series,  $y_n$ ,  $n = 1, 2, 3, \dots, N$ . The successive values of the time series  $y_n$  are prescribed at equal increments of time,  $\delta$ . Using Parseval's theorem (e.g., Percival and Walden, 1993), we write

$$V_N = \frac{1}{N} \sum_{n=1}^N (y_n - \bar{y})^2 = \frac{2}{N^2 \delta^2} \sum_{m=1}^{N/2} |Y_m|^2 = \frac{2}{N \delta} \sum_{m=1}^{N/2} S_m. \quad (52)$$

The variance,  $V_N$ , is proportional to the summation of  $S_m$ , the power-spectral density function. Parseval's theorem states that the total power in a signal is the same whether it is computed in the time domain or the

frequency domain. Note that many authors take  $\bar{y} = 0$  in writing Parseval's theorem. Equation (52) gives the result that the variance of a discrete time series of length  $N$  is proportional to the sum of the power-spectral density coefficients,  $S_m$ .

### 2.3. The Relation of $\beta$ , $Ha$ , and $D$

Using a derivation from Voss (1985c), we now obtain a relationship between the power  $\beta$ , the Hausdorff exponent  $Ha$ , and the fractal dimension  $D$ . Consider a time series  $y_1(t)$  specified over the interval  $0 \leq t \leq rT$ . Next consider two time series that are based on  $y_1(t)$ :  $y_1(rt)$  with  $0 \leq t \leq T$ , and  $y_2(t)$  also with  $0 \leq t \leq T$ . These are related by

$$y_2(t) = \frac{1}{r^{Ha}} y_1(rt), \quad 0 \leq t \leq T, \quad (53)$$

where  $Ha$  is the Hausdorff exponent. This process is illustrated in Fig. 7 for  $r = 0.2$ ,  $Ha = 0.5$ , and  $T = 1.0$ . In Fig. 7a, we show a time series  $y_1(t)$ ,  $0 \leq t \leq T$ , with the area under the curve of  $y_1(t)$  shaded from  $0 \leq t \leq rT$ . Figure 7b shows  $y_1(rt)$  from  $0 \leq t \leq T$ ; i.e., the time axis of  $y_1(t)$  in Fig. 7a has been "stretched out" in Fig. 7b by a factor of  $(1/r) = 5$ . Finally, in Fig. 7c, we have stretched the amplitude of  $y_1(rt)$  by a factor of  $(1/r)^{-Ha} = 5^{0.5} \approx 2.32$ . The fundamental property of a self-affine time series is that  $y_1(t)$  taken over the time period  $rT$  (shaded part in Fig. 7a) has the same statistical properties as  $y_2(t)$  taken over the time period  $T$  (shaded part in Fig. 7c), with  $y_1(rt)$  and  $y_2(t)$  related by Eq. (53).

The Fourier transform, Eq. (32), of  $y_2(t)$  taken over  $T$  has a continuous range of frequencies,  $f$ , and is given by

$$Y_2(f, T) = \int_0^T y_2(t) e^{2\pi i f t} dt. \quad (54)$$

Substituting Eq. (53) and making the change of variable  $t' = rt$ , we obtain

$$Y_2(f, T) = \int_0^{rT} \frac{y_1(t')}{r^{Ha}} e^{2\pi i f t'/r} \frac{dt'}{r}. \quad (55)$$

Simplifying Eq. (55), substituting  $f' = f/r$  and  $T' = T/r$  into Eq. (55), and using Eq. (32), we have

$$Y_2(f, T) = \frac{1}{r^{Ha+1}} \int_0^{T'} y_1(t') e^{2\pi i f' t'} dt' = \frac{1}{r^{Ha+1}} Y_1(f', T'). \quad (56)$$

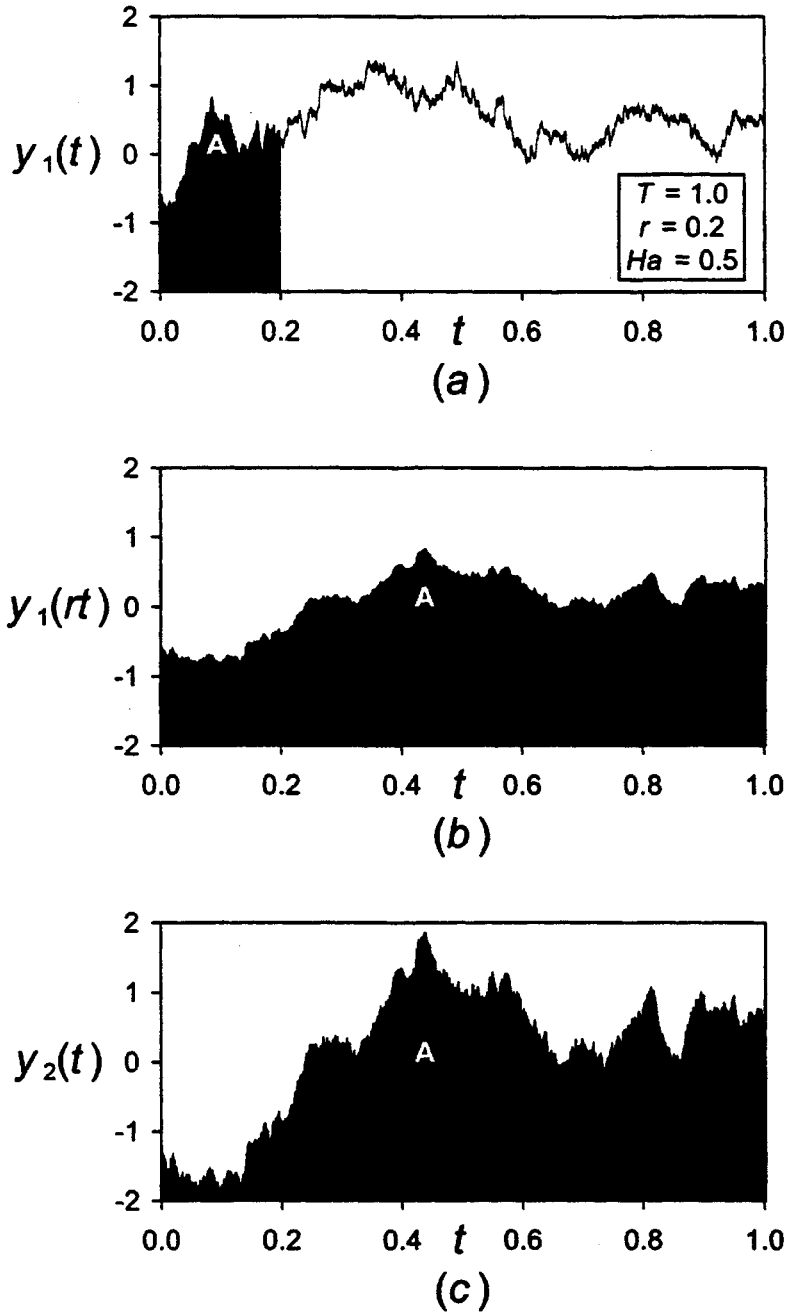


FIG. 7. Rescaling a self-affine time series. (a) A Brownian motion ( $Ha = 0.5$ ) is given by the time series  $y_1(t)$ , with  $0 \leq t \leq T$ . The Brownian motion has a Hausdorff exponent,  $Ha = 0.5$ , and was obtained by summing a Gaussian white noise. For this example, we let  $r = 0.2$  and  $T = 1.0$ . The area under the curve of  $y_1(t)$  is shaded from  $0 \leq t \leq rT$ . (b) The time axis of  $y_1(t)$ , the time series shown in Fig. 7a, is “stretched” by a factor of  $(1/r) = 5$ . The new time series,  $y_1(rt)$ , is shown for  $0 \leq t \leq T$ . The shaded area represents the part of  $y_1(t)$  from Fig. 7a that was expanded. The “A” in all three figures is to aid the eye in following the part of the time series that is rescaled from step to step. (c) The amplitude of the “stretched” time series from Fig. 7b,  $y_1(rt)$ , is now expanded by a factor of  $(1/r)^{-Ha} = 5^{0.5} = 2.32$ , giving a new time series  $y_2(t)$ ,  $0 \leq t \leq T$ . Since the original time series,  $y_1(t)$ , was self-affine, the new time series,  $y_2(t)$ , has the same statistical properties as the original time series.

From the definition of the power-spectral density, Eq. (38), and using it in the right-hand side of Eq. (56), we obtain

$$S_2(f) = \lim_{T \rightarrow \infty} \left\{ \frac{1}{T} |Y_2(f, T)|^2 \right\} = \lim_{T \rightarrow \infty} \left\{ \frac{1}{T} \left| \frac{1}{r^{Ha+1}} Y_1(f', T') \right|^2 \right\}. \quad (57)$$

Simplifying Eq. (57), substituting  $T' = T/r$ , and again comparing with the definition of the power-spectral density, Eq. (38), we arrive at

$$S_2(f) = \frac{1}{r^{2Ha+1}} \lim_{T' \rightarrow \infty} \left\{ \frac{1}{T'} |Y_1(f', T')|^2 \right\} = \frac{1}{r^{2Ha+1}} S_1(f'). \quad (58)$$

We next use the fact that the power-spectral density has a power-law dependence on frequency in Eq. (39) and assume  $S_2(f) = Af^{-\beta}$  and  $S_1(f') = A(f')^{-\beta}$ , where  $A$  is a constant of proportionality. Then Eq. (58) becomes

$$Af^{-\beta} = \frac{A(f')^{-\beta}}{r^{2Ha+1}}. \quad (59)$$

The frequency  $f' = f/r$ , so

$$f^{-\beta} = \frac{1}{r^{2Ha+1}} \left( \frac{f}{r} \right)^{-\beta}, \quad (60)$$

which simplifies to

$$1 = \frac{r^\beta}{r^{2Ha+1}}. \quad (61)$$

For the right-hand side of Eq. (61) to be 1, and from the fact that  $Ha = 2 - D$ , Eq. (27), it follows that

$$\beta = 2Ha + 1 = 5 - 2D. \quad (62)$$

For a self-affine fractal ( $0 \leq Ha \leq 1$ ,  $1 \leq D \leq 2$ ) we have  $1 \leq \beta \leq 3$ . For a Brownian motion with  $Ha = \frac{1}{2}$  ( $D = \frac{3}{2}$ ) we have  $\beta = 2$ . Although  $Ha$ , the Hausdorff exponent, is only applicable for self-affine time series from  $0 \leq Ha \leq 1$ , the spectral-power exponent,  $\beta$ , is a measure of the strength of persistence which is valid for all  $\beta$ , not just  $1 \leq \beta \leq 3$ . For self-affine time series, a white noise has  $\beta = 0$ , an antipersistent time series has  $\beta < 0$ , and a persistent time series has  $\beta > 0$ . Brown (1987) obtains the fractal dimension directly by converting self-affine time series to self-similar time series and then using the ruler method to determine the fractal dimension (also see De Santis, 1997).

## 2.4. Weak vs Strong Persistence

We now look at the strength of persistence of a self-affine time series and relate it to the stationarity of the time series. Substitution of the power-law dependence in Eq. (42) of the power-spectral density coefficients,  $S_m$ , on frequency,  $f_m$ , into (52) gives

$$V_N = \frac{2}{N\delta} \sum_{m=1}^{N/2} S_m = \frac{A}{N\delta} \sum_{m=1}^{N/2} (f_m)^{-\beta}, \quad (63)$$

where the frequency associated with each  $S_m$  is  $f_m = m/N$ ,  $A$  is a positive constant of proportionality, and  $V_N$  is the variance of the discrete time series,  $y_n$ ,  $n = 1, 2, 3, \dots, N$ . The minimum value for the frequency  $f_m$  is  $f_m = 1/N$ ; this will approach 0 as  $N$  approaches infinity. The maximum value for  $f_m$  will always be a constant,  $f_m = (N/2)/N = 0.5$ . We convert the sum in Eq. (63) to an integral by dividing the limits of the sum into  $(N - 1)$  intervals of  $\Delta f = (1/N\delta)$ , with the result

$$V_N = A \sum_{m=1}^{N/2} \frac{\Delta f}{f_m^\beta} = A \int_{1/N}^{1/2} \frac{df}{f^\beta} = V(N). \quad (64)$$

We consider the definite integral in Eq. (64) for two cases,  $\beta < 1$  and  $\beta > 1$ :

$$V(N) = \begin{cases} \left( \frac{A}{1-\beta} \right) \left[ \left( \frac{1}{2} \right)^{1-\beta} - \left( \frac{1}{N} \right)^{1-\beta} \right], & \text{if } \beta < 1, \\ \left( \frac{A}{1-\beta} \right) (2^{\beta-1} - N^{\beta-1}), & \text{if } \beta > 1. \end{cases} \quad (65)$$

The factor  $[A/(1 - \beta)]$  is positive for  $\beta < 1$  and negative for  $\beta > 1$ . As  $N$  becomes large, the variance converges for values of  $\beta < 1$  and diverges for  $\beta > 1$ . This is illustrated in Fig. 8, where the variance,  $V(N)$ , from Eq. (65) is given as a function of  $N$  (i.e., the length of the series considered) for several values of  $\beta$  in the range  $-1 \leq \beta \leq 3$ . The variance converges to a finite value for large  $N$  when  $\beta < 1$ , but diverges to infinity as  $N \rightarrow \infty$  when  $\beta > 1$ . The value  $\beta = 1$  is a natural crossover between weak and strong persistence in a self-affine (long-range persistent) time series. Below this value, the time series is stationary (weakly stationary, see Section 1.4);

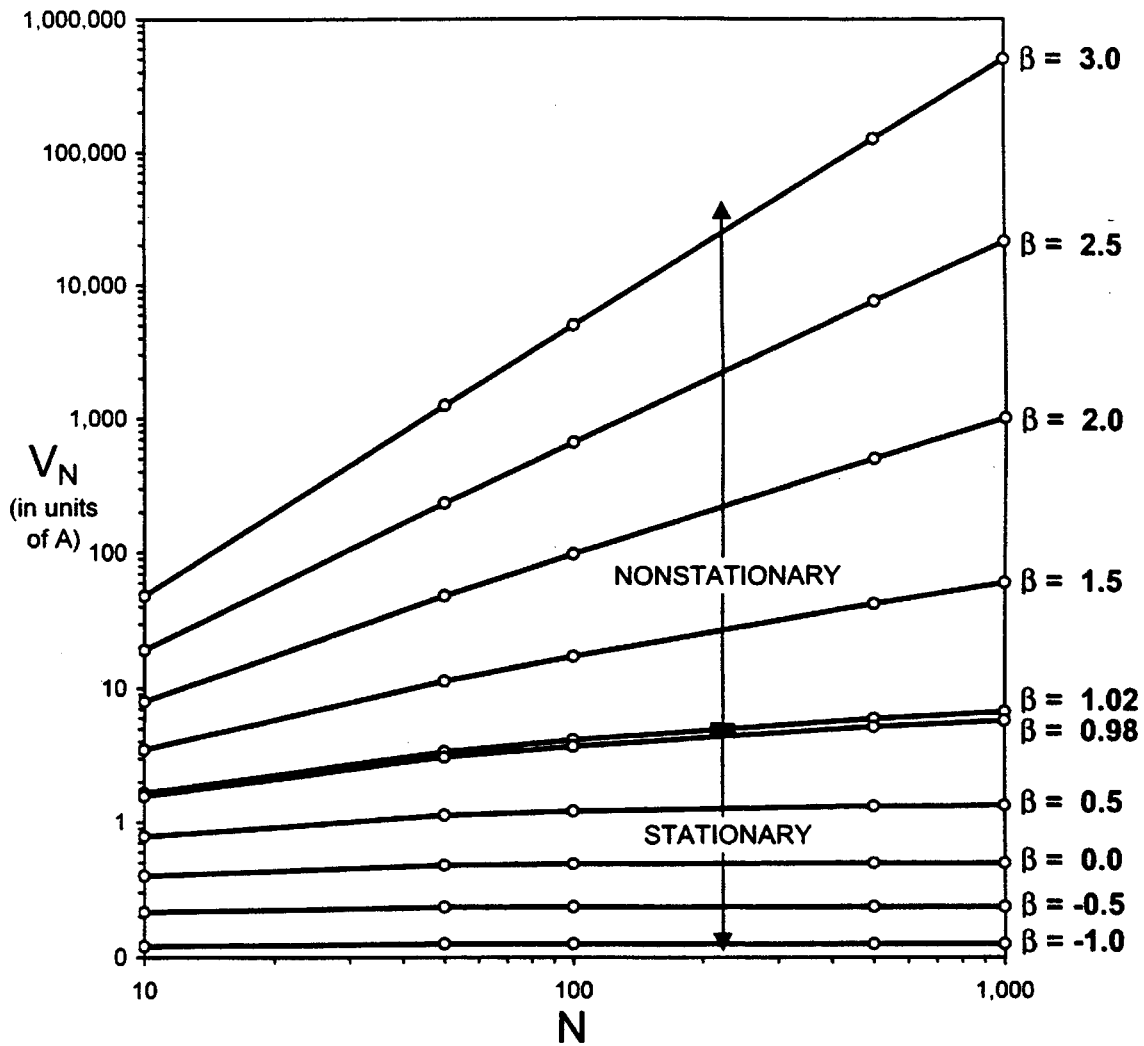


FIG. 8. The variance,  $V_N$ , Eq. (65), of a time series,  $y_n$ , is plotted as a function of the length of record,  $N$ , for values of  $\beta$  in the range  $-1 \leq \beta < 1$  and  $1 < \beta \leq 3$ . As  $N$  gets larger the variance quickly converges for values of  $\beta < 1$  and diverges for  $\beta > 1$ . Self-affine time series are stationary for  $\beta < 1$  and nonstationary for  $\beta > 1$ .

above this value, the time series is nonstationary. This classification is

$\beta > 1$	strong persistence	nonstationary,	
$1 > \beta > 0$	weak persistence	stationary,	
$\beta = 0$	uncorrelated	stationary,	(66)
$\beta < 0$	antipersistence	stationary.	

## 2.5. Spectral Variance and Leakage

The discrete Fourier transform given in Eq. (34) does not always provide an accurate representation of the actual statistics of a time series. Two of the main problems in using a discrete Fourier transform are spectral

variance and leakage. These have been discussed comprehensively by many authors, for example, Priestley (1981) and Percival and Walden (1993).

The first problem, spectral variance, concerns the large amount of scatter of the  $S_m$  with respect to the best-fit straight line. A clear illustration of spectral variation is seen in Figs. 6b, d. The standard deviation of  $S_m$  is 100% of the mean value of  $S_m$  (i.e., the value after many realizations) at  $f_m$  (Press *et al.*, 1994). Thus when plotted on logarithmic scales, the periodogram exhibits approximately the same scatter at all frequencies; i.e., the “width” of the scatter on a log–log plot is constant. One solution to spectral variance is to average over many realizations of the time series of interest. For each realization, calculate  $S_m$ ,  $m = 1, 2, 3, \dots, N/2$ , and then average at each corresponding  $f_m$  all of the values for  $S_m$ . This method will reduce the standard deviation of the scatter by the square root of the number of realizations (Press *et al.*, 1994). In this article, we choose not to reduce the amount of scatter, as the general trend of the periodograms is very clear, even with scatter.

Leakage is also a serious problem. For a discrete Fourier transform, a discrete set of frequencies  $f_m = m/(N\delta)$ ,  $m = 1, 2, 3, \dots, N/2$ , is considered. The width of a frequency bin is  $\Delta f = 1/(N\delta)$ . For a stochastic time series, there is generally a continuous range of associated frequencies possible with both integer and noninteger (fractional)  $m$ . Ideally, in one frequency bin,  $\Delta f$ , we would like the  $S_m$  that represent the whole bin to be some sort of an average of all of the  $S_m$  associated with the continuous  $f_m$  in the bin. This is not the case. The power associated with frequencies that have integer- $m$  is correctly represented in the frequency domain. However, the power that is associated with frequencies that have fractional- $m$  is distributed to not only its own bin, but also “leaks” into other bins. The result is a bias that can seriously affect the resulting power-spectral distribution. One method to reduce leakage is “prewhitening,” where in its simplest form one removes the trend and obvious periodicities from the original time series. A good discussion of the advantages and disadvantages of prewhitening is given in Percival and Walden (1993). We choose to use another method to reduce leakage, called windowing.

Windowing (also called tapering, weighting, shading, fading) involves multiplying the  $N$  values of a time series,  $y_n$ ,  $n = 1, 2, 3, \dots, N$ , by the  $N$  values of the “window,”  $w_n$ ,  $n = 1, 2, 3, \dots, N$ , before carrying out the Fourier transform. If  $w_n = 1$  for all  $n$ , then  $w_n$  is a rectangular window (the original series is left unmodified). The window (or taper) is normally constructed to change gradually from zero to a maximum to zero as  $n$  goes from 1 to  $N$ . For a complete discussion of the statistics involved with tapering, the reader is referred to Percival and Walden (1993). Many books discuss the mechanics of how and which windows to use, including

Press *et al.* (1994) and Smith and Smith (1995). Two commonly used windows are

$$w_n = 1 - \left( \frac{n - (N/2)}{(N/2)} \right)^2, \quad n = 1, 2, 3, \dots, N, \quad \text{Welch window,} \quad (67)$$

$$w_n = \frac{1}{2} \left[ 1 - \cos \left( \frac{2\pi n}{N} \right) \right], \quad n = 1, 2, 3, \dots, N, \quad \text{Hann window.} \quad (68)$$

The Fourier coefficients from Eq. (34) are then given by

$$Y_m = \delta \sum_{n=1}^N w_n y_n e^{2\pi i n m / N}, \quad m = 1, 2, 3, \dots, N. \quad (69)$$

Windowing significantly reduces the leakage when Fourier transforms are carried out on self-affine time series, particularly for those with high positive  $\beta$ 's (above  $\beta = 2$ ) and negative  $\beta$ 's.

The variance of  $y_n$  will be different from the variance of  $(w_n y_n)$ ; this will affect the total power (variance) in the periodogram, and the amplitude of the power-spectral density function will be shifted. One remedy is to normalize the time series  $y_n$  so it has a mean of 0, calculate the Fourier coefficients  $Y_m$  based on Eq. (69), and then calculate the final  $S_m$  using

$$S_m = \frac{1}{W_{ss}} \left[ \frac{2|Y_m|^2}{N\delta} \right], \quad m = 1, 2, 3, \dots, \frac{N}{2}, \quad (70)$$

where

$$W_{ss} = \frac{1}{N} \sum_{n=1}^N (w_n)^2. \quad (71)$$

This will normalize the variance of  $(w_n y_n)$  so that it now has the variance of the original unwindowed  $y_n$ .

We close this section with a brief discussion of detrending. Many statistical packages and books recommend removing the trend and the mean of a time series before performing a Fourier analysis. The mean of a time series can be set equal to 0; this will not affect the resulting Fourier coefficients. If a window is to be used, then the mean of the original time series should be set equal to 0, or the resulting power-spectra will be improperly biased by the window. The variance of a time series can be normalized to 1, and the slope ( $-\beta$ ) of the resulting power-spectral density function will not be affected. However, detrending a time series is

controversial, and care should be taken. One way of detrending is to take the best-fit straight line to the time series and subtract it from all of the values. Another way of detrending is to connect a line from the first point and the last point, and subtract this line from the time series; this forces  $y_1 = y_N$ . If a time series shows a clear linear trend, where the series appears to be closely scattered around a straight line, the trend can be safely removed without affecting any but the lowest frequencies in the power spectrum. However, if there is no clear linear trend, detrending can cause the statistics of the periodogram (in particular the slope) to change significantly.

### 3. SYNTHETIC FRACTIONAL NOISES AND MOTIONS

#### 3.1. What Are They?

As discussed above, a Brownian motion has a power-law spectrum such that Eq. (39) is applicable with  $\beta = 2$ . We now generate synthetic time series that have power-law spectra with arbitrary values of  $\beta$ . These are referred to as fractional noises and motions, which were first introduced by Kolmogorov (1940). Extensive studies of fractional noises and motions have been carried out by Mandelbrot and Wallis (1968, 1969a, b, c) and by Mandelbrot and Van Ness (1968). A range of applications has been discussed by Voss (1985a, b, c, 1986, 1988, 1989).

#### 3.2. Spectral Analysis

Fractional Gaussian noises can be generated synthetically from Gaussian white noises using the following steps:

- (1) A Gaussian white noise sequence is generated. Four examples are given in Fig. 4a.
- (2) A discrete Fourier transform as given in Eq. (34) is taken of a Gaussian white noise sequence; the resulting Fourier spectrum will be flat, that is,  $\beta = 0$  in Eq. (42). Except for the statistical scatter, the amplitudes of the  $|Y_m|$  will be equal. An example of the power spectrum of a white noise is given in Fig. 9b.
- (3) The resulting Fourier coefficients  $Y_m$  are filtered using the relation

$$Y'_m = \left(\frac{m}{N}\right)^{-\beta/2} Y_m. \quad (72)$$

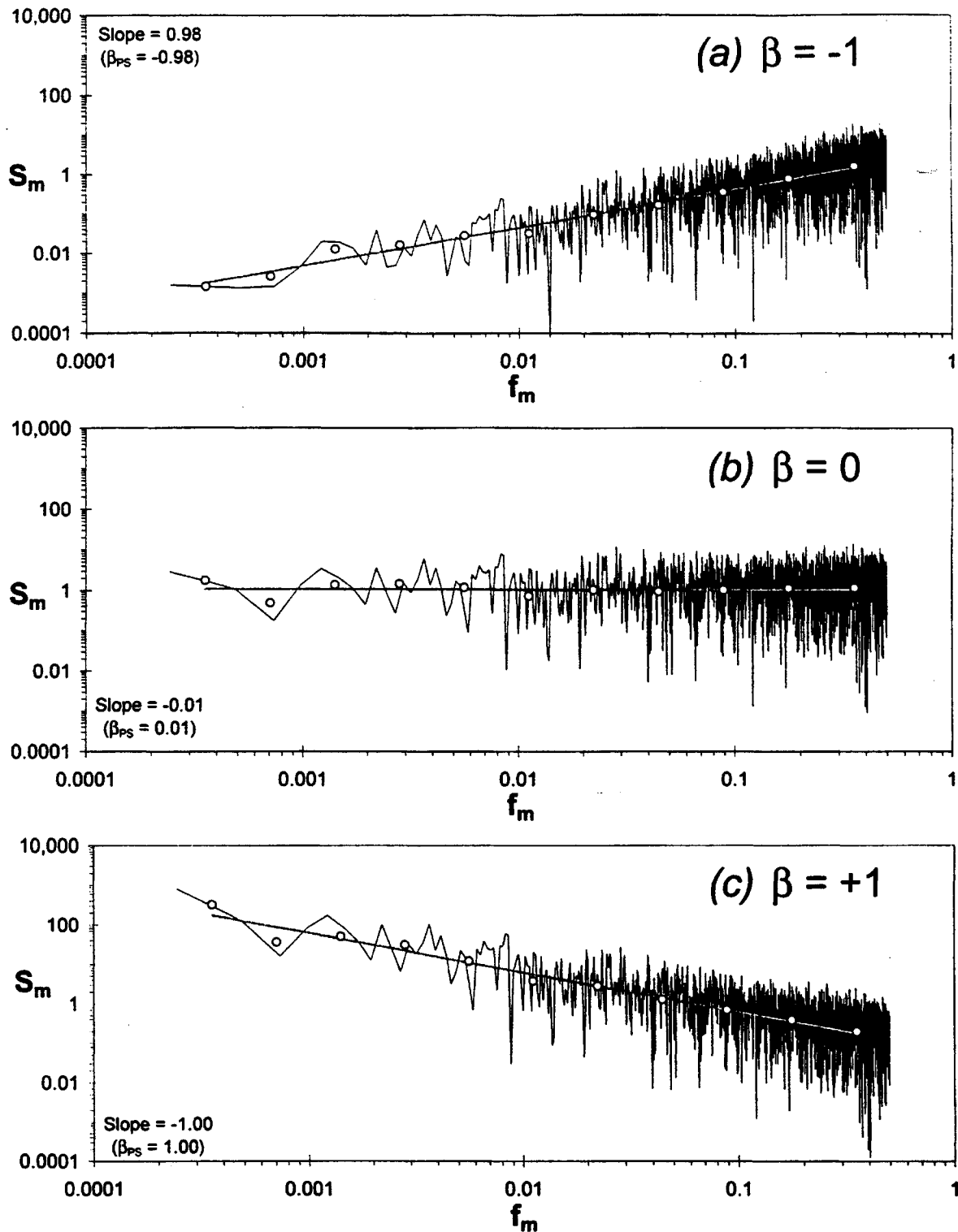


FIG. 9. An example of power-spectral filtering. The Fourier power spectrum of a Gaussian white noise with  $N = 4096$  points is given in (b). The Fourier coefficients of the spectrum have been filtered using Eq. (72) to give spectra with  $\beta = -1$  (a) and  $\beta = 1$  (c). The power-spectral density function,  $S_m$ , equal to  $2/N$  multiplied by the square of the amplitudes of the complex Fourier coefficients, is given as a function of frequency  $f_m = m/N$ , where  $m = 1, 2, 3, \dots, N/2$ . The value for  $\beta_{PS}$  is the negative of the slope of the best-fit straight line to the circles using a least-squares fit and log-log scales.

The exponent  $\beta/2$  is used because the power-spectral density is proportional to the amplitude squared of the Fourier coefficients. The amplitudes of the small- $m$  coefficients correspond to short wavelengths and high frequencies. The large- $m$  coefficients correspond to long wavelengths and low frequencies. Examples for  $\beta = -1$  and  $\beta = 1$  are given in Figs. 9a, c.

- (4) An inverse discrete Fourier transform, Eq. (35), is taken of the filtered Fourier coefficients. The result is a fractional Gaussian noise. To remove edge effects (periodicities), only the central portion is retained.

Using the steps given above, several examples of fractional Gaussian noises are given in Fig. 10 for  $\beta = -1.0, -0.5, 0.5, 1.0$ . Note that the range of  $\beta$ 's corresponding to fractional Gaussian noises is  $-1 \leq \beta \leq 1$ .

Just as a Gaussian white noise ( $\beta = 0$ ) can be summed to give a Brownian motion ( $\beta = 2$ ), fractional Gaussian noises can be summed to give fractional Brownian motions (see Section 2.2). In each case analogous to Eq. (50),  $\beta_{\text{fBm}} = 2 + \beta_{\text{fGn}}$ . Fractional Brownian motions are self-affine fractals and are restricted to the range  $1 \leq \beta \leq 3$  as discussed above. The white and fractional Gaussian noises in Fig. 10a ( $\beta = -1.0, -0.5, 0.0, 0.5, 1.0$ ) have been summed using Eq. (17) to give the fractional Brownian motions illustrated in Fig. 10b ( $\beta = 1.0, 1.5, 2.0, 2.5, 3.0$ ). Each fractional noise and motion given in Fig. 10 has  $N = 512$  points and has been rescaled (normalized) to have zero mean ( $\bar{y} = 0$ ) and unit variance ( $V = 1$ ). The fractional Gaussian noise in Fig. 10a with  $\beta = 1.0$  is statistically identical to the fractional Brownian motion in Fig. 10b with  $\beta = 1.0$ .

In Fig. 4a, four white noises were created by randomly choosing values from a Gaussian distribution with zero mean ( $\bar{y} = 0$ ) and unit variance ( $V = 1$ ). Although the distribution from which these white noises were derived had a zero mean ( $\bar{y} = 0$ ), the white noises have a mean that is slightly nonzero when taken over the  $N$  values. The white noises were summed to give the Brownian motions illustrated in Fig. 4b. Because the mean of each white noise is not identically zero, the values at the beginning and the end of the Brownian motion are not the same,  $y_1 \neq y_N$ . However, in the fractional noises illustrated in Fig. 10a, each noise has been forced to have a mean of exactly 0 over the  $N$  values in the time series. Thus, the Brownian motion is now forced to begin and end at the same value,  $y_1 = y_N$ . In the analyses that will follow, there is little difference between allowing the beginning and ending points of the distribution to be the same, or letting them be different. Statistically, the underlying persistence is the same.

In Fig. 10, as the value of  $\beta$  is increased from  $-1$  to  $+3$ , the contribution of the high-frequency (short-period) terms is reduced. With

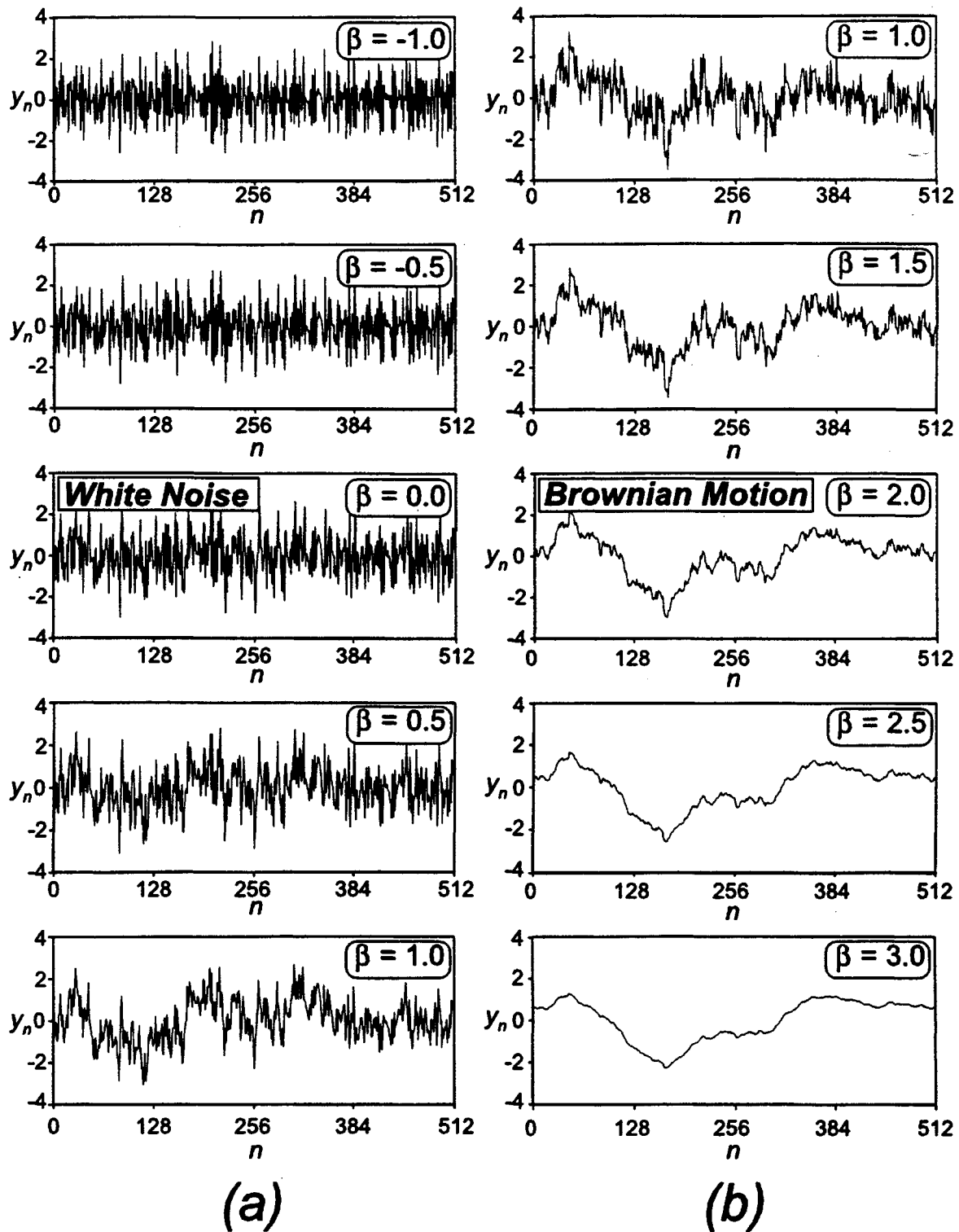


FIG. 10. (a) The Fourier coefficients of the white Gaussian noise ( $\beta = 0$ ) have been filtered to give fractional Gaussian noises with  $\beta = -1.0, -0.5, 0.5, 1.0$ . (b) Each of these fractional Gaussian noises with  $\beta_{fGn}$  has been summed using Eq. (17) to give fractional Brownian motions with  $\beta_{fBm} = 2 + \beta_{fGn}$ ,  $\beta = 1.0, 1.5, 2.0, 2.5, 3.0$ . Each fractional Gaussian noise and fractional Brownian motion has  $N = 512$  points, and has been rescaled to have zero mean ( $\bar{y} = 0$ ) and unit variance ( $V = 1$ ).

$\beta = -1.0$  and  $-0.5$ , the high-frequency contributions dominate over the low-frequency contributions. These time series are antipersistent; adjacent values are anticorrelated relative to a white noise ( $\beta = 0$ ). For an antipersistent time series, a value larger than the mean tends to be followed by a value smaller than the mean. With  $\beta = 0$ , the high-frequency contributions are equal to the low-frequency contributions. The result is an uncorrelated time series; adjacent values have no correlation with one another.

With  $\beta = 0.5, 1.0, 1.5, 2.0, 2.5, 3.0$ , the low-frequency contributions become increasingly dominant over the high-frequency contributions. The result is that adjacent values in the time series become more strongly correlated and profiles are smoothed. The persistence in the time series is increased. For a persistent time series, a value larger than the mean tends to be followed by another value larger than the mean. As the persistence becomes greater, the tendency for large to be followed by large becomes greater.

As previously discussed in Section 2.4, we use the division between fractional noises,  $\beta < 1$ , and fractional motions,  $\beta > 1$ , to define weak persistence as  $0 < \beta < 1$  and strong persistence as  $\beta > 1$ . In all cases, however, a self-affine time series with a nonzero  $\beta$  has long-range (as well as short-range) persistence and antipersistence. For small  $\beta$ , the correlations with large lag are small but are nonzero. This can be contrasted with time series that are not self-affine; these may have only short-range persistence (either strong or weak).

The fractional Gaussian noises with  $-1 \leq \beta \leq 1$ , generated using the Fourier filtering technique, can be summed to give fractional Brownian motions with  $1 \leq \beta \leq 3$ . Similarly, the fractional Brownian motions with  $1 \leq \beta \leq 3$  can be differenced to give fractional Gaussian noises with  $-1 \leq \beta \leq 1$ . We can repeat the differencing and obtain extended fractional Gaussian noises with  $-3 \leq \beta \leq -1$ . Similarly, extended fractional Brownian motions with  $3 \leq \beta \leq 5$  can be obtained by summing fractional Brownian motions with  $1 \leq \beta \leq 3$ . In this article, we use the Fourier filtering technique to generate synthetic fractional-noise self-affine time series, each with  $N = 4096$  points over the range  $-1 \leq \beta \leq 1$ . These are extended over the range  $-3 \leq \beta \leq 5$  by appropriately differencing and summing (Table I). We will verify the  $\beta$  ascribed to these self-affine time series by using power-spectral analysis.

We now illustrate the effects of windowing on power-spectral analysis. An example of windowing using the Welch window, Eq. (67), is given for two time series; the first, with  $\beta = 2.5$ , is illustrated in Fig. 11a, and the second, with  $\beta = 1.5$ , is illustrated in Fig. 12a. Each of these two time series has been rescaled to zero mean and unit variance. For illustration

TABLE I LEGEND FOR SYMBOLS USED IN FRACTIONAL GAUSSIAN NOISE  
AND BROWNIAN MOTION ANALYSES

Symbol	Symbol represents results of analyses on ...	Which have a range of Beta that is ...	And were created by ...
□	Extended fractional motions	$3 \leq \beta \leq 5$	<b>Summing</b> the fractional Brownian motions
○	Fractional Brownian motions	$1 \leq \beta \leq 3$	<b>Summing</b> the Fourier filtered fractional Gaussian noises
△	Fractional Gaussian noises	$-1 \leq \beta \leq 1$	<b>Filtering</b> the Fourier coefficients of a white noise
◇	Extended fractional Gaussian noises	$-3 \leq \beta \leq -1$	<b>Differencing</b> the Fourier filtered fractional Gaussian noises

purposes, the values at the beginning and the end of each time series are not the same,  $y_1 \neq y_N$ . The time series before and after windowing, along with the Welch window, are shown in Figs. 11a, b for the noise with  $\beta = 2.5$  and Figs. 12a, b for  $\beta = 1.5$ . The power-spectral density function with and without the Welch window is shown in Figs. 11c, d ( $\beta = 2.5$ ) and Figs. 12c, d ( $\beta = 1.5$ ). For the time series with  $\beta = 2.5$ , the best-fit lines have slopes resulting in  $\beta_{PS} = 1.9$  without windowing (Fig. 11c) and  $\beta_{PS} = 2.5$  with windowing (Fig. 11d). For the time series with  $\beta = 1.5$ , the best-fit lines have slopes resulting in  $\beta_{PS} = 1.5$  without windowing (Fig. 12c) and  $\beta_{PS} = 1.5$  with windowing (Fig. 12d). Windowing clearly makes a difference for the time series constructed with  $\beta = 2.5$ .

The spectral exponent obtained by power-spectral analysis is denoted by  $\beta_{PS}$ . Results of these power-spectral analyses,  $\beta_{PS}$  vs  $\beta$ , are given in Fig. 13. We have used the Welch window from Eq. (67). As expected, there is excellent correlation between  $\beta_{PS}$  vs  $\beta$ , for  $\beta < 4$ . Since it is rare to find examples of natural self-affine time series with  $\beta > 4$ , the Welch window is probably fine to use.

In addition to being self-affine time series, the fractional Brownian motions given in Fig. 10b with  $1 \leq \beta \leq 3$  have, from Eq. (62),  $1 \leq D \leq 2$ ; thus they are self-affine fractals. Although the mathematical definition of self-affine fractals restricts the applicable range of  $\beta$  to  $1 \leq \beta \leq 3$ , naturally occurring self-affine time series with a power-law dependence of the power-spectral density on frequency have values of  $\beta$  outside this range.

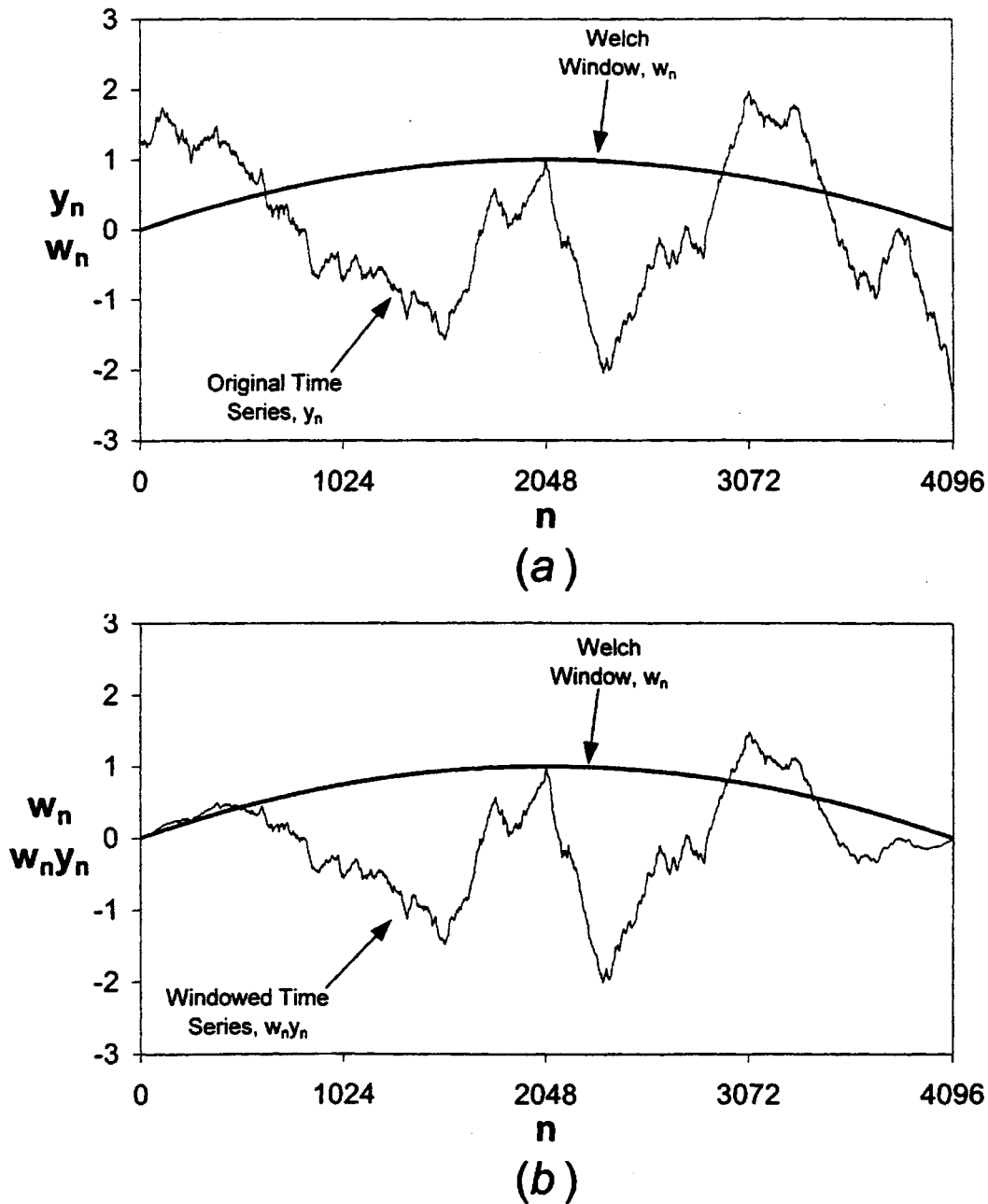
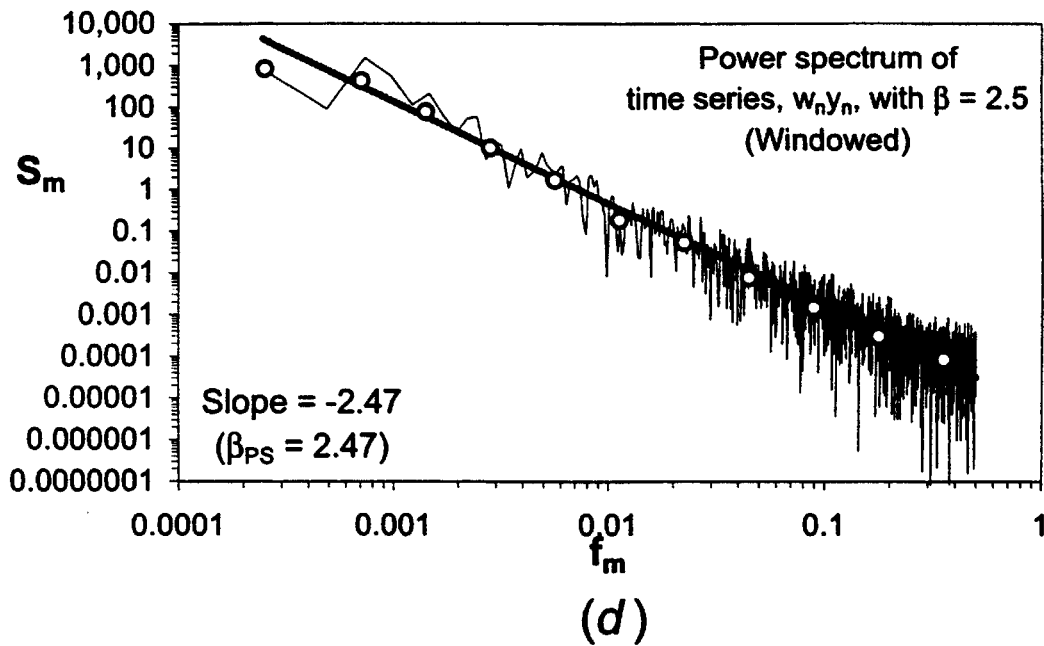
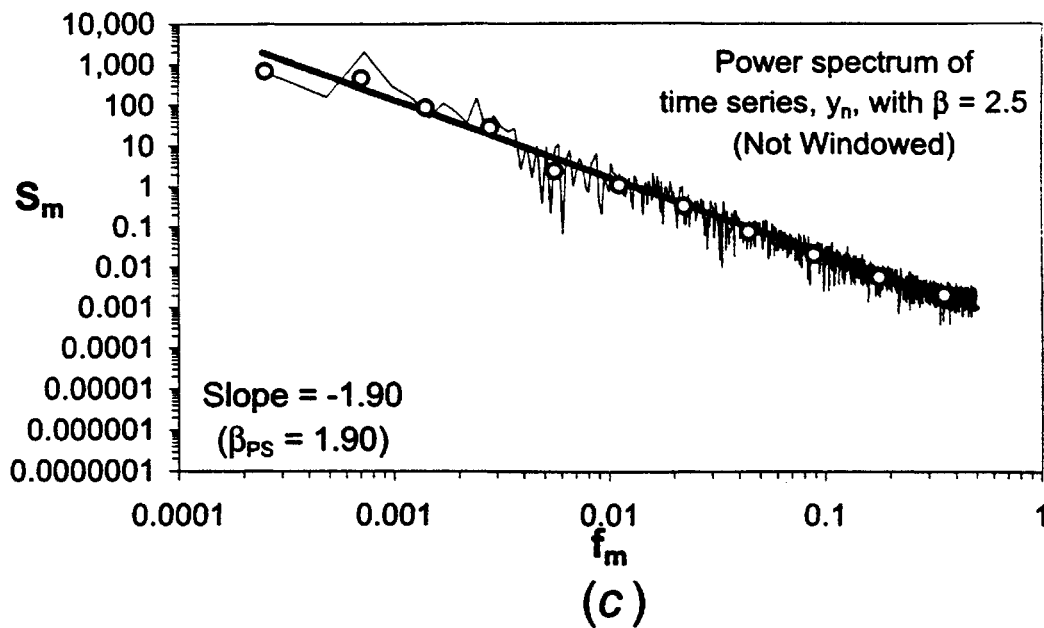


FIG. 11. Example of power-spectral density with and without a window. (a) A fractional Brownian motion ( $y_n$ ) constructed to have  $\beta = 2.5$  is convolved with the Welch window ( $w_n$ ) given in Eq. (67), resulting in (b) the new windowed time series ( $w_n y_n$ ). The original discrete time series,  $y_n$ ,  $n = 1, 2, 3, \dots, N$ , was constructed with  $N = 4096$  points, a mean,  $\bar{y} = 0$ , a variance,  $V = 1$ , and  $\beta = 2.5$ . This same time series is presented later in Fig. 15d. (c) Periodogram of  $y_n$ , where using log-log scales, the power-spectral density,  $S_m$  from Eq. (42), is plotted as a function of  $f_m$ ,  $f_m = 1, 2, 3, \dots, N/2$ . The value for  $\beta_{PS}$  is the negative of the slope of the best-fit straight line to the circles using a least-squares fit and log-log scales. (d) Periodogram of the windowed time series, ( $w_n y_n$ ), where  $S_m$  from Eq. (71) is now based on a normalization by  $W_{ss}$ , the window squared and summed. The power-spectral analyses for the (a) nonwindowed time series,  $y_n$ , results in (c)  $\beta_{PS} \approx 1.9$  and for the (b) windowed time series,  $w_n y_n$ , results in (d)  $\beta_{PS} \approx 2.5$ .

FIG. 11. *Continued.*

In the succeeding article (Pelletier and Turcotte, 1999), power-spectral analyses have been carried out on a variety of naturally occurring time series in geophysics. It is found that many of these time series exhibit self-affine behavior. In some of the time series, a single value of  $\beta$  is applicable over all frequencies; in other cases, subsets of the frequency domain are characterized by different values of  $\beta$ . Their article also includes extensive references to time series analyses of geophysical data sets.

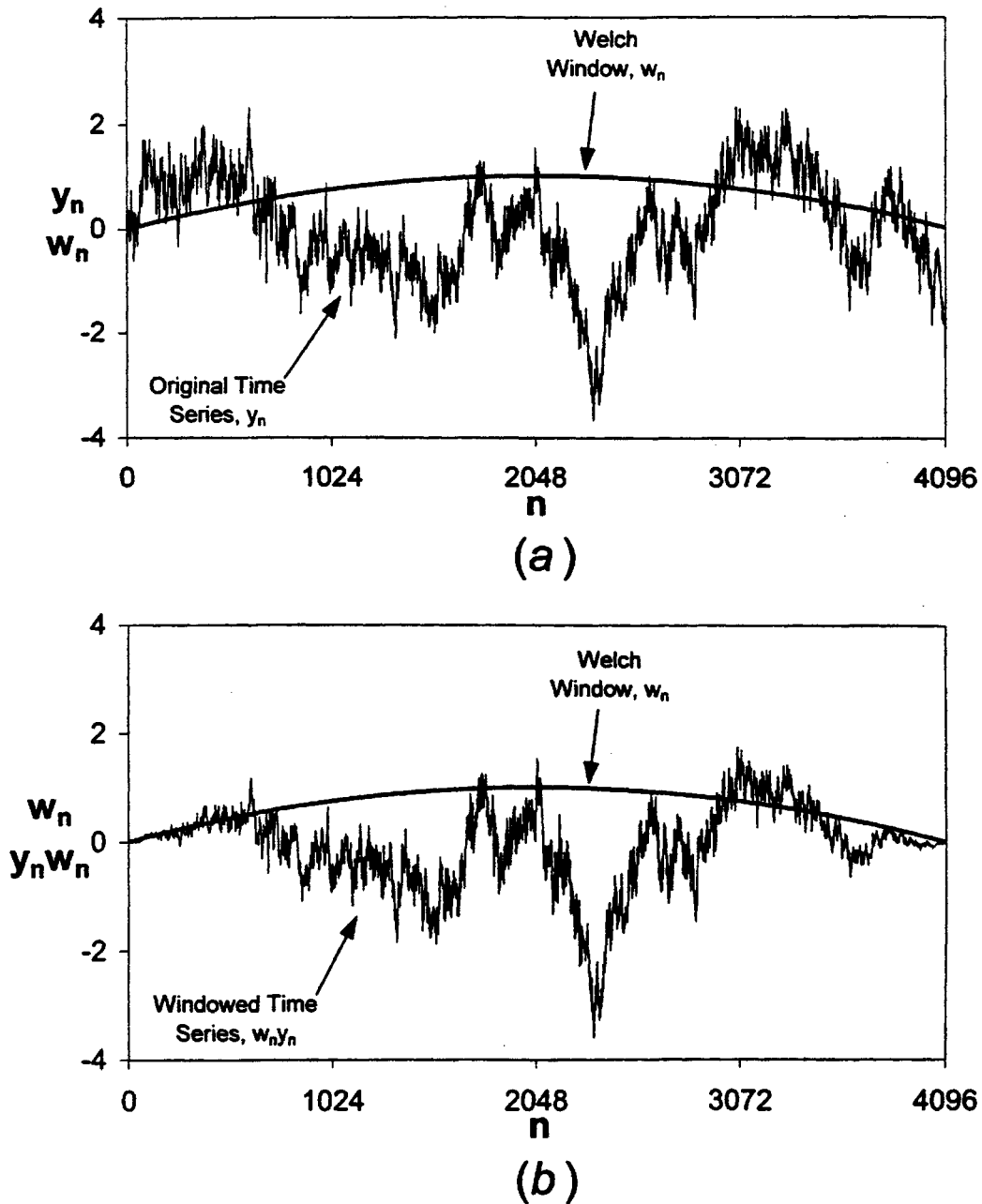
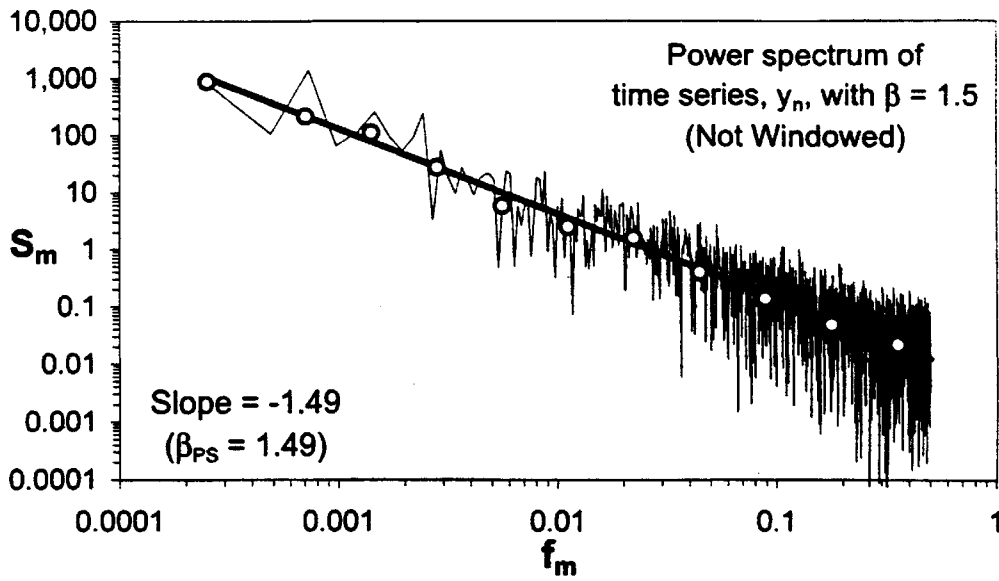


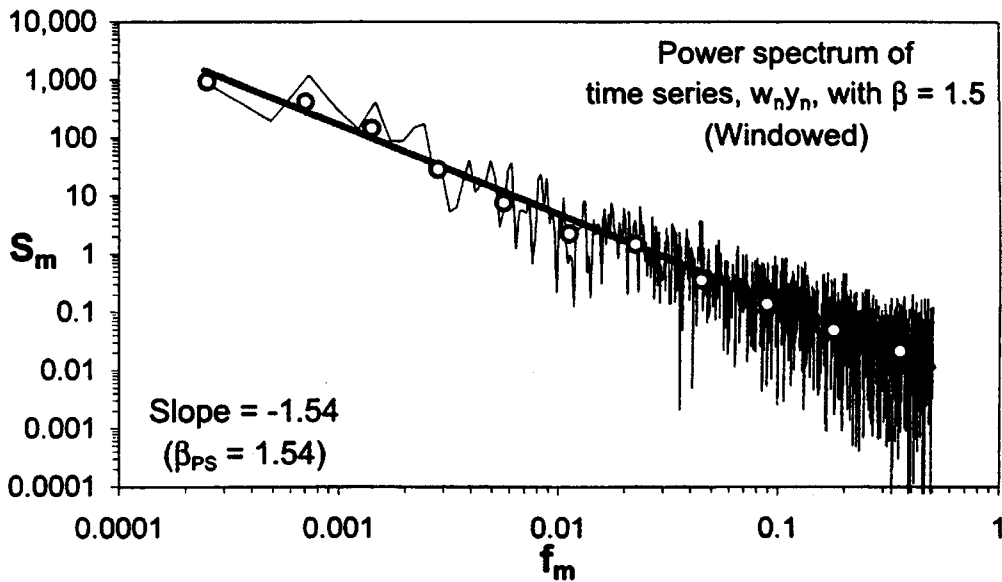
FIG. 12. Same as Fig. 11, but for a fractional Brownian motion constructed to have  $\beta = 1.5$ . This same time series is presented later in Fig. 15b. For both the (a) nonwindowed time series,  $y_n$ , and (b) windowed time series,  $w_n y_n$ , power-spectral analysis (c) and (d) results in equivalent  $\beta_{PS} \approx 1.5$ .

### 3.3. Method of Successive Random Additions

An alternative method for the direct generation of fractional Brownian motions is the method of successive random additions (Voss 1985a, b, 1988). Consider the time interval  $0 \leq t_n \leq 1$  as illustrated in Fig. 14. The values of  $t_n$  are discrete, with  $t_n = n/N$ ,  $n = 1, 2, \dots, N$ . Random values



(c)



(d)

FIG. 12. *Continued.*

for  $y_1(t_n)$  are generated based on a Gaussian probability distribution with zero mean,  $\bar{y} = 0$ , and unit variance,  $V(1) = 1$ . Three of these values ( $N = 3$ ,  $n = 1, 2, 3$ ) are placed at  $t_n = 0, \frac{1}{2}, 1$  as shown in Fig. 14a. Note that the mean of these three values is not forced to 0, but rather the Gaussian distribution from which the three values are randomly chosen has a mean of 0. Two straight lines are drawn between these three points. The midpoints of these two line segments are taken as initial values for  $y_2(t_n)$  at  $t_n = \frac{1}{4}$  and  $\frac{3}{4}$  as illustrated in Fig. 14b.

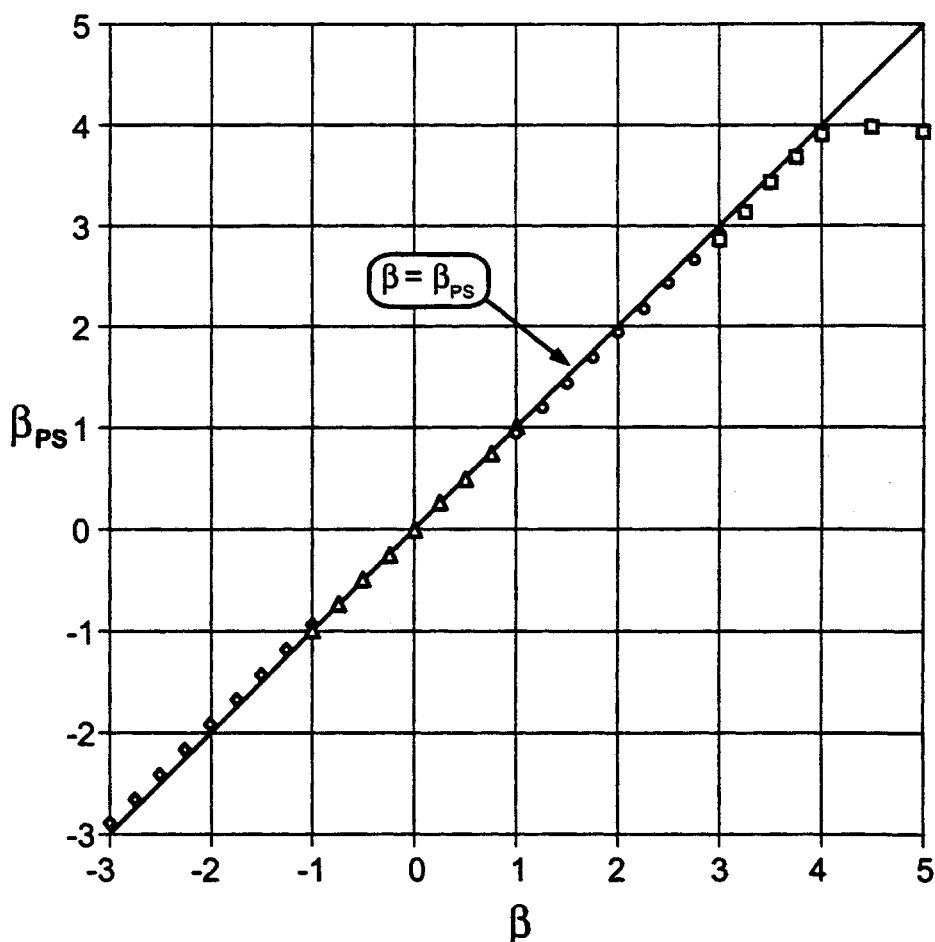
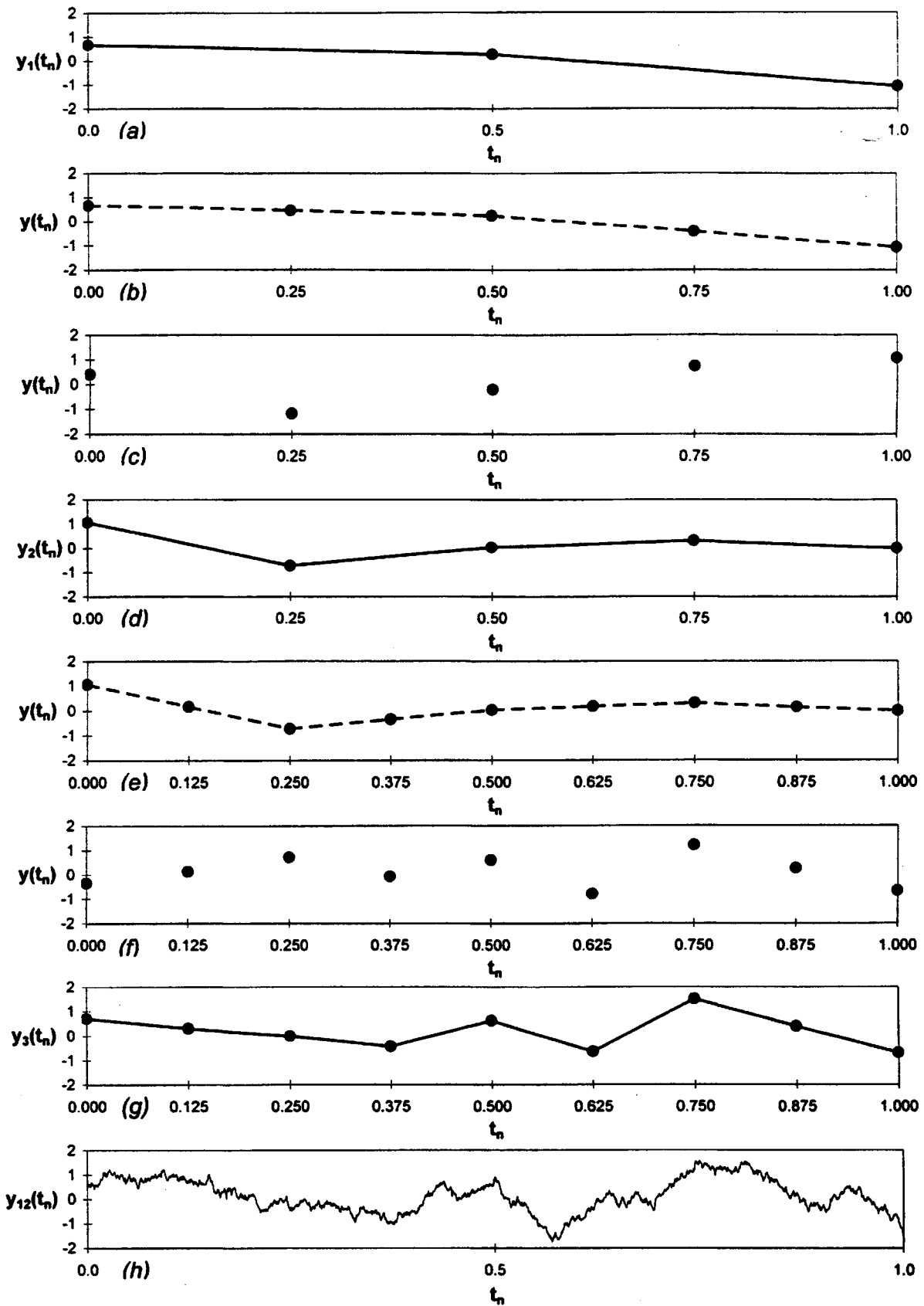


FIG. 13. The dependence of the power-spectral exponent,  $\beta_{PS}$ , on  $\beta$  for a series of synthetic fractional Gaussian noises and fractional Brownian motions with  $N = 4096$  points. The fractional noises and motions are constructed to have a theoretical power-spectral exponent,  $\beta$ , using the Fourier filtering technique (Section 3.2). The synthetic noises and motions are then windowed using the Welch window, Eq. (67). Finally, we verify the power-spectral exponent of each synthetic fractional noise and motion by finding the best fit of  $S \sim f^{-\beta}$ , Eq. (39), and denoting it by  $\beta_{PS}$ . Results are given for  $-3 \leq \beta \leq 5$ ; each symbol represents the best-fit  $\beta_{PS}$  at a given  $\beta$ . The straight-line correlation is  $\beta = \beta_{PS}$ . The diamonds ( $-3 \leq \beta \leq -1$ ), triangles ( $-1 \leq \beta \leq 1$ ), circles ( $1 \leq \beta \leq 3$ ), and squares ( $3 \leq \beta \leq 5$ ) are explained in Table I.

The five points are now given random additions. These random additions are also based on a Gaussian probability distribution with zero mean,  $\bar{y} = 0$ , but with a reduced variance given by  $V(T) = (T)^{2Ha}$ , from Eq. (23). Since the interval has been reduced by a factor of 2, the variance is given by  $V(\frac{1}{2}) = (\frac{1}{2})^{2Ha}$ . For our example, we take  $Ha = \frac{1}{2}$  so that  $V(\frac{1}{2}) = \frac{1}{2}$ . The five resulting random additions are given in Fig. 14c. After addition to the five values of  $y(t_n)$  in Fig. 14b, the resulting five values for  $y_2(t_n)$  are given in Fig. 14d. Again the five points are connected by four straight-line segments and the four midpoints are taken as initial values for  $y_3(t_n)$  at



$t = \frac{1}{8}, \frac{3}{8}, \frac{5}{8},$  and  $\frac{7}{8}$  as illustrated in Fig. 14e. All nine points are now given random additions using a Gaussian probability distribution with zero mean but a further reduced variance from Eq. (23),  $V(\frac{1}{4}) = (\frac{1}{4})^{2Ha}$ . Again, taking  $Ha = \frac{1}{2}$  gives  $V(\frac{1}{4}) = \frac{1}{4}$ . The nine random additions are given in Fig. 14f. After addition to the nine values of  $y(t_n)$  given in Fig. 14e, the resulting nine values for  $y_3(t_n)$  are given in Fig. 14g. The process is repeated until the desired number of points is obtained. A 12th-order construction,  $y_{12}(t_n)$  with 4097 points, is given in Fig. 14h. With  $Ha = \frac{1}{2}$  and  $\beta = 2$ , this is a Brownian motion and strongly resembles the Brownian motions given in Figs. 4 and 10.

A sequence of fractional Brownian motions generated by the method of successive random additions is given in Fig. 15. Fractional Brownian motions are given for  $Ha = 0.00$  ( $\beta = 1.0$ ),  $Ha = 0.25$  ( $\beta = 1.5$ ),  $Ha = 0.50$  ( $\beta = 2.0$ , same as Fig. 14h),  $Ha = 0.75$  ( $\beta = 2.5$ ) and  $Ha = 1.00$  ( $\beta = 3.0$ ); in each case 4097 points are given. As expected, these noises closely resemble those generated by the Fourier filtering technique (Fig. 10). The method of successive random additions generates fractional Brownian motions with  $1 \leq \beta \leq 3$ . These can be differenced to give fractional Gaussian noises with  $-1 \leq \beta \leq 1$  and summed to give extended fractional Brownian motions with  $3 \leq \beta \leq 5$ .

A detailed comparison of fractional Gaussian noises and fractional Brownian motions using the Fourier filtering technique and the method of successive random additions has been given by Gallant *et al.* (1994). These authors also considered a third method of generating synthetic fractional noises using Weierstrass–Mandelbrot functions. Other relevant studies include those carried out by Li and McLeod (1986) and Osborne and Provenzale (1989).

### 3.4. Semivariograms

Using the definition for the semivariogram,  $\gamma_k$ , given in Eq. (8), semivariograms for several fractional Gaussian noises and fractional Brownian

---

FIG. 14. Illustration of the generation of a fractional Brownian motion using the method of successive random additions. (a) Three random numbers are generated using a Gaussian distribution with zero mean and unit variance; these are placed at  $t = 0, \frac{1}{2}, 1$ . (b) Values at  $t = \frac{1}{4}$  and  $\frac{3}{4}$  are obtained by linear interpolation. (c) Assuming  $Ha = \frac{1}{2}$ , five random numbers are generated using a Gaussian distribution with zero mean and  $V = (\frac{1}{2})^{2Ha} = \frac{1}{2}$ . (d) The random numbers in (c) are added to the values in (b). (e) Values at  $t = \frac{1}{8}, \frac{3}{8}, \frac{5}{8}, \frac{7}{8}$  are obtained by linear interpolation. (f) Nine random numbers are generated using a Gaussian distribution with zero mean and  $V = (\frac{1}{4})^{2Ha} = \frac{1}{4}$ . (g) The random numbers in (f) are added to the values in (d). (h) The construction has been continued to 4097 points; the result is a Brownian motion.

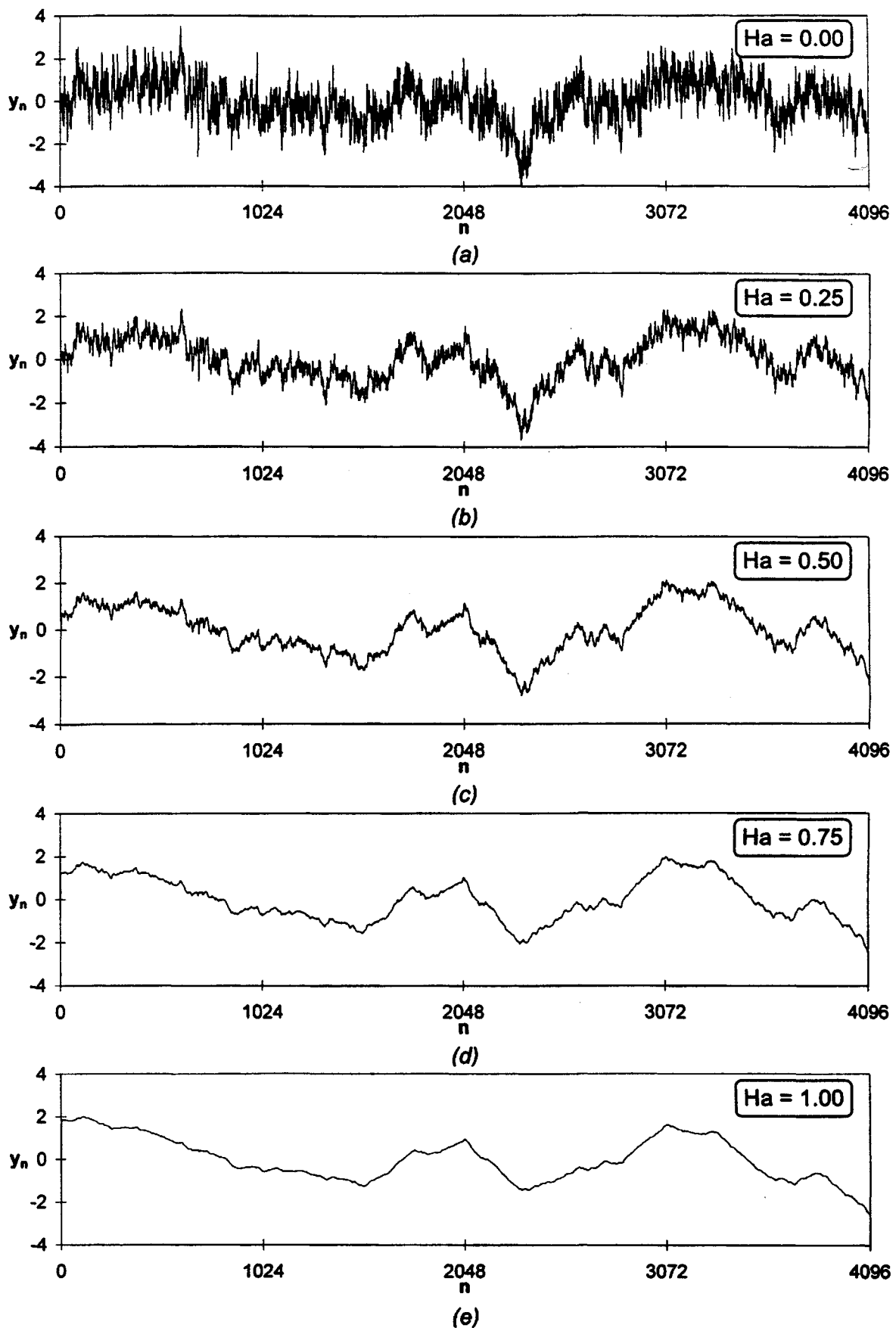


FIG. 15. A sequence of fractional Brownian motions generated by the method of successive random additions. (a)  $H_a = 0.00$  ( $\beta = 1.0$ ). (b)  $H_a = 0.25$  ( $\beta = 1.5$ ). (c)  $H_a = 0.50$  ( $\beta = 2.0$ , a Brownian motion same as Fig. 14h). (d)  $H_a = 0.75$  ( $\beta = 2.5$ ). (e)  $H_a = 1.00$  ( $\beta = 3.0$ ).

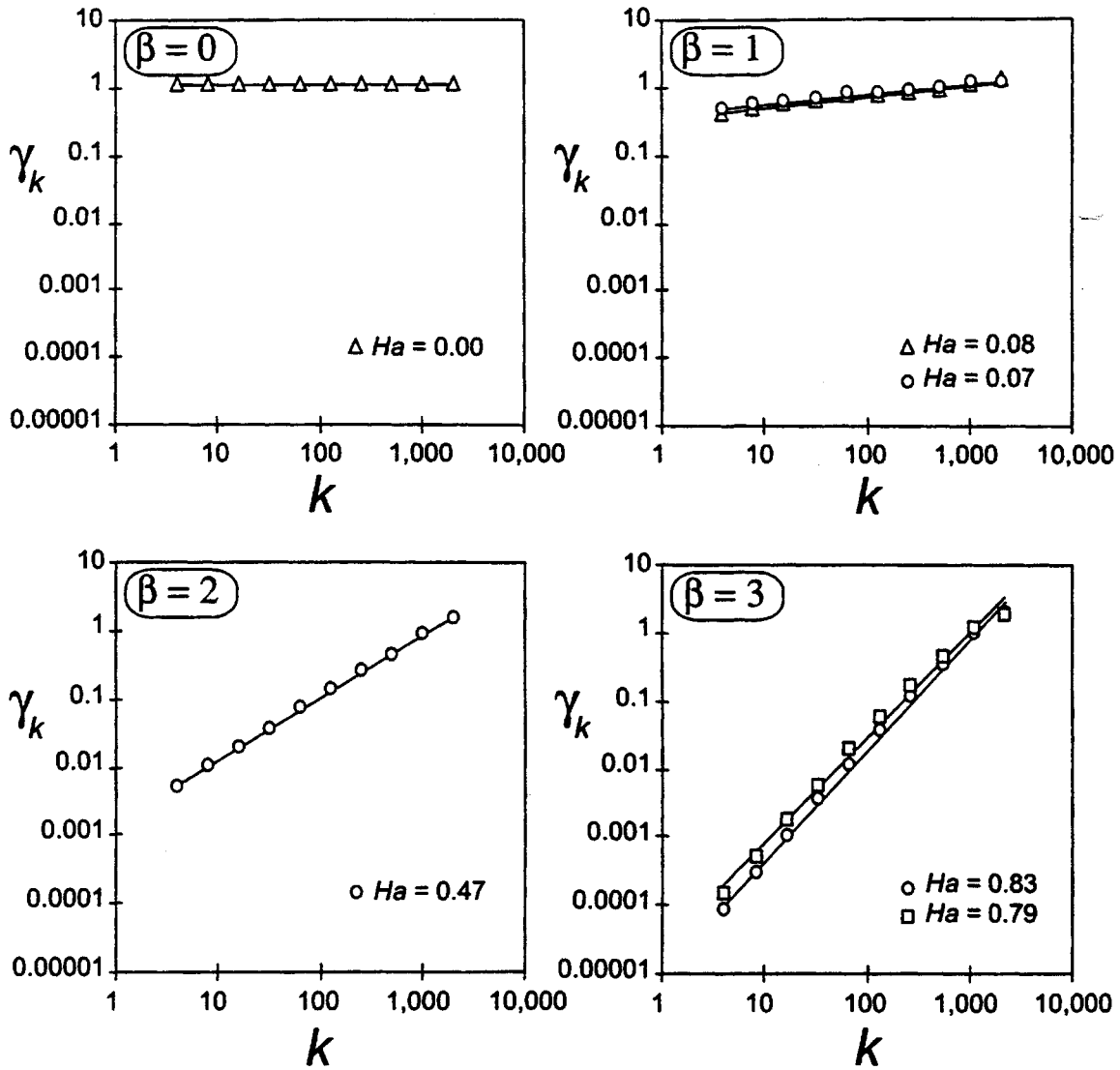


FIG. 16. Semivariograms for several fractional Gaussian noises and fractional Brownian motions. Each semivariogram is obtained using Eq. (8) with lag  $k = 4, 8, 16, \dots, 2048$ , and applied to fractional Gaussian noises and fractional Brownian motions with  $N = 4096$  points. Examples of time series with  $N = 512$  points and the same characteristics are illustrated in Fig. 10. The straight-line correlations are with  $\gamma \sim k^{2Ha}$ , Eq. (29). The slope of the best-fit straight line for  $\log(\gamma)$  vs  $\log(k)$  is  $2Ha$ . Values for one-half of the slope,  $Ha$ , are given for each of the examples. The triangles ( $\beta = 0, 1$ ), circles ( $\beta = 1, 2, 3$ ), and squares ( $\beta = 3$ ) are explained in Table I.

motions, each with 4096 points, are given in Fig. 16. For the uncorrelated Gaussian white noise ( $\beta = 0$ ), the semivariogram is about  $\gamma_k = 1$ , the same as the variance of the time series,  $V = 1$ . For  $\beta = 1, 2$ , and  $3$ , excellent correlations are obtained with  $\gamma_k \sim k^{2Ha}$ , Eq. (29). For  $\beta = 2$ ,  $Ha = 0.47$  compared satisfactorily to the expected value  $Ha = 0.50$ .

The values of  $Ha$  obtained from the best fit of Eq. (29) to the semivariograms in the range  $-1 \leq \beta \leq 5$  are given in Fig. 17. The straight-line correlation is with the self-affine fractal relation  $\beta = 2Ha + 1$ , Eq. (62).

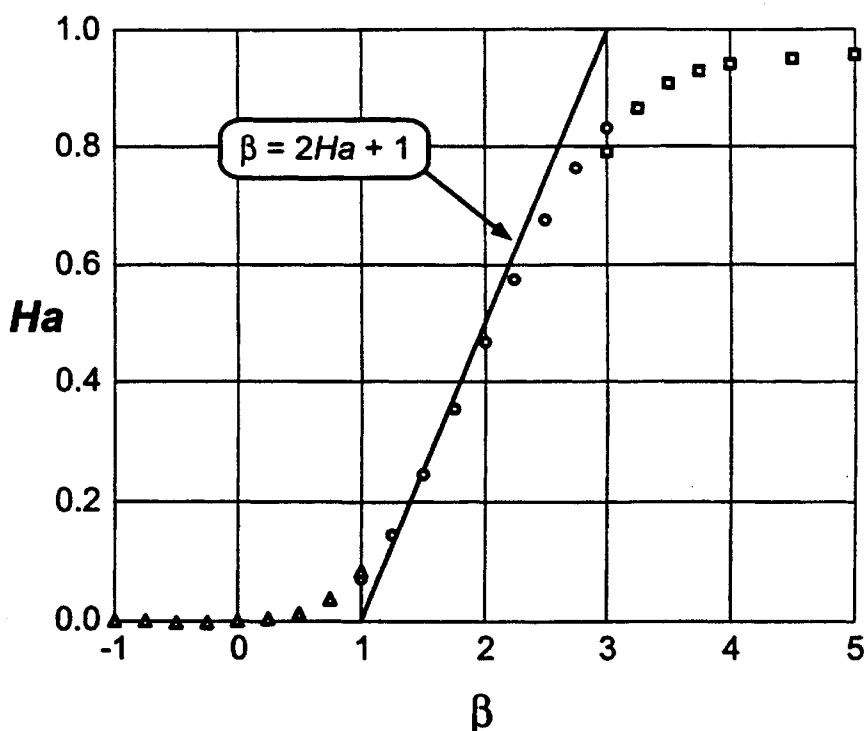


FIG. 17. The dependence of the Hausdorff exponent,  $Ha$ , on  $\beta$ , for fractional Gaussian noises and fractional Brownian motions with  $N = 4096$  points. The values for  $Ha$  have been obtained from the best fit of  $\gamma \sim k^{2Ha}$ , Eq. (29). Results are given for  $-1 \leq \beta \leq 5$ ; each symbol represents the best fit for  $Ha$  at that  $\beta$ . Examples of obtaining  $Ha$  from semivariograms are given in Fig. 16. The straight-line correlation is with the self-affine fractal relation  $\beta = 2Ha + 1$ , Eq. (62), for  $1 \leq \beta \leq 3$ . The triangles ( $-1 \leq \beta \leq 1$ ), circles ( $1 \leq \beta \leq 3$ ), and squares ( $3 \leq \beta \leq 5$ ) are explained in Table I.

Quite good agreement is found in the range  $1 \leq \beta \leq 3$ , where the fractional Brownian motions are expected to be self-affine fractals.

From Fig. 17, it is seen that  $Ha \approx 0$  for fractional Gaussian noises in the range  $-1 \leq \beta \leq 1$ . From Eq. (20),  $\sigma_n \sim n^{Ha}$ , one can conclude that, in this range of  $\beta$ , the standard deviation,  $\sigma_n$ , and thus the variance,  $V_n$ , are independent of the length of the signal,  $n$ . Therefore, these fractional noises are (weakly) stationary even though adjacent values may be correlated or anticorrelated. For these fractional noises, each with variance  $V = 1$ , and in the range  $-1 \leq \beta \leq 1$ , the semivariogram has a value of  $\gamma_k \approx 1$ . For fractional Gaussian noises ( $-1 \leq \beta \leq 1$ ), semivariograms are not a measure of persistence or antipersistence strength in a self-affine time series. We note that theoretically this result might appear to be inconsistent with Eq. (12), where the semivariogram is  $\gamma_k = (V_n - c_k)$ . The only case where the autocovariance  $c_k = 0$  is for a white noise ( $\beta = 0$ ) and  $k \neq 0$ . However, for  $-1 < \beta < 1$  and at large  $k$ , the autocovariance  $c_k \approx 0$ , giving the result that  $\gamma_k \approx V_n$ .

For the fractional Brownian motions in the range  $1 \leq \beta \leq 3$ ,  $Ha$  varies from 0 to 1. From Eq. (20),  $\sigma_n \sim n^{Ha}$ , we conclude that the standard

deviation,  $\sigma_n$ , and thus the variance,  $V_n$ , both have a power-law dependence on the length of the signal  $n$ . Therefore, these fractional Brownian motions are clearly nonstationary.

#### 4. LOG-NORMAL NOISES AND MOTIONS

##### 4.1. Log-Normal Distributions

The fractional Gaussian noises and fractional Brownian motions we have considered have been based on a Gaussian (normal) frequency-size distribution of values; therefore, the resulting time series have both positive and negative values. The standard form of a Gaussian distribution is obtained by taking  $\bar{y} = 0$  and  $\sigma_y = 1$ . All Gaussian distributions can be rescaled to the normalized standard form using linear transformations. The value of  $\beta$  completely specifies a normalized fractional Gaussian noise or fractional Brownian motion.

However, many naturally occurring time series have only positive values. For example, the volumetric flow in a river,  $Q(t)$ , is always positive as illustrated in Fig. 1b. One of the most widely used positive distributions is the log-normal distribution. A normal distribution can be converted to a log-normal distribution using the relation

$$x(t) = e^{y(t)}, \quad (73)$$

where  $x(t)$  has a log-normal distribution of values and  $y(t)$  has a normal distribution of values. In order to specify a log-normal distribution, it is necessary to specify the mean of the distribution,  $\bar{x}$ , and its coefficient of variation,  $c_v$ , which is the ratio of the standard deviation of the log-normal distribution to its nonzero mean:

$$c_v = \frac{\sigma_x}{\bar{x}}. \quad (74)$$

The coefficient of variation,  $c_v$ , is a measure of the relative dispersion of a time series; the standard deviation is a measure of the absolute dispersion. If  $c_v \ll 1$ , it may be appropriate to consider a Gaussian distribution. In many cases, however, this will be a poor approximation.

Although normal distributions have a universal form, i.e., zero mean ( $\bar{y} = 0$ ) and unit variance ( $V = 1$ ), this is not the case for the log-normal distribution; no standard form exists. The coefficient of variation,  $c_v$ , classifies a family of log-normal distributions. The probability distribution functions,  $f(x)$ , for the log-normal distribution are given in Fig. 18 for  $\bar{x} = 1$  and  $c_v = 0.25, 0.50, 1.00$ . It is seen that the shape of the log-normal

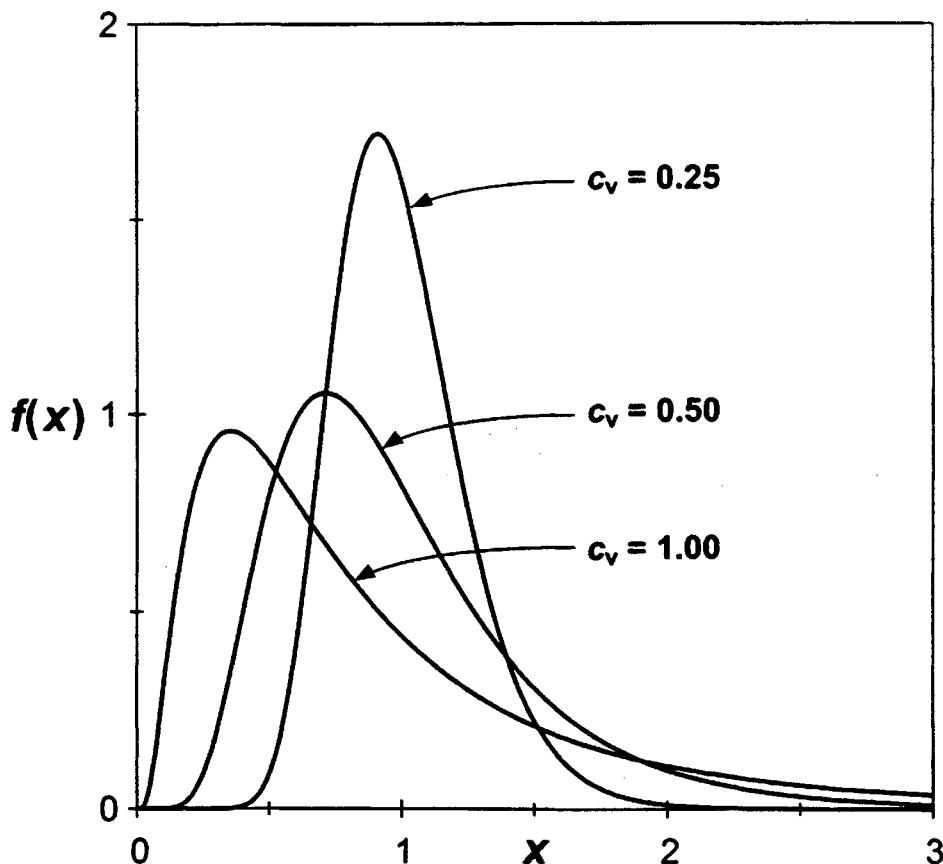


FIG. 18. The probability distribution function  $f(x)$  for the log-normal distribution with unit mean ( $\bar{x} = 1$ ) and several values of the coefficient of variation,  $c_v = 0.25, 0.50, 1.00$ .

distribution changes systematically for different  $c_v$ . As the value of  $c_v$  becomes smaller, the distribution narrows and the maximum value for  $f(x)$  occurs at a value of  $x$  approaching 1. In the limit  $c_v \rightarrow 0$ , the distribution is a delta function centered at  $x = 1$ . As  $c_v$  becomes larger, the distribution spreads out and the maximum value for  $f(x)$  occurs at smaller  $x$ . The distribution of log-normal values has an asymmetric tail extending toward values that are more positive. Whereas the normal distribution is symmetric, the asymmetry for the log-normal distribution increases with increasing coefficient of variation,  $c_v$ . As an example of a time series with an approximately log-normal distribution, Fig. 1b is a plot of daily river discharges for  $T = 75$  years from the Salt River in Arizona, with a coefficient of variation,  $c_v = 2.6$ .

Log-normal distributions are a one-parameter family of distributions depending on the appropriate value of  $c_v$ . This has important implications in terms of applications. It is often appropriate to approximate the distribution of annual rainfalls at a station by a log-normal distribution. A maritime station, for instance Seattle, would have little year-to-year variation in rainfall and a small value for  $c_v$ . On the other hand, an arid station,

for instance Phoenix, would have large year-to-year variations in rainfall and a large value for  $c_v$ .

#### 4.2. Fractional Log-Normal Noises and Motions

A Gaussian white-noise sequence can be converted to a log-normal, white-noise sequence using Eq. (73) along with

$$\sigma_y = [\ln(1 + c_v^2)]^{1/2}, \quad (75)$$

$$\bar{y} = \ln \left[ \frac{\bar{x}}{(1 + c_v^2)^{1/2}} \right], \quad (76)$$

where  $\bar{x}$  is the mean of the log-normal distribution, and  $\bar{y}$  and  $\sigma_y$  are the mean and standard deviation of the normal distribution. Log-normal white-noise sequences ( $\beta = 0$ ) with unit mean ( $\bar{x} = 1$ ) are given in Fig. 19 for  $c_v = 0.2, 0.5, 1.0, 2.0$ . With  $c_v = 0.2$ , the standard deviation is small compared with the mean, the distribution is nearly symmetric, and it closely resembles a Gaussian white noise. With  $c_v = 2$ , the variance is large compared with the mean and the distribution is strongly asymmetrical.

Just as a Gaussian white-noise sequence can be converted to a log-normal white-noise sequence, so too can fractional Gaussian noises and fractional Brownian motions be converted to fractional log-normal noises and motions using Eqs. (73) to (76). Several examples are given in Fig. 19. In each case the mean is unity ( $\bar{x} = 1$ ). This is a two-parameter family of noises and motions. The values of  $\beta$  are a measure of the persistence of the time series. The values of  $c_v$  are a measure of the asymmetry of the distribution of values. Extensive studies of fractional log-normal noises and motions have been given by Mandelbrot and Wallis (1969a). These authors referred to the dependence on  $c_v$  as the Noah effect and the dependence on  $\beta$  as the Joseph effect. The different time series in Fig. 19 resemble typical river flow time series. Increasing  $c_v$ , the Noah effect, is indicative of a climate where there is large variability in river flow. Increasing  $\beta$ , the Joseph effect, is indicative of more strongly correlated values. With higher values of  $\beta$ , a year of flood is more likely to follow a previous year of flood, and a year of drought is more likely to follow a previous year of drought.

#### 4.3. Spectral Analysis

In Section 3.2 we used the Fourier spectral filtering method to create fractional Gaussian noises and motions with  $-3 \leq \beta \leq 5$ . Using Eqs. (73)

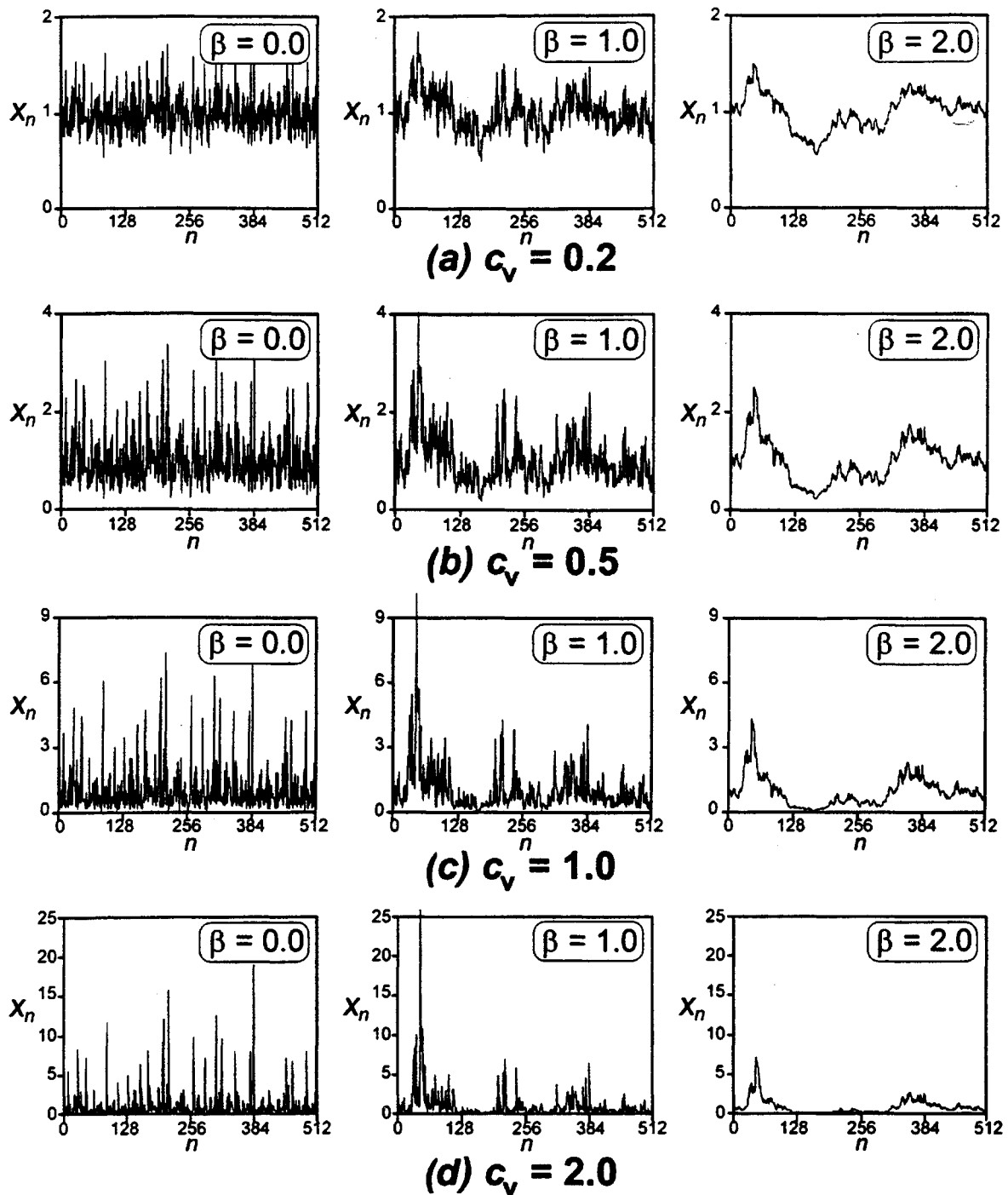


FIG. 19. Examples of fractional log-normal noises and motions with  $N = 512$  points. In each case a fractional Gaussian noise or a fractional Brownian motion has been converted to a fractional log-normal noise or motion; examples are given for  $\beta = 0, 1, 2$ . The conversions were made using Eqs. (73) to (76). Examples are given for (a)  $c_v = 0.2$ , (b)  $c_v = 0.5$ , (c)  $c_v = 1.0$ , and (d)  $c_v = 2.0$ . In all cases the mean of the series is unity ( $\bar{x} = 1$ ).

TABLE II LEGEND FOR SYMBOLS USED IN FRACTIONAL LOG-NORMAL NOISE AND MOTION ANALYSES

Symbol <sup>a</sup>	Symbol represents results of analyses on ...	Which have a range of Beta that is ...	And were created by taking the log-normal distribution of ...
□ ■ ■	Fractional log-normal motions	$3 \leq \beta \leq 5$	Extended fractional motions
○ ● ●	Fractional log-normal motions	$1 \leq \beta \leq 3$	Fractional Brownian motions
△ ▲ ▲	Fractional log-normal noises	$-1 \leq \beta \leq 1$	Fractional Gaussian noises
◇ ◆ ◆	Fractional log-normal noises	$-3 \leq \beta \leq -1$	Extended fractional Gaussian noises

<sup>a</sup>Different shading of the symbol represents the coefficient of variation,  $c_v$ , of the log-normal noise or motion on which the analysis was performed: white ( $c_v = 0.2$ ), gray ( $c_v = 0.5$ ), black ( $c_v = 1.0$ ).

to (76), each of the fractional Gaussian noises and motions has been converted to its log-normal equivalent with three different coefficients of variation,  $c_v = 0.2, 0.5, 1.0$ ,  $N = 4096$  points, and  $\beta$  ranging over  $-3 \leq \beta \leq 5$ . Table II provides a legend for symbols that are used in the log-normal noise and motion analyses that follow in subsequent portions of this article.

We verify the  $\beta$  ascribed to the log-normal self-affine time series by using Fourier power-spectral analysis. The resulting spectral exponent is again denoted by  $\beta_{PS}$ . Before doing a spectral analysis, each of the log-normal time series is first rescaled to zero mean and then multiplied by the Welch window, Eq. (67). Results of these power-spectral analyses,  $\beta_{PS}$  vs  $\beta$ , are given in Fig. 20. For log-normal time series, there is excellent correlation between  $\beta_{PS}$  vs  $\beta$ , for  $0 < \beta < 4$ . For  $\beta < 0$  and  $\beta > 4$ , the correlation is poor.

A recommended technique (e.g., Hewett, 1986) is to convert the values of a non-Gaussian distribution to those of a Gaussian distribution. However, we recommend that this only be used if the resulting  $\beta$  from Fourier

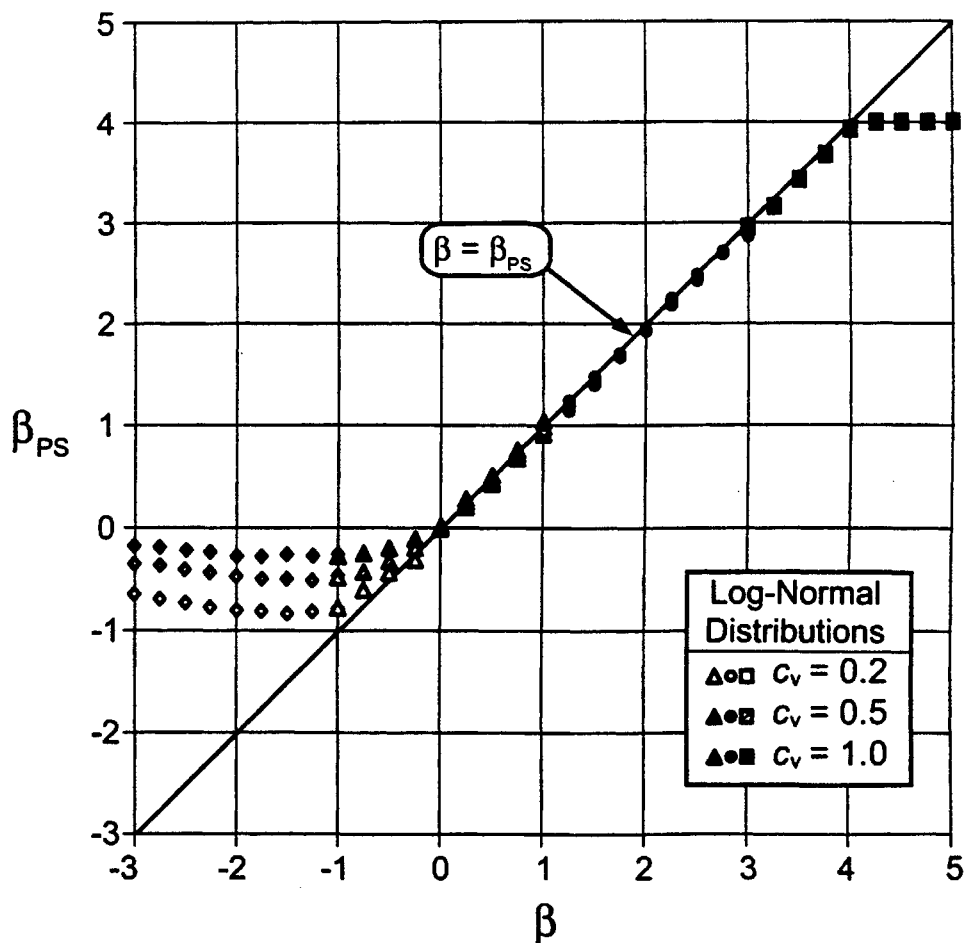


FIG. 20. The dependence of the power-spectral exponent,  $\beta_{PS}$ , on  $\beta$ , for synthetic fractional log-normal noises and motions with  $N = 4096$  points. The fractional log-normal noises and motions were each constructed to have a theoretical power-spectral exponent,  $\beta$ , by using Eqs. (73) to (76) applied to fractional Gaussian noises and motions. The synthetic noises and motions are windowed using the Welch window, Eq. (67). We then verify the power-spectral exponent of each synthetic fractional log-normal noise and motion by finding the best fit of  $S \sim f^{-\beta}$ , Eq. (39), and denoting it by  $\beta_{PS}$ . Results are given for  $-1 \leq \beta \leq 5$  and  $c_v = 0.2$  (white),  $0.5$  (gray), and  $1.0$  (black); each symbol represents the best fit for  $\beta_{PS}$  at that  $\beta$ . The straight-line correlation is with  $\beta = \beta_{PS}$ . The diamonds ( $-3 \leq \beta \leq -1$ ), triangles ( $-1 \leq \beta \leq 1$ ), circles ( $1 \leq \beta \leq 3$ ), and squares ( $3 \leq \beta \leq 5$ ) are explained in Table II.

power-spectral analysis is less than 0. In this case, we do recommend that the series be converted to their normal equivalent before performing a discrete Fourier transform.

#### 4.4. Semivariograms

Using the definition for the semivariogram,  $\gamma_k$ , given in Eq. (8), semivariograms for several fractional log-normal noises and motions, each with 4096 points and  $c_v = 0.5$ , are given in Fig. 21. The results are generally

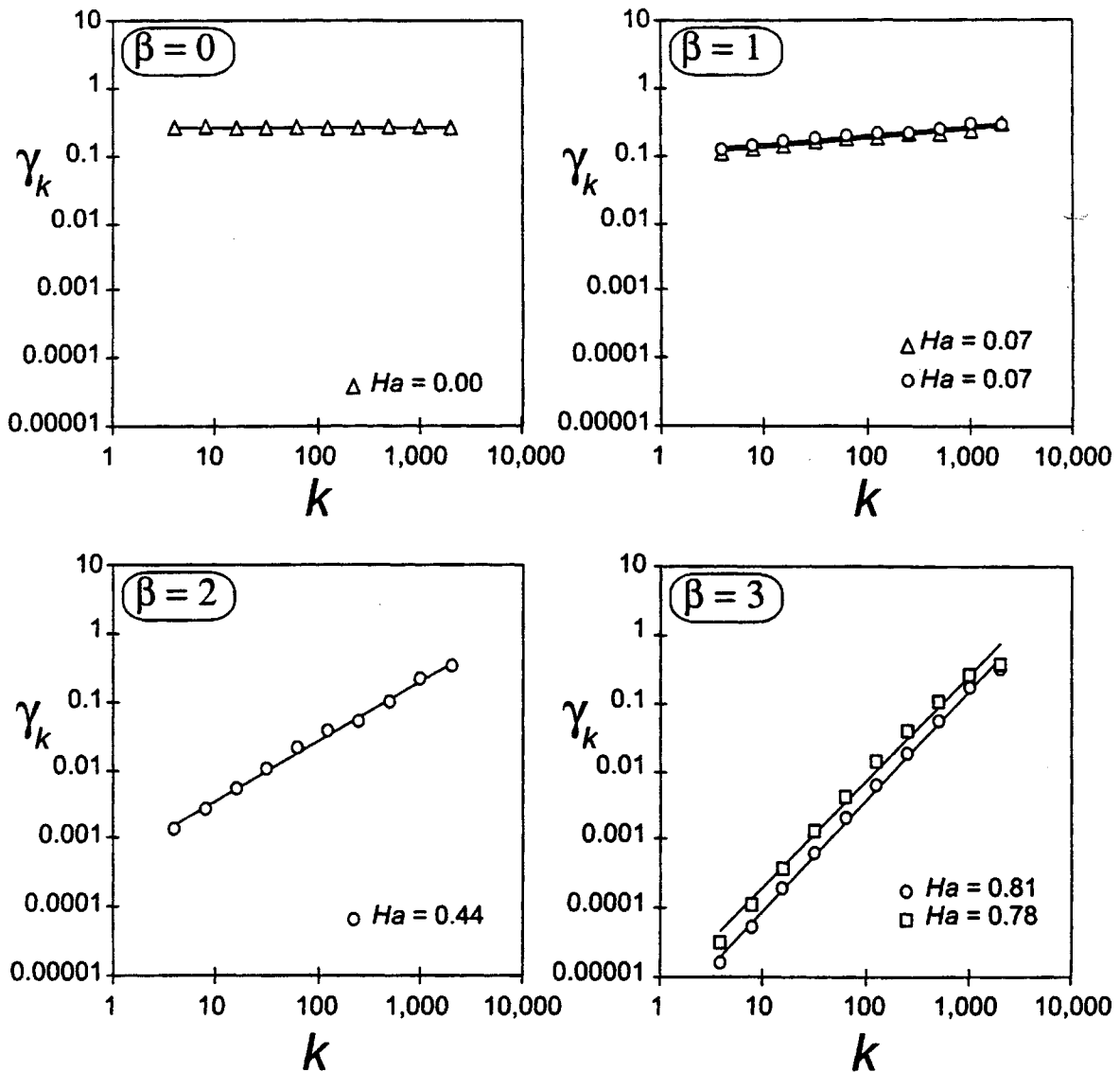


FIG. 21. Semivariograms for several fractional log-normal noises and motions with  $c_v = 0.5$ . Each semivariogram is obtained using Eq. (8) with lag  $k = 4, 8, 16, \dots, 2048$ , and applied to fractional log-normal noises and motions with  $N = 4096$  points. Examples of time series with  $N = 512$  points and the same characteristics are illustrated in Fig. 19. The straight-line correlations are with  $\gamma \sim k^{2Ha}$ , Eq. (29). The slope of the best-fit straight line for  $\log(\gamma)$  vs  $\log(k)$  is  $2Ha$ . Values for one-half of the slope,  $Ha$ , are given for each of the examples. The fractional log-normal noises and motions were each obtained by using Eqs. (73) to (76) applied to fractional Gaussian noises and motions, and letting  $c_v = 0.5$ . The triangles ( $\beta = 0, 1$ ), circles ( $\beta = 1, 2, 3$ ), and squares ( $\beta = 3$ ) are explained in Table II.

similar to those obtained for fractional Gaussian noises and fractional Brownian motions given in Fig. 16. For  $\beta = 1, 2, 3$ , excellent correlations are obtained with  $\gamma_k \sim k^{2Ha}$ , Eq. (29).

The values of  $Ha$  obtained from the best fit of Eq. (29) to the semivariograms in the range  $-1 \leq \beta \leq 5$  are given in Fig. 22. Results are given for  $c_v = 0.2, 0.5$  (illustrated in Fig. 21), and 1.0. The straight-line correlation is

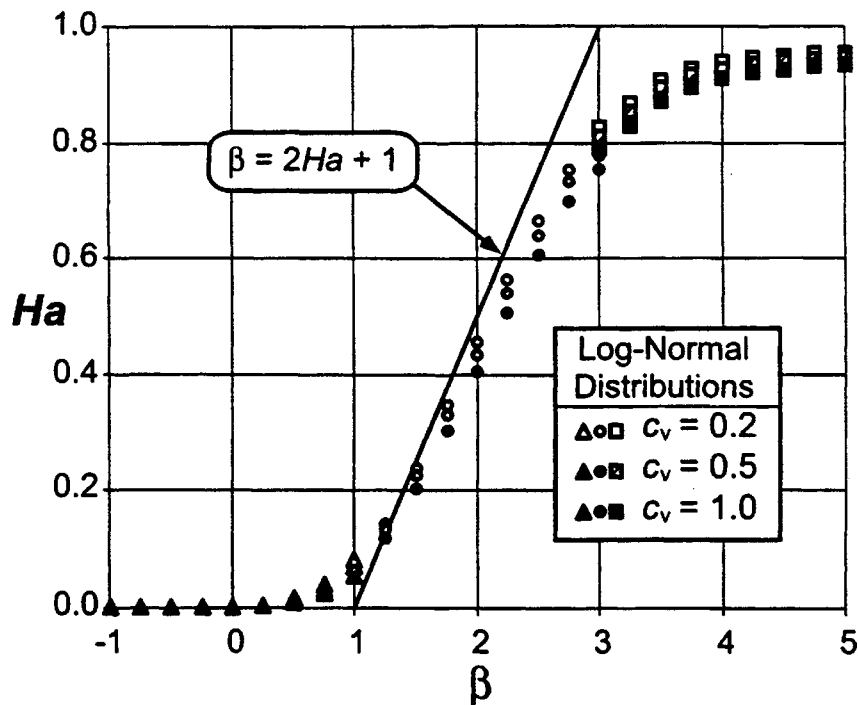


FIG. 22. The dependence of the Hausdorff exponent,  $Ha$ , on  $\beta$ , for fractional log-normal noises and motions with  $N = 4096$  points. The values for  $Ha$  have been obtained from the best fit of  $\gamma \sim k^{2Ha}$ , Eq. (29). Results are given for  $-1 \leq \beta \leq 5$  and  $c_v = 0.2$  (white), 0.5 (gray), and 1.0 (black); each symbol represents the best fit for  $Ha$  at that  $\beta$ . Examples of obtaining  $Ha$  from semivariograms are given in Fig. 21. The straight-line correlation is with the self-affine fractal relation  $\beta = 2Ha + 1$ , Eq. (62), for  $1 \leq \beta \leq 3$ . The triangles ( $-1 \leq \beta \leq 1$ ), circles ( $1 \leq \beta \leq 3$ ), and squares ( $3 \leq \beta \leq 5$ ) are explained in Table II.

with the self-affine fractal relation,  $\beta = 2Ha + 1$ , Eq. (62). The results are, again, very similar to those obtained for fractional Gaussian noises and fractional Brownian motions, given in Fig. 17. Again, good agreement with  $\beta = 2Ha + 1$ , Eq. (62), is found in the range  $1 \leq \beta \leq 3$ , where the fractional motions are expected to be self-affine fractals. We can conclude that semivariograms are very good at quantifying the strength of persistence for nonstationary self-affine time series with  $1 \leq \beta \leq 3$ , both for Gaussian and log-normal distributions.

## 5. RESCALED-RANGE (R/S) ANALYSIS

### 5.1. The Method

An alternative approach to the quantification of correlations in time series was developed by Harold E. Hurst (Hurst, 1951; Hurst *et al.*, 1965).

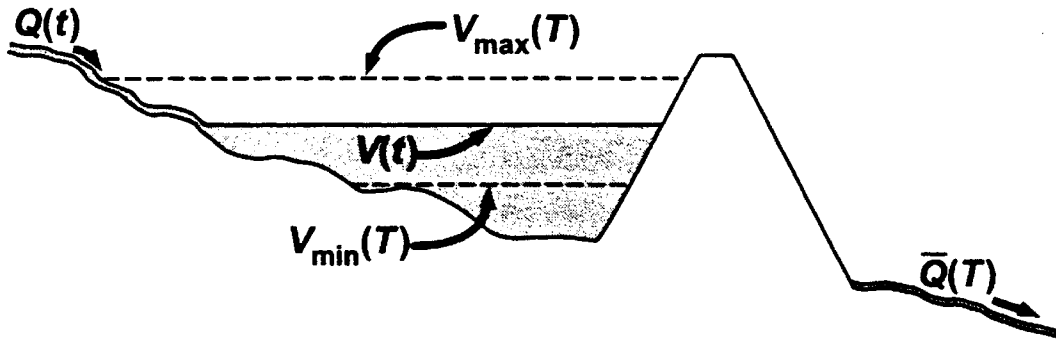


FIG. 23. Illustration of how rescaled-range ( $R/S$ ) analysis is carried out. The flow into a reservoir is  $Q(t)$  and the average flow out is  $\bar{Q}(T)$ , where  $0 \leq t \leq T$ . The maximum volume of water in the reservoir during the period  $T$  is  $V_{\max}(T)$  and the minimum is  $V_{\min}(T)$ ; the difference is the range  $R(T) = V_{\max}(T) - V_{\min}(T)$ .

Hurst spent his life studying the hydrology of the Nile River, in particular the record of floods and droughts. He considered a river flow as a time series and determined the storage limits in an idealized reservoir. Based on these studies, he introduced empirically the concept of rescaled-range ( $R/S$ ) analysis. His method is illustrated in Fig. 23. Consider a reservoir behind a dam that never overflows or empties; the flow into the reservoir is the flow in the river upstream of the dam,  $Q(t)$ . The flow out of the reservoir,  $\bar{Q}(T)$ , is assumed to be the mean of the flow into the reservoir over a period  $T$ :

$$\bar{Q}(T) = \frac{1}{T} \int_0^T Q(t) dt. \quad (77)$$

The volume of water in the reservoir as a function of time,  $V(t)$ , is given by

$$V(t) = V(0) + \left( \int_0^t Q(t') dt' \right) - t\bar{Q}(T), \quad (78)$$

where  $V(0)$  is the volume of water at  $t = 0$ . Taking  $t = T$  and substituting Eq. (77) into Eq. (78), we have  $V(T) = V(0)$ ; in other words, the volume in the reservoir is the same at  $t = 0$  and  $t = T$ . The range  $R(T)$  is defined to be the difference between the maximum volume of water  $V_{\max}$  and the minimum volume of water  $V_{\min}$  during the period  $T$ :

$$R(T) = V_{\max}(T) - V_{\min}(T). \quad (79)$$

The rescaled range is defined to be  $R(T)/S(T)$ , where  $S(T)$  is the standard deviation of the flow  $Q(t)$  during the period  $T$ :

$$S(T) = \left[ \frac{1}{T} \int_0^T \{Q(t') - \bar{Q}(T)\}^2 dt' \right]^{1/2}. \quad (80)$$

This is identical to the definition of the standard deviation,  $\sigma(T)$ . We use  $S$  here to maintain the standard  $R/S$  nomenclature. The period  $T$  can be broken up into subintervals  $\tau$ , for instance  $\tau = T/2, T/4, T/8$ , and so forth. For a given value of  $\tau$ ,  $R(\tau)$  and  $S(\tau)$  are calculated for each of the  $T/\tau$  subdivisions, by substituting  $\tau$  for  $T$  in Eqs. (79) and (80). The  $T/\tau$  individual values for  $R(\tau)/S(\tau)$  are then averaged.

Hurst (1951) and Hurst *et al.* (1965) found empirically that many data sets in nature satisfy the power-law relation

$$\left[ \frac{R(\tau)}{S(\tau)} \right]_{\text{av}} = \left( \frac{\tau}{2} \right)^{Hu}, \quad (81)$$

where  $Hu$  is known as the Hurst exponent. For  $\tau = 2$ ,  $R(\tau)/S(\tau) = 1$  by definition. Examples included river discharges, lake levels, tree ring thicknesses, varve thicknesses, sunspot numbers, and atmospheric temperature and pressure. They generally found that  $0.70 < Hu < 0.80$ . Hurst's data sets are included in the McLeod–Hipel Time-Series Datasets Collection (McLeod and Hipel, 1995), which contains over 300 time series in electronic format and is available over the Internet.

The  $R/S$  analysis is easily extended to a discrete time series,  $y_n$ ,  $n = 1, 2, 3, \dots, N$ . The running sum,  $y_m$ , of the time series,  $y_n$ , relative to its mean is

$$y_m = \sum_{n=1}^m (y_n - \bar{y}_N) = \left( \sum_{n=1}^m y_n \right) - m\bar{y}_N. \quad (82)$$

The range is defined by

$$R_N = (y_m)_{\text{max}} - (y_m)_{\text{min}} \quad (83)$$

with

$$S_N = \sigma_N, \quad (84)$$

where  $\bar{y}_N$  and  $\sigma_N$  are the mean and standard deviation of all  $N$  values in the time series,  $y_n$ . From Eqs. (82) to (84), we have a value of  $(R_N/S_N)$  for the time series,  $y_n$ ,  $n = 1, 2, 3, \dots, N$ . Since we are interested in how

$(R/S)$  varies with successive subintervals  $\tau$  of  $N$ , we substitute  $\tau$  for  $N$  in Eqs. (82) to (84). The Hurst exponent,  $Hu$ , is obtained from

$$\left(\frac{R_\tau}{S_\tau}\right)_{av} = \left(\frac{\tau}{2}\right)^{Hu}. \quad (85)$$

For example, if 64 values of  $y_n$  are available for a time series, the  $R_N$  and  $S_N$  for  $N = 64$  are obtained. Then the data are broken into two parts, each with  $\tau = 32$  (1, 2, ..., 32 and 33, 34, ..., 64). The values for  $R_{32}$  and  $S_{32}$  are obtained for the two parts. The two values of  $R_{32}/S_{32}$  are then averaged to give  $(R_{32}/S_{32})_{av}$ . The data set is then broken into four parts, each with  $\tau = 16$  (1, 2, ..., 16; 17, 18, ..., 32; 33, 34, ..., 48; and 49, 50, ..., 64). The values for  $R_{16}/S_{16}$  are obtained for the four parts and are averaged to give  $(R_{16}/S_{16})_{av}$ . This process is continued for  $\tau = 8$  and  $\tau = 4$  to give  $(R_8/S_8)_{av}$  and  $(R_4/S_4)_{av}$ . For  $\tau = 2$ , the value for  $R_2 = S_2$  so that  $R_2/S_2 = 1$ . The values of  $\log(R_\tau/S_\tau)_{av}$  are plotted against  $\log(\tau/2)$  and the best-fit straight line gives  $Hu$  from Eq. (85). In practice, there is generally some curvature of  $(R_\tau/S_\tau)_{av}$  for small values of  $\tau/2$  and they are therefore omitted (Tapiero and Vallois, 1996).

The running sum of a Gaussian white noise ( $\beta = 0$ ) is a Brownian motion ( $\beta = 2$ ) and  $Ha = 0.5$ . This would imply that

$$\beta = 2Hu - 1. \quad (86)$$

From Eq. (62) we have  $\beta = 2Ha + 1$ , giving

$$Hu(\beta - 2) = Ha(\beta). \quad (87)$$

Since a white noise ( $\beta = 0$ ) is a random process that has adjacent values which are uncorrelated, it is appropriate to conclude that  $Hu = 0.5$  implies a time series that is uncorrelated. It follows that  $0.5 < Hu \leq 1.0$  implies persistence and that  $0 \leq Hu < 0.5$  implies antipersistence.

It should be noted that not all authors use the running sum when applying the rescaled-range method. The technique can be applied directly to the specified time series, i.e., substituting  $y_n$  for  $y_m$  in Eq. (83). If this is done, the resulting Hurst exponent from Eq. (85) varies from 0 to 1 when  $\beta$  is in the range 1 to 3; i.e., the results in Fig. 25 (discussed in the next section) will be shifted by  $\beta + 2$ . Care should be taken to specify which version of rescaled range is being used, as there is currently some confusion in the literature. In this article, we will use the running sum as given in Eq. (82) when applying rescaled range to a discrete time series.

## 5.2. Applications to Fractional Gaussian Noises and Motions

The Hurst rescaled-range analysis was first applied to fractional Gaussian noises and fractional Brownian motions by Mandelbrot and Wallis (1969c). The dependence of  $\log(R/S)_{av}$  on  $\log(\tau/2)$  for several fractional noises and motions with 4096 points, similar to those illustrated in Fig. 10, are given in Fig. 24. For  $\beta = 0, 1$ , and 2, excellent correlations with the

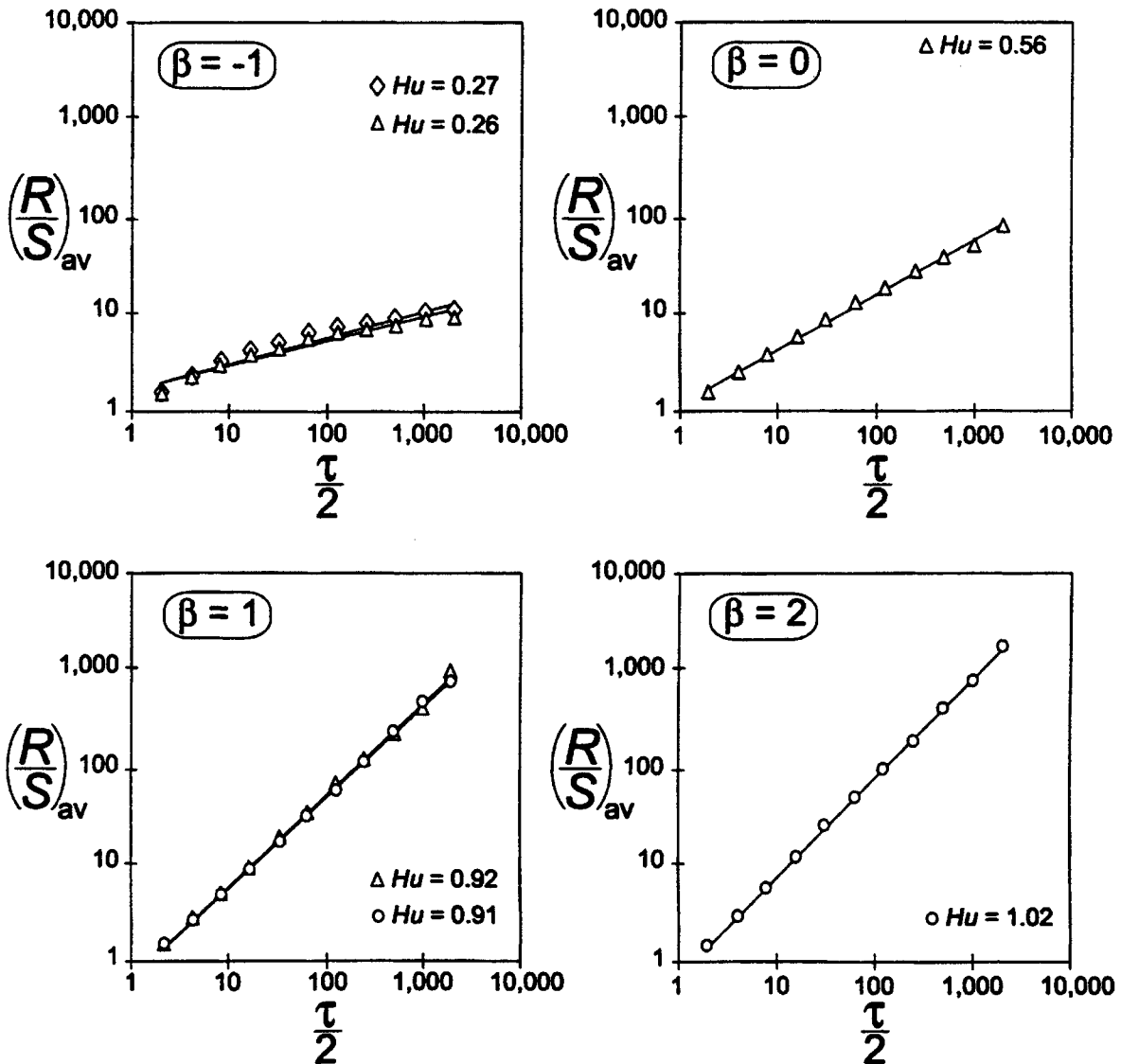


FIG. 24. Hurst rescaled-range  $(R/S)$  analyses for several fractional Gaussian noises and fractional Brownian motions with  $N = 4096$  points. Average values of  $R/S$  are given as a function of the interval  $\tau/2$  for  $\tau = 4, 8, 16, \dots, 4096$ , where  $R$  and  $S$  are calculated using Eqs. (82) to (84). Examples of time series with  $N = 512$  points and the same characteristics as the noises and motions with 4096 points are illustrated in Fig. 10. The straight-line correlations are with  $(R/S)_{av} \sim (\tau/2)^{Hu}$ , Eq. (85). The slope of the best-fit straight line for  $\log(R/S)_{av}$  vs  $\log(\tau/2)$  is  $Hu$ . Values for  $Hu$  are given for each of the examples. The diamonds ( $\beta = -1$ ), triangles ( $\beta = -1, 0, 1$ ), and circles ( $\beta = 1, 2$ ) are explained in Table I.

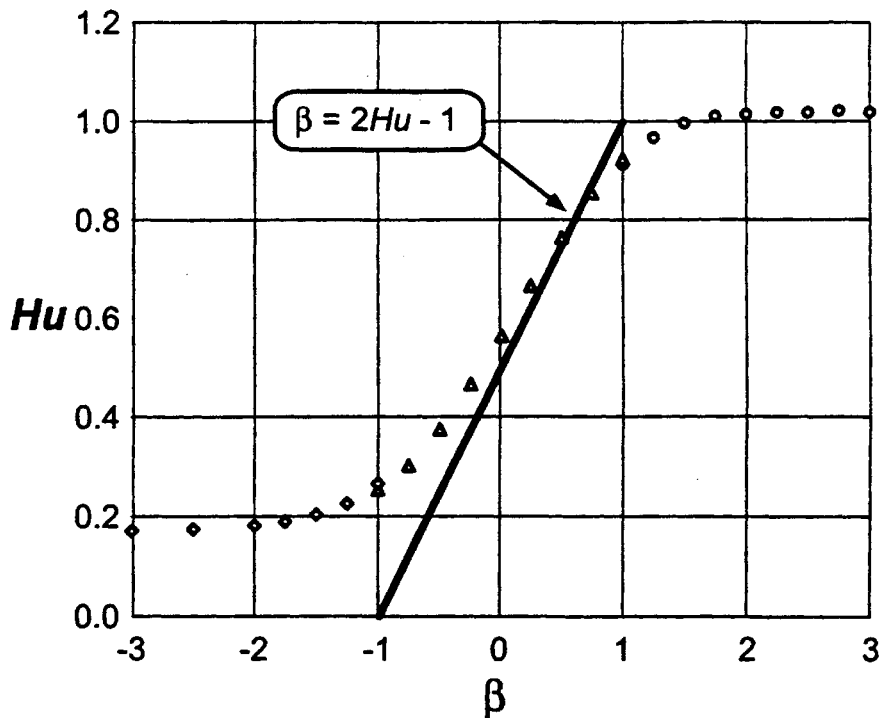


FIG. 25. The dependence of the Hurst exponent,  $Hu$ , on  $\beta$ , for fractional Gaussian noises and fractional Brownian motions with  $N = 4096$  points. The values for  $Hu$  have been obtained from the best fit of  $(R/S)_{av} \sim (\tau/2)^{Hu}$ , Eq. (85). Results are given for  $-3 \leq \beta \leq 3$ ; each symbol represents the best fit for  $Hu$  at that  $\beta$ . Examples of obtaining  $Hu$  from rescaled-range  $(R/S)$  analyses are given in Fig. 24. The straight-line correlation is with the relation  $\beta = 2Hu - 1$ , Eq. (86), for  $-1 \leq \beta \leq 1$ . The diamonds ( $-3 \leq \beta \leq -1$ ), triangles ( $-1 \leq \beta \leq 1$ ), and circles ( $1 \leq \beta \leq 3$ ) are explained in Table I.

Hurst relation,  $(R/S)_{av} \sim (\tau/2)^{Hu}$ , Eq. (85), are obtained. For  $\beta = 0$ , we find  $Hu = 0.56$  compared with the expected value of 0.5 for the uncorrelated white Gaussian noise.

The values of  $Hu$  obtained for the best fit to the Hurst relation, Eq. (85), in the range  $-3 \leq \beta \leq 3$  are given in Fig. 25. The straight-line correlation is with  $\beta = 2Hu - 1$ , Eq. (86). Reasonably good agreement is found in the range  $-1 \leq \beta \leq 1$ ; however, for  $\beta < 0$ ,  $Hu$  definitely begins to deviate from the straight-line correlation. The Hurst exponent provides a quantitative measure of the strength of persistence and antipersistence for fractional Gaussian noises ( $-1 \leq \beta \leq 1$ ), but the only place it is exactly correlated with  $\beta = 2Hu - 1$ , Eq. (86), is at  $Hu = 0.7$ . Extensive  $R/S$  analyses of fractional Gaussian noises and fractional Brownian motions have been carried out by Bassingthwaite and Raymond (1994). They found, when using synthetic self-affine noises and motions constructed to have certain values of  $\beta$ , that  $Hu$  converges very slowly to the expected value of  $\beta = 2Hu - 1$ , Eq. (86), for large sample sizes,  $N$ . For

values of  $N \ll 4096$ , we have found that  $Hu$  gets steadily worse, with  $Hu = 0.5$  when  $\beta < 0$ .

### 5.3. Applications to Fractional Log-Normal Noises and Motions

In Fig. 26, we apply rescaled-range analysis to several fractional log-normal noises and motions with  $N = 4096$  points and  $c_v = 0.5$ . Log-normal noises and motions similar to these are given in Fig. 19. The values for  $Hu$ , the Hurst exponent, have been obtained from the best fit of  $(R/S)_{av} \sim (\tau/2)^{Hu}$ , Eq. (85). We find good correlations for  $\beta = -1, 0, 1$ , and 2.

The values of  $Hu$  obtained for the best fit to Eq. (85) in the range  $-3 \leq \beta \leq 3$  with  $c_v = 0.2, 0.5$  (illustrated in Fig. 26), and 1.0 are given in Fig. 27. The straight-line correlation is with  $\beta = 2Hu - 1$ , Eq. (86). The agreement obtained for  $c_v = 0.2$  is similar to that found in Fig. 25, where the same analyses have been applied to fractional Gaussian noises and motions. For  $c_v = 0.5$  and 1.0, the asymptotic values for negative  $\beta$ 's become systematically higher. For log-normal noises with  $\beta < 0$ , values for  $Hu$  are clearly biased towards higher and higher values as  $c_v$  increases.

We recommend that if rescaled range is to be used, then the non-Gaussian distribution should first be converted (Hewett, 1986; Press *et al.*, 1994) to its Gaussian equivalent. However, even for a Gaussian distribution, the Hurst rescaled-range analysis is a poor estimator of the strength of antipersistence. Rescaled-range analysis has also been applied to fractional log-normal noises and motions by Mandelbrot and Wallis (1969c).

## 6. AVERAGE EXTREME-VALUE ANALYSIS

### 6.1. The Method

For many time series, the primary goal is to understand the frequency-size distribution of the extreme values. An example is a river discharge time series. The extreme values of this time series are floods. Flood hazard assessments require statistical estimators of these extreme values.

For a Gaussian white noise, the frequency-size distribution of the extreme values are clearly Gaussian. However, what about fractional noises and motions? In order to specify the extreme values of a time series we consider average extreme-value analysis. Taking a synthetic time series of length  $N$ , we first force the time series to have a mean of 0 by subtracting  $\bar{y}_N$ , the mean of the data series taken over  $N$ , from each successive value in the time series. We still use  $y_n$ ,  $n = 1, 2, 3, \dots, N$ , to

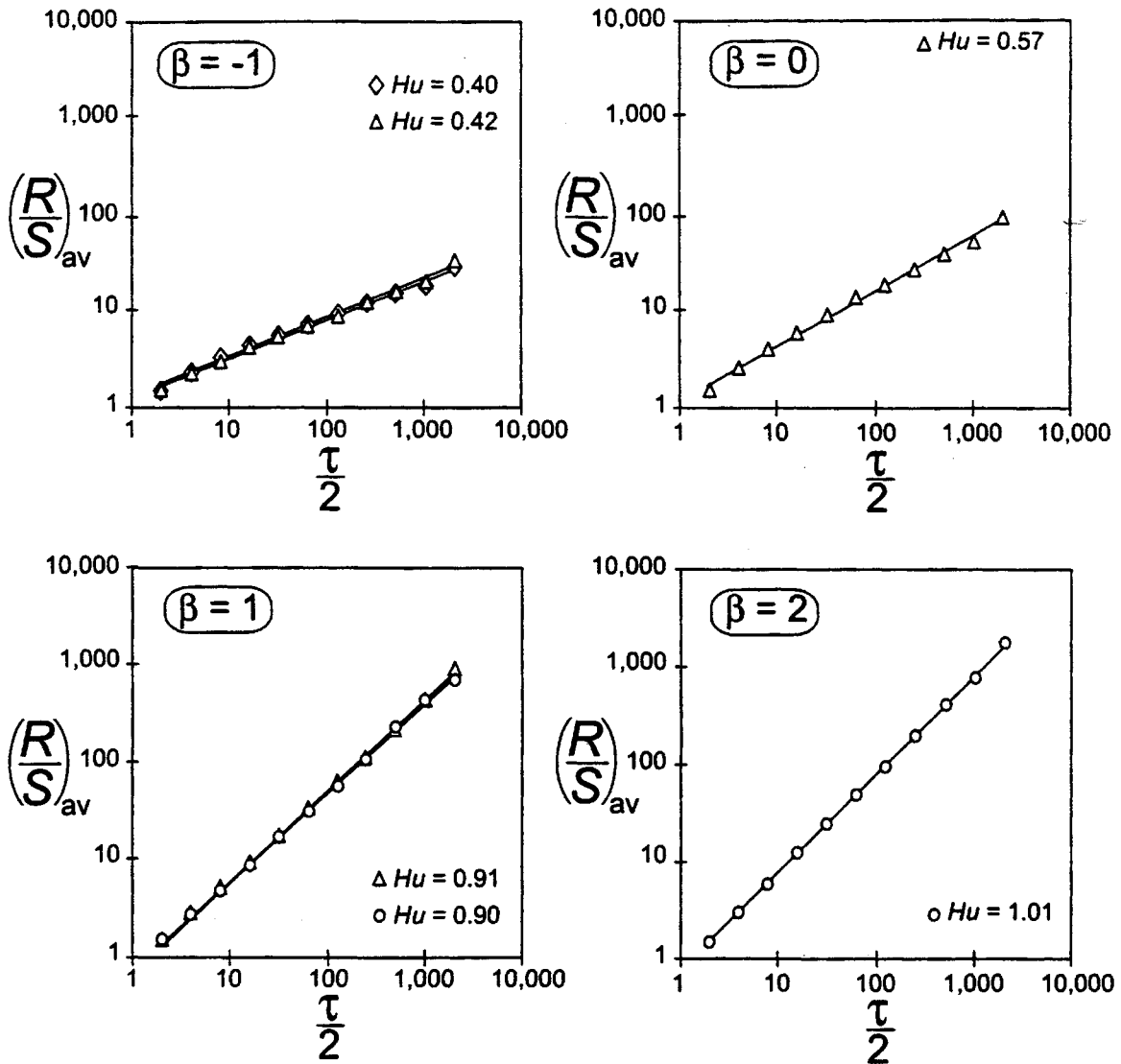


FIG. 26. Hurst rescaled-range  $(R/S)$  analyses for several fractional log-normal noises and motions with  $N = 4096$  points and  $c_v = 0.5$ . Average values of  $R/S$  are given as a function of the interval  $\tau/2$  for  $\tau = 4, 8, 16, \dots, 4096$ , where  $R$  and  $S$  are calculated using Eqs. (82) to (84). The fractional log-normal noises and motions were each obtained by using Eqs. (73) to (76) applied to fractional Gaussian noises and motions, and letting  $c_v = 0.5$ . Examples of time series with  $N = 512$  points and the same characteristics are illustrated in Fig. 19. The straight-line correlations are with  $(R/S)_{av} \sim (\tau/2)^{Hu}$ , Eq. (85). The slope of the best-fit straight line for  $\log(R/S)_{av}$  vs  $\log(\tau/2)$  is  $Hu$ . Values for  $Hu$  are given for each of the examples. The diamonds ( $\beta = -1$ ), triangles ( $\beta = -1, 0, 1$ ), and circles ( $\beta = 1, 2$ ) are explained in Table II.

represent the time series with zero mean. The maximum value of  $y_n$  over the  $N$  points,  $y_e$ , is assigned a period  $\tau = N$ . The period is then broken into two parts each of length  $N/2$  and the maximum value for each part is found. The average,  $(y_e)_{av}$ , of the two values  $y_e$  is assigned the period  $\tau = N/2$ . The process is repeated for  $\tau = N/4, N/8, N/16, \dots$ . To deter-

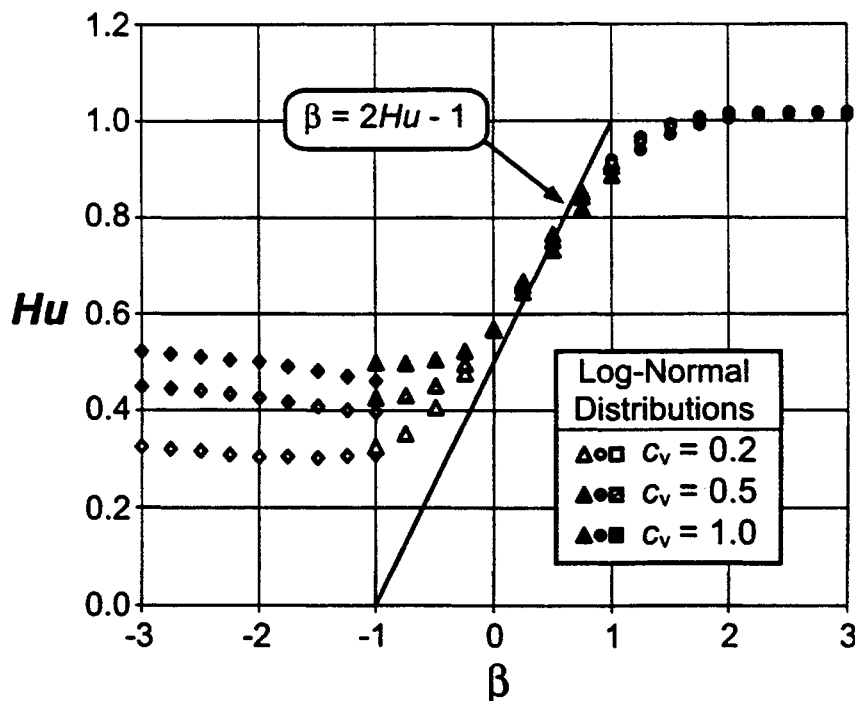


FIG. 27. The dependence of the Hurst exponent,  $Hu$ , on  $\beta$ , for fractional log-normal noises and motions with  $N = 4096$  points. The values for  $Hu$  have been obtained from the best fit of  $(R/S)_{av} \sim (\tau/2)^{Hu}$ , Eq. (85). Results are given for  $-3 \leq \beta \leq 3$  and  $c_v = 0.2$  (white), 0.5 (gray), and 1.0 (black); each symbol represents the best fit for  $Hu$  at that  $\beta$ . Examples of obtaining  $Hu$  from rescaled-range  $(R/S)$  analyses are given in Fig. 26. The straight-line correlation is with the relation  $\beta = 2Hu - 1$ , Eq. (86), for  $-1 \leq \beta \leq -3$ . The diamonds ( $-3 \leq \beta \leq -1$ ), triangles ( $-1 \leq \beta \leq 1$ ), and circles ( $1 \leq \beta \leq 3$ ) are explained in Table II.

mine whether the extreme values have a power-law dependence on the length of time considered, we correlate the results with

$$(y_e)_{av} \sim \tau^{He}, \quad (88)$$

where  $He$  is the extreme-value exponent. Consider the relation

$$\beta = 2He + 1, \quad (89)$$

which is analogous to  $\beta = 2Ha + 1$ , Eq. (62), where  $Ha$  is the Hausdorff exponent.

## 6.2. Applications to Fractional Gaussian Noises and Motions

We have applied average extreme-value analyses to several fractional noises and motions with 4096 points, similar to those noises illustrated in Fig. 10. The results are given in Fig. 28 for  $\beta = 0, 1, 2, 3$ . Good correlations with Eq. (88) are found. The values of  $He$  obtained from the best fit of

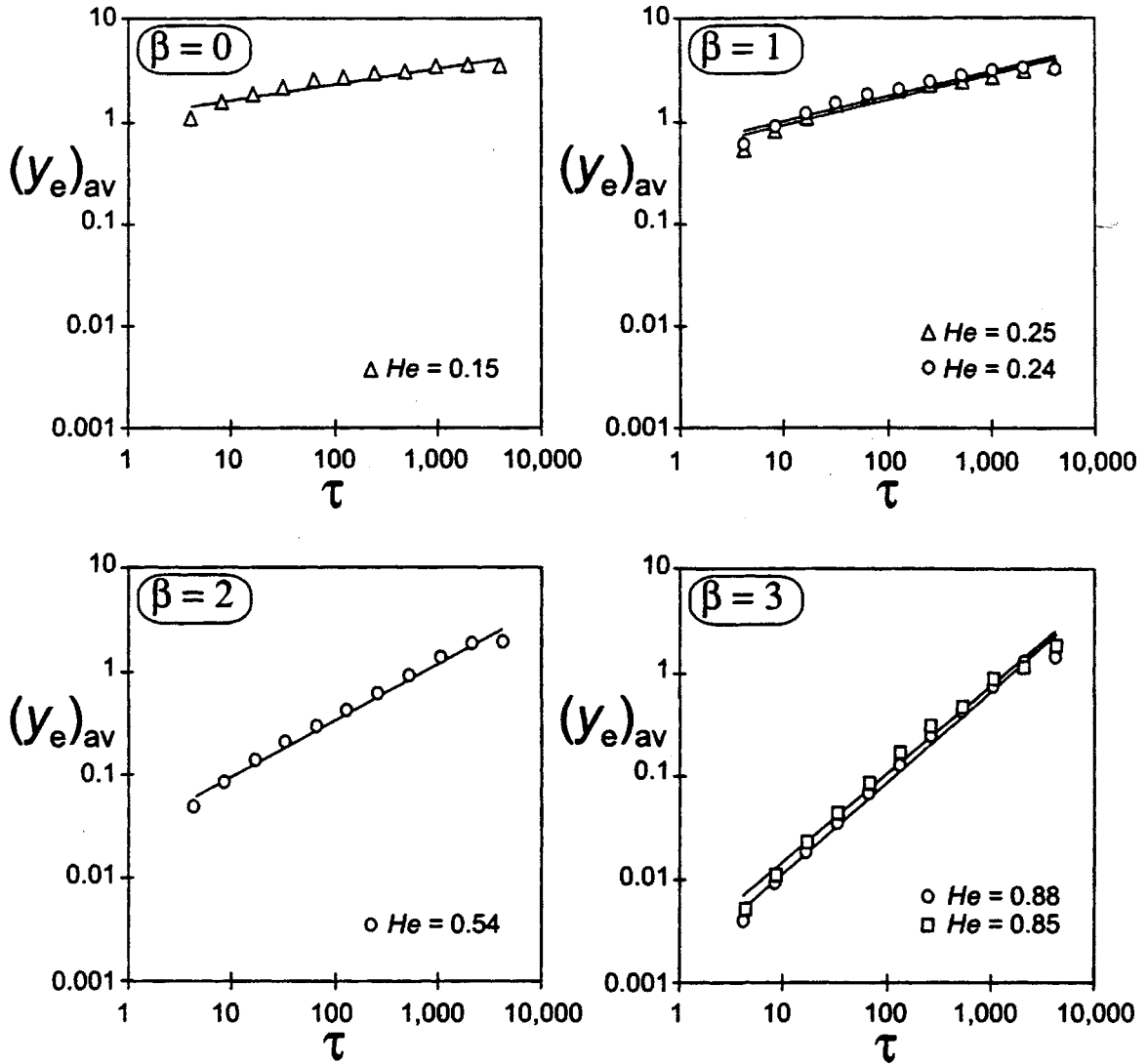


FIG. 28. Average extreme-value analyses for several fractional Gaussian noises and fractional Brownian motions with  $N = 4096$  points. Examples of time series with  $N = 512$  points and the same characteristics as the noises and motions we use here are illustrated in Fig. 10. The time series is forced to have a mean of 0. Average values of the extreme values in each interval,  $(y_e)_{av}$ , are given as a function of the interval  $\tau$  for  $\tau = 8, 16, 32, \dots, 4096$ . The straight-line correlations are with  $(y_e)_{av} \sim \tau^{He}$ , Eq. (88). The slope of the best-fit straight line for  $\log(y_e)_{av}$  vs  $\log(\tau)$  is  $He$ . Values for  $He$  are given for each of the examples. The triangles ( $\beta = 0, 1$ ), circles ( $\beta = 1, 2, 3$ ), and squares ( $\beta = 3$ ) are explained in Table I.

Eq. (88) in the range  $-1 \leq \beta \leq 5$  are given in Fig. 29. The straight-line correlation is with  $\beta = 2Ha + 1$ , Eq. (89). Reasonably good agreement is found in the range  $1 \leq \beta \leq 3$ , where the fractional Brownian motions are expected to be self-affine fractals; however, for  $\beta < 2$ ,  $He$  becomes more positive than the straight-line fit given by Eq. (89). More interestingly, for the fractional Gaussian noises and fractional Brownian motions, the extreme-value behavior illustrated in Fig. 29 is essentially identical to the

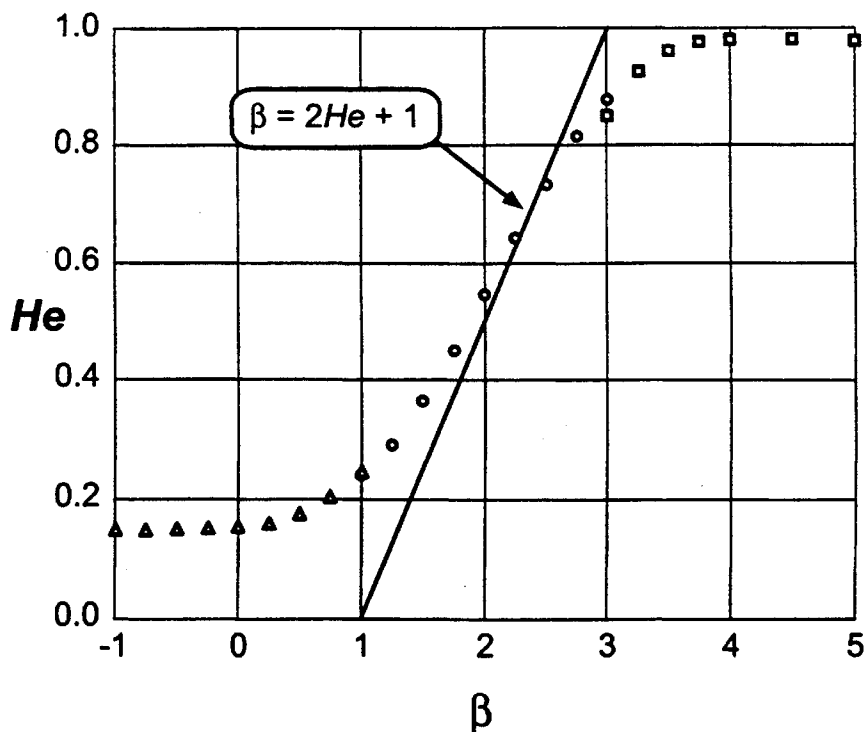


FIG. 29. The dependence of the extreme-value exponent,  $He$ , on  $\beta$ , for fractional Gaussian noises and fractional Brownian motions with  $N = 4096$  points. The values for  $He$  have been obtained from the best fit of  $(y_e)_{av} \sim \tau^{He}$ , Eq. (88). Results are given for  $-1 \leq \beta \leq 5$ ; each symbol represents the best fit for  $He$  at that  $\beta$ . Examples of obtaining  $He$  from average extreme-value analysis are given in Fig. 28. The straight-line correlation is with the relation  $\beta = 2He + 1$ , Eq. (89), for  $1 \leq \beta \leq 3$ . The triangles ( $-1 \leq \beta \leq 1$ ), circles ( $1 \leq \beta \leq 3$ ), and squares ( $3 \leq \beta \leq 5$ ) are explained in Table I.

rescaled-range analysis behavior illustrated in Fig. 25, with each point in the figure shifted by a  $\beta$  of 2:

$$Hu(\beta) = He(\beta + 2). \quad (90)$$

The two techniques result in an identical pattern of values for  $Hu$  and  $He$ , except that rescaled-range analysis measures the strength of persistence (and antipersistence) for fractional Gaussian noises ( $-1 \leq \beta \leq 1$ ), and average extreme-value analysis measures the strength of persistence for fractional Brownian motions ( $1 \leq \beta \leq 3$ ). The effect of Eq. (82) is to take the running sum of  $y_n$ , which results in the time series being shifted by a  $\beta$  of 2. This is similar to shifting  $\beta$  by 2 when summing a white noise to construct a Brownian motion. The range,  $R(\tau)$ , from Eq. (83) is then similar to taking the maximum value,  $y_e$ , in each subperiod,  $\tau$ .

The fractional Gaussian noises and fractional Brownian motions illustrated in Fig. 10 have both positive maximum values,  $y_{max}$ , and negative minimum values,  $y_{min}$ . The average extreme-value analysis just presented

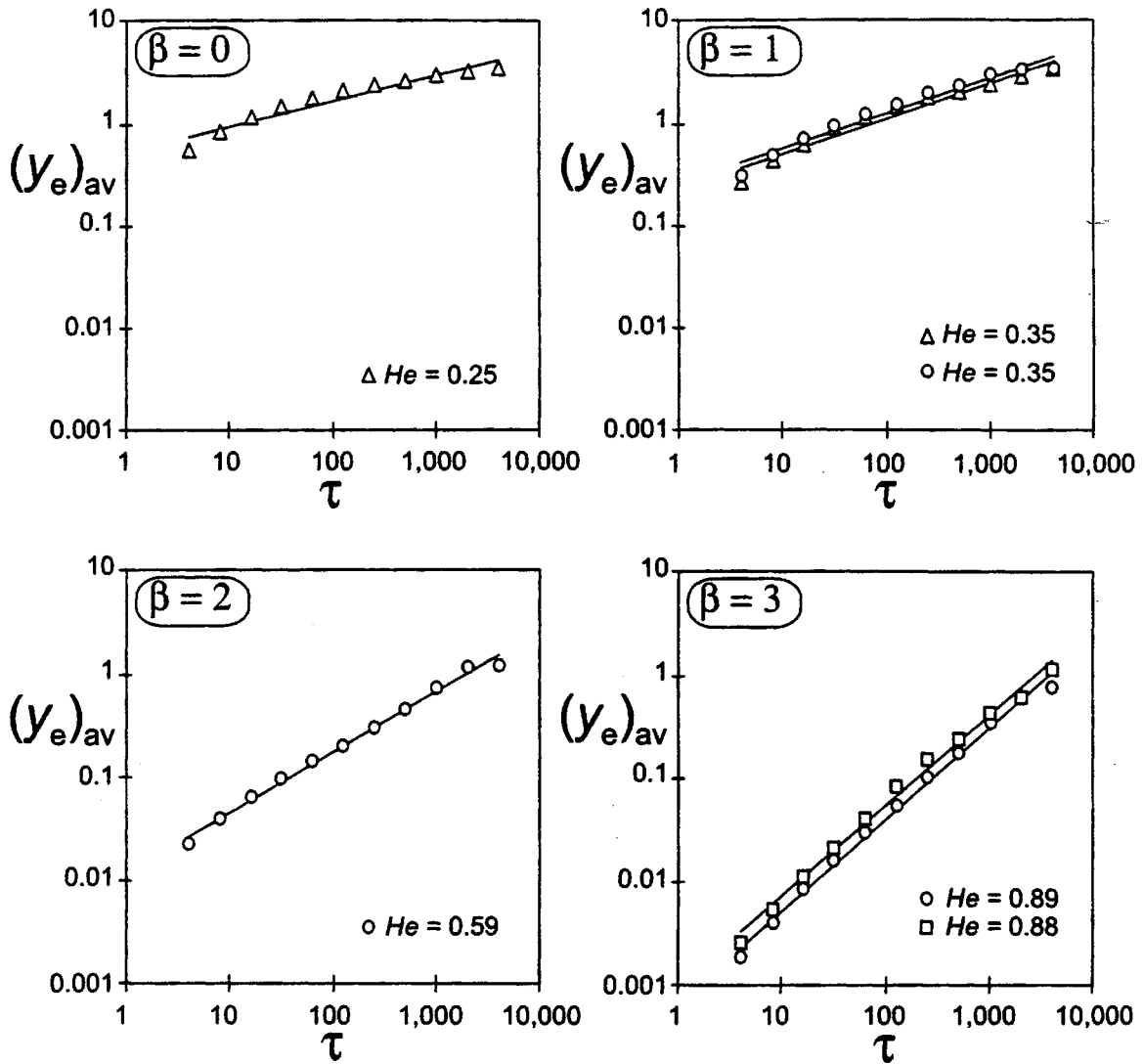


FIG. 30. Average extreme-value analyses for several fractional log-normal noises and motions with  $N = 4096$  points and  $c_v = 0.5$ . The fractional log-normal noises and motions were obtained by using Eqs. (73) to (76) applied to fractional Gaussian noises and motions, and letting  $c_v = 0.5$ . Examples of time series with 512 points and the same characteristics are illustrated in Fig. 19. The time series is forced to have a mean of 0. Average values of the extreme values in each interval,  $(y_e)_{av}$ , are given as a function of the interval  $\tau$  for  $\tau = 8, 16, 32, \dots, 4096$ . The straight-line correlations are with  $(y_e)_{av} \sim \tau^{He}$ , Eq. (88). The slope of the best-fit straight line for  $\log(y_e)_{av}$  vs  $\log(\tau)$  is  $He$ . Values for  $He$  are given for each of the examples. The triangles ( $\beta = 0, 1$ ), circles ( $\beta = 1, 2, 3$ ), and squares ( $\beta = 3$ ) are explained in Table II.

was on the most positive maximum values,  $y_{max}$ , for fractional noises and motions  $y_n, n = 1, 2, 3, \dots, N$ , with  $N = 4096$  points and  $-1 \leq \beta \leq 5$ . We have also applied average extreme-value analysis to the most negative values,  $y_{min}$ , obtained by taking the negative of the fractional noise time series. The results were essentially the same.

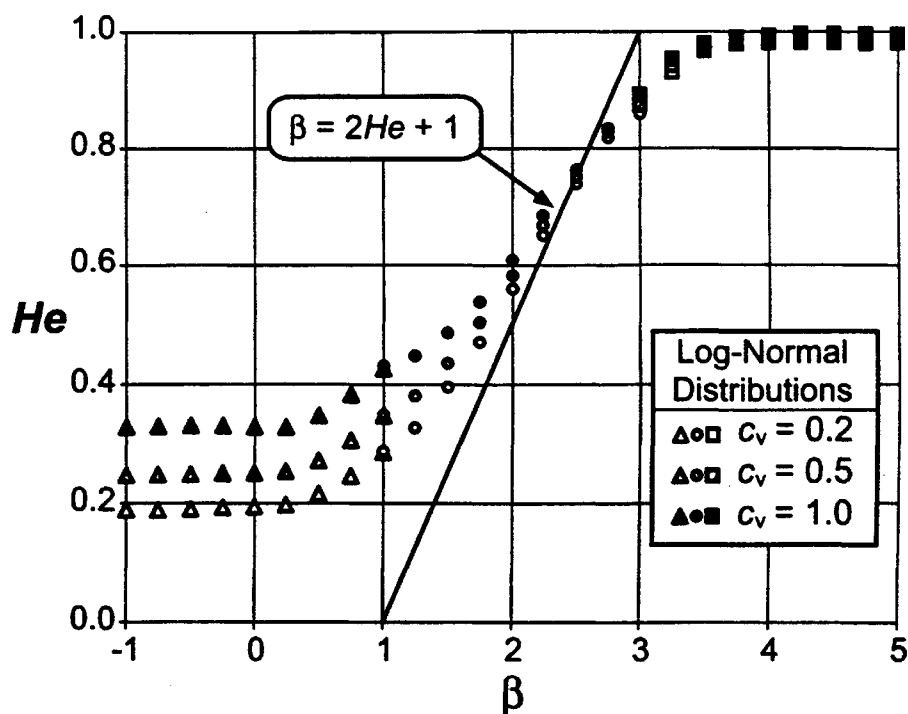


FIG. 31. The dependence of the extreme-value exponent,  $He$ , on  $\beta$ , for fractional log-normal noises and motions with  $N = 4096$  points. The values for  $He$  have been obtained from the best fit of  $(y_e)_{av} \sim \tau^{He}$ , Eq. (88). Results are given for  $-1 \leq \beta \leq 5$  and  $c_v = 0.2$  (white),  $0.5$  (gray), and  $1.0$  (black); each symbol represents the best fit for  $He$  at that  $\beta$ . Examples of obtaining  $He$  from average extreme-value analysis are given in Fig. 30. The straight-line correlation is with the relation  $\beta = 2He + 1$ , Eq. (89), for  $1 \leq \beta \leq 3$ . The triangles ( $-1 \leq \beta \leq 1$ ), circles ( $1 \leq \beta \leq 3$ ), and squares ( $3 \leq \beta \leq 5$ ) are explained in Table II.

### 6.3. Applications to Fractional Log-Normal Noises and Motions

Average extreme-value analysis has been applied to several fractional log-normal noises and motions, each with 4096 points, similar to those illustrated in Fig. 19. Results for  $c_v = 0.5$  and  $\beta = 0, 1, 2, 3$  are given in Fig. 30. In general, the correlations with  $(y_e)_{av} \sim \tau^{He}$ , Eq. (88), are quite good. The values of  $He$  obtained from the best fit of Eq. (88) in the range  $-1 \leq \beta \leq 5$  and  $c_v = 0.2, 0.5$  (illustrated in Fig. 30), and  $1.0$  are given in Fig. 31. The straight-line correlation is with  $\beta = 2He + 1$ , Eq. (89). As expected, the results for the fractional log-normal noises and motions with a low coefficient of variation,  $c_v = 0.2$  (Fig. 31), are very similar to the fractional Gaussian noises and motions in Fig. 29. Reasonably good agreement is found in the range  $1 \leq \beta \leq 3$ , where the fractional Brownian motions are expected to be self-affine fractals. For  $\beta < 2$ ,  $He$  becomes increasingly more positive than the straight-line fit given by Eq. (89). As the coefficient of variation becomes greater,  $c_v = 0.5$  and  $c_v = 1.0$  (Fig. 31),  $He$  deviates farther away from the straight-line fit given by

$\beta = 2He + 1$ , Eq. (89). This is very similar to the behavior seen in Fig. 27 for the results of rescaled-range analysis applied to fractional log-normal noises and motions. Rescaled-range analysis exhibits an increasing  $Hu$  (for  $\beta < 0$ ) as a function of an increasing coefficient of variation,  $c_v$ ; similarly, average extreme-value analysis exhibits an increasing  $He$  (for  $\beta < 2$ ) as a function of increasing  $c_v$ .

## 7. WAVELET ANALYSIS

### 7.1. The Method

Fourier transforms have a long history of applications to a wide variety of problems. For example, they have great utility in terms of obtaining the frequency content of a time series. Despite the many advantages of Fourier transforms, there are also disadvantages. For instance, they do not provide spatial resolution. To overcome some of these disadvantages, Grossmann and Morlet (1984) introduced the wavelet transform. This transform provides information on both the spatial and frequency dependence of a time series. The transform has a fractal basis and is particularly useful when applied to nonperiodic multiscaled time series. The method can also be applied to nonstationary processes. Two excellent discussions of the wavelet transform are given by Hubbard (1996) and Wornell (1996). Hubbard (1996) is particularly useful because she provides a complete history of wavelets, along with a very easy to understand introduction to wavelet mathematics.

The wavelet transform is a filter  $g[(t' - t)/a]$  which is passed over a time series  $f(t')$ . The effective width of the filter is generally increased by powers of 2. The generalized form of the wavelet transform is given by

$$W(t, a) = \frac{1}{a^{1/2}} \int_{-\infty}^{\infty} g\left(\frac{t' - t}{a}\right) f(t') dt'. \quad (91)$$

The filter is centered at  $t$ , the position parameter, with  $a$  the scale parameter. The effective width of the filter is normally taken to be a constant multiple of the scale parameter. The quantity  $g(t')$  is known as the “mother wavelet.” Other wavelets are rescaled versions of the mother wavelet. The factor  $a^{0.5}$  in Eq. (91) is an energy normalization so that the transformed signal will have the same energy at all scales. The area of

each wavelet must sum to zero so that

$$\int_{-\infty}^{\infty} g(t') dt' = 0. \quad (92)$$

When  $a$  is increased by powers of 2, a suite of wavelets is generated that can accommodate a wide range of scales in the signal  $f(t')$ . Small values of the scale parameter  $a$  are equivalent to examining the high-frequency contributions to a time series; large values of  $a$  are equivalent to examining low frequencies.

A commonly used mother wavelet that satisfies Eq. (92) is the ‘‘Mexican hat’’ wavelet, which is the negative of the second derivative of the Gaussian distribution. It takes the form

$$g(t') = \left(\frac{1}{2\pi}\right)^{1/2} (1 - t'^2)e^{-t'^2/2} \quad (93)$$

and is illustrated in Fig. 32. The effective width of the illustrated filter is  $16a$ , where  $a$  is the scale parameter. Substitution of Eq. (93) into Eq. (91) gives

$$W(t, a) = \left(\frac{1}{2a\pi}\right)^{1/2} \int_{-\infty}^{\infty} \left[1 - \left(\frac{t' - t}{a}\right)^2\right] e^{-(t' - t)^2/(2a^2)} f(t') dt'. \quad (94)$$

The filter in this case is the Mexican hat wavelet. For an effective width of  $16a$ , with  $a = 1$ , seventeen values from the Mexican hat as given in Eq. (93) are being convolved with the time series  $W(t, a)$  in Eq. (94); for  $a = 2$ , thirty-three values from the Mexican hat are being convolved with the time series, and so forth.

Many other wavelet transforms have been proposed in the literature. For example, a simple box wavelet known as the Haar wavelet has found wide use. A disadvantage of most wavelet transforms, including the Mexican hat and Haar, is that the sequence of wavelets is not orthogonal; i.e., as with Fourier transforms, the complete set can be inverted to reproduce the original signal. To overcome this difficulty, Daubechies (1988) introduced an orthogonal wavelet. Unfortunately, this wavelet transform has an extremely complex waveform. Because we find very good results in quantifying the strength of persistence when we use the Mexican hat wavelet, we have not extensively examined other wavelets.

## 7.2. Applications to Fractional Gaussian Noises and Motions

The wavelet transform from Eq. (94) has been applied to several fractional Gaussian noises and fractional Brownian motions, each with

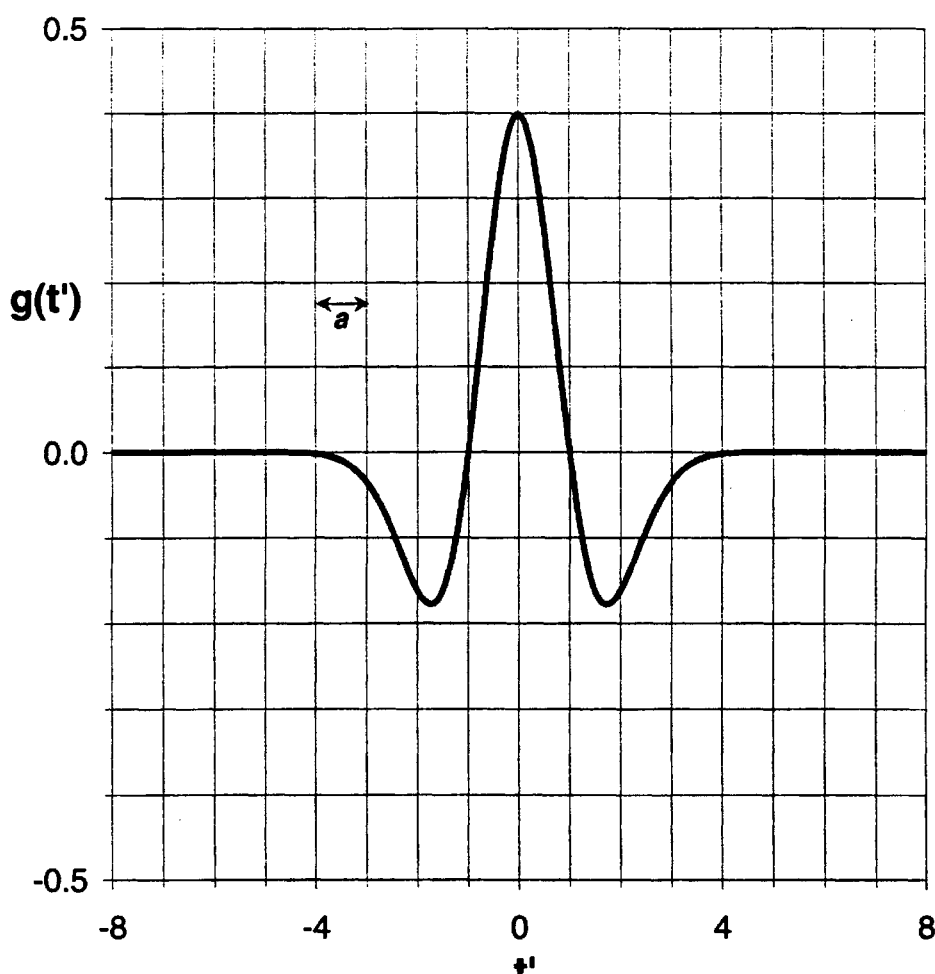
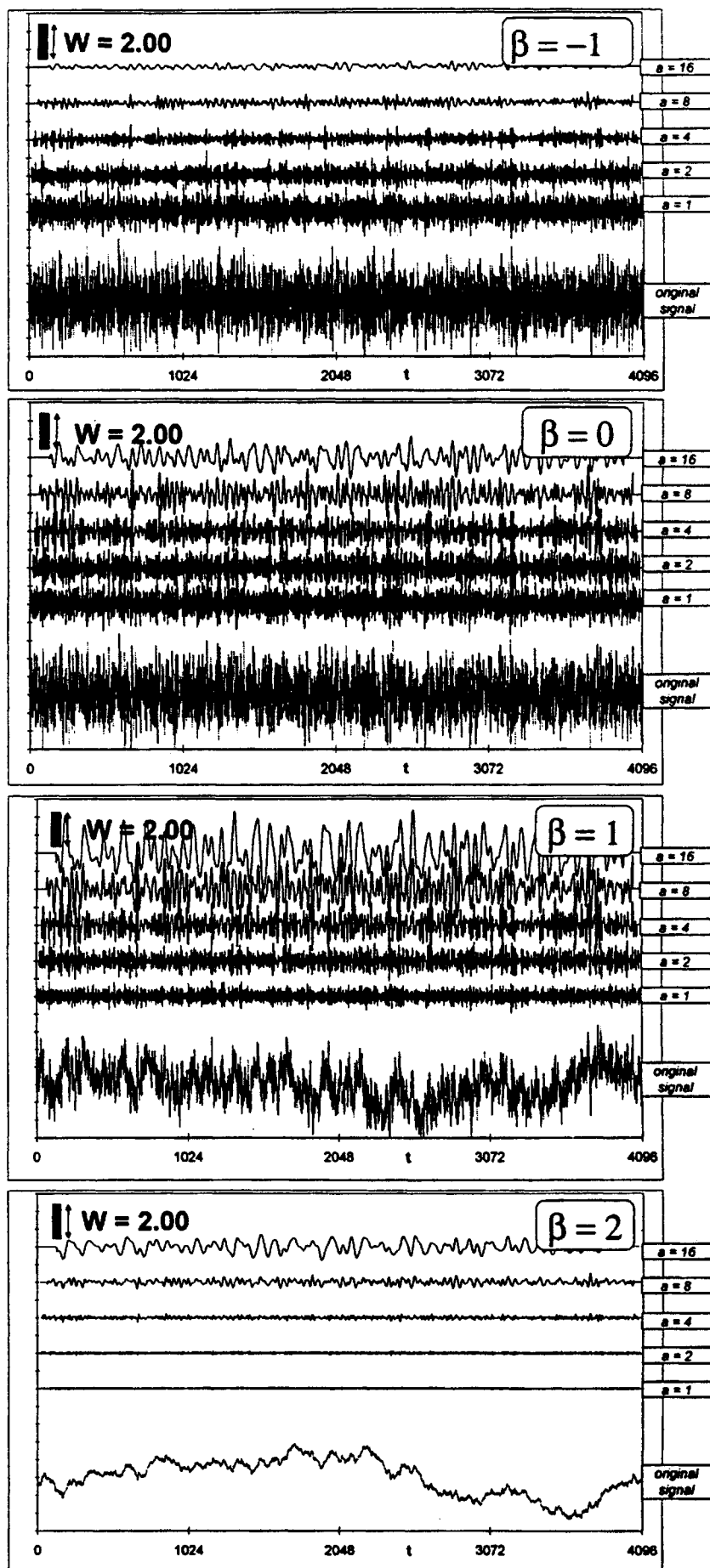


FIG. 32. Mother Mexican hat wavelet  $g(t')$  from Eq. (93), where  $g(t')$  is the negative of the second derivative of a normal distribution. The width of this wavelet is  $16a$ .

$N = 4096$  points. A Mexican hat wavelet, Eq. (93), with an effective width of  $16a$  is convolved,  $16a$  points at a time, with the time series  $y_n$ ,  $n = 1, 2, 3, \dots, N$ . The first convolution is centered at  $n = 8a$ ,  $n$  increasing at  $+1$  intervals, and the last convolution is centered at  $N - 8a$  ( $n = 8a, 8a + 1, 8a + 2, \dots, N - 8a$ ). In Fig. 33, results for  $W(t, a)$  are shown for noises with  $\beta = -1, 0, 1, 2$  and Mexican hats with a scale parameter,  $a = 1, 2, 4, 8, 16$ . The original time series,  $y_n$ , is shown at the bottom of each graph. As we would expect, for an antipersistent ( $\beta = -1$ ) time series, the amplitude,  $W(t, a)$ , of the resulting wavelet transform is strongest for high frequencies ( $a$  small). For an uncorrelated signal (a Gaussian white noise,  $\beta = 0$ ),  $W(t, a)$  is equal for all  $a$ ; in other words, the signal is stationary, so there is no change in the variance at different  $a$ . For persistent signals ( $\beta = 1, 2$ ), the wavelet amplitude,  $W(t, a)$ , is strongest for the low frequencies ( $a$  large).



In order to quantify the dependence of  $W$  on  $a$  and  $\beta$ , we determine  $V_w$ , the variance of  $W$ , as a function of  $a$ . The results using fractional noises with  $\beta = -2, -1, 0, 1, 2, 3$ , are given in Fig. 34. In each case, we find an excellent correlation with the relation

$$V_w \sim a^{Hw}. \quad (95)$$

Flandrin (1992, 1993) applied a similar approach to fractional Brownian motions, finding a power-law behavior of the variance of  $W$ , from which he calculated an estimate for the fractal dimension of the fractional Brownian motions.

Fig. 35 gives the values of  $Hw$  as a function of  $\beta$ , obtained from the best fit of Eq. (95) in the range  $-3 \leq \beta \leq 5$ . A good correlation with the relation

$$\beta = Hw \quad (96)$$

is obtained over the entire range. The wavelet transform provides a powerful measure of the strength of persistence or antipersistence over the complete range of fractional Gaussian noises and fractional Brownian motions. Moreover, because the wavelet transform is not sensitive to nonstationarities like Fourier analysis, one does not need to worry about detrending, windowing, spectral variance, etc.

### 7.3. Applications to Fractional Log-Normal Noises and Motions

The wavelet transform from Eq. (94) has been applied to several fractional log-normal noises and motions, each with 4096 points. In Fig. 36, results for  $W(t, a)$  are shown for noises with  $c_v = 0.5$  and  $\beta = -1, 0, 1, 2$ , using Mexican hats with a scaling parameter,  $a = 1, 2, 4, 8, 16$ . The original time series is shown at the bottom of each graph. For decreasing  $a$ , the signal,  $W(t, a)$ , increases when  $\beta = -1$ , is almost constant when  $\beta = 0$ , decreases when  $\beta = 1$ , and decreases even more when  $\beta = 2$ .

In order to quantify the dependence of  $W$  on both  $a$  and  $\beta$ , we determine  $V_w$ , the variance of  $W$ , as a function of  $a$ . The results for  $\beta = -2, -1, 0, 1, 2, 3$  are given in Fig. 37. Again, excellent fits are found with Eq. (95). Fig. 38 presents the values of  $Hw$  as a function of  $\beta$ , obtained from the best fit of Eq. (95) in the range  $-3 \leq \beta \leq 5$ . For

---

FIG. 33. Wavelet transform  $W(t, a)$  of four fractional Gaussian noises and fractional Brownian motions ( $\beta = -1, 0, 1, 2$ ) with  $N = 4096$  points. The "Mexican hat" wavelet from Eq. (94) is used with a width of  $16a$ , for  $a = 1, 2, 4, 8, 16$ . The fractional noises and motions used in each wavelet analysis are given at the bottom of each figure, and above the time series,  $W(t, a)$  is given for each value of  $a$ .

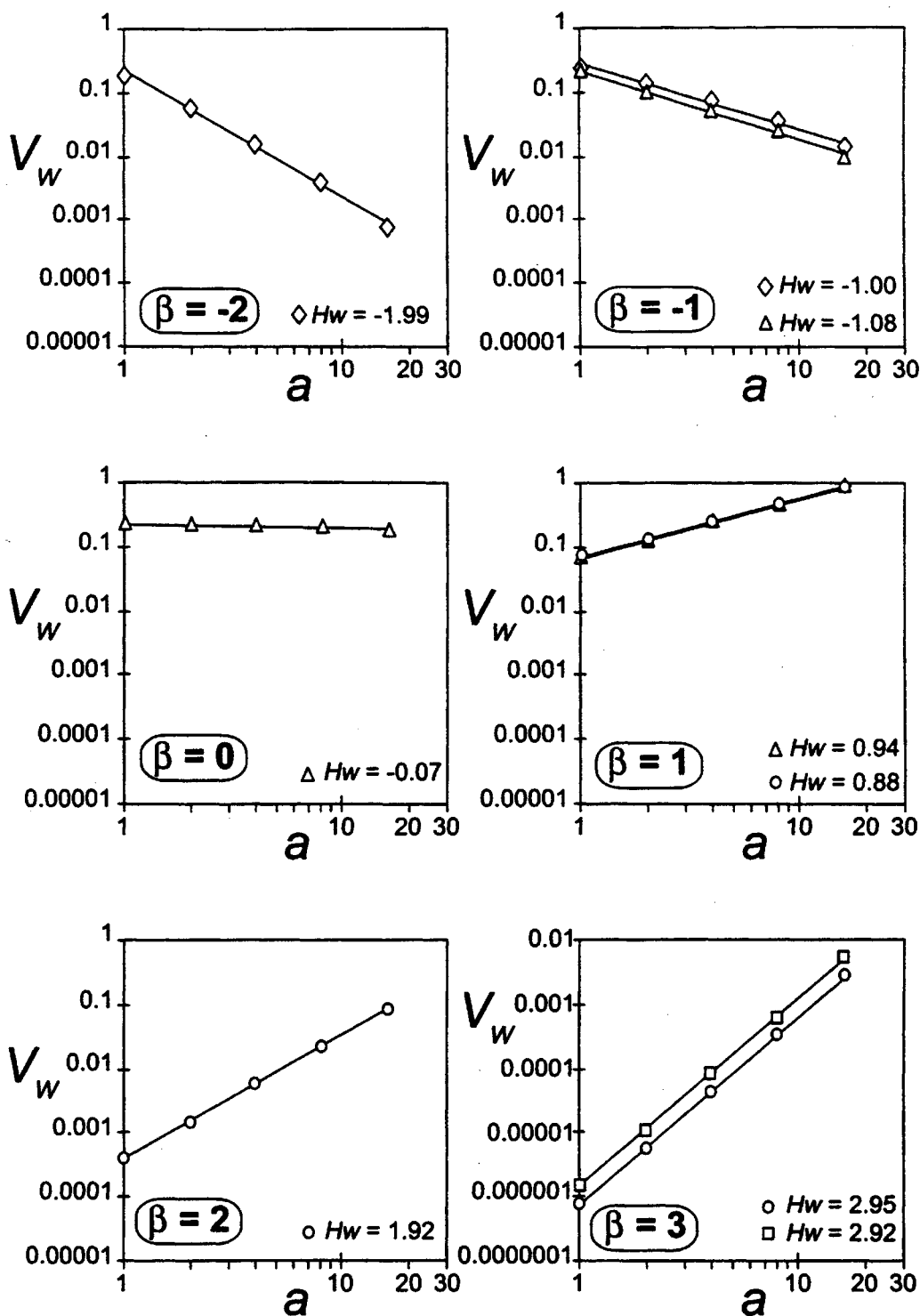


FIG. 34. Wavelet variance analyses for several fractional Gaussian noises and fractional Brownian motions with  $N = 4096$  points. The “Mexican hat” filter, with a filter width of  $16a$ , has been applied to the noises and motions. Examples of time series with  $N = 512$  points and the same characteristics as the noises and motions we use here are illustrated in Fig. 10. The population variance of the wavelet amplitude,  $V_w$ , is given as a function of the wavelet width,  $a$ , for  $a = 1, 2, 4, 8, 16$ . The straight-line correlations are with  $V_w \sim a^{H_w}$ , Eq. (95). The slope of the best-fit straight line for  $\log(V_w)$  vs  $\log(a)$  is  $H_w$ . Values for  $H_w$  are given for each of the examples. The diamonds ( $\beta = -2, -1$ ), triangles ( $\beta = -1, 0, 1$ ), circles ( $\beta = 1, 2, 3$ ), and squares ( $\beta = 3$ ) are explained in Table I.

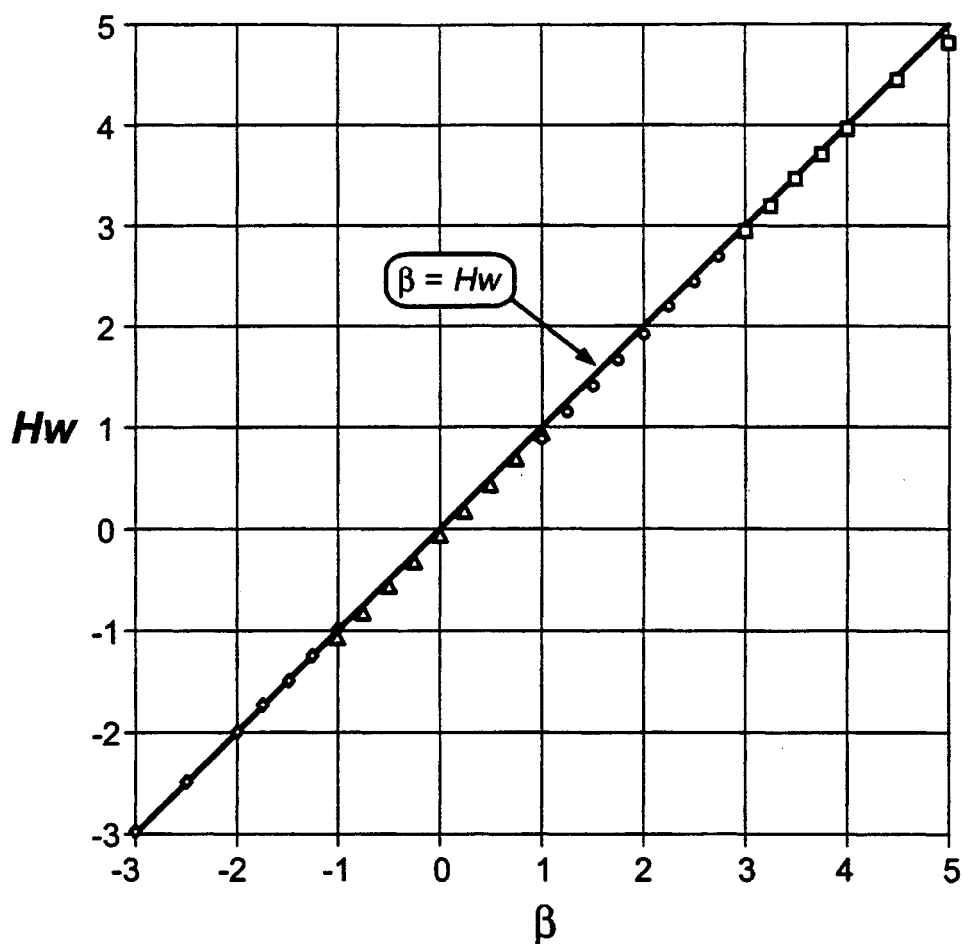
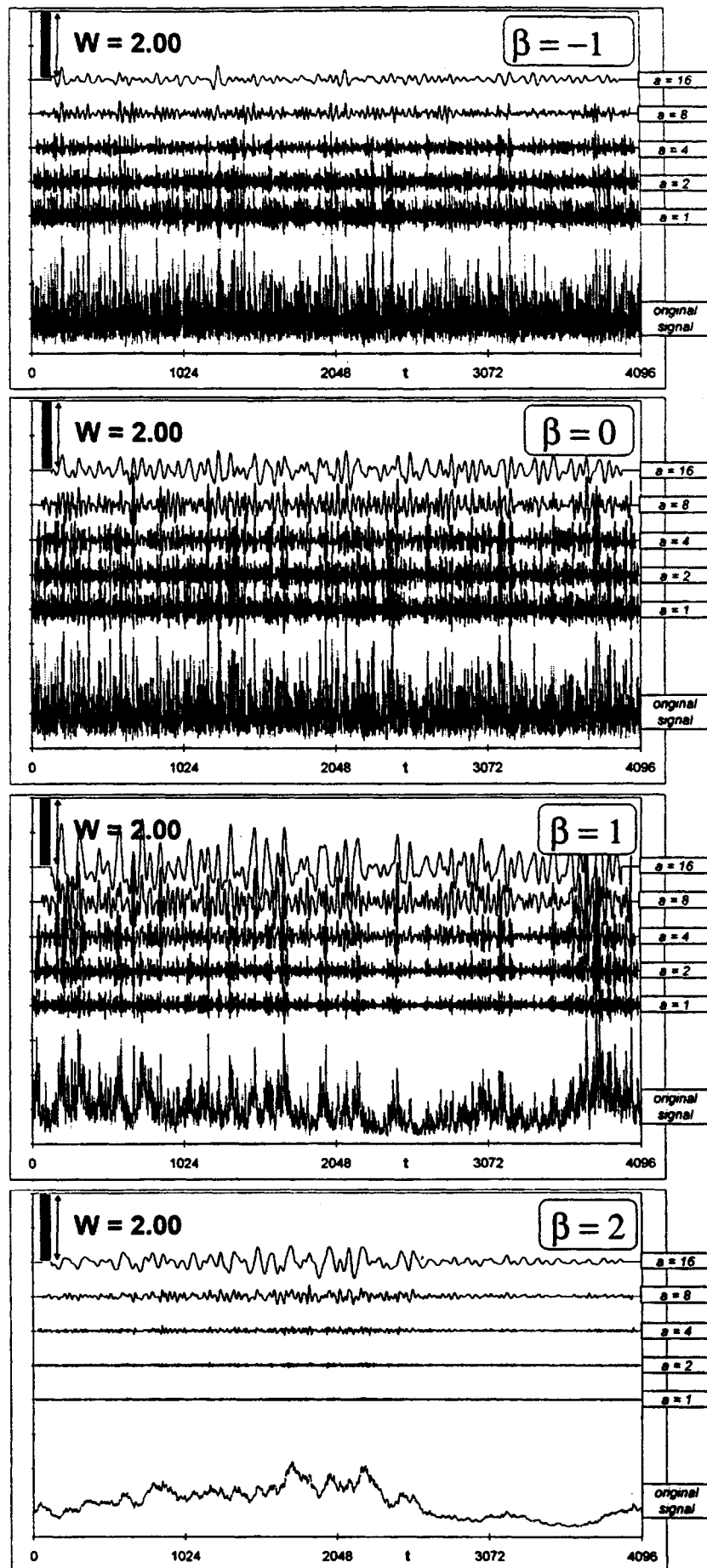


FIG. 35. The dependence of the wavelet variance exponent,  $Hw$ , on  $\beta$ , for fractional Gaussian noises and fractional Brownian motions with  $N = 4096$  points. The values for  $Hw$  have been obtained from the best fit of  $V_w \sim a^{Hw}$ , Eq. (95). Results are given for  $-3 \leq \beta \leq 5$ ; each symbol represents the best fit for  $Hw$  at that  $\beta$ . Examples of obtaining  $Hw$  from wavelet variance analysis are given in Fig. 34. The straight-line correlation is with the relation  $\beta = Hw$ , Eq. (91), for  $-3 \leq \beta \leq 5$ . The diamonds ( $-3 \leq \beta \leq -1$ ), triangles ( $-1 \leq \beta \leq 1$ ), circles ( $1 \leq \beta \leq 3$ ), and squares ( $3 \leq \beta \leq 5$ ) are explained in Table I.

$c_v = 0.2$ , an extremely good correlation with  $\beta = Hw$ , Eq. (96), is found for  $\beta = 5$  down to about  $\beta = -1$ ; for values of  $\beta$  more negative than  $\beta = -1$ ,  $Hw$  is more positive than expected. For higher coefficients of variation,  $c_v = 0.5$  and  $c_v = 1.0$ , the deviation gets worse, and  $Hw$  fails to predict the expected value for values of  $\beta$  more negative than  $\beta = -0.5$  and  $-0.2$ , respectively.

The wavelet transform provides a very powerful measure of persistence or antipersistence for log-normal fractional noises and motions with  $\beta > 0$ . For negative values of  $\beta$  it does not do as good a job. We recommend a transformation to a Gaussian distribution for non-Gaussian distributions with  $\beta < 0$ .



## 8. SUMMARY

The basic concepts of self-affine time series have been introduced in this article. In a self-affine time series, the power-spectral density as defined in Eq. (38) scales as a power-law function of the frequency, Eq. (39). Time series are quantified by their statistical distribution of values and by their persistence or antipersistence. Persistence can be classified in terms of range, short-range or long-range, and in terms of strength, weak or strong. The distribution of values is usually either Gaussian (normal) or log-normal. The basic characteristic of a self-affine time series is that the persistence is scale invariant. Thus, a self-affine time series has long-range persistence by definition.

In this chapter, we have examined a variety of techniques to quantify the strength of long-range persistence in self-affine time series. These include Fourier power-spectral analysis, semivariogram analysis, rescaled-range analysis, average extreme-event analysis, and wavelet variance analysis. Other techniques to examine long-range persistent series, not discussed in this article, include dispersional analysis (Basingthwaite and Raymond, 1995), maximum likelihood estimators (Beran, 1994), and the roughness-length technique (Malinverno, 1990). The roughness-length technique is similar to the rescaled-range method applied to the original time series, in that the “roughness” of the time series is found to have a power-law dependence on the window length. The roughness is defined as the root-mean-square residual on a linear trend over the length of the window.

In addition, Beran (1994), along with other authors, discusses long-range persistence techniques that examine composite long-memory processes, such as fractional autoregressive integrated moving average (FARIMA) models. Composite long-memory processes are characterized by more than two parameters; in this article we have restricted our analysis to single-parameter long-memory processes, i.e., processes where the persistence is characterized by one parameter,  $\beta$ ,  $H_a$ ,  $H_u$ ,  $H_e$ , or  $H_w$ .

Synthetic self-affine time series were generated using spectral techniques and the method of successive random additions. Although the spectral technique can be used to generate fractional noises with any value of  $\beta$ , we used the technique to generate noises in the range  $-1 \leq \beta \leq 1$ . These discrete noises were summed to give fractional motions in the range

---

FIG. 36. Wavelet transform  $W(t, a)$  of four fractional log-normal noises and motions ( $\beta = -1, 0, 1, 2$ ) with  $N = 4096$  points and coefficient of variation,  $c_v = 0.5$ . The “Mexican hat” wavelet from Eq. (94) is used with a width of  $16a$ , for  $a = 1, 2, 4, 8, 16$ . The fractional log-normal noises and motions used in each wavelet analysis are given at the bottom of each figure, and above the time series,  $W(t, a)$  is given for each value of  $a$ .

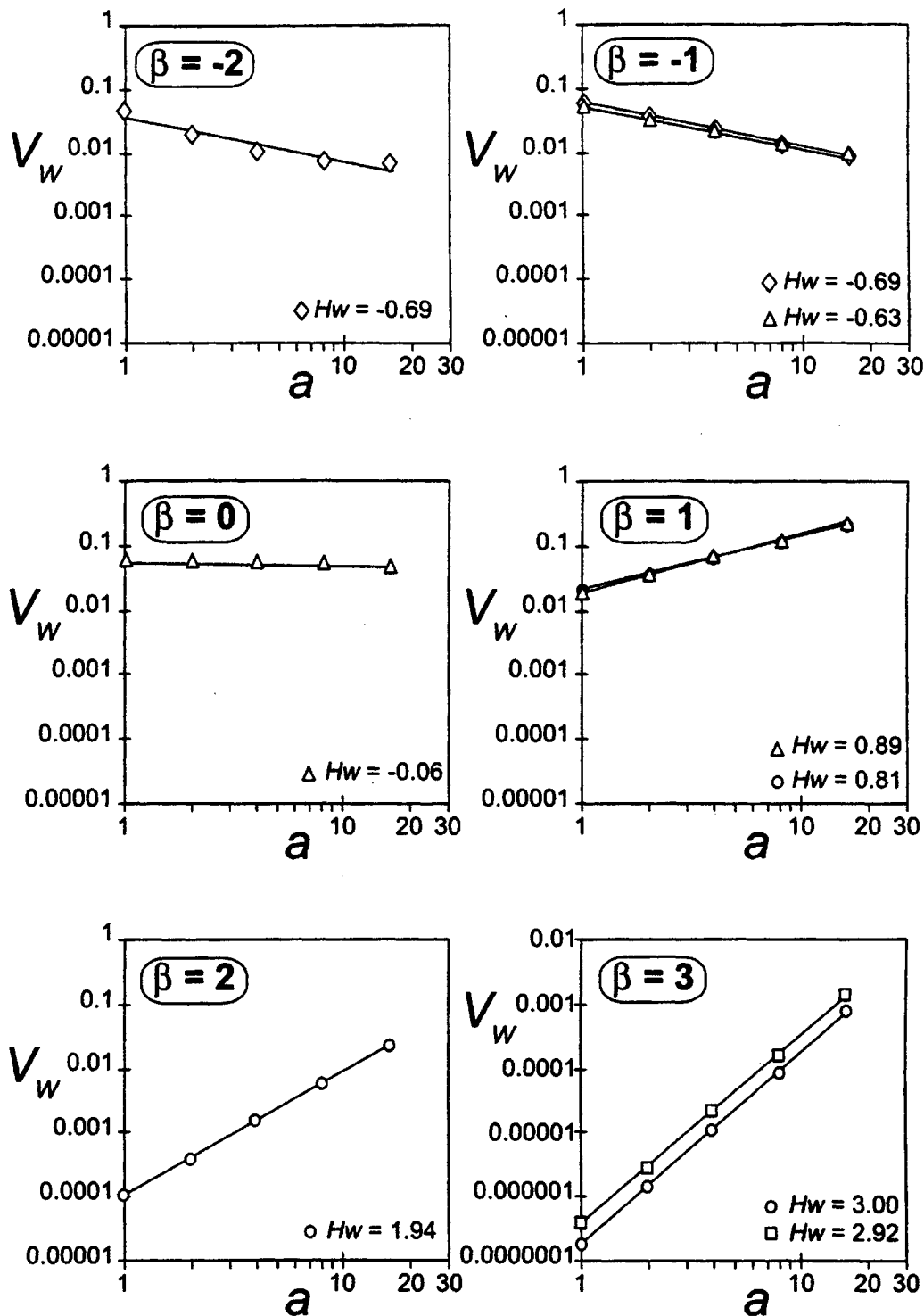


FIG. 37. Wavelet variance analyses for several fractional log-normal noises and motions with  $N = 4096$  points and  $c_v = 0.5$ . The “Mexican hat” filter, with a filter width of  $16a$ , has been applied to the log-normal noises and motions. The fractional log-normal noises and motions were each obtained by using Eqs. (73) to (76) applied to fractional Gaussian noises and motions, and letting  $c_v = 0.5$ . Examples of time series with  $N = 512$  points and the same characteristics as the noises and motions we use here are illustrated in Fig. 19. The population variance of the wavelet amplitude,  $V_W$ , is given as a function of the wavelet width,  $a$ , for  $a = 1, 2, 4, 8, 16$ . The straight-line correlations are with  $V_W \sim a^{Hw}$ , Eq. (95). The slope of the best-fit straight line for  $\log(V_W)$  vs  $\log(a)$  is  $Hw$ . Values for  $Hw$  are given for each of the examples. The diamonds ( $\beta = -2, -1$ ), triangles ( $\beta = -1, 0, 1$ ), circles ( $\beta = 1, 2, 3$ ), and squares ( $\beta = 3$ ) are explained in Table II.

## 8. SUMMARY

The basic concepts of self-affine time series have been introduced in this article. In a self-affine time series, the power-spectral density as defined in Eq. (38) scales as a power-law function of the frequency, Eq. (39). Time series are quantified by their statistical distribution of values and by their persistence or antipersistence. Persistence can be classified in terms of range, short-range or long-range, and in terms of strength, weak or strong. The distribution of values is usually either Gaussian (normal) or log-normal. The basic characteristic of a self-affine time series is that the persistence is scale invariant. Thus, a self-affine time series has long-range persistence by definition.

In this chapter, we have examined a variety of techniques to quantify the strength of long-range persistence in self-affine time series. These include Fourier power-spectral analysis, semivariogram analysis, rescaled-range analysis, average extreme-event analysis, and wavelet variance analysis. Other techniques to examine long-range persistent series, not discussed in this article, include dispersional analysis (Basingthwaite and Raymond, 1995), maximum likelihood estimators (Beran, 1994), and the roughness-length technique (Malinverno, 1990). The roughness-length technique is similar to the rescaled-range method applied to the original time series, in that the “roughness” of the time series is found to have a power-law dependence on the window length. The roughness is defined as the root-mean-square residual on a linear trend over the length of the window.

In addition, Beran (1994), along with other authors, discusses long-range persistence techniques that examine composite long-memory processes, such as fractional autoregressive integrated moving average (FARIMA) models. Composite long-memory processes are characterized by more than two parameters; in this article we have restricted our analysis to single-parameter long-memory processes, i.e., processes where the persistence is characterized by one parameter,  $\beta$ ,  $H_a$ ,  $H_u$ ,  $H_e$ , or  $H_w$ .

Synthetic self-affine time series were generated using spectral techniques and the method of successive random additions. Although the spectral technique can be used to generate fractional noises with any value of  $\beta$ , we used the technique to generate noises in the range  $-1 \leq \beta \leq 1$ . These discrete noises were summed to give fractional motions in the range

---

FIG. 36. Wavelet transform  $W(t, a)$  of four fractional log-normal noises and motions ( $\beta = -1, 0, 1, 2$ ) with  $N = 4096$  points and coefficient of variation,  $c_v = 0.5$ . The “Mexican hat” wavelet from Eq. (94) is used with a width of  $16a$ , for  $a = 1, 2, 4, 8, 16$ . The fractional log-normal noises and motions used in each wavelet analysis are given at the bottom of each figure, and above the time series,  $W(t, a)$  is given for each value of  $a$ .

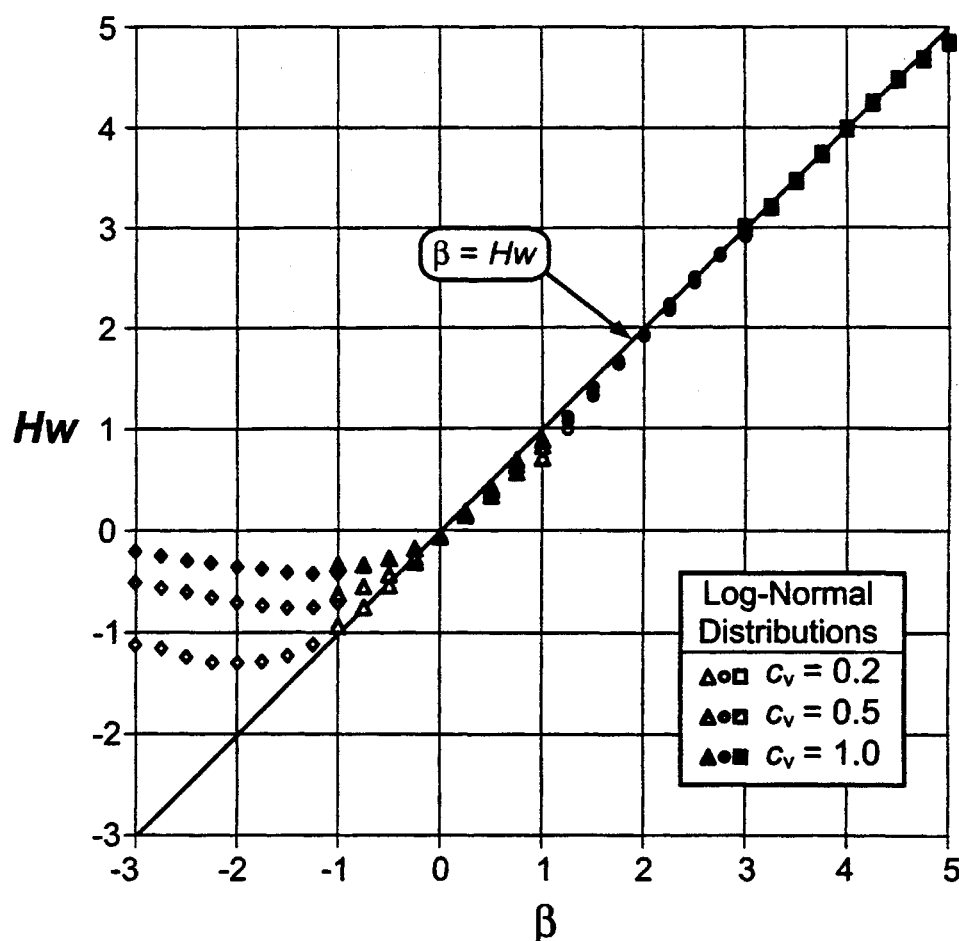


FIG. 38. The dependence of the wavelet variance exponent,  $Hw$ , on  $\beta$ , for fractional log-normal noises and motions with  $N = 4096$  points. The values for  $Hw$  have been obtained from the best fit of  $V_w \sim a^{Hw}$ , Eq. (95). Results are given for  $-3 \leq \beta \leq 5$  and  $c_v = 0.2$  (white), 0.5 (gray), and 1.0 (black); each symbol represents the best fit for  $Hw$  at that  $\beta$ . Examples of obtaining  $Hw$  from wavelet variance analysis are given in Fig. 37. The straight-line correlation is with the relation  $\beta = Hw$ , Eq. (96), for  $-3 \leq \beta \leq 5$ . The diamonds ( $-3 \leq \beta \leq -1$ ), triangles ( $-1 \leq \beta \leq 1$ ), circles ( $1 \leq \beta \leq 3$ ), and squares ( $3 \leq \beta \leq 5$ ) are explained in Table II.

$1 \leq \beta \leq 3$ , and differenced to give extended fractional noises in the range  $-3 \leq \beta \leq -1$ . The method of successive random additions was used to generate fractional motions in the range  $1 \leq \beta \leq 3$ . The discrete motions could then be summed to give extended fractional motions in the range  $3 \leq \beta \leq 5$  and differenced to give fractional noises in the range  $-1 \leq \beta \leq 1$ .

Self-affine time series with  $\beta > 1$  have a systematically different behavior than self-affine time series with  $\beta < 1$ . With  $\beta > 1$ , the time series are nonstationary and moments of the time series depend upon its length. Over the range  $1 \leq \beta \leq 3$ , the time series are self-affine fractals with fractal dimension,  $1 \leq D \leq 2$ . These time series are known as fractional motions; with  $\beta = 2$ , the time series is a Brownian motion. Time series in the range  $-1 \leq \beta \leq 1$  are known as fractional noises and are stationary.

With  $\beta = 0$ , the time series is a white noise. We define the self-affine time series with  $\beta > 1$  to have strong persistence and the self-affine time series with  $\beta < 1$  to have weak persistence.

We have used a variety of techniques to quantify the strength of persistence of synthetic self-affine time series with  $-3 \leq \beta \leq 5$ :

(1) **Semivariograms** quantify the strength of persistence in the range  $1 \leq \beta \leq 3$ . Self-affine time series in this range are nonstationary and are considered to be self-affine fractals. The characteristic measure of a semivariogram is the Hausdorff exponent,  $Ha$ . For both fractional Gaussian motions and fractional log-normal motions,  $1 \leq \beta \leq 3$ , there is a good correlation with  $\beta = 2Ha + 1$ .

(2) **Rescaled-range analyses** quantify the strength of persistence in the range  $-1 \leq \beta \leq 1$ . Self-affine time series in this range are stationary. The characteristic measure of  $R/S$  analysis is the Hurst exponent,  $Hu$ . For fractional Gaussian noises, the correlation with  $\beta = 2Hu - 1$  is relatively poor, particularly for  $\beta < 0$ . For fractional log-normal noises, the correlation becomes worse. The convergence of  $Hu$  to  $Hu = (\beta + 1)/2$  is poor for long record lengths.

(3) **Average extreme-value analyses** quantify the strength of persistence in the range  $1 \leq \beta \leq 3$ . The characteristic measure of average extreme-value analysis is the extreme-value exponent,  $He$ . The correlation with  $\beta = 2He + 1$  is the same as the correlation of  $Hu$  with  $\beta = 2Hu - 1$ , except that  $Hu(\beta) = He(\beta + 2)$ .

(4) **Spectral techniques** can, in principle, quantify the strength of persistence for all values of  $\beta$ . Both stationary and nonstationary self-affine time series can be considered. For a self-affine time series with a prescribed  $\beta$ , Fourier spectral techniques provide a direct confirmation of this  $\beta$  using the power-law dependence of  $S_m$  on  $f_m$ . For fractional Gaussian noises and motions, biased results can be found for  $\beta > 2$  and  $\beta < 0$ , unless windowing is applied to the time series. When windowing is applied, spectral techniques accurately quantify the persistence for almost all values of  $\beta$ . For fractional log-normal noises and motions, even with windowing,  $\beta$  does not provide a reliable measure of persistence for  $\beta < 0$ ; we recommend for all  $\beta < 0$  non-Gaussian distribution time series that the time series be converted to a Gaussian distribution before applying spectral techniques.

(5) **Wavelet variance analyses** quantify the strength of persistence for all  $\beta$ . Self-affine time series in this range are both stationary and nonstationary. The characteristic measure of wavelet variance analysis is the wavelet exponent,  $Hw$ . In many ways, wavelet analyses are the most satisfactory measure of the strength of persistence, particularly for data sets that are nonstationary. Wavelet analyses do not have many of the inherent prob-

lems that are found in Fourier power-spectral analysis, such as windowing and detrending. For  $\beta > 0$ ,  $Hw$  correlates well with  $Hw = \beta$  for both fractional Gaussian and fractional log-normal noises and motions. For  $\beta < 0$ ,  $Hw$  correlates well with  $Hw = \beta$  for both fractional Gaussian noises and motions, but is poor for fractional log-normal noises and motions. We recommend for  $\beta < 0$  that a non-Gaussian distribution of values be converted to a Gaussian distribution.

Self-affine time series are found in a wide variety of geophysical applications. Examples include the natural variability of climate, variations in sedimentation, and the variability of the Earth's magnetic field. Stochastic differential equations can generate self-affine time series with a variety of values for  $\beta$ . Geophysical applications and relevant models are discussed in the article following this one (Pelletier and Turcotte, 1999).

#### ACKNOWLEDGMENTS

The authors gratefully acknowledge numerous long and thought-provoking discussions with Jon Pelletier (Cornell University) regarding both the theoretical and practical applications of examining persistence in self-affine time series. This work was supported by NASA Grant NAGW-4072 and is contribution 246 of the Department of Geological Sciences, Cornell University.

#### APPENDIX

##### ABBREVIATIONS AND SYMBOLS

Symbol	Description	Equation introduced	Section introduced
$a$	Scale parameter in wavelet analysis	91	7.1
$A$	Constant of proportionality	59	2.3
$( )_{av}$	Average value of $( )$ , normally over a given interval $\tau$	81	5.1
Bm	Brownian motion	18	1.6
$c_0$	Covariance of $y_n$ at zero lag	4, 6	1.4
$c(0)$	Covariance of $y(t)$ at zero lag	1, 3	1.4
$c_k$	Covariance of $y_n$ at lag $k$	4, 5	1.4
$c(s)$	Covariance of $y(t)$ at lag $s$	1, 2	1.4
$c_v$	Coefficient of variation	74	4.1

(continued)

ABBREVIATIONS AND SYMBOLS (*continued*)

Symbol	Description	Equation introduced	Section introduced
$D$	Fractal dimension	13	1.5
DFT	Discrete Fourier transform		1.6
$e$	Exponential, $e = 2.718$	30	2.1
$\Delta f$	Width of a frequency bin, $\Delta f = 1/(N\delta)$	64	2.4
$f$	Continuous frequency	30	2.1
$f_m$	Discrete frequency, $f_m = m/(N\delta)$	42	2.1
$f(x)$	Function of $x$		1.5
fBm	Fractional Brownian motion		3.2
fGn	Fractional Gaussian noise		3.2
$G(f)$	Fourier transform of $g(t)$	30	2.1
$g(t)$	Periodic continuous function	30	2.1
$g(t')$	Mother wavelet; filter	91	7.1
$\Delta h(L)$	Difference in elevation between a pair of points	15	1.5
$h$	Elevation		1.2
$h_0$	Height of rectangular region		1.5
$Ha$	Hausdorff exponent	14	1.5
$He$	Extreme value exponent	88	6.1
$Hu$	Hurst exponent	81	5.1
$Hw$	Wavelet variance analysis exponent	95	7.2
$i$	Square root of $-1$	30	2.1
$k$	Lag for a discrete time series, $y_n$	4	1.4
ln	Natural logarithm (base $e$ )		
log	Common logarithm (base 10)		
$m$	Running variable in the frequency domain, $Y_m, S_m, f_m$ ,	34	2.1
	Running variable for the running sum, $y_m$	82	5.1
$n$	Running variable for a discrete time series, $y_n$	5	1.2
$N$	Length of a discrete time series $1 \leq n \leq N$	5	1.2
	Number of subintervals in an interval $T$	22	1.6
$N_b, N_{bi}$	Number of boxes	22, 26	1.6
$N_i$	Number of objects with linear size $r_i$	13	1.5
$Q(t)$	Volumetric flow in a river	77	4.1
$\bar{Q}(T)$	Mean of the volumetric flow over a period $T$	77	5.1
$r$	Scaling factor	14	1.5

*(continued)*

ABBREVIATIONS AND SYMBOLS (*continued*)

Symbol	Description	Equation introduced	Section introduced
$r_0$	Width of rectangular region		1.5
$r_i$	Characteristic linear dimension	13	1.5
$r_k$	Autocorrelation function for $y_n$ at lag $k$	4	1.4
$R_N, R_\tau$	Range over $N$ or $\tau$ values; rescaled-range analysis	83, 85	5.1
$r(s)$	Autocorrelation function for $y(t)$ at lag $s$	1	1.4
$R(T), R(\tau)$	Range over period $T$ or $\tau$ ; rescaled-range analysis	79, 81	5.1
$s$	Lag for a continuous time series	1	1.4
$S(f)$	Power-spectral density of $y(t)$	38	2.2
$S_m$	Power-spectral density of $y_n$	40	2.2
$S_N, S_\tau$	Standard deviation over $N$ or $\tau$ values; rescaled-range analysis	84, 85	5.1
$S(T), S(\tau)$	Standard deviation over time $T$ or $\tau$ , rescaled-range analysis	80, 81	5.1
$t$	Running variable for a continuous time series $y(t)$	2	1.2
	Position parameter in wavelet analysis	91	7.1
$T$	Length of a continuous time series, $0 \leq t \leq T$	2	1.2
	Period of a continuous function $g(t)$	32	2.1
$t_n$	Discrete values of $t$ , $t_n = n\delta$		1.2
	Discrete values, $t_n = n/N$ , $n = 1, 2, \dots, N$		3.3
$V$	Variance of $y(t)$ over the interval $T$	3	1.4
	Variance of $y_n$ over $N$ values	6	1.4
$V_\varepsilon$	Variance of $\varepsilon_n$ over $N$ values		1.6
$V_{\max}, V_{\min}$	Maximum and minimum volumes of water during $T$	79	5.1
$V_n$	Variance of $y_n$ over the first $n$ values	18	1.6
$V_N$	Variance of $y_n$ over $N$ values	52	2.2
$V(t)$	Volume of water in a reservoir as a function of $t$	78	5.1
$V(T)$	Variance over the interval $T$		3.3
$V_W$	Variance of the wavelet transform $W(t, a)$	95	7.2

(*continued*)

ABBREVIATIONS AND SYMBOLS (*continued*)

Symbol	Description	Equation introduced	Section introduced
$w_n$	Window used in power-spectral analysis	67	2.5
wn	White noise	17	1.6
$W_{ss}$	Window squared and summed	70	2.5
$W(t, a)$	Wavelet transform	91	7.1
$\bar{x}$	Average of $x(t)$ , log-normal distribution of values	74	4.1
$x(t)$	Log-normal distribution of values	73	4.1
$\bar{y}$	Average of $y(t)$ over the interval $T$	2	1.4
	Average of $y_n$ over $N$ values, $n = 0, 1, 2, \dots, N$	5	1.4
$y_e$	Maximum value of $y_n$ during an interval $\tau$	88	6.1
$Y(f, T)$	Fourier transform of $y(t)$ over the interval $0 \leq t \leq T$	32	2.1
$y_m$	Running sum of $y_n$	82	5.1
$Y_m$	Discrete Fourier coefficients of $y_n, m = 1, 2, \dots, N$	34	2.1
$ Y_m $	Complex modulus of $Y_m$	36	2.1
$y_n$	Set of values in a discrete time series, $n = 1, 2, 3, \dots, N$	5	1.2
$\bar{y}_N$	Average of $y_n$ over $N$ values, $n = 0, 1, 2, \dots, N$	82	5.1
$y(t)$	Set of values in a continuous time series	2	1.2
	Gaussian (normal) set of values	73	4.1
$\beta$	Power-spectral density exponent	39	2.2
$\beta_{PS}$	Exponent obtained by power-spectral analysis		2.2
$\gamma_k$	Semivariogram of $y_n$ at lag $k$	8	1.4
$\gamma(s)$	Semivariogram of $y(t)$ at lag $s$	7	1.4
$\delta$	Time between successive $n$ in a time series, $y_n$ , with $T = N\delta$	34	1.2
$\varepsilon_n$	Gaussian distribution of values that are uncorrelated	17	1.6
$\pi$	Pi, $\pi = 3.1416\dots$	30	2.1
$\sigma_\varepsilon$	Standard deviation of $\varepsilon_n$ over $N$ values	18	1.6
$\sigma_n$	Standard deviation of $y_n$ over the first $n$ values in series	19	1.6

*(continued)*

ABBREVIATIONS AND SYMBOLS (*continued*)

Symbol	Description	Equation introduced	Section introduced
$\sigma(T), \sigma_T$	Standard deviation of $y(t)$ taken over the interval $T$	22, 23	1.6
$\sigma(\tau), \sigma_\tau$	Standard deviation of $y(t)$ taken over the subinterval $\tau$	22, 24	1.6
$\sigma_x$	Standard deviation of the log-normal distribution $x(t)$	74	4.1
$\sigma_y$	Standard deviation of the Gaussian distribution $y(t)$	75	4.1
$\Sigma$	Summation	5	1.4
$\tau, \tau_i$	Subintervals of a length $T$ or $N$	22, 26	1.6
$\omega$	Angular frequency		2.1
$\sim$	Proportional	13	1.5
$\infty$	Infinity	30	2.1
$\approx$	Approximately equal to		
$\equiv$	Equal by definition		

## REFERENCES

- Ahnert, F. (1984). Local relief and the height limits of mountain ranges. *Am. J. Sci.* **284**, 1035–1055.
- Barabási, A.-L., and Stanley, H. E. (1995). "Fractal Concepts in Surface Growth." Cambridge University Press, Cambridge.
- Bassingthwaighte, J. B., Liebovitch, L. S., and West, B. J. (1994). "Fractal Physiology." Oxford University Press, Oxford.
- Bassingthwaighte, J. B., and Raymond, G. M. (1994). Evaluating rescaled range analysis for time series. *Ann. Biomed. Eng.* **22**, 432–444.
- Bassingthwaighte, J. B., and Raymond, G. M. (1995). Evaluation of the dispersional analysis method for fractal time series. *Ann. Biomed. Eng.* **23**, 491–505.
- Beran, J. (1992). Statistical methods for data with long-range dependence. *Statist. Sci.* **7**, 404–427.
- Beran, J. (1994). "Statistics for Long-Memory Processes." Monographs on Statistics and Probability 61. Chapman & Hall, London.
- Box, G. E. P., Jenkins, G. M., and Reinsel, G. C. (1994). "Time Series Analysis: Forecasting and Control," 3rd ed. Prentice-Hall, Englewood Cliffs, NJ.
- Bras, R. L., and Rodriguez-Iturbe, I. (1993). "Random Functions and Hydrology." Dover, New York.
- Brown, S. R. (1987). A note on the description of surface roughness using fractal dimension. *Geophys. Res. Lett.* **14**, 1095–1098.
- Chatfield, C. (1996). "The Analysis of Time Series," 5th ed. Chapman & Hall, London.
- Daubechies, I. (1988). Orthonormal bases of compactly supported wavelets. *Commun. Pure Appl. Math.* **41**, 909–996.

- De Santis, A. (1997). A direct divider method for self-affine fractal profiles and surfaces. *Geophys. Res. Lett.* **24**, 2099–2102.
- Feder, J. (1988). "Fractals." Plenum Press, New York.
- Flandrin, P. (1992). Wavelet analysis and synthesis of fractional Brownian motion. *IEEE Trans. Inform. Theory* **38**, 910–917.
- Flandrin, P. (1993). Fractional Brownian motion and wavelets. In "Wavelets, Fractals, and Fourier Transforms" (M. Farge, J. C. R. Hunt, and J. C. Vassilicos, eds.), Clarendon Press, Oxford, pp. 109–122.
- Gallant, J. C., Moore, I. D., Hutchinson, M. F., and Gessler, P. (1994). Estimating fractal dimension of profiles: A comparison of methods. *Math. Geol.* **26**, 455–481.
- Grossmann, A., and Morlet, J. (1984). Decomposition of Hardy functions into square integrable wavelets of constant shape. *SIAM J. Math. Anal.* **15**, 723–736.
- Hall, P. (1997). Defining and measuring long-range dependence. *Fields Institute Commun.* **11**, 153–159.
- Harvard Centroid-Moment Tensor Database. (1997). Electronic Data. Department of Earth and Planetary Sciences, Harvard University, Cambridge, MA.
- Hastings, H. M., and Sugihara, G. (1993). "Fractals: A User's Guide for the Natural Sciences." Oxford University Press, Oxford.
- Hewett, T. A. (1986). Fractal distribution of reservoir heterogeneity and their influence on fluid transport. *Society of Petroleum Engineering Paper* **15386**, 1–16.
- Hubbard, B. B. (1996). "The World According to Wavelets: The Story of a Mathematical Technique in the Making." A. K. Peters, Wellesley, MA.
- Hurst, H. E. (1951). Long-term storage capacity of reservoirs. *Trans. Am. Soc. Civil Engineers* **116**, 770–808.
- Hurst, H. E., Black, R. P., and Simaika, Y. M. (1965). "Long-Term Storage." Constable, London.
- Jenkins, G. M., and Watts, D. G. (1968). "Spectral Analysis and its Applications." Holden-Day, San Francisco.
- Journel, A. G., and Huijbregts, Ch. J. (1978). "Mining Geostatistics." Academic Press, New York.
- Kolmogorov, A. N. (1940). Wiener'sche spiralen und einige andere interessante kurven in hilbertschen raum. *Comp. rend. (Doklady) Acad. Sci. URSS (N.S.)* **26**, 115–118.
- Korvin, G. (1992). "Fractal Models in the Earth Sciences." Elsevier, Amsterdam.
- Li, W. K., and McLeod, A. I. (1986). Fractional time series modeling. *Biometrika* **73**, 217–221.
- Malinverno, A. (1990). A simple method to estimate the fractal dimension of a self-affine series. *Geophys. Res. Lett.* **17**, 1953–1956.
- Malinverno, A. (1995). Fractals and ocean floor topography: A review and a model. In "Fractals in the Earth Sciences" (C. C. Barton and P. R. LaPointe, eds.), Plenum Press, New York, pp. 107–130.
- Mandelbrot, B. B. (1967). How long is the coast of Britain? Statistical self-similarity and fractional dimension. *Science* **156**, 636–638.
- Mandelbrot, B. B. (1982). "The Fractal Geometry of Nature." Freeman, New York.
- Mandelbrot, B. B. (1985). Self-affine fractals and fractal dimension. *Phys. Scripta* **32**, 257–260.
- Mandelbrot, B. B. (1986). Self-affine fractal sets, I: The basic fractal dimensions; II: Length and surface dimensions; III: Hausdorff dimension anomalies and their implications. In "Fractals in Physics" (L. Pietronero and E. Tosatti, eds.), Elsevier, Amsterdam, pp. 21–28.
- Mandelbrot, B. B., and Van Ness, J. W. (1968). Fractional Brownian motions, fractional noises and applications. *SIAM Rev.* **10**, 422–437.

- Mandelbrot, B. B., and Wallis, J. R. (1968). Noah, Joseph and operational hydrology. *Water Resour. Res.* 4, 909–918.
- Mandelbrot, B. B., and Wallis, J. R. (1969a). Computer experiments with fractional Gaussian noises. Parts I, II, and III. *Water Resour. Res.* 5, 228–267.
- Mandelbrot, B. B., and Wallis, J. R. (1969b). Some long-run properties of geophysical records. *Water Resour. Res.* 5, 321–340.
- Mandelbrot, B. B., and Wallis, J. R. (1969c). Robustness of the rescaled range  $R/S$  in the measurement of noncyclic long-run statistical dependence. *Water Resour. Res.* 5, 967–988.
- Matheron, G. (1962). “Traité de Géostatistique Appliquée, Tome I, Théorie Générale.” Editions Technip., Paris.
- Matheron, G. (1963a). “Traité de Géostatistique Appliquée, Tome II, Le Krigéage.” Editions Technip., Paris.
- Matheron, G. (1963b). Principles of geostatistics. *Econom. Geol.* 58, 1246–1266.
- McLeod, A. I., and Hipel, K. W. (1995). “The McLeod–Hipel Time-Series Datasets Collection.” Electronic data available from the StatLib electronic database, Carnegie Mellon University Statistics Department. The datasets collection accompanies Hipel, K.W. and McLeod, A.I. (1994), “Time Series Modeling of Water Resources and Environmental Systems,” Elsevier, Amsterdam.
- Meakin, P. (1988). The growth of fractal aggregates and their measures. In “Phase Transitions and Critical Phenomena,” vol. 12 (C. Domb and J. L. Lebowitz, eds.), Academic Press, New York, pp. 335–489.
- Oliver, M., and Webster, R. (1986). Semi-variograms for modeling the spatial pattern of landform and soil properties. *Earth Surf. Proc. Landforms* 11, 491–504.
- Osborne, A. R., and Provenzale, A. (1989). Finite correlation dimension for stochastic systems with power-law spectra. *Physica D* 35, 357–381.
- Pelletier, J. D., and Turcotte, D. L. (1999). Self-affine time series: II. Applications and models. In “Advances in Geophysics” (R. Dmowska and B. Saltzman, eds.), Vol. 40, Academic Press, San Diego, pp. 91–166.
- Percival, D. B., and Walden, A. T. (1993). “Spectral Analysis for Physical Applications: Multitaper and Conventional Univariate Techniques.” Cambridge University Press, Cambridge.
- Press, W. H., Teukolsky, S. A., Vetterling, W. T., and Flannery, B. P. (1994). “Numerical Recipes in C: The Art of Scientific Computing,” 2nd ed. Cambridge University Press, Cambridge.
- Priestley, M. B. (1981). “Spectral Analysis and Time Series.” Academic Press, London.
- Salas, J. D. (1993). Analysis and modeling of hydrologic time series. In “Handbook of Hydrology” (D. R. Maidment, ed.), McGraw-Hill, New York, pp. 19.1–19.72.
- Schepers, H. E., van Beek, J. H. G. M., and Bassingthwaite, J. B. (1992). Four methods to estimate the fractal dimension from self-affine signals. *IEEE Eng. Medicine Biol.* 11, 57–64, 71.
- Schmittbuhl, J., Vilotte, J.-P., and Roux, S. (1995). Reliability of self-affine measurements. *Phys. Rev. E* 51, 131–147.
- Slack, J. R., and Landwehr, J. M. (1992). “Hydro-Climatic Data network (HCDN): A U.S. Geological Survey Streamflow Data Set for the United States for the Study of Climate Variations, 1874–1988.” U.S. Geological Survey Open-File Report 92-129. U.S. Geological Survey, Reston, VA, 193 p. and CD ROM.
- Smith, W. W., and Smith, J. M. (1995). “Handbook of Real-Time Fast Fourier Transforms.” IEEE Press, New York.

- Stedinger, J. R., Vogel, R. M., and Foufoula-Georgiou, E. (1993). Frequency analysis of extreme events. In "Handbook of Hydrology" (D. R. Maidment, ed.), McGraw-Hill, New York, pp. 18.1–18.66.
- Tapiero, C. S., and Vallois, P. (1996). Run length statistics and the Hurst exponent in random and birth–death random motions. *Chaos, Solitons & Fractals* 7, 1333–1341.
- Turcotte, D. L. (1997). "Fractals and Chaos in Geology and Geophysics," 2nd ed. Cambridge University Press, Cambridge.
- Voss, R. F. (1985a). Random fractals: Characterization and measurement. In "Scaling Phenomena in Disordered Systems" (R. Pynn and A. Skjeltorp, eds.), Plenum Press, New York, pp. 1–11.
- Voss, R. F. (1985b). Random fractal forgeries: From mountains to music. In "Science and Uncertainty" (S. Nash, ed.), Science Reviews, London, pp. 69–85.
- Voss, R. F. (1985c). Random fractal forgeries. In "Fundamental Algorithms for Computer Graphics" (R. A. Earnshaw, ed.), NATO ASI Series, Vol. F17, Springer-Verlag, New York, pp. 805–835.
- Voss, R. F. (1986). Characterization and measurement of random fractals. *Phys. Scripta* T13, 27–32.
- Voss, R. F. (1988). Fractals in nature: From characterization to simulation. In "The Science of Fractal Images" (H.-O. Peitgen and D. Saupe, eds.), Springer-Verlag, New York, pp. 21–70.
- Voss, R. F. (1989). Random fractals: Self affinity in noise, music, mountains, and clouds. *Physica D* 38, 362–371.
- Wang, M. C., and Uhlenbeck, G. E. (1945). On the theory of the Brownian motion, II. *Rev. Mod. Phys.* 17, 323–342.
- Wornell, G. W. (1996). "Signal Processing with Fractals: A Wavelet-Based Approach." Prentice-Hall, Englewood Cliffs, NJ.



## SELF-AFFINE TIME SERIES: II. APPLICATIONS AND MODELS

JON D. PELLETIER AND DONALD L. TURCOTTE

*Department of Geological Sciences  
Cornell University  
Ithaca, New York 14853-1504*

### 1. INTRODUCTION

In the previous article (Malamud and Turcotte, 1999, hereafter referred to as MT), the authors considered various theoretical aspects of self-affine time series. Several techniques for generating synthetic, self-affine time series were discussed and alternative methods for analyzing time series were presented. A primary means of identifying a self-affine time series is in terms of its Fourier spectrum. For self-affinity the power spectrum or power-spectral density,  $S$ , must have a power-law dependence on frequency,  $f$ :  $S \propto f^{-\beta}$  (MT, Eq. 39).

When considering self-similar processes in nature, there are generally upper and lower limits to the validity of power-law statistics. An example is a power-law distribution for the frequency-size distribution of fragments. There will always be a largest and a smallest fragment. In many cases power-law statistics will be applicable over a limited range of sizes. In other cases two power-law regimes are found with different slopes. There are also upper and lower limits to the self-affine behavior of naturally occurring time series. In some cases two or more power-law regimes are found with different values of  $\beta$ . In this paper we consider several applications of self-affine time series in geophysics. The coverage of topics is not meant to be complete. Instead, we consider three examples in some detail and present applicable models.

The first application we consider is time-series data for local atmospheric temperature. The spectral behavior for time scales between 200 kyr and 500 yr is obtained from deuterium concentrations in the Vostok ice core. Historical temperature records are analyzed to give the spectral behavior between time scales of 300 yr and 1 day. The obvious daily and annual periodicities are removed and we focus on the stochastic content of the time series. We find that self-affine behavior is applicable over well-defined frequency bands. The self-affine behavior is associated with interactions between the atmosphere, the space above (through the radiation of heat), and the oceans and continents below. Solutions to a stochastic diffusion equation for a layer with a substrate reproduce the observed

statistics. The results are closely related to those for heat diffusion through a metallic film over a substrate and to variations of solar luminosity. We have also carried out power-spectral analyses of mean river discharges and tree ring thicknesses. Both exhibit self-affine behavior with  $\beta \approx 0.5$ . This corresponds to a Hurst exponent  $Hu \approx 0.7$ , consistent with the previous results as discussed by MT (Section 5.2). The implications of a self-affine river-discharge time series for drought assessment are also considered.

In our second application we consider porosity variations in sedimentary basins. A model developed for the growth of atomic surface layers is modified so that it is applicable to the spatial and temporal variations in deposition and erosion. Self-affine variability is found with  $\beta = 2$  in space and  $\beta = 1.5$  in time. The spatial variability is a Brownian motion. This has been widely observed as the spectral behavior of topography. We show that this variability is also consistent with the spatial distribution of oil pools in sedimentary basins. The temporal variability of sedimentation is associated with the vertical variability of porosity. Self-affine spectra with  $\beta \approx 1.5$  are good approximations to observed data. The vertical variability of sedimentation and erosion can also be used to model the completeness of the sedimentary record. It has been observed that the rate of sedimentation,  $R$ , has a power-law dependence on the time period of sedimentation,  $T$ , with  $R \propto T^{-0.76}$ . A self-affine spectrum with  $\beta = 1.5$  gives  $R \propto T^{-0.75}$ .

Our third application considers the variability of the earth's magnetic field. We argue that intensity variations and reversals of the magnetic field are a natural consequence of the inherent variability generated by dynamo action and magnetic diffusion in the core. The field exhibits a binormal behavior and when a fluctuation crosses the zero intensity value a reversal occurs. The spectral behavior of the field on time scales of 100 yr to 4 Myr has been obtained from paleomagnetic data. Over this range it is well approximated by a  $1/f$  ( $\beta = 1$ ) self-affine time series. Synthetic  $1/f$  time series have been used to generate reversal statistics and these are found to be in good agreement with observations. The reversal statistics are sensitive to the values of  $\beta$  and we conclude that the agreement is strong support for  $1/f$  behavior over the entire record of reversals. A model that generates the observed  $1/f$  behavior is a two-dimensional stochastic diffusion equation.

## 2. NATURAL VARIABILITY OF CLIMATE

### 2.1. Temperature Spectra

Understanding the natural variability of climate is one of the most important tasks facing climatologists. The Intergovernmental Panel on

Climate Change (1995) concluded that the “balance of evidence suggests a discernible human impact on the climate system.” This conclusion is based, however, on comparisons with the variability exhibited by general circulation models (GCM). Model runs often exhibit significantly lower variability, by a factor of up to 10, and a different frequency dependence on time than paleoclimatic data (Santer *et al.*, 1995). Other model results give natural variability comparable in magnitude to that observed in the last 100 years (Barnett *et al.*, 1992).

In this section we consider the power spectrum of temporal variations in atmospheric temperature on time scales of 200 kyr to 1 day. We will show that at the longest time scales, at frequencies smaller than  $f \approx 1/(40 \text{ kyr})$  the power spectrum is flat (white noise). At frequencies between  $f \approx 1/(40 \text{ kyr})$  and  $f \approx 1/(2 \text{ kyr})$  the power spectrum is proportional to  $f^{-2}$  (a Brownian motion). At frequencies greater than  $f \approx 1/(2 \text{ kyr})$  the power spectrum is proportional to  $f^{-1/2}$ . At very high frequencies (above  $f \approx 1/(1 \text{ month})$ ) the spectrum varies as  $f^{-3/2}$  for continental stations and remains proportional to  $f^{-1/2}$  for maritime stations. Thus we find a sequence of self-affine spectra, each with a characteristic value of  $\beta$ , over different frequency bands.

We will further show that the observed power spectrum of atmospheric temperature is identical to the power spectrum of variations due to the stochastic diffusion of heat in a metallic film that is in thermal equilibrium with a substrate (Van Vliet *et al.*, 1980). Temperature variations in the film and the substrate occur as a result of fluctuations in the heat transport by electrons undergoing Brownian motion. The top of the film absorbs and emits blackbody radiation. In our analogy we associate the atmosphere with the metallic film and the oceans with the substrate. Turbulent eddies in the atmosphere and oceans are analogous to the electrons undergoing Brownian motion in a metallic film in contact with a substrate.

We first consider the spectral behavior of the deuterium concentrations in the Vostok (East Antarctica) ice core. A 220-kyr record of temperature fluctuations is obtained using the conversion  $5.6\delta D(\%) = 1^\circ\text{K}$  (Jouzel *et al.*, 1987). The plot of variations in temperature versus age is given in Fig. 1. Jouzel and Merlivat (1984) have concluded that the Vostok deuterium record is a proxy for local atmospheric temperature. Because the data are unevenly sampled we utilized the Lomb periodogram (Press *et al.*, 1992) to estimate the power spectrum. The results are given in Fig. 2. We associate the power spectrum with three regions of different self-affine behavior. The first region, at frequencies less than  $f \approx 1/(40 \text{ kyr})$ , is a white noise ( $\beta \approx 0$ ). The second region, between  $f \approx 1/(40 \text{ kyr})$  and  $f \approx 1/(2 \text{ kyr})$ , is a Brownian motion ( $\beta \approx 2$ ). In the third region, with frequencies greater than  $f \approx 1/(2 \text{ kyr})$ , there is a change to a lower value of  $\beta$ . This change is associated with rapid variations in the Vostok core.

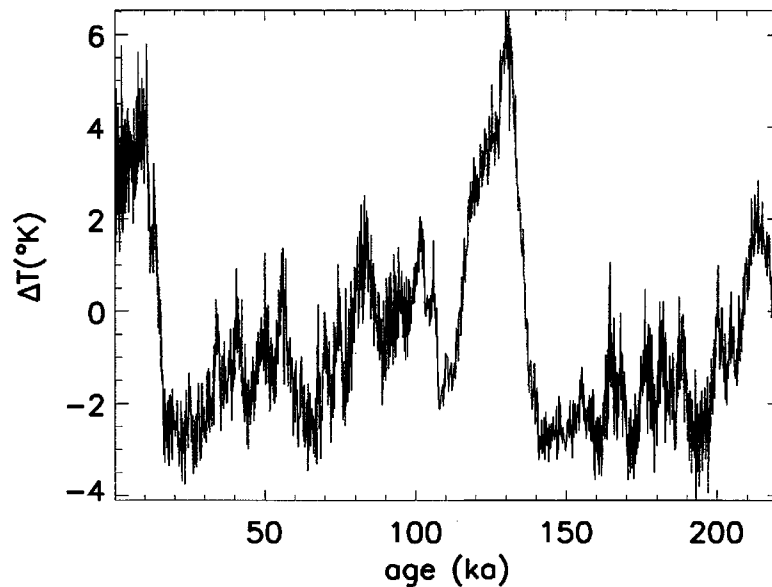


FIG. 1. Atmospheric temperatures at Vostok, Antarctica inferred from deuterium concentrations in the Vostok ice core. From Jouzel *et al.*, (1987).

This is also observed in ice cores from Greenland (Yiou *et al.*, 1995). Details of this analysis have been given by Pelletier (1997a).

In order to extend our analyses to higher frequencies we have carried out power-spectral analyses on data for atmospheric temperature variations from weather stations. One of the longest available records is for the

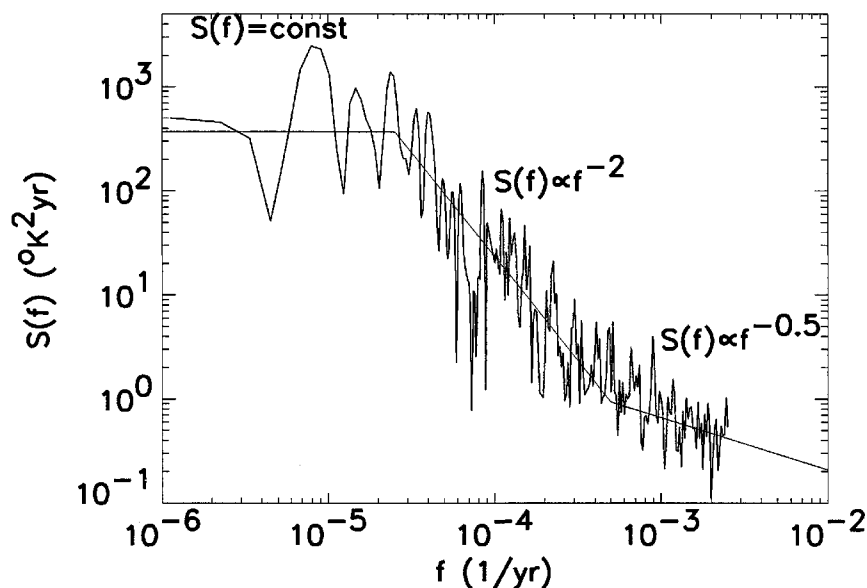


FIG. 2. Power-spectral density estimated with the Lomb periodogram of the temperature inferred from the deuterium concentrations in the Vostok (East Antarctica) ice core. The power-spectral density  $S$  is given as a function of frequency for time scales of 500 yr to 200 kyr.

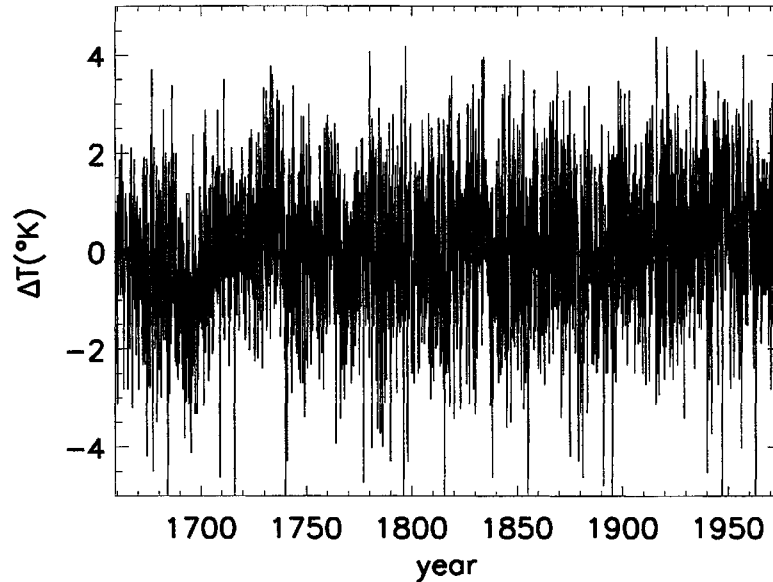


FIG. 3. Average monthly atmospheric temperature for central England (Manley, 1974) with the yearly periodicity removed.

average monthly temperature in central England, 1659–1973. The data are tabulated in Manley (1974). The yearly periodicity was removed from these data by subtracting from each value the average temperature of that month for the entire record. The resulting time series is given in Fig. 3. This time series exhibits rapid fluctuations from year to year superimposed on more gradual, lower frequency variations. The power spectrum estimated as the square of the coefficients of the fast Fourier transform (FFT) is presented in Fig. 4 along with a least-squares power-law fit to the data with  $\beta \approx 0.47$ . We have also determined the average power spectrum of the time series of monthly mean temperatures from 94 stations worldwide with the yearly trend removed. We obtained the power spectra  $S(f)$  of all complete temperature series of length greater than or equal to 1024 months from the climatological database compiled by Vose *et al.* (1992). The yearly trend was removed by subtracting from each monthly data point the average temperature for that month in the 86-year record for each station. All of the power spectra were then averaged at equal frequency values. The results are given in Fig. 5. The data yield a straight line on a log–log plot with slope close to  $-0.5$ , indicating that  $S(f) \propto f^{-1/2}$  in this frequency range.

Finally we consider the average power spectrum of time series of daily mean temperature (estimated by taking the average of the maximum and minimum temperature of each day) from 50 continental and 50 maritime stations over 4096 days. Maritime stations are sites on small islands far from any large land masses. Continental stations are well inland on large

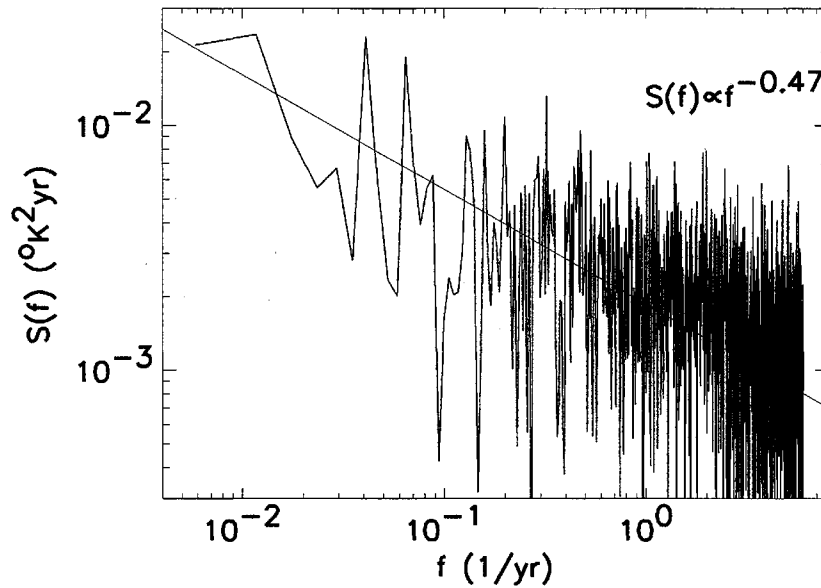


FIG. 4. Power-spectral density of the time series of central England temperatures in Fig. 3.

continents, far from any large bodies of water. We chose 50 stations at random from the complete records (those with greater than 4096 nearly consecutive days of data) of the Global Daily Summary database (National Climatic Data Center, 1994). Once again the yearly periodicities were removed. The results are given in Figs. 6 and 7. Continental stations

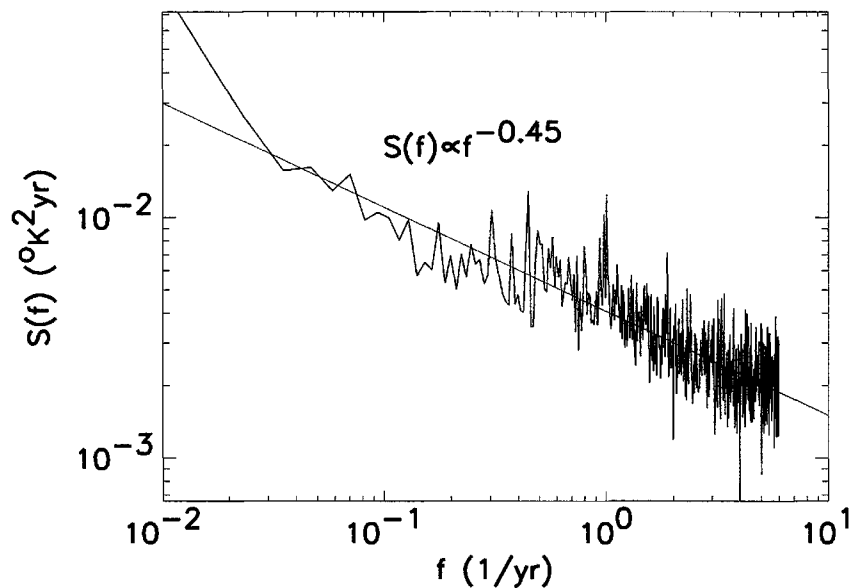


FIG. 5. Average power-spectral density of 94 complete monthly temperature time series from the data set of Vose *et al.* (1992) plotted as a function of frequency in  $\text{yr}^{-1}$ . The power-spectral density  $S$  is given as a function of frequency for time scales of 2 months to 100 yr.

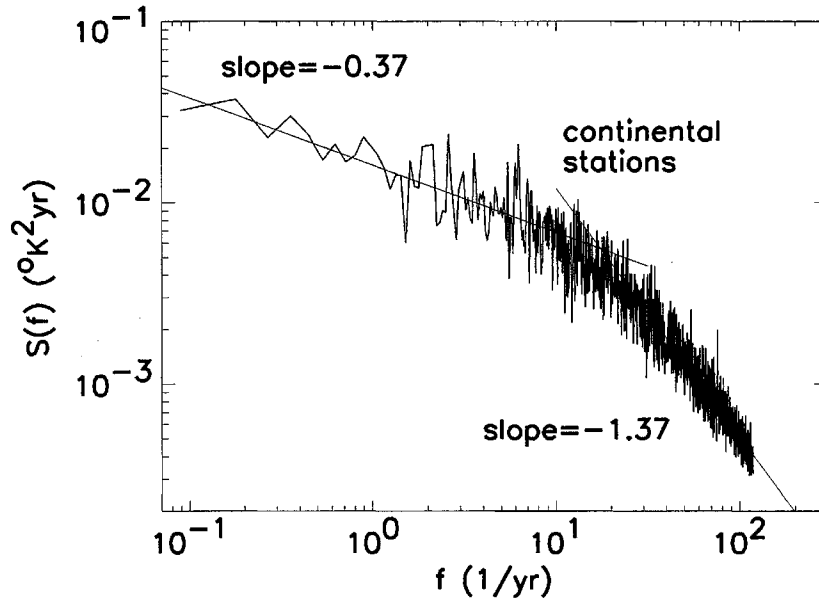


FIG. 6. Average power-spectral density of 50 continental daily temperature time series from the National Climatic Data Center (1994) as a function of frequency in  $\text{yr}^{-1}$ . The power-spectral density  $S$  is given as a function of frequency for time scales of 2 days to 10 yr.

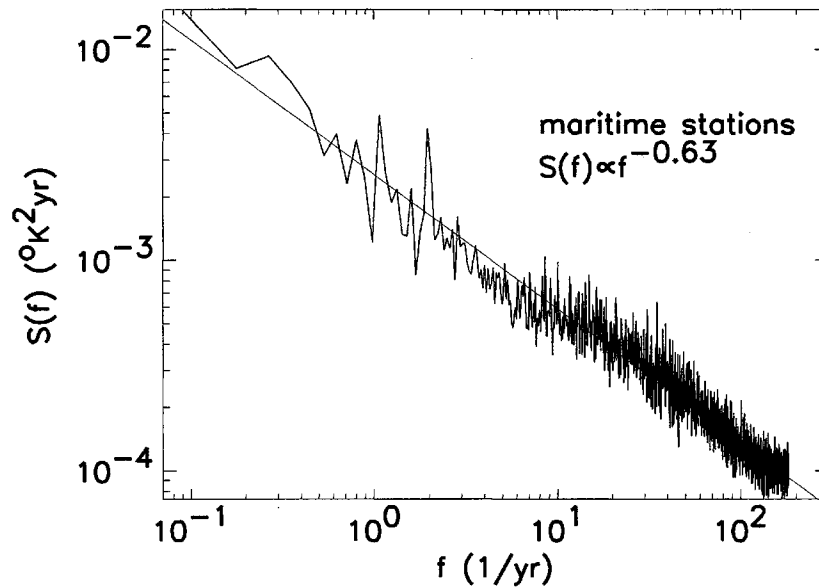


FIG. 7. Average power-spectral density of 50 maritime daily temperature time series from the data set of the National Climatic Data Center (1994) as a function of frequency in  $\text{yr}^{-1}$ . The power-spectral density  $S$  is given as a function of frequency for time scales of 2 days to 10 yr.

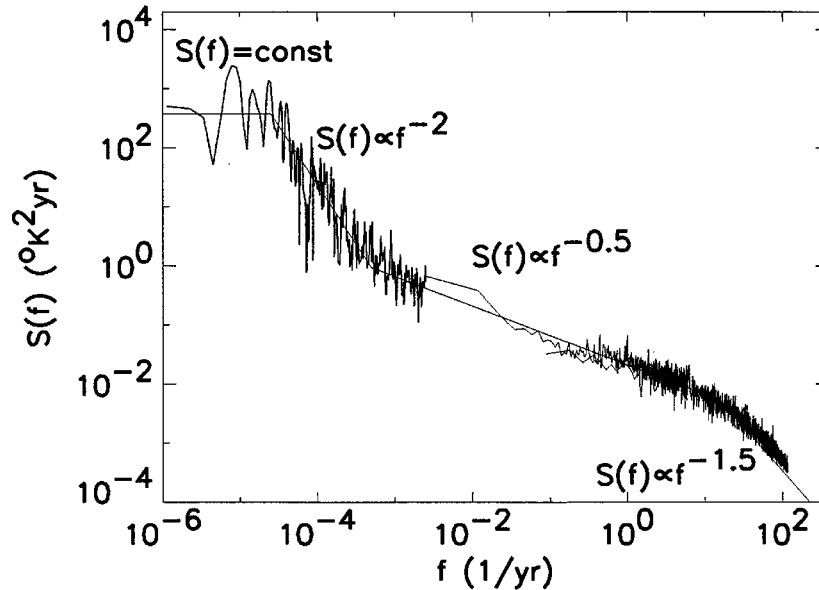


FIG. 8. Power-spectral density of local atmospheric temperature from instrumental data and inferred from ice cores for time scales of 200 kyr to 2 days. The high-frequency data are for continental stations. Piecewise power-law trends are indicated.

(Fig. 6) correlate with a  $f^{-3/2}$  high-frequency region. Maritime stations (Fig. 7) correlate with a  $f^{-1/2}$  scaling up to the highest frequency. The crossover frequency for the continental spectra is  $f \approx 1/(1 \text{ month})$ . The difference between continental and maritime stations results from the air mass above maritime stations exchanging heat with both the atmosphere above and the oceans below while the air mass above continental stations exchanges heat only with the atmosphere above it. Because of the low thermal conductivity of the solid earth, it does not act as a thermal buffer. The three spectra have been combined in Fig. 8 to give a continuous spectral behavior of atmospheric temperature from frequencies of  $10^{-6}$  to  $10^2 \text{ yr}^{-1}$ .

## 2.2. River-Discharge and Tree-Ring Spectra

Before presenting a theoretical basis for the temperature time-series spectra given above, we will consider two additional time series. We first give power-spectral analyses of hydrological time series. Figure 9 presents the results of power-spectral analyses of monthly mean river-discharge data in the United States from the Hydro-Climatic Data Network compiled by Slack and Landwehr (1992). The annual variabilities were removed and the power spectra were computed in the same manner as for the temperature data. For the streamflow data we chose all complete records with a

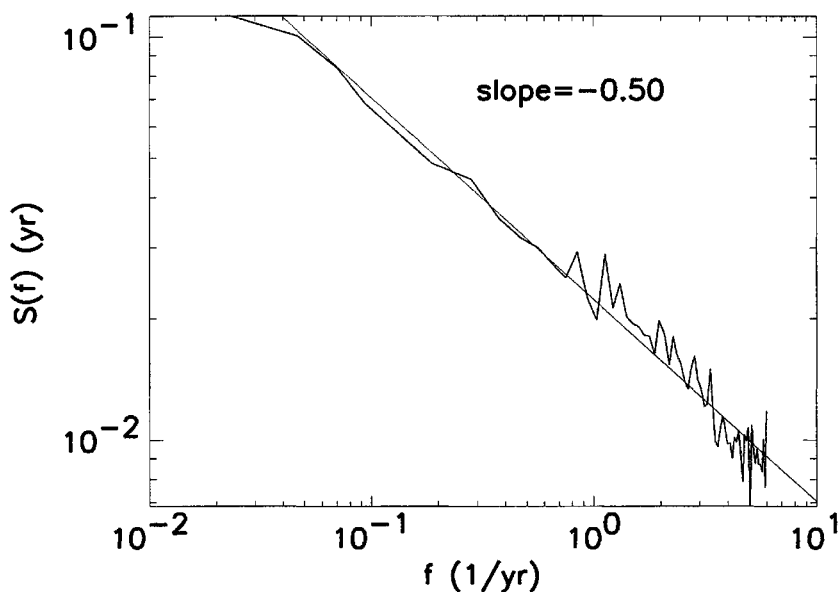


FIG. 9. Average normalized power-spectral density of 636 monthly river-discharge series as a function of frequency in  $\text{yr}^{-1}$ .

duration greater than or equal to 512 months and included 636 records in our analysis. Since river discharges can vary by orders of magnitude between river basins, we normalized the variance of each series before averaging the spectra. A least-squares fit to the data gives  $\beta \approx 0.50$ , consistent with the value observed for the temperature data in the same frequency range. We have taken advantage of the large number of available stations to investigate the possible regional variability of the power spectra. We have averaged the power spectra for each of the 18 hydrologic regions of the U.S. defined by the United States Geological Survey and given in Wallis *et al.* (1991). All of the regions exhibit the same spectral dependence with an average  $\beta$  value of 0.52 and a standard deviation of 0.03, indicating little variation.

The second time series we consider is the sequence of annual tree-ring widths. We have performed spectral analyses of tree-ring width chronologies in the western United States obtained from the International Tree Ring Database. Tree rings in the western U.S. are strongly correlated with precipitation (Landwehr and Matalas, 1986). The chronologies are time series in which the nonstationarities in growth rates have been removed and spatial averaging has been performed in an attempt to isolate climatic effects. Tree-ring series have the advantage of being much longer than most historical records. We obtained 43 chronologies in the western U.S. greater than 1024 years in length. The average normalized power spectrum

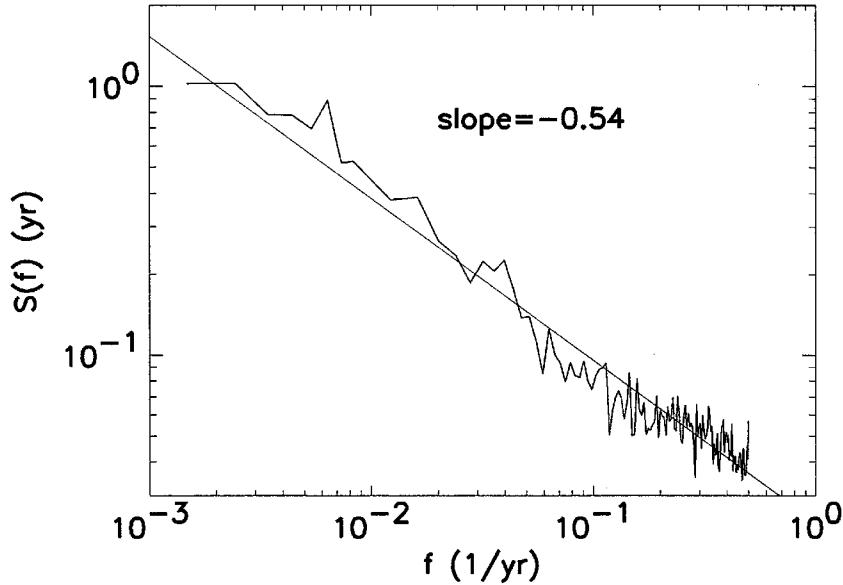


FIG. 10. Average normalized power-spectral density of 43 tree-ring chronologies in the western U.S. as a function of frequency in  $\text{yr}^{-1}$ .

of those records is presented in Fig. 10. The least-squares fit indicates that for tree-ring time series,  $S(f)$  is nearly proportional to  $f^{-1/2}$ .

In the frequency range  $f \approx 1/(2 \text{ kyr})$  to  $1/(1 \text{ month})$  the three data sets, atmospheric temperature, river discharge, and tree-ring widths, all yield spectra with a slope  $\beta \approx 0.5$ . In Section 5.2 of MT the application of the rescaled-range technique was discussed. It was pointed out that Hurst *et al.* (1965) applied the rescaled-range method to time-series data for atmospheric temperature, river discharge, precipitation, tree-ring widths, and other climatological time series. Good correlations were obtained with the Hurst relation (MT, Eq. 81) taking  $Hu = 0.73$  on average. From the correlation between  $Hu$  and  $\beta$  given for fractional Gaussian noises in MT, Fig. 25, we see that  $Hu = 0.73$  is entirely consistent with the observed value  $\beta \approx 0.5$ .

### 2.3. Stochastic Diffusion Model

To see how time series with power-law power spectra arise, we present the results from the simulation of a discrete, one-dimensional stochastic diffusion process. A discrete version of the diffusion equation for the density of particles on a one-dimensional grid of points is

$$n_i(t_{j+1}) - n_i(t_j) \propto n_{i+1}(t_j) - 2n_i(t_j) + n_{i-1}(t_j). \quad (1)$$

We establish a one-dimensional lattice of 32 sites with periodic boundary conditions at the ends of the lattice. At the beginning, we place 10

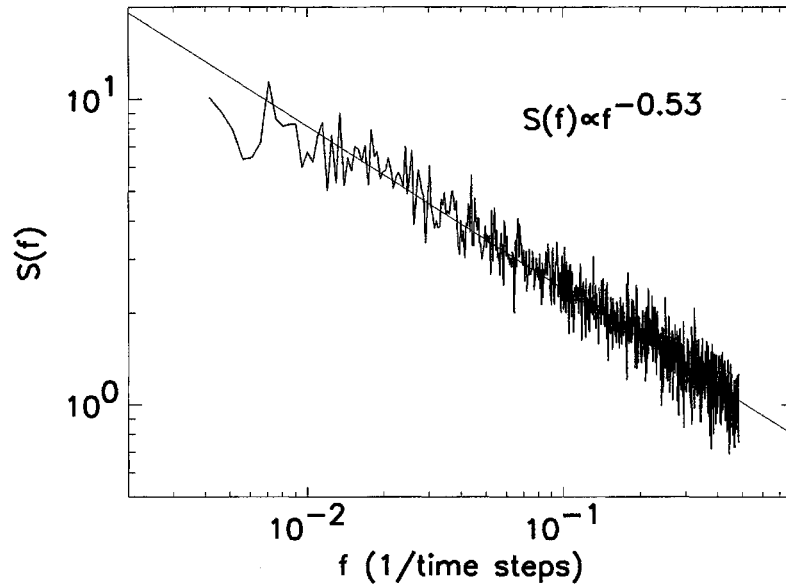


FIG. 11. Average power-spectral density of the number of random walkers in the central site of a lattice. The average of 50 simulations is presented.

particles on each site of the lattice. At each time step, a particle is chosen at random and moved to the left with probability  $\frac{1}{2}$  and to the right if it does not move to the left. In this way, the average rate at which particles leave a site is proportional to the number of particles in the site. The average rate at which particles enter a site  $i$  is proportional to the number of particles on each side multiplied by one-half since the particles to the left and the right of site  $i$  move into site  $i$  only half of the time. This is a stochastic model satisfying Eq. (1). The probabilistic nature of this model causes fluctuations to occur in the local density of random walkers. These fluctuations do not occur in a deterministic model of diffusion.

In Fig. 11 we present the average of 50 power spectra, each spectrum from a time series of the number of particles in a central site of the 32-site lattice. The figure shows a power spectrum of the form  $S(f) \propto f^{-1/2}$ . In Fig. 12 we plot the cumulative probability distribution of the time series produced by the stochastic diffusion model. The solid circles represent data. The curve represents the cumulative log-normal distribution fit to the data. A good fit is obtained.

Since the distribution of values in a hydrological time series is often log-normal, we have shown that a simple model of stochastic diffusion gives rise to both the power spectrum and the distribution observed for hydrological time series. Below we study the stochastic diffusion of heat energy in a region with boundary conditions appropriate to the coupled atmosphere-ocean system. Although the discussion is applied to transport

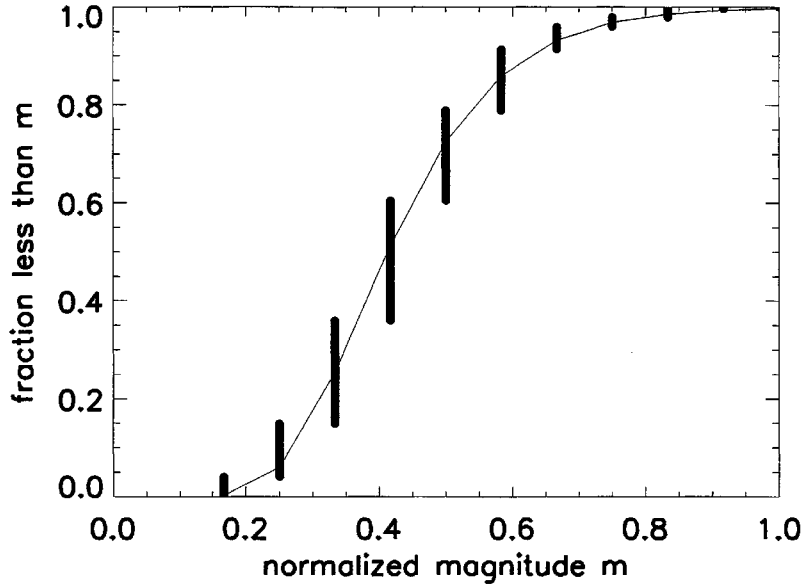


FIG. 12. Cumulative distribution function of the time series produced by the stochastic diffusion model (solid lines). The curve represents the cumulative log-normal distribution function fit to the data.

of heat energy and the resultant temperature fluctuations in the atmosphere, the same model can be applied to the turbulent transport of water vapor in the atmosphere and the resultant variations in precipitation through time. Therefore, this model provides a means to understand why the variations in temperature and in precipitation have similar statistics.

A stochastic diffusion process can be studied analytically by adding a noise term to the flux of a deterministic diffusion equation (Van Kampen, 1981):

$$\rho c \frac{\partial \Delta T}{\partial t} = - \frac{\partial J}{\partial x}, \quad (2)$$

$$J = - \sigma \frac{\partial \Delta T}{\partial x} + \eta(x, t), \quad (3)$$

where  $J$  is the heat flux,  $\Delta T$  is the fluctuation in temperature from equilibrium,  $\rho$  is the density,  $c$  is the heat capacity per unit mass,  $\sigma$  is the thermal conductivity, and  $\eta$  is a Gaussian white noise in space and time.

Equation (2) is conservation of energy. Equation (3) is Fourier's law of heat transport with random advection of heat superimposed. The random-advection term models the effects of local convective instabilities which randomly advect heat vertically in the atmosphere. Novikov (1963) has proposed this method for studying turbulent fluctuations.

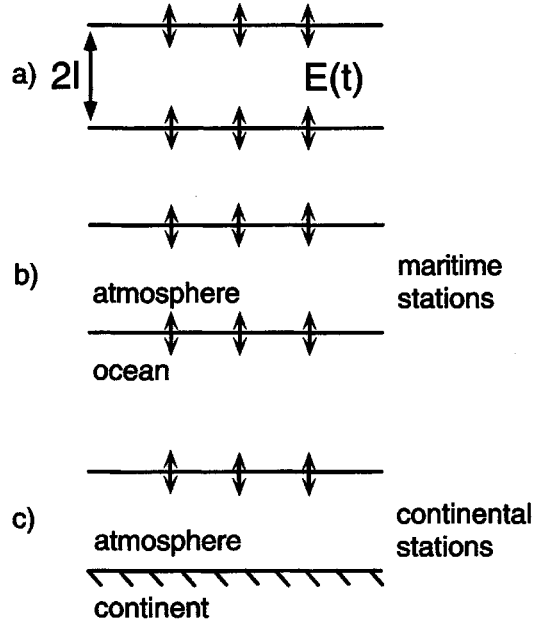


FIG. 13. (a) Geometry of the one-dimensional diffusion calculation detailed in the text. (b) Boundary conditions appropriate to the air masses above the ocean (maritime stations), where the ocean acts as a thermal conductor. (c) Boundary conditions appropriate to the air masses above the continents (continental stations), where the continents act as a thermal insulator.

We now determine the behavior of the stochastic diffusion model in terms of the power spectrum of temperature fluctuations in a layer of width  $2l$  embedded in an infinite space in which Eqs. (2) and (3) are applicable. The presentation we give is similar to that of Voss and Clarke (1976). The variations in total heat energy in the layer of width  $2l$  are determined by the heat flow across the boundaries. Figure 13a illustrates the geometry of the layer exchanging thermal energy with diffusing regions above and below it. A diffusion process has a frequency-dependent correlation length  $\lambda = (2\alpha/f)^{1/2}$  (Voss and Clarke, 1976), where  $\alpha$  is the diffusion coefficient,  $\alpha = \sigma/(\rho c)$ . Two different situations arise as a consequence of the length scale,  $2l$ , of the geometry. For high frequencies  $\lambda \ll 2l$ , the fluctuations in heat flow across the two boundaries are independent. For low frequencies  $\lambda \gg 2l$ , the fluctuations in heat across the two boundaries are in phase.

First we consider high frequencies. Since the boundaries fluctuate independently, we can consider the flow across one boundary only. The flux of heat energy is given by Eq. (2). Its Fourier transform is given by

$$J(k, \omega) = \frac{i\omega\eta(k, \omega)}{\alpha k^2 + i\omega}, \quad (4)$$

where  $f = 2\pi\omega$  and  $k$  is the wave number. The flux of heat energy out of the layer at the boundary at  $x = l$  (the other boundary is located at  $x = -l$ ) is the rate of change of the total energy in the layer  $E(t)$ :  $dE(t)/dt = J(l, t)$ . The Fourier transform of this equation is

$$E(\omega) = -\frac{i}{(2\pi)^{1/2}\omega} \int_{-\infty}^{\infty} dk e^{ikl} J(k, \omega). \quad (5)$$

Therefore, the power spectrum of variations in  $E(t)$ ,  $S_E(\omega) = \langle |E(\omega)|^2 \rangle$ , is

$$S_E(\omega) \propto \int_{-\infty}^{\infty} \frac{dk}{\alpha^2 k^4 + \omega^2} \propto \omega^{-3/2}. \quad (6)$$

In the above expression, the noise term  $\eta$  does not appear because, since it is white noise in space and time, its average amplitude is independent of  $\omega$  and  $k$ , i.e., it is just a constant. Since  $\Delta T \propto \Delta E$ , the power spectrum of temperature has the same form as  $S_E$  and  $S_T(\omega) \propto \omega^{-3/2}$ .

If we include the heat flux out of both boundaries, the rate of change of energy in the layer will be given by the difference in heat flux:  $dE(t)/dt = J(l, t) - J(-l, t)$ . The Fourier transform of  $E(t)$  is now

$$E(\omega) = \frac{1}{(2\pi)^{1/2}\omega} \int_{-\infty}^{\infty} dk \sin(kl) J(k, \omega). \quad (7)$$

Then,

$$S_T(\omega) \propto S_E(\omega) \propto \int_{-\infty}^{\infty} \frac{dk \sin^2(kl)}{\alpha^2 k^4 + \omega^2} \propto \omega^{-3/2} (1 - e^{-\theta} (\sin \theta + \cos \theta)), \quad (8)$$

where  $\theta = (\omega/\omega_0)^{1/2}$  and  $\omega_0 = \alpha/2l^2$  is the frequency at which the correlation length is equal to the width of the layer. When  $\lambda \ll 2l$ , the above expression reduces to  $S_T(f) \propto f^{-3/2}$ . When  $\lambda \gg 2l$ ,  $S_T(f) \propto f^{-1/2}$  (Voss and Clarke, 1976). In this limit the boundaries fluctuate in phase, and heat that enters into the region from one boundary can diffuse out of the other boundary. The result is a sequence of fluctuations which are less persistent ( $\beta$  is smaller) than in the single-boundary  $f^{-3/2}$  case.

In Section 2.1 we presented evidence that continental stations exhibit a  $f^{-3/2}$  high-frequency region and maritime stations exhibit  $f^{-1/2}$  scaling up to the highest frequency considered. This observation can be interpreted in terms of the diffusion model presented above. The power spectrum of temperature variations in an air mass exchanging heat by one-dimensional stochastic diffusion is proportional to  $f^{-1/2}$  if the air mass is bounded by two diffusing regions and is proportional to  $f^{-3/2}$  if it interacts with only

one. The boundary conditions appropriate to maritime and continental stations are presented in Figs. 13b and 13c, respectively. The layer considered is taken to have an upper boundary embedded in the atmosphere and a lower boundary at the earth's surface. For maritime stations heat is transferred across this lower boundary into the oceans, so it is equivalent to the case  $\lambda/l > 1$  and therefore the power spectrum of temperature variations is  $S(f) \propto f^{-1/2}$ . For continental stations the lower boundary is insulating, so it is equivalent to the case  $\lambda/l < 1$  and therefore  $S(f) \propto f^{-3/2}$ . At low frequencies, horizontal heat exchange between continental and maritime air masses limits the variance of the continental stations. This crossover should occur at the time scale when the air masses above continents and above oceans become mixed. The time scale for one complete Hadley or Walker circulation which mixes the air masses is approximately 1 month, the same time scale as the observed crossover (Pelletier, 1997a).

Next we consider the stochastic diffusion model in a geometry appropriate for a coupled atmosphere–ocean model with an atmosphere of uniform density (equal to the density at sea level) in thermal contact with oceans of uniform density. The height of our model atmosphere is the scale height of the atmosphere (height at which the pressure falls by a factor of  $e$  from its value at sea level). Figure 14 illustrates the geometry and constants chosen with  $\sigma$  the vertical heat conductivity,  $\rho$  the density,  $c$  the specific heat per unit mass,  $\alpha$  the vertical thermal diffusivity, and  $g$  the thermal conductance of heat out of the Earth by emission of radiation. Primed constants denote values for the oceans. The physical constants which enter the model are the density, specific heat, vertical thermal diffusivity, depths of the oceans and the atmosphere, and the thermal conductance by emission of radiation. The density and the specific heat of air and water are well-known constants. We choose an ocean depth of 4 km and an atmospheric height equal to the scale height of 8 km as used by Hoffert *et al.* (1980) in their climate modeling studies. The eddy diffusivity we employ for the oceans is  $6 \times 10^{-5} \text{ m}^2/\text{s}$ . This value has been obtained from tritium dispersion studies (Garrett, 1984). The vertical eddy diffusivity for the atmosphere we use is  $1 \text{ m}^2/\text{s}$ , as quoted by Pleune (1990) and Seinfeld (1986) for stable air conditions. This eddy diffusivity implies an equilibration time of the tropospheric air column of 2 years. This value is roughly consistent with the 1 year decay time of the Pinatubo and El Chichon aerosols (Hofmann and Rosen, 1987; Rosen *et al.*, 1994).

Since the time scales of horizontal diffusion in the atmosphere and the oceans are so much smaller than the time scales of vertical diffusion, the rate-limiting step for thermal equilibration is vertical transport. For this

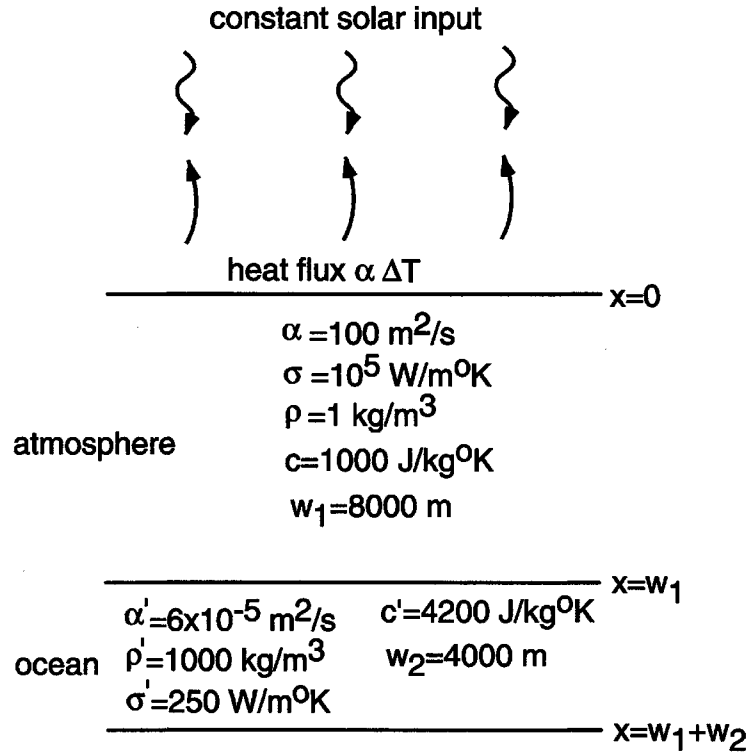


FIG. 14. Geometry of the coupled atmosphere–ocean model and the constants chosen.

reason, we consider only the variations in local temperature resulting from vertical heat exchange in the atmosphere and oceans.

The equation for temperature fluctuations in space and time in the model from Eqs. (2) to (5) is

$$\frac{\partial \Delta T(x, t)}{\partial t} - \alpha(x) \frac{\partial^2 \Delta T(x, t)}{\partial x^2} = - \frac{\partial \eta(x, t)}{\partial x}. \quad (9)$$

The mean value of  $\eta$  is zero and the flux of heat is proportional to the temperature:

$$\langle \eta(x, t) \rangle = 0, \quad (10)$$

$$\langle \eta(x, t) \eta(x', t') \rangle \propto \sigma(x) \langle T(x) \rangle^2 \delta(x - x') \delta(t - t'). \quad (11)$$

The delta functions indicate that the white-noise term  $\eta$  is uncorrelated in space and time.

North and Cahalan (1981) analyzed a similar model of climate change with respect to predictability. They studied the diffusion equation in two dimensions as a model for horizontal heat transport in the atmosphere. They included a white-noise term on the right-hand side of the diffusion equation (they used  $\eta(x, t)$  where we use  $\partial \eta(x, t) / \partial x$ ) to represent

variations in heat transport by turbulent eddies. However, a noise term in the *flux* of temperature rather than in the temperature itself is more appropriate as a model for variations in turbulent heat transfer.

The boundary conditions are that no heat flows out of the bottoms of the oceans and that there is continuity of temperature and heat flux at the atmosphere–ocean boundary:

$$\sigma' \frac{\partial T}{\partial x} \Big|_{x=w_2} = 0, \quad (12)$$

$$\Delta T(x = w_1^+) = \Delta T(x = w_1^-), \quad (13)$$

$$\sigma \frac{\partial \Delta T}{\partial x} \Big|_{x=w_1^-} = \sigma' \frac{\partial \Delta T}{\partial x} \Big|_{x=w_1^+}. \quad (14)$$

At the top of the atmosphere we impose a blackbody-radiation boundary condition. Most (65%) of the energy incident on the Earth is reradiated as long-wavelength blackbody radiation from the water and carbon dioxide in the atmosphere (Peixoto and Oort, 1992). This radiated energy depends on the temperature of the atmosphere at the point of emission according to the Stefan–Boltzmann law. It is common practice to assume that temperature variations about equilibrium are small. This is a good approximation since the global mean temperature fluctuated by only about ten degrees Kelvin during the last glaciation, as illustrated in Fig. 1. With a linear approximation, the radiated energy is proportional to the temperature difference from equilibrium (Ghil, 1983). The boundary condition at the scale height of the atmosphere (which we take to be representative of the average elevation where radiation is emitted from the atmosphere) is then

$$\sigma \frac{\partial \Delta T}{\partial x} \Big|_{x=0} = g \Delta T(x = 0). \quad (15)$$

We will use the value  $g = 1.7 \text{ W/m}^2 \text{ }^\circ\text{K}$  as used by Ghil (1983) and (Harvey and Schneider (1985)). It is often assumed that a feedback exists between atmospheric or sea-surface temperature and cloud cover. If such a feedback existed, it might be necessary to parameterize radiated energy in terms of cloud cover or atmospheric water vapor. However, no evidence for such a feedback has been found (Arking and Ziskin, 1994).

The existence of two layers of different diffusivity makes the study of the two-layer model much more complex than that of the one-layer models applied to the atmosphere above the continents and the oceans. Van Vliet *et al.* (1980) used Green's functions to solve this two-layer model. The Green's function of the Laplace-transformed diffusion equation is defined

by

$$i\omega G(x, x', i\omega) - \alpha(x) \frac{\partial^2 G(x, x', i\omega)}{\partial x^2} = \delta(x - x'), \quad (16)$$

where  $G$  is governed by the same boundary conditions as  $\Delta T$ . This equation can be solved by separating  $G$  into two parts:  $G_a$  and  $G_b$  with  $x < x'$  and  $x > x'$ , respectively.  $G_a$  and  $G_b$  satisfy the homogeneous (unforced) diffusion equation with a jump condition relating  $G_a$  and  $G_b$ :

$$\left. \frac{\partial G_a}{\partial x} \right|_{x=x'} - \left. \frac{\partial G_b}{\partial x} \right|_{x=x'} = \frac{1}{\alpha(x')}. \quad (17)$$

The power spectrum of the average temperature in the atmosphere in terms of  $G$  is given by Van Vliet *et al.* (1980) as

$$S_{\Delta T}(f) \propto \text{Re} \left( \int_0^{w_1} \int_0^{w_1} G_1(x, x', i\omega) dx dx' \right) \quad (18)$$

$$\begin{aligned} &\propto \text{Re} \left( \int_0^{w_1} \int_0^x G_{1b}(x, x', i\omega) dx dx' \right. \\ &\quad \left. + \int_0^{w_1} \int_x^{w_1} G_{1a}(x, x', i\omega) dx dx' \right), \quad (19) \end{aligned}$$

where  $G_1$  stands for the solution to the differential equation for  $G$  where the source point is located in the atmosphere and  $\text{Re}$  denotes the real part of the complex expression. Two forms of  $G_{1a}$  and  $G_{1b}$  are necessary for  $x$  located above and below  $x'$ , respectively, due to the discontinuity in the derivative of  $G_1$  created by the delta function. The solutions of  $G_1$  which satisfy the above differential equation and boundary conditions are

$$\begin{aligned} G_{1a} = &\frac{L}{\alpha K} \left( \frac{\sigma' L}{\sigma L'} \sinh \left( \frac{w_1 - x'}{L} \right) \sinh \left( \frac{w_2}{L'} \right) \right. \\ &\left. + \cosh \left( \frac{w_1 - x'}{L} \right) \cosh \left( \frac{w_2}{L'} \right) \right) \left( \sinh \left( \frac{x}{L} \right) + \frac{\sigma}{Lg} \cosh \left( \frac{x}{L} \right) \right) \quad (20) \end{aligned}$$

and

$$G_{1b} = G_{1a} + \frac{L}{\alpha} \sinh \left( \frac{x' - x}{L} \right), \quad (21)$$

where

$$\begin{aligned} K = &\left( \sinh \left( \frac{w_1}{L} \right) + \frac{\sigma}{Lg} \cosh \left( \frac{w_1}{L} \right) \right) \frac{\sigma' L}{\sigma L'} \sinh \left( \frac{w_2}{L'} \right) \\ &+ \left( \cosh \left( \frac{w_1}{L} \right) + \frac{\sigma}{Lg} \sinh \left( \frac{w_1}{L} \right) \right) \cosh \left( \frac{w_2}{L'} \right) \quad (22) \end{aligned}$$

and  $L = (\alpha/i\omega)^{1/2}$  and  $L' = (\alpha'/i\omega)^{1/2}$ . Performing the integration, van Vliet *et al.* (1981) obtained

$$\begin{aligned}
 S_{\Delta T}(f) \propto \operatorname{Re} \left( L^2 \left\{ \frac{\sigma' L}{\sigma L'} \tanh\left(\frac{w_2}{L'}\right) \left[ \frac{-2gL \cosh(w_1/L) - 1}{\sigma \cosh(w_1/L)} \right. \right. \right. \\
 \left. \left. \left. + \left(-1 + \frac{gw_1}{\sigma}\right) \tanh\left(\frac{w_1}{L}\right) + \frac{w_1}{L} \right] + \left[ \frac{gw_1}{\sigma} + \left(\frac{-gL}{\sigma} + \frac{w_1}{L}\right) \right. \right. \\
 \left. \left. \cdot \tanh\left(\frac{w_1}{L}\right) \right] \right\} \left\{ \left[ \tanh\left(\frac{w_1}{L}\right) + \frac{\sigma}{Lg} \right] \frac{\sigma' L}{\sigma L'} \tanh\left(\frac{w_2}{L'}\right) \right. \right. \\
 \left. \left. + \left(1 + \frac{\sigma}{Lg} \tanh\left(\frac{w_1}{L}\right)\right) \right\}^{-1} \right) \quad (23)
 \end{aligned}$$

For very low frequencies, several approximations can be made:

$$\tanh\left(\frac{w_1}{L}\right) \approx \frac{w_1}{L}, \quad \tanh\left(\frac{w_2}{L'}\right) \approx \frac{w_2}{L'}, \quad (24)$$

$$\frac{\cosh(w_1/L) - 1}{\cosh(w_1/L)} \approx \frac{1}{2} \frac{w_1^2}{L^2}. \quad (25)$$

Reducing Eq. (23)

$$S_{\Delta T}(f) \propto \frac{1}{1 + \omega^2/\omega_0^2} \propto \frac{1}{f^2 + f_0^2}. \quad (26)$$

This is the low-frequency Lorentzian spectrum observed in the Vostok data. The crossover frequency as a function of the constants chosen for the model is

$$f_0 = \frac{g}{w_1 c \rho + w_2 c' \rho' (1 + gw_1/\sigma)}. \quad (27)$$

At high frequencies the following approximations hold:

$$\tanh\left(\frac{w_1}{L}\right) \approx \frac{w_1}{L}, \quad \tanh\left(\frac{w_2}{L'}\right) \approx 1, \quad (28)$$

$$\frac{\cosh(w_1/L) - 1}{\cosh(w_1/L)} \approx \frac{1}{2} \frac{w_1^2}{L^2}; \quad (29)$$

then

$$S_{T_{av}}(f) \propto \frac{1}{2} \left( \frac{2gw_1}{\sigma} \right)^{1/2} \left( \frac{c\rho\sigma}{c'\rho'\sigma'} \right)^{1/2} \left( \frac{g}{w_1\rho cf} \right)^{1/2} \propto f^{-1/2}. \quad (30)$$

This is the broad  $f^{-1/2}$  region observed in the power spectrum of the temperature data and predicted based on the simpler one-layer model exchanging heat with regions above and below. The high- and low-frequency spectra meet at

$$f_1 = \frac{g}{w_1\rho c} \left( \frac{\sigma}{2gw_1} \right)^{1/3} \left( \frac{c'\rho'\sigma'}{c\rho\sigma} \right)^{1/3} 4^{1/3} \left( \frac{c\rho w_1}{c'\rho'w_2} \right)^{4/3} \quad (31)$$

$$\approx 1/(10 \text{ kyr}). \quad (32)$$

This value agrees within an order of magnitude with that observed in the Vostok data ( $f \approx 1/(2 \text{ kyr})$ ).

The three crossover time scales in the composite spectrum of Fig. 8 are fundamental time scales of the climate system. The 1-month time scale for the crossover between  $f^{-3/2}$  and  $f^{-1/2}$  behavior in continental stations may be associated with the time scale for one complete Hadley or Walker circulation. These circulations bring continental air masses in contact with oceanic air masses and allow the variations in heat energy of continental air masses to damp out more quickly through this connection to the ocean heat sink.

For time scales greater than 1 month but less than 2 kyr, fluctuations in the heat loss from the atmosphere by radiative cooling causes temperature variations in the atmosphere which can be damped by the oceans. At frequencies lower than 2 kyr, the time scale of vertical ocean mixing, the atmosphere and the oceans are in thermal equilibrium. The oceans can no longer absorb thermal fluctuations in the atmosphere resulting from fluctuations in the radiative emission on this time scale. The variance in temperature of the atmosphere and the oceans is then determined solely by the radiation boundary condition. The fluctuating temperature at the top of the atmosphere will result in a white-noise flux out of the atmosphere–ocean system. The average temperature of the atmosphere and the oceans at these time scales will be given by the sum of a white noise, a Brownian motion. This is observed in the Vostok data between time scales of 2 kyr and 40 kyr.

The power spectrum of temperature variations flattens out at frequencies lower than  $f \approx 1/(40 \text{ kyr})$  as a result of a negative feedback mechanism: as the coupled atmosphere and oceans warm up (cool down) due to nonstationary fluctuations resulting from the random heat flux out into

space, the system will radiate, on average, more (less) radiation, limiting the variance at low frequencies. This can be described by a linear damping equation for the global temperature difference from equilibrium:

$$\frac{\partial \Delta T}{\partial t} = -\frac{1}{\tau_0} \Delta T + \eta(t), \quad (33)$$

where  $\tau_0 = 1/f_0$  and  $f_0$  is given by Eq. (27). The temperature variations  $\Delta T$  from this equation have a spectrum which is a Lorentzian with a crossover time scale of  $\tau_0$ . This can be shown with Fourier transforms. The Fourier transform of Eq. (33) is given by

$$\Delta T(\omega) = \frac{\eta(\omega)}{\tau_0^{-1} + i\omega}. \quad (34)$$

The power spectrum  $S_{\Delta T}(\omega) = \langle |\Delta T(\omega)|^2 \rangle$  is then given by Eq. (26). Now we must consider whether the observed low-frequency crossover time scale of 40 kyr is consistent with the model prediction given by

$$\tau_0 = \frac{w_1 c \rho + w_2 c' \rho' (1 + g w_1 / \sigma)}{g}. \quad (35)$$

If we neglect the heat capacity of the atmosphere relative to that of the ocean, this reduces to

$$\tau_0 = \frac{c' \rho' w_2}{g} + \frac{w_1 w_2 c' \rho'}{\sigma}. \quad (36)$$

The first term is the time scale for radiative damping of the heat energy of the coupled atmosphere–ocean system into space. The second term is the time scale for transport of the heat energy of the ocean to the top of the atmosphere where it can be radiated from clouds. If the time scale for one of these processes is much larger than the time scale for the other, the crossover time scale will be determined by that rate-limiting step. For the Earth's climate system, the transport of the oceans' heat through the atmosphere appears to be the rate-limiting step. This process takes a long time because the atmosphere has a low heat capacity compared to the oceans and is therefore a poor heat conductor. The time scale of radiative damping is estimated to be 600 yr from the well-known constants listed in Fig. 14. The time scale for vertical transport of the oceans' heat through the atmosphere can only be estimated to within an order of magnitude since this time scale is linearly dependent on the average vertical diffusivity of the atmosphere. Only rough estimates are available for this parameter. Estimates of  $1 \text{ m}^2/\text{s}$  for this parameter have been given by Pleune

(1990) and Seinfeld (1986). In order for the time scale of vertical advection of the oceans' heat through the atmosphere to be 40 kyr, a vertical diffusivity of  $0.1 \text{ m}^2/\text{s}$  is required, a factor of 10 lower but roughly in agreement with the values quoted above.

Besides the frequency dependence of the power spectrum, the model we have presented predicts that the distribution of temperature variations from equilibrium obeys a Gaussian distribution. This is because the stochastic term obeys a Gaussian distribution function and the temperature fluctuations are related to the stochastic term through a linear transformation. By definition, the probability density function is only defined for time scales in which the temperature-fluctuation time series are stationary. Gaussian time series with power-law power spectra of the form  $S(f) \propto f^{-\beta}$  are stationary if  $\beta < 1$  and nonstationary if  $\beta \geq 1$  (MT, Section 2.4). Thus, a unique probability density function only exists for very long time scales (greater than 100 kyr) where the power spectrum is constant ( $\beta = 0$ ) and for the range of time scales in which the power spectrum obeys  $S(f) \propto f^{-\beta}$  with  $\beta = 0.5$ . Matteucci (1990) has computed the probability distribution function for climatic variations at very long time scales with the SPECMAP stack. He obtained a Gaussian distribution. Similarly, Janosi and Vattay (1992) have obtained a Gaussian distribution with monthly temperature data sets of several decades length with the annual variability removed.

Manabe and Stouffer (1996) have completed power-spectral analyses of variations in local atmospheric temperature in control runs of a coupled atmosphere-ocean-land surface model. They computed the power spectrum of temperature time series of each surface grid point and then averaged the power spectra at equal frequency values, as in our observational power-spectral analyses. Their results are presented in Fig. 15. They found different spectra for continental and maritime gridpoints. Maritime gridpoints exhibited power-law power spectra for time scales of one month to several hundred years with an exponent of close to  $-0.25$ . Continental gridpoints, however, showed flat spectra up to time scales of about 100 yr, in contrast to observations. Exploring the similarities and differences between the approach in this paper, GCM results such as those of Manabe and Stouffer (1996), and observations should enable us to learn more about this fundamental problem in earth science.

Time-series analyses of paleoclimatic data often exhibit a dominant peak near 100 kyr as well as smaller periodicities near 40 kyr and 20 kyr (Thomson, 1990). Although variations in the eccentricity of the Earth's orbit occur with this frequency, this variation is not expected to produce a linear influence on climate change since this orbital variation results in only a fraction of a percent change in the amount of radiation incident on

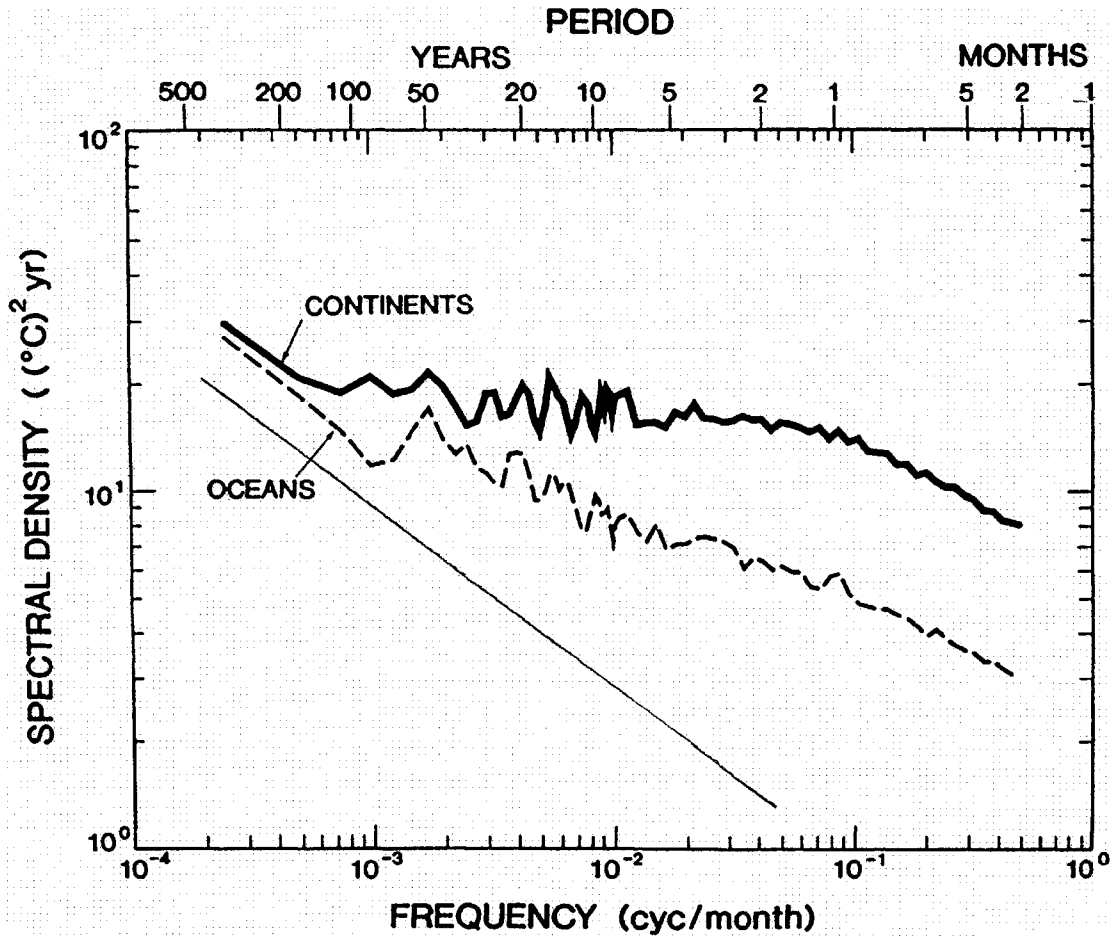


FIG. 15. Average power-spectral density of atmospheric temperature above continents and oceans for each grid point in the general circulation model calculations of Manabe and Stouffer (1996). The straight line corresponding to  $f^{-1/2}$  is included for comparison.

the Earth (Hays *et al.*, 1976). Although there are nonlinear models that predict a 100-kyr periodicity, it is generally agreed that the underlying mechanism for this peak is not well understood (Kerr, 1978). The model presented in this section leaves the question open as it does not predict any periodicity. The only component of the system thought to have a characteristic time scale of 100 kyr is the cryosphere (Mitchell, 1976). Perhaps the cryosphere can produce a 100-kyr peak in the power spectrum when forced by the background spectrum predicted by the model of this paper. Studies incorporating the cryosphere into our model are an important extension of our work that may lead to new insights into the nature of the 100-kyr periodicity.

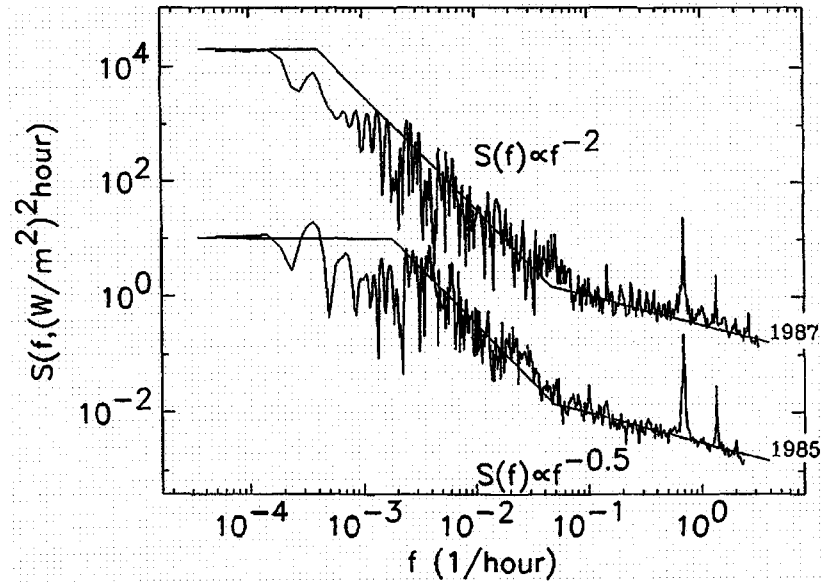


FIG. 16. Power-spectral density of variations in the solar irradiance in 1987 and 1985 from the ACRIM project as a function of frequency in  $\text{hour}^{-1}$ .

#### 2.4. Variations in Solar Luminosity

We have applied the same model presented in Section 2.3 to variations in the solar luminosity for time scales of minutes to months (Pelletier, 1996). In Fig. 16 we present the power spectra estimated with the Lomb periodogram of ACRIM solar irradiance data sampled during 1987 and 1985 plotted as a function of the frequency in  $\text{hours}^{-1}$ . The same sequence of power-law behavior is observed in these data as is observed in the Vostok data. Large peaks appear at the orbital frequency of the satellite and its harmonics. These peaks are an artifact of the spectral estimation. A stochastic diffusion model of the turbulent heat transfer between the granulation layer of the sun, modeled as a homogeneous thin layer with a radiative boundary condition, and the rest of the convection zone, modeled as a homogeneous thick layer with thermal and diffusion constants appropriate to the lower convection zone, predicts the same spectral form observed in solar irradiance data. The time scales of thermal and radiative equilibrium of the solar convection zone based upon thermal and diffusion constants estimated from mixing-length theory match those observed in the ACRIM data. Further details are discussed in Pelletier (1996).

## 2.5. Drought Hazard Assessment

One of the principal applications of time-series analysis is to drought hazard assessment. A major question is whether “short-memory” models are adequate or whether “long-memory” models such as self-affine noises and motions are required (Bras and Rodriguez-Iturbe, 1985).

Since hydrologic droughts are phenomena requiring multiple years of low flow, the frequency of occurrence will be affected by correlations in the time series of discharge. We now illustrate how fractional noises can be used to estimate drought frequencies. The use of fractional noises that exhibit the Hurst phenomenon has been proposed by Booy and Lye (1989) for use in flood-frequency analysis. The goal of stochastic hydrology is to generate synthetic time series of river discharge that accurately reproduce hydrological time series. Based on evidence for the applicability of a fractional noise with  $\beta \approx 0.5$ , we generated synthetic time series with two-parameter log-normal distributions that fit the historical records of river discharge. We first discuss the techniques and results of drought-frequency analyses for series with different log-normal distributions. Then we discuss the results of a comparison between drought frequencies for the Colorado river based upon a fractional noise with exponent of  $-1/2$  and a short-memory first-order autoregressive (AR(1)) model. An AR(1) model is a time series in which each value is equal to a constant factor multiplied by the last value in the series plus a random variable.

Techniques for generating synthetic log-normal fractional noises have been discussed by Malamud and Turcotte (MT, Section 4.2). We utilize synthetic noises with  $\beta = 0.5$  and  $c_v = 0.2, 0.4, \text{ and } 0.6$ . There is no unique definition of a drought; several alternatives were discussed in a recent drought assessment of the southwestern U.S. by Tarboton (1994). Perhaps the most straightforward definition is that proposed by Yevjevich (1967). He defined a drought as any year or consecutive number of years during which average annual streamflow is continuously below the long-term mean annual runoff. The magnitude is the average deficit during the drought. The principal drawback to this definition is that two 5-year droughts separated by one wet year will only be recognized as 5-year droughts even though the succession of droughts results in ten or eleven years of critically low supply. In Fig. 17 we present the results of drought-frequency analyses based on this definition of a drought. Each part is a two-dimensional contour plot of the logarithm (base 10) of the recurrence interval in years of a drought of a given duration and magnitude, with the magnitude normalized to the mean flow. Figures 17a, b, and c represent coefficients of variation 0.2, 0.4, and 0.6, respectively. To construct each

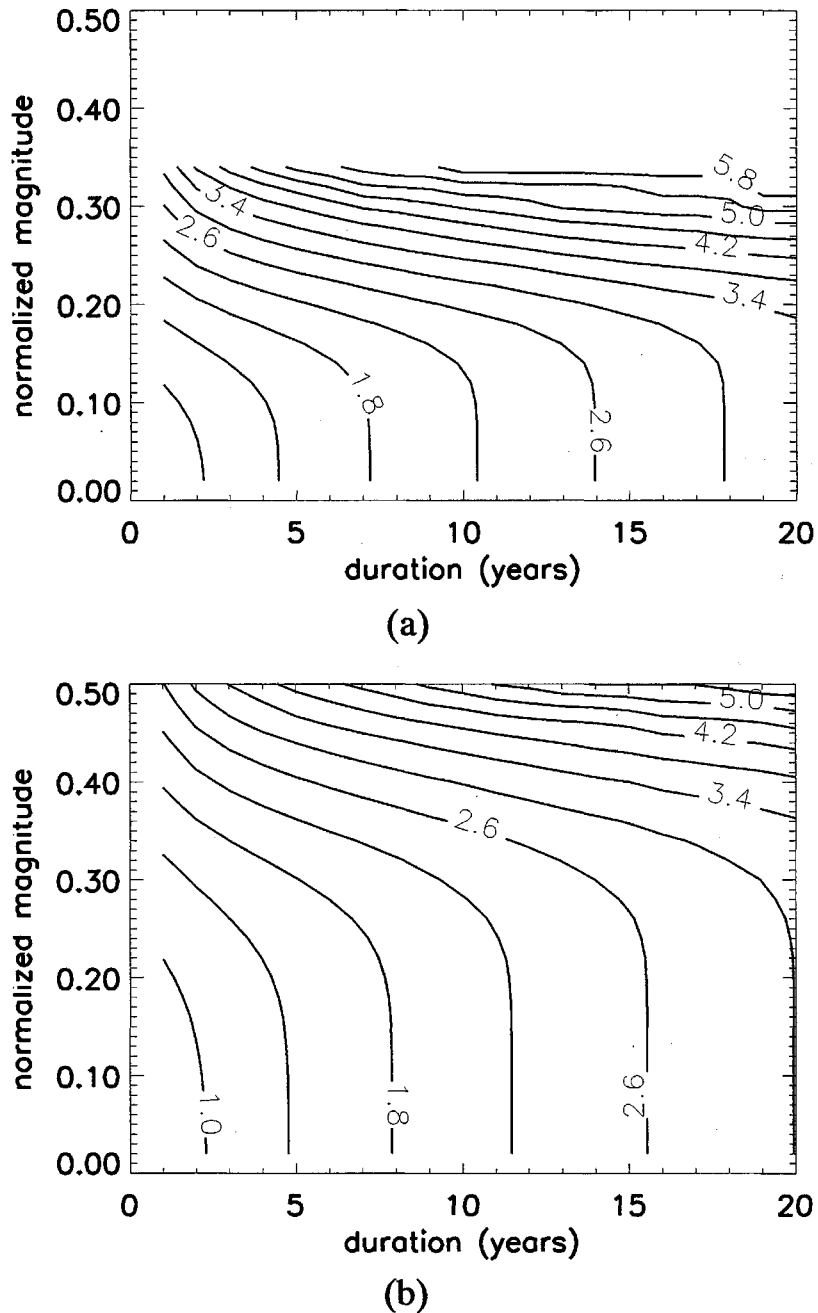
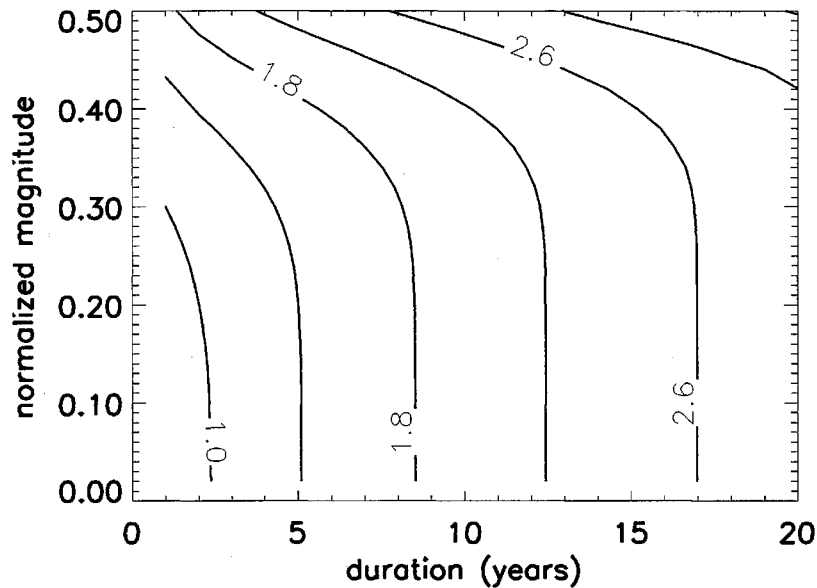


FIG. 17. Contours of the logarithm (base 10) of the recurrence interval in years as a function of drought duration and magnitude (normalized to the mean annual flow) for a log-normal distribution with coefficient of variation (a) 0.2, (b) 0.4, and (c) 0.6.

figure we generated synthetic records of one million years in length and searched them for drought occurrences.

In order to assess the importance of long-range persistence on the likelihood of severe drought, we have compared a drought-frequency analysis using a first-order autoregressive model for the Colorado river at



(c)

FIG. 17. *Continued.*

Lees Ferry (Kendall and Dracup, 1991) with a fractional noise model for the same location. The synthetic time series were one million years in length. We found that for droughts of ten years duration and small magnitude, 100-year events according to the fractional noise model, the difference in recurrence interval for the two models is a factor of 5. We conclude that the presence of long-range persistence has a significant effect on the likelihood of severe drought. The presence of long-range persistence does not, however, appear to improve the ability to predict future climatological and hydrological time series to any significant degree (Noakes *et al.*, 1988).

### 3. VARIATIONS IN SEDIMENTATION

#### 3.1. Introduction

We now turn to porosity variations in sedimentary basins. We show that these variations are self-affine motions in both the horizontal and vertical directions. We show that the observed distributions can be reproduced using a standard model for surface growth. We will further show that this model is consistent with the observed variations and episodicity in sediment deposition.

In the past decade many studies have documented the scale invariance of porosity and density variations in sedimentary basins. Power-law power spectra of vertical density and porosity well logs have been reported by Hewett (1986), Walden and Hosken (1985), Pilkington and Todoeschuck (1990), Todoeschuck *et al.* (1990), Holliger (1996), Shiomi *et al.* (1997), Dolan *et al.* (1997), and Pelletier and Turcotte (1996). Tubman and Crane (1995) and Deshpande *et al.* (1997) have presented evidence for scale-invariant horizontal variations in density and porosity from well logs and seismic data. In addition, Dunne *et al.* (1995) presented evidence that the topography of alluvial plains along the channel strike is also scale invariant. They performed spectral analyses on fluvial microtopographic transects of an alluvial plain in Kenya. They obtained power spectra with  $S(k) \propto k^{-\beta}$ , where  $k$  is the wave number and  $\beta$  ranges from 1.5 to 2. Based on his original observation, Hewett (1986) developed a fractal-based interpolation scheme for determining the three-dimensional porosity variations in sedimentary basins using available well logs. The validity of the interpolated structure was subsequently verified in a variety of ways. This approach was applied to modeling groundwater migration by Molz and Boman (1993).

### 3.2. Stochastic Diffusion Model

Before considering the observed spectra further, we present a model for the filling of sedimentary basins which will be predictive of both vertical and horizontal porosity variations. We will refer to this model as the stochastic diffusion model. The model is called that because the dynamic rules of the model are equivalent to a diffusion process, as we will show. At each time step, a site on a one-dimensional lattice is chosen at random. During that time step, a unit of sediment is deposited on that site or on one of its nearest neighbors, depending on which site has the lowest elevation. This is the simplest model combining randomness and the tendency for sediment to be deposited in low-lying areas of an alluvial plain. The model is illustrated in Fig. 18. The cross-hatched block shows the unit of sediment being added to the surface. In each case, an arrow points towards the site upon which the unit of sediment will be deposited. In Fig. 18a the chosen site has a lower elevation than either of its nearest neighbors, so the sediment is deposited at the chosen site. In Fig. 18b one of the nearest neighboring sites has a lower elevation and the sediment is deposited at that lower site. In the case of a tie for the lowest elevation between two or three sites, the site on which the sediment is deposited is chosen randomly between the sites of the same elevation, as in Fig. 18c.

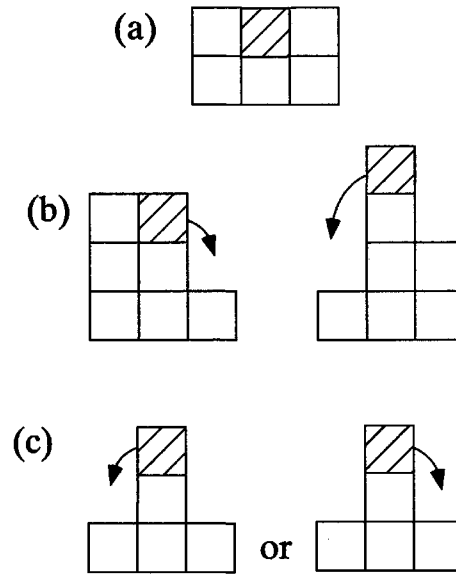


FIG. 18. Illustration of the sediment deposition model. In each case a site is chosen randomly (the center of the three sites in each of the above pictures). The dashed block is the unit of sediment being added to the surface. The arrows point toward the site upon which the unit of sediment will be deposited. (a) The chosen site has a lower elevation than either of its nearest neighbors, so the sediment is deposited at the chosen site. (b) One of the nearest neighboring sites has a lower elevation and the sediment is deposited at that lower site. (c) In the case of a tie for the lowest elevation between two or three sites, the site on which the sediment is deposited is chosen randomly between the sites of the same elevation.

The local elevation is the total number of units of sediment that have been deposited at the site.

This stochastic diffusion model was first analyzed by Family (1986) with applications to the growth of atomic surface layers. He reported the results of computer simulations which showed that the model produces scale-invariant variations of the surface in space and time. He found that the standard deviation,  $\sigma$ , of the surface follows the relation

$$\sigma(L, T) \propto L^{1/2} T^{1/4}, \quad (37)$$

where  $L$  is a length scale and  $T$  is a time scale. Surfaces with scale-invariant standard deviations  $\sigma(L, T) \propto L^{Ha_x} T^{Ha_t}$  have a power-law dependence of the power-spectral density,  $S(k)$ , on wave number  $k$  of the form  $S(k) \propto k^{-2Ha_x-1}$  (i.e.,  $\propto k^{-2}$  for  $Ha_x = 1/2$ ) and a power-law dependence on frequency of the form  $S(f) \propto f^{-2Ha_t-1}$  (i.e.,  $\propto f^{-3/2}$  for  $Ha_t = 1/4$ ).

An example of the topography produced by the stochastic diffusion model with 1024 grid points is given in Fig. 19. The average dependence of the power-spectral density on wave number from 50 independent simulations is given in Fig. 20. The power spectrum is proportional to  $k^{-2}$ ,

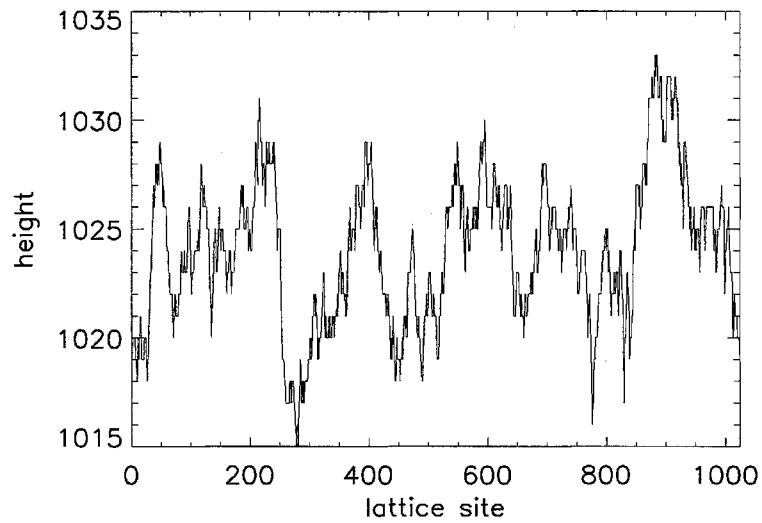


FIG. 19. A typical surface produced by the deposition model with 1024 grid points.

indicating that the surface is a Brownian motion. Other lattice sizes yield similar results. The synthetic topography given in Fig. 19 is very similar to the one-dimensional transect of Kenyan topography obtained by Dunne *et al.* (1995) and plotted in Fig. 21. Hooke and Rohrer (1979) have mapped the topographic profiles of alluvial fans perpendicular to the flow direction. The synthetic profile is also strikingly similar to their alluvial fan profiles.

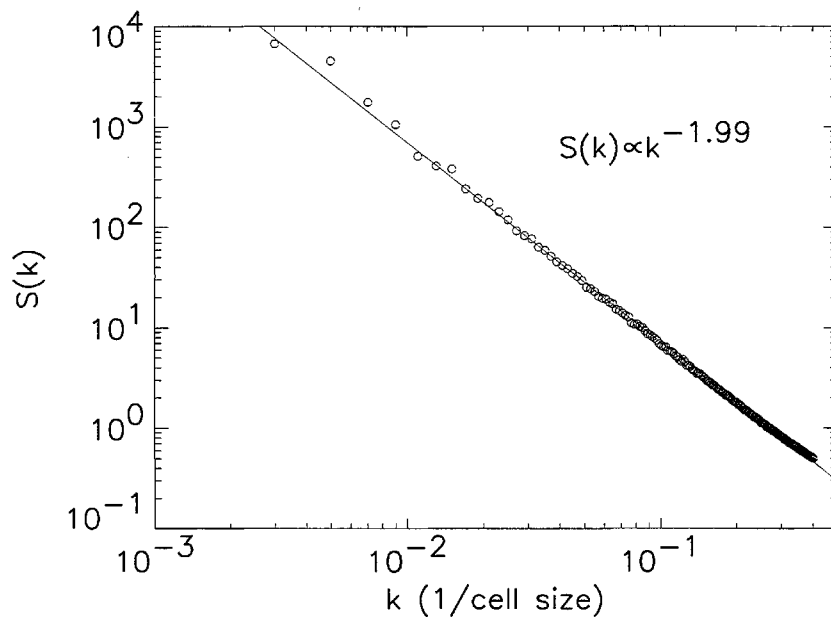


FIG. 20. Average power spectrum of the surfaces constructed from 50 independent simulations on 1024 grid points as a function of the wave number  $k$ . The model surfaces are Brownian motions.

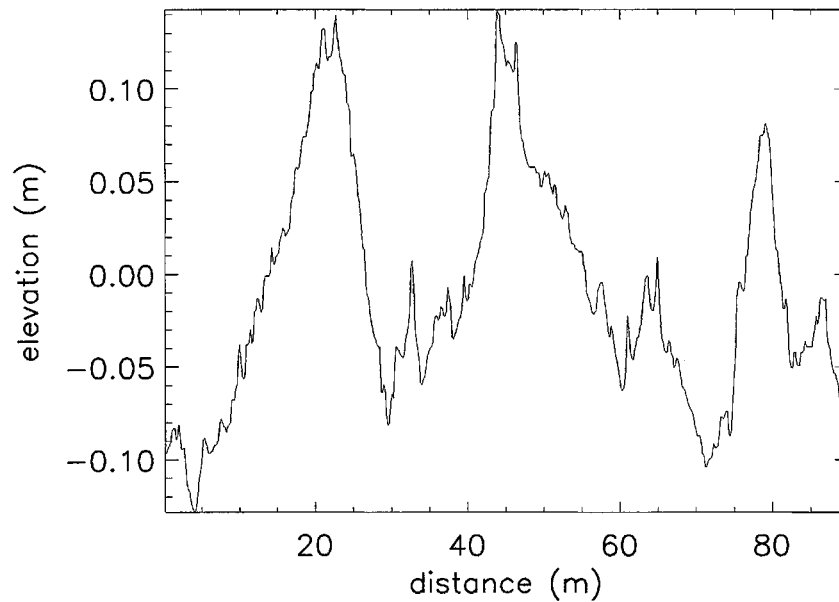


FIG. 21. One-dimensional transect of hillslope topography perpendicular to the channel dip. Obtained with the use of laser altimetry. From Dunne *et al.* (1995).

In Fig. 22 we plot the variations in surface elevation (subtracted from the mean height of the landscape) at the central site of our simulation after the simulation has reached a dynamic steady state. In Fig. 23 we present the average power spectrum of the difference from the mean height of the central site produced in 50 simulations. The power spectrum

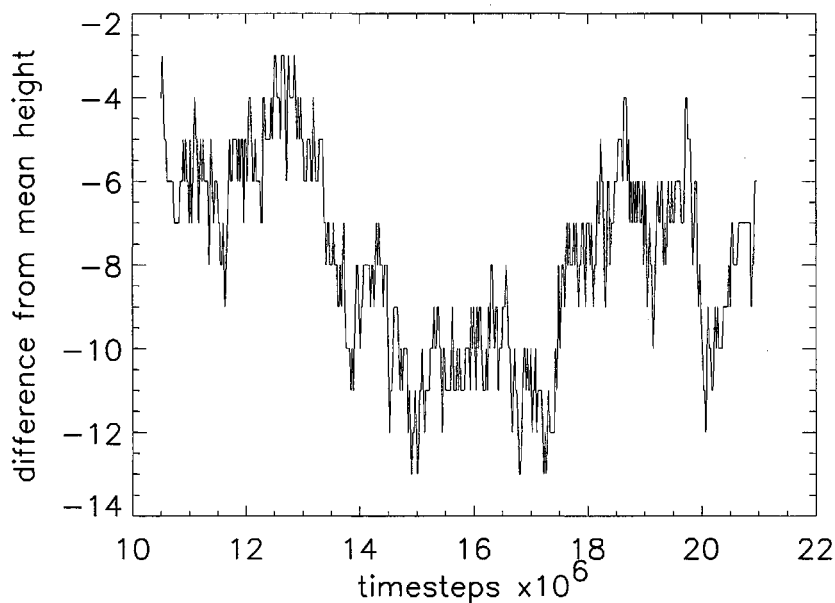


FIG. 22. Difference from the mean height of the central site of the lattice as a function of time.

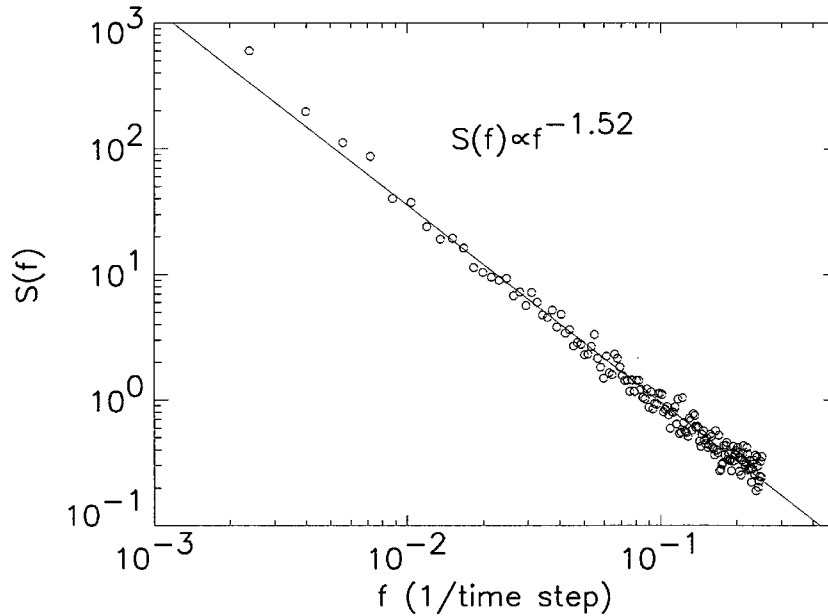


FIG. 23. Average power spectrum of the difference from the mean height of the central site for 50 independent simulations as a function of frequency  $f$ . The power spectrum is proportional to  $f^{-3/2}$ .

is proportional to  $f^{-3/2}$ . An alternative approach to the problem of deposition and erosion is the random-walk model (Tipper, 1983). This model considers the deposition and the erosion at a point to be a white noise. The elevation of topography at that point is the sum of the deposition and the erosion and therefore is a random walk with power spectrum  $S(f) \propto f^{-2}$ . The model of basin filling in which erosion and deposition occur independently will be referred to as the random-walk model. The random-walk model has been analyzed as a model for sedimentary bed formation. The effect of directing the sediment to lower elevations in our stochastic diffusion model is to preferentially fill low-lying areas of the alluvial plain. This results in an anticorrelated sequence of deposition and erosion: after an area has aggraded, it has a higher elevation and a lower rate of future aggradation. Without the filling in of low-lying areas, the horizontal surface would be a white noise. The random-walk model, therefore, results in a very unrealistic alluvial plain topography.

We can also include the effects of erosion in our stochastic diffusion model. Although deposition generally occurs in topographic depressions, tending to smooth out the floodplain, erosion is less consistent. Erosion can downcut in a channel or, during a large flood, can lower alluvial ridges. We have modified our simulation to include the effects of erosion by choosing randomly at each time step whether to deposit or to erode

sediment during that time step. The probability of deposition must be greater than 0.5 in order to accumulate a sedimentary basin over time. We have studied the modified stochastic diffusion model assuming that erosion occurs preferentially on channel floors, randomly on the landscape, or preferentially on alluvial ridges. In the simulations in which we assumed erosion to occur preferentially on the channel floors, we have included an erosion rule that takes away rather than deposits a unit of sediment at a randomly chosen site or one of its nearest neighbors, depending on which has the lowest elevation. We have also investigated rules that remove a unit of sediment only from the chosen site (to simulate random erosion on the floodplain) and a rule that removes sediment from the chosen site or one of its nearest neighbors, depending on which site is highest, to simulate the preferential erosion of alluvial ridges. The exponents of the power-law power spectra obtained in the stochastic diffusion model without erosion are unchanged for any of these modified models with erosion.

In the simplest version of the stochastic diffusion model which includes only deposition, the probability that a particle is added to the site is proportional to 2 if both of a site's neighbors have a higher elevation, is proportional to 1 if only one of the neighbors is higher, and is zero if both neighbors are lower. The model may be described mathematically with a stochastic difference equation of the form

$$h_{i,t+1} - h_{i,t} \propto \Theta(h_{i+1,t}, h_{i,t}) + \Theta(h_{i-1,t}, h_{i,t}), \quad (38)$$

where  $h_{i,t+1} - h_{i,t}$  represents the most probable growth rate of the surface and  $\Theta$  is the Heavyside function defined by  $\Theta(x, x_0) = 1$  if  $x > x_0$  or 0 if  $x < x_0$ . Averaging this equation over a time long compared to the time required to grow a single layer of unit height of sediment, the equation for the average surface growth rate is

$$\langle h_{i,t+1} - h_{i,t} \rangle \propto \langle h_{i+1,t} - h_{i,t} \rangle + \langle h_{i-1,t} - h_{i,t} \rangle \quad (39)$$

$$\propto \langle h_{i+1,t} \rangle - 2\langle h_{i,t} \rangle + \langle h_{i-1,t} \rangle. \quad (40)$$

This is a discrete version of the diffusion equation. Directing sediment to lower elevations smooths out the surface and is equivalent to a diffusion process. As recognized by Family (1986), a continuous version of the discrete model is provided by a one-dimensional diffusion equation with a Gaussian white-noise term:

$$\frac{\partial h(x, t)}{\partial t} = D \frac{\partial^2 h(x, t)}{\partial x^2} + \eta(x, t). \quad (41)$$

The term  $\eta(x, t)$  represents actual deposition and erosion. The assumed Gaussian white noise is characterized by a mean,  $\bar{\eta}$ , and a standard deviation,  $\sigma$ . If  $\bar{\eta} = 0$  there is no net deposition and sedimentation balances erosion. For  $\bar{\eta} > 0$  there is net deposition and for  $\bar{\eta} < 0$  there is net erosion. The ratio  $\sigma/\bar{\eta}$  is a measure of the amplitude of fluctuations in the sedimentation process. The diffusion term in Eq. (41) introduces both spatial and temporal correlations in the sedimentation process not present in the random-walk model.

### 3.3. Observations

We will next consider some observed spectra of the vertical variations of porosity in sedimentary basins and compare them with the results we have obtained. Our model for variations in paleotopographic elevation (or stratigraphic position) with time may be comparable to porosity variations with depth since high porosity is often associated with low stratigraphic position such as in poorly sorted, sandy channel-fill deposits (Curry and Curry, 1972; Coleman and Prior, 1982). Porosity as a function of depth is routinely measured at equal intervals in formation well logs (Hewett, 1986). As a specific example we have considered porosity logs from 15 wells in the Gulf of Mexico. One of the logs is plotted in Fig. 24. The wells are drilled in a deltaic sedimentary environment with a few large, nearly vertical faults (Alexander, 1995). The power spectra for these wells are given in Fig. 25 as a function of the wave number  $k$  in  $\text{m}^{-1}$ . At spatial

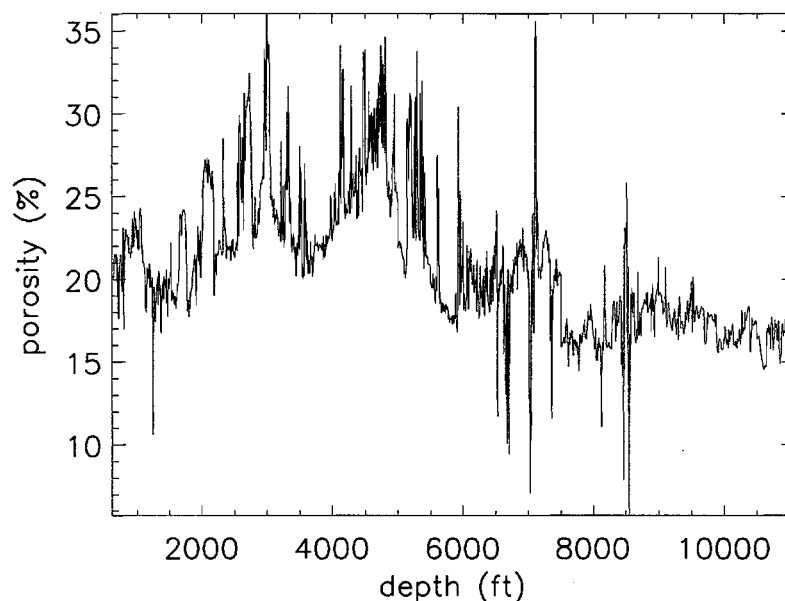


FIG. 24. Vertical porosity well log from the Gulf of Mexico.

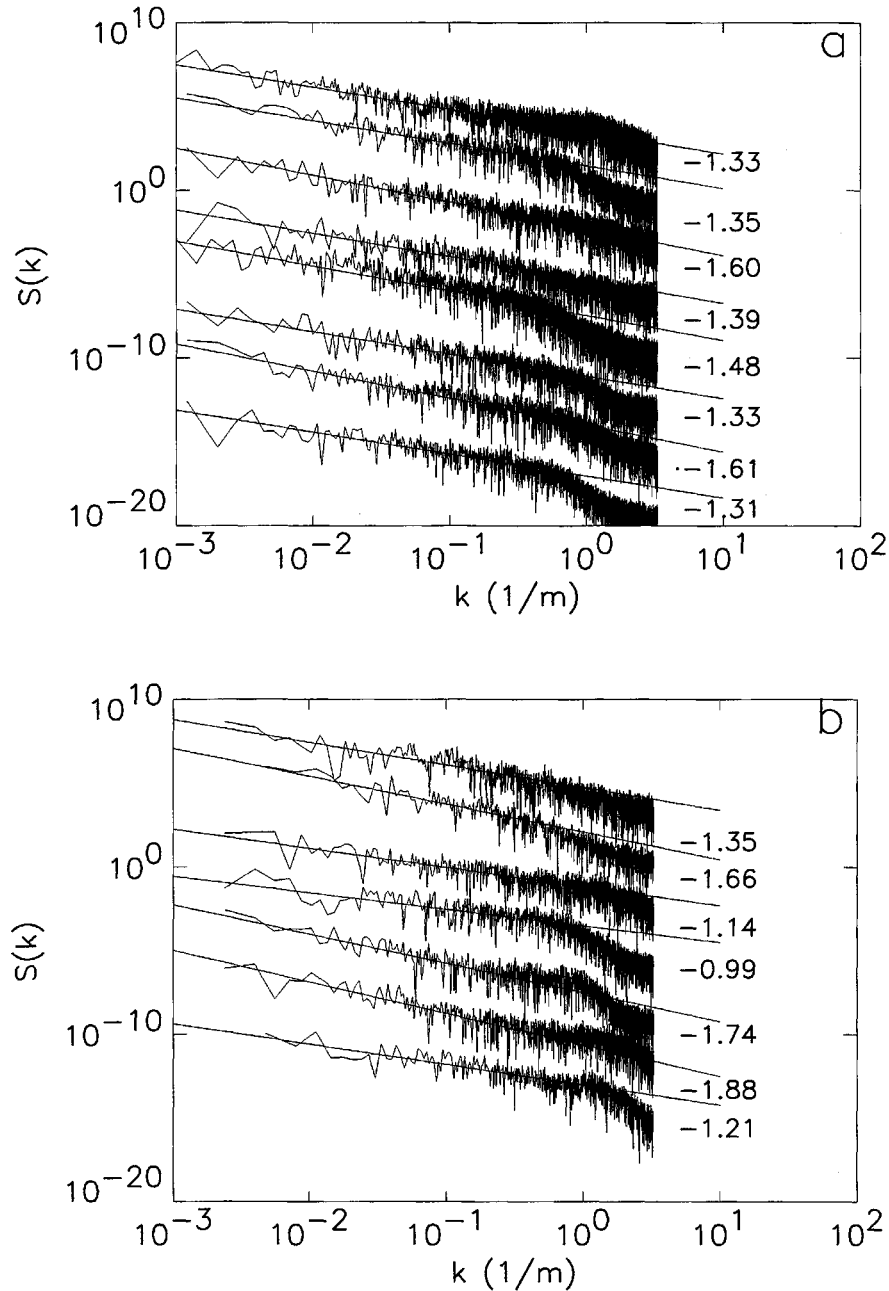


FIG. 25. (a) and (b) Power-spectral density of porosity as a function of wave number in units of  $m^{-1}$  in 15 wells from the Gulf of Mexico. The spectra are offset so that they may be placed on the same graph.

scales larger than  $\approx 3$  m, the power spectra are well approximated by a power law. Below this scale the power-spectral density decreases sharply in most of the wells. This decrease may be the result of a transition from second-order heterogeneities (dominated by variations in porosity within the larger genetic units) to third-order heterogeneities which result from the geometrical arrangements of individual depositional units. The transi-

tion from second- to third-order heterogeneities occurs at the scale of meters (Allen and Allen, 1990) and is consistent with the 3-m scale of the break observed in the power spectra. We estimate  $\beta$  from the slope of the least-squares linear fits to the log-log plots at scales greater than 3 m. The values of  $\beta$  obtained exhibit considerable variability from well to well. However, the average  $\beta = 1.4$  is close to the value 1.5 predicted by the model. The standard deviation is 0.2.

Dolan *et al.* (1998) reported ranges of values of  $\beta$  from time-series analyses of vertical density and porosity variations in well logs. They obtained average power-spectral exponents  $\beta = 1.50, 1.62,$  and  $1.46$  using three different numerical procedures for a cluster of ten wells in a fluvial sedimentary environment. These values are in excellent agreement with the ones we obtained and with our model. Holliger (1996) has reported values of  $\beta$  from 1.2 to 1.4, somewhat smaller, but roughly consistent with the values reported here.

We will next consider several observational studies relevant to the horizontal variations of porosity in sedimentary basins. Direct measurements of topography on relevant scales have been carried out by Dunne *et al.* (1995). These authors have performed power-spectral analyses of fluvial microtopographic transects perpendicular to the fall line from two hillslopes obtained with laser altimetry from scales of 0.1 to 100 m. Their work provides us with a direct test of our model for the topographic variations of an alluvial plain. They obtained power spectra with a power-law dependence on wave number as predicted. The exponents of the power spectra had an average of  $\beta = 1.6$  with a standard deviation of 0.2, somewhat smaller than our model prediction of  $\beta = 2$ .

In addition to the power-spectral behavior of the surface in space and time discussed above, the stochastic diffusion model also predicts a Gaussian distribution of the surface elevation. This is true of any linear stochastic differential equation with Gaussian noise. The microtopographic transects obtained by Dunne *et al.* (1995) enable us to test this prediction. In Fig. 26 we present the distribution of elevations from the 15 profiles published by the authors. The profiles were digitally scanned for the analysis. Also plotted in Fig. 26 is the nonlinear least-squares fit to a Gaussian distribution. A good fit is obtained.

We will next show that the distribution of producing oil and gas wells is consistent with  $\beta = 2$  horizontal porosity variations. Barton and Scholz (1995) have presented the spatial distribution of drilled wells and wells showing hydrocarbons in the Denver and Powder River basins. These basins evolved from sediment deposition in a meandering alluvial environment (Berg, 1968). Using the box-counting technique, Barton and Scholz (1995) found that the fractal dimensions for the drilled wells in the two

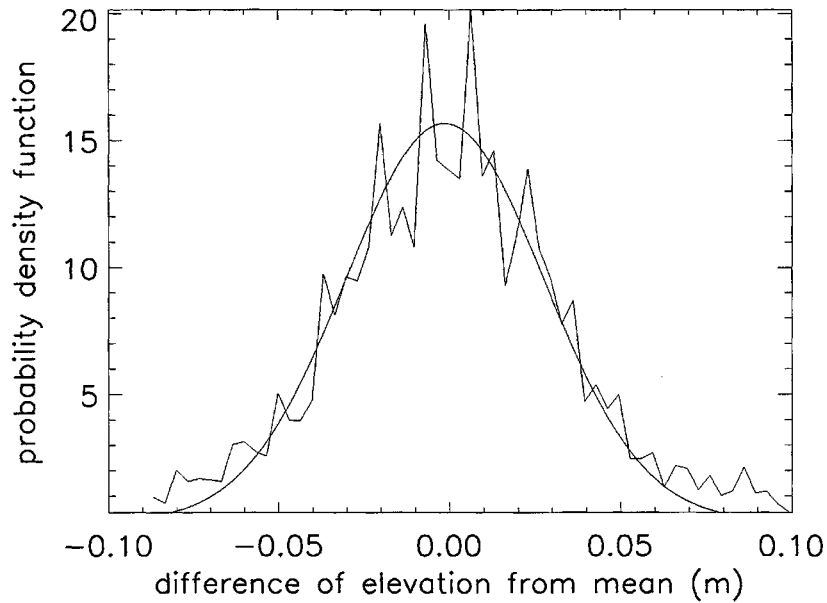


FIG. 26. Probability density function for elevation of topographic transects from Dunne *et al.* (1995).

basins were 1.80 and 1.86 and that the fractal dimensions of wells showing hydrocarbons were 1.43 and 1.49, respectively. After petroleum is generated and migrates from source rocks, it will move from sites of high potential energy to sites of low potential energy. Hydrocarbons are found in traps that are the crests of low-porosity caprock that have obstructed its upward migration (Allen and Allen, 1990). The caprock will mimic the floodplain relief at the time of its deposition. This is consistent with the observation that hydrocarbons are often found in geometries which mimic the topography of the alluvial plain at the time of deposition in a variety of fluvial depositional environments such as meandering (Curry and Curry, 1972), deltaic (Coleman and Prior, 1982), and submarine fans (Garcia, 1981; Wilde *et al.*, 1978). A simple model for the horizontal spatial distribution of hydrocarbons in a reservoir is one in which hydrocarbons are assumed to be accumulated in all of the crests of the caprock above a certain elevation.

The spatial distribution of wells showing hydrocarbons in the Powder River and Denver basins is given in Fig. 27. We have set the width of each basin to be 128 units so as to facilitate comparisons with a synthetic reservoir constructed on a  $128 \times 128$  grid. We analyzed the data with the pair-correlation function, which we believe to be a better estimator of correlations for point processes than box counting.

The two-dimensional pair-correlation function  $C(r)$  is defined as the number of pairs of wells whose separation is between  $r$  and  $r + \Delta r$ , per

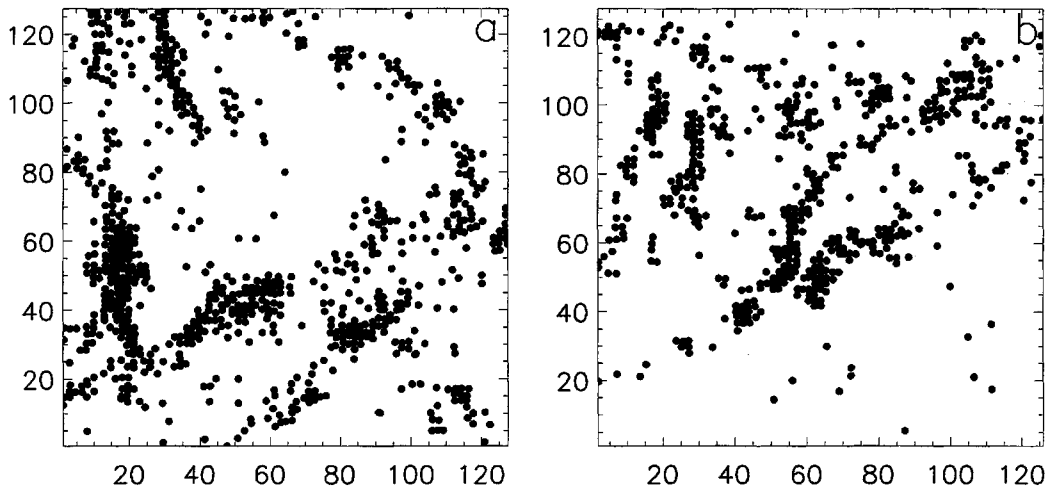


FIG. 27. Wells producing hydrocarbons in the (a) Powder River and (b) Denver basins. From Barton and Scholz (1995). Distance units are scaled such that the basin is  $128 \times 128$ .

unit area (Vicsek, 1992). The pairs are binned in logarithmically spaced intervals  $\Delta r$ . For a data set with scale-invariant clustering,  $C(r) \propto r^{-\alpha}$ , where  $\alpha$  is related to the fractal dimension through  $D = 2 - \alpha$  in two dimensions (Vicsek, 1992). The pair-correlation function is commonly employed in the analysis of diffusion-limited aggregation. However, studies incorporating it in the earth sciences are rare. Kagan and Knopoff (1980) have applied it to the spatial clustering of earthquakes. Figure 28 shows the pair-correlation function of the Denver and Powder River basin wells

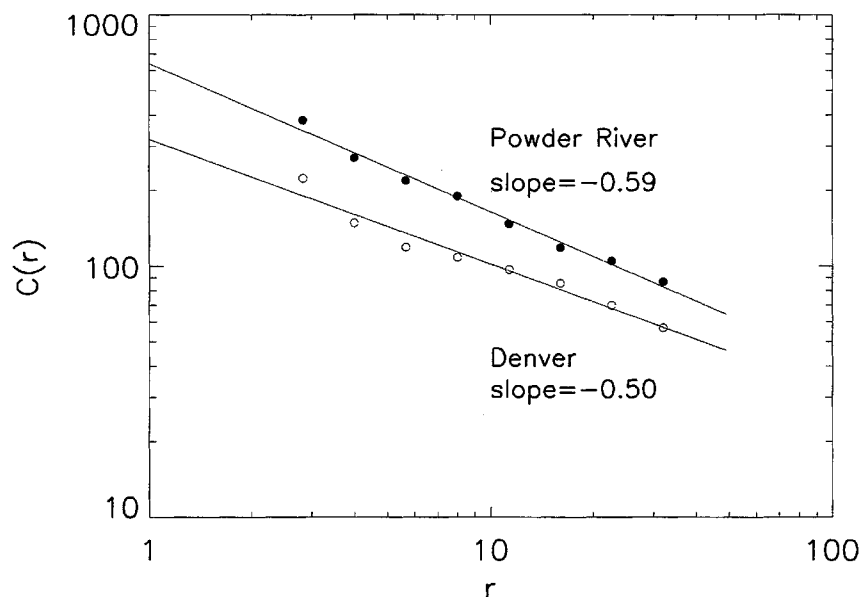


FIG. 28. Pair-correlation function of the Powder River and Denver basins as a function of the pair separation.

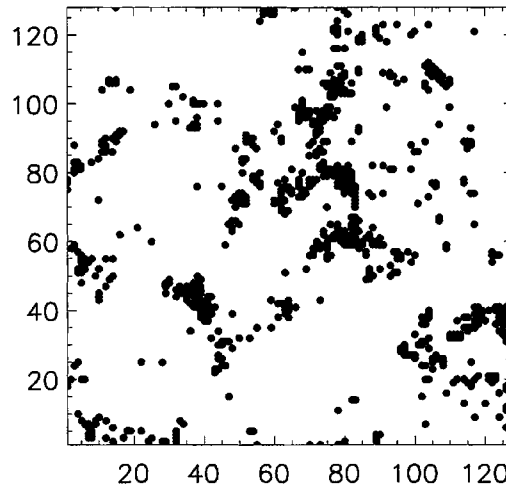


FIG. 29. Synthetic reservoir constructed from a source and caprock with a two-dimensional Brownian-motion topography constructed on a  $128 \times 128$  grid where all the sites with porosity greater than a fixed level are showing.

on a log-log plot. The least-squares fits to the correlation function yield exponents of  $\alpha = 0.59$  for Powder River and  $\alpha = 0.50$  for the Denver basin, implying  $D = 1.41$  and  $D = 1.5$ , respectively. The results obtained by the pair-correlation method are in close agreement with the results obtained by Barton and Scholz (1995) using box counting.

To show that these correlation functions are consistent with a caprock with Brownian-motion topography, we have constructed synthetic reservoirs where hydrocarbon traps are regions where the caprock elevation is larger than a threshold value. In order to do this we synthesized two-dimensional fractional Brownian motions on a  $128 \times 128$  lattice with the Fourier-filtering technique discussed in MT, Section 3.2. The threshold value for showing hydrocarbons was chosen such that the resulting synthetic reservoir had the same percentage of showing wells as the Denver and Powder River basins (about 5%). Figure 29 shows a synthetic reservoir produced with  $\beta = 2.0$  (a Brownian motion). The synthetic reservoir shows a degree of clustering similar to that of the Denver and Powder River basins. In Fig. 30 we have plotted the pair-correlation functions for the showing wells in synthetic reservoirs constructed with  $\beta = 2.5, 2.0, 1.5$ , and  $1.0$ . The pair-correlation functions show a gradual decrease with decreasing  $\beta$ . The synthetic reservoirs whose scaling exponents,  $\alpha$ , most closely match those of the Denver and Powder River basins are  $\beta = 2.0$  and  $\beta = 1.5$ . Although we cannot precisely determine the scaling exponent of the porosity variations with this method, we conclude that  $\beta$  is close to 2, consistent with the stochastic diffusion model.

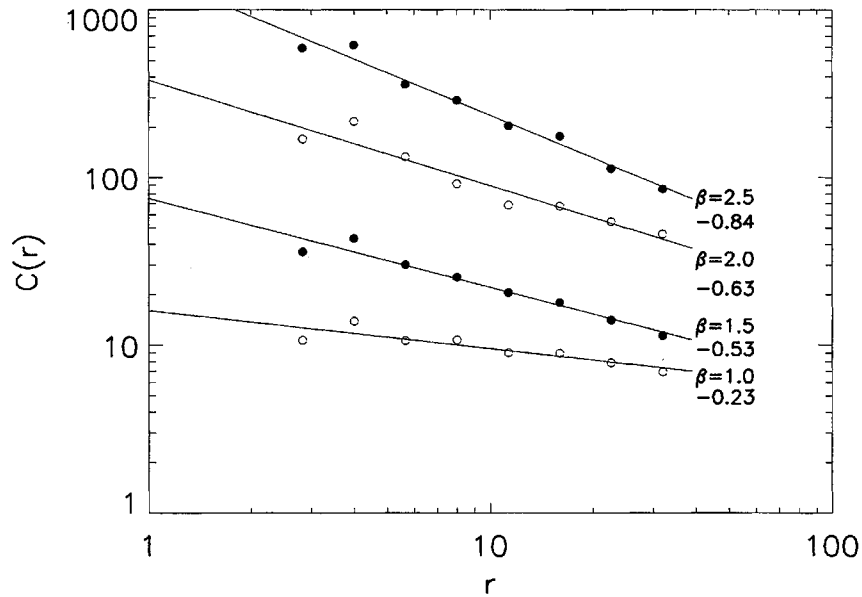


FIG. 30. Pair-correlation functions for synthetic reservoirs with caprocks constructed with different values of  $\beta$ . The plots are offset so that they may be placed on the same graph.

Besides the pair-correlation function, two other fractal relations allow us to infer Brownian-motion paleotopography from horizontal variations in sedimentary basins. Agterberg (1982) has computed the fractal dimension of the perimeter of sand isopach contours from the Lloydminster oil field to be 1.3, close to the value of 1.25 measured for coastlines and topographic contours (Turcotte, 1992). Barton and Scholz (1995) have presented frequency–size distributions of oil pools. They found that the cumulative number of oil fields has a power-law dependence on the volume of the fields with exponent close to  $-1$ :  $N(> V) \propto V^{-1}$ . Kondev and Henley (1995) have related the length distribution of contour lengths of Gaussian surfaces to the Hausdorff measure  $Ha$ . Pelletier (1997b) has shown that their results imply that the cumulative frequency–area distribution of areas enclosed by contours of a Brownian-motion surface is  $N(> A) \propto A^{-3/4}$ . Since volume and area for producing wells are observed to be related by  $V \propto A^{3/2}$  (Harbaugh *et al.*, 1977), our model of the migration of hydrocarbon into regions with caprock topography above a threshold elevation then predicts  $N(> V) \propto V^{-9/8}$ , in close agreement with the cumulative frequency–size distributions of Barton and Scholz (1995). Pelletier (1997b) has employed the same techniques to infer the self-affinity of the top of the convective boundary layer from the size distribution of cumulus cloud fields.

### 3.4. Completeness of the Sedimentary Record

A problem related to topography and porosity variations in sedimentary basins is the statistics of preserved sections. Stratigraphic sections are formed by alternating periods of deposition and erosion or nondeposition. The resulting stratigraphic section contains the deposited sediments that were not subsequently eroded. Various stochastic models have been proposed to explain aspects of sedimentary bed formation, including the frequency distribution of bed thicknesses. Beginning with Kolmogorov's work (Kolmogorov, 1951), many studies have investigated random-walk models of sedimentation. Random-walk models assume that the magnitudes of alternating depositional and erosional events are independent. These models are applied by letting the typical episodes of deposition and erosion define minimal units of a discrete time scale. The lengthy periods of nondeposition, as well as any long intervals of deposition and erosion, are treated as multiples of these units. There have been a number of variants of Kolmogorov's work: Schwarzacher (1975) described a process of bed formation that results in a random walk on the integers, Vistelius and Feigel'son (1965) allowed different types of sediment to be deposited, Dacey (1979) considered both exponential and geometrical probability distributions for the amount of sediment deposited and eroded, and Strauss and Sadler (1989) have considered a continuous version of the random-walk model. These models are generally considered to be successful at predicting observed bed-thickness distributions (Strauss and Sadler, 1989).

Tipper (1983) was the first to apply the random-walk model to the problem of stratigraphic completeness: given that deposited sediment is often later eroded, how much of the depositional history is preserved in a given stratigraphic section? Sadler (1981) obtained a solution to this problem by investigating the dependence of sedimentation rate on the time span over which the sedimentation rate was measured. If the dependence of the sedimentation rate on time span can be assessed, then for a single stratigraphic section, the ratio of the overall accumulation rate to the average rate at time span  $T$  is the completeness (Sadler and Strauss, 1990). Sadler (1981) quantified the sedimentation rate,  $R$ , as a power-law function for a time span,  $T$ , with exponent  $-0.65$ :  $R \propto T^{-0.65}$ . McShea and Raup (1986) have critically reviewed Sadler's approach, indicating possible biases in the data he compiled. Sadler interpreted the decreasing sedimentation rate with time as the result of including longer and longer hiatuses of erosion or nondeposition in the average at longer time intervals. Plotnick (1986) introduced a fractal model for the length distribution

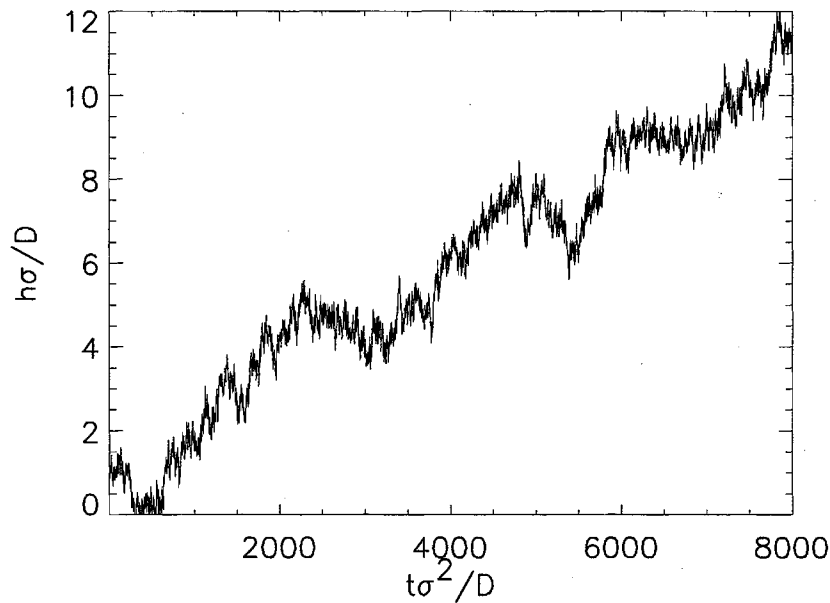


FIG. 31. The nondimensional thickness of sediments  $h\sigma/D$  in a sedimentary basin is given as a function of nondimensional time  $t\sigma^2/D$  for a sequence in which the ratio of the standard deviation to the mean of sedimentation,  $\sigma/\bar{\eta}$ , is 0.1.

of stratigraphic hiatuses that is consistent with this interpretation and that predicts a power-law dependence of sedimentation rate on time span. Tipper (1983), Strauss and Sadler (1989), and Sadler and Strauss (1990) have addressed the issue of stratigraphic completeness with the random-walk model of sedimentation. The random-walk model predicts a power-law dependence of sedimentation rate on time with exponent  $-\frac{1}{2}$ :  $R \propto T^{-1/2}$ .

The time history of sedimentation at a point based on our model is given in Figs. 31 and 32. Figure 31 is the complete history of deposition and erosion at a point in the basin. The time series of deposition and erosion is represented by a fractional Brownian motion with power spectrum  $S(f) \propto f^{-3/2}$ . This fractional Brownian motion represents the elevation of total height of sediment deposited locally in a fluvial sedimentary basin, superimposed on a constant rate of subsidence. The time series is scale invariant in terms of the nondimensional sedimentary thickness,  $h\sigma/D$ , and time,  $t\sigma^2/D$ ; it is characterized by the single parameter  $\sigma/\bar{\eta}$ . If  $\sigma/\bar{\eta}$  is small the fluctuations in sedimentation rate are small compared to the subsidence rate; if  $\sigma/\bar{\eta}$  is large the fluctuations are large. For the example given in Fig. 31,  $\sigma/\bar{\eta} = 0.1$ . Figure 32 is produced from Fig. 31 by removing any deposited sediment that is subsequently eroded. In the "staircase" plot of Fig. 32, beds are defined as a time interval of continuous deposition, i.e., a series of consecutive time steps with increasing

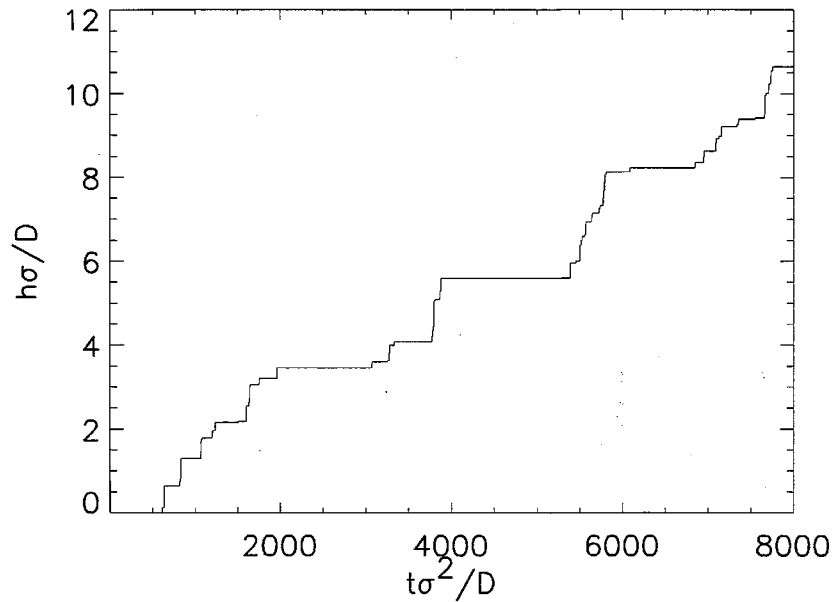


FIG. 32. For the model given in Fig. 31 the age of the sediments is given as a function of depth. Only those sediments which are not later eroded are preserved.

elevations. Hiatuses are defined as periods in which no sediment is preserved, i.e., a series of consecutive time steps with the same elevation.

We will next discuss the relationship between sedimentation rate and time span with the stratigraphic model of Plotnick (1986) based on a deterministic fractal distribution of hiatus lengths. The age of sediments in this model is given as a function of depth in Fig. 33a. As illustrated, the vertical segments (beds) are of equal thickness. The positions of the transitions from beds to hiatuses are given by a second-order Cantor set. Eight kilometers of sediments have been deposited in this model sedimentary basin in a period of 9 Myr so that the mean rate of deposition is  $R(9 \text{ Myr}) = 8 \text{ km}/9 \text{ Myr} = 0.89 \text{ mm/yr}$  over this period. However, there is a major unconformity at a depth of 4 km. The sediments immediately above this unconformity have an age of 3 Ma and the sediments immediately below it have an age of 6 Ma. There are no sediments in the sedimentary pile with ages between 3 and 6 Ma. In terms of the Cantor set, this is illustrated in Fig. 33b. The line of unit length is divided into three parts and the middle third, representing the period without deposition, is removed. The two remaining parts are placed on top of each other as shown.

During the first three million years of deposition (the lower half of the sedimentary section) the mean rates of deposition are  $R(3 \text{ Myr}) = 4 \text{ km}/3 \text{ Myr} = 1.33 \text{ mm/yr}$ . Thus the rate of deposition increases as the period considered decreases. This is shown in Figure 33c.

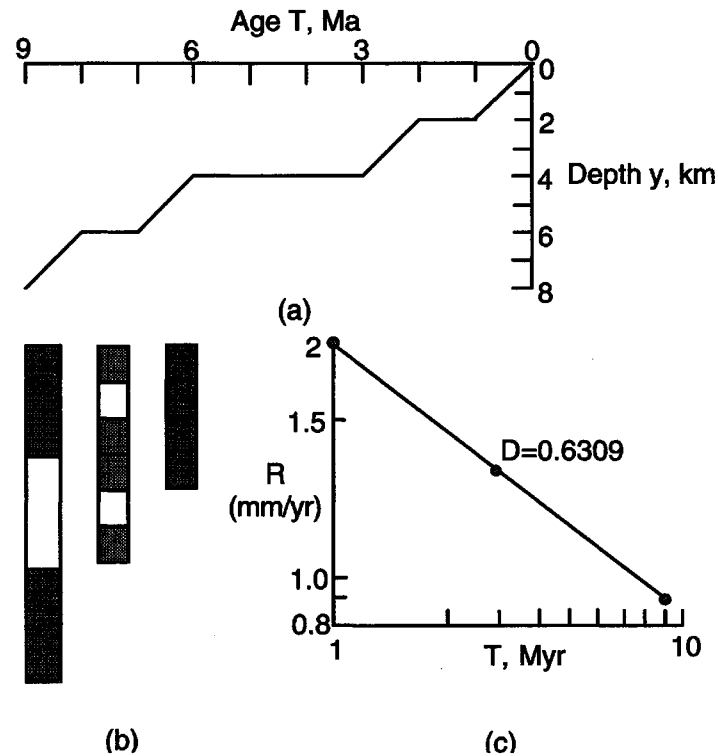


FIG. 33. Illustration of a model for sediment deposition based on a devil's staircase associated with a second-order Cantor set. (a) Age of sediments  $T$  as a function of depth  $y$ . (b) Illustration of how the Cantor set is used to construct the sedimentary pile. (c) Average rate of deposition  $R$  as a function of the period  $T$  considered.

There is also an unconformity at a depth of two kilometers. The sediments immediately above this unconformity have an age of 1 Ma and sediments below have an age of 2 Ma. Similarly, there is an unconformity at a depth of 6 km; the sediments above this unconformity have an age of 7 Ma and sediments below have an age of 8 Ma. There are no sediments in the pile with ages between 8 and 7 Ma or between 2 and 1 Ma. This is clearly illustrated in Fig. 33a. In terms of the Cantor set, Fig. 33b, the two remaining line segments of length  $1/3$  are each divided into three parts and the middle thirds are removed. The four remaining segments of length  $1/9$  are placed on top of each other as shown. During the periods 9 to 8, 7 to 6, 3 to 2, and 1 to 0 Myr, the rates of deposition are  $R(1 \text{ Myr}) = 2 \text{ km}/1 \text{ Myr} = 2 \text{ mm/yr}$ . This rate is also included in Figure 33c.

The rate of deposition clearly has a power-law dependence with respect to the length of the time interval considered. The results illustrated in Fig. 33 are based on a second-order Cantor set but the construction can be extended to any order desired and the power-law results given in Fig. 33c would be extended to shorter and shorter time intervals.

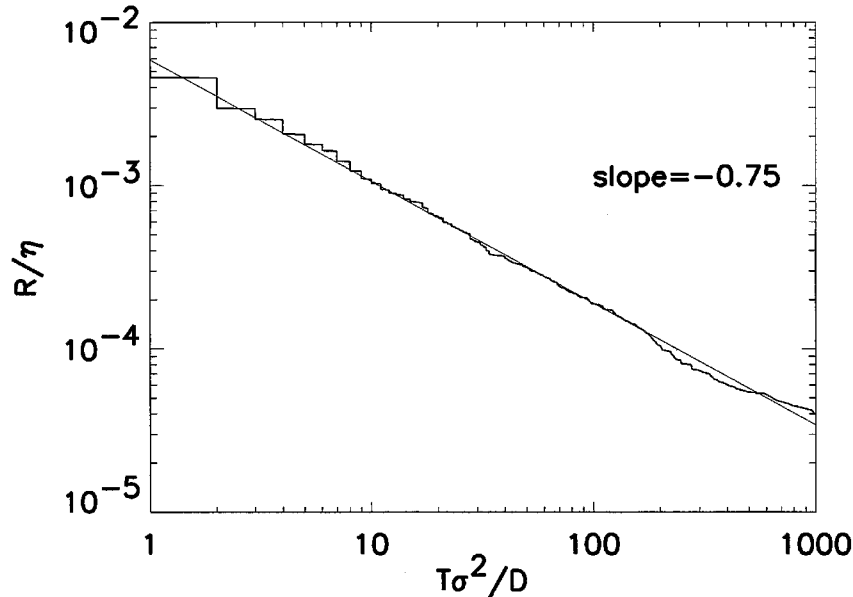


FIG. 34. Average rate of sedimentation,  $R/\bar{\eta}$ , as a function of time span,  $T\sigma^2/D$ , for the sediment column of Fig. 32.

The sedimentation rate has been calculated in this way based on the sedimentation history of Fig. 32. The results are plotted in Fig. 34 on a logarithmic scale. The sedimentation rate has a power-law dependence on time span with exponent  $-3/4$ :  $R \propto T^{-3/4}$ . Sadler and Strauss (1990) have shown that the random-walk model results in a power-law relationship with exponent  $-1/2$ . Our result is a better fit to the data of Sadler (1981), who has compiled measurements of fluvial sedimentation rates from the geological literature for time scales of minutes to 100 million years. His data are plotted in Fig. 35, where they are averaged in bin sizes with an equal spacing on a logarithmic scale. In this plot we have not included the data on time scales from  $10^5$  to  $10^8$  years since these time scales include unconformities resulting from regressive and transgressive events on active margins. Variations in sea level are beyond the scope of the model and it would be inappropriate to compare the model to sedimentation rates on those time scales. A least-squares linear fit to the log-log plot yields a slope of  $-0.76$ . This result differs from the original exponent of  $-0.65$  quoted by Sadler (1981) since we have averaged the data in logarithmically spaced bins so that each portion of the data has equal weight in the least-squares fit. An exponent of  $-0.76$  is consistent with the stochastic diffusion model result given in Fig. 34.

These results can also be obtained from theoretical fractal relations. Fractional Brownian motions have the property that the standard deviation of the time series has a power-law dependence on time with a

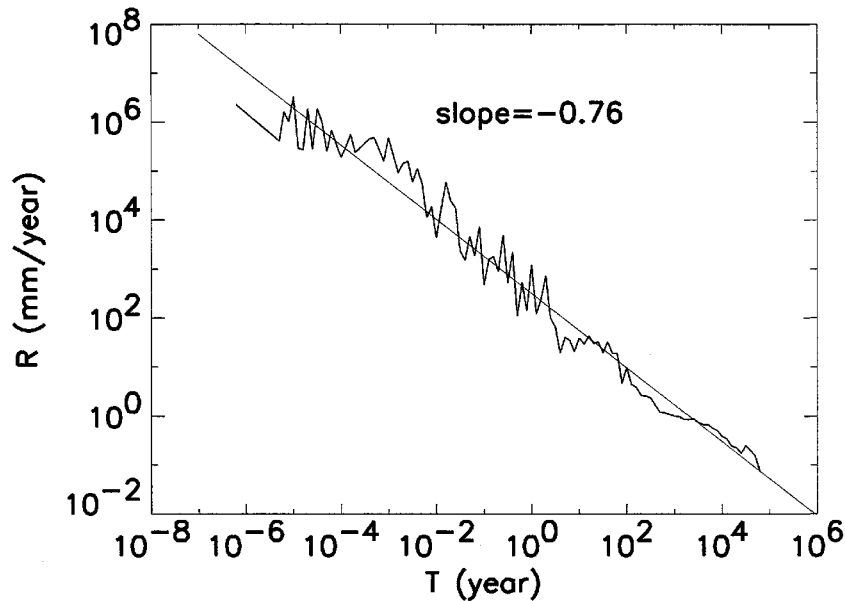


FIG. 35. Observed sedimentation rates as a function of time span from the data of Sadler (1995). The data have been binned in equally spaced bins in log space. A least-squares linear fit to the logarithms of the data yields a slope of  $-\frac{3}{4}$ , indicating that  $R \propto T^{-3/4}$ .

fractional exponent  $Ha$ , the Hausdorff measure:  $\sigma \propto T^{Ha}$  as given by MT, Eq. 20. The rate of change of the time series for a given time interval,  $T$ , is then the sedimentation rate  $R = \sigma/T \propto T^{Ha-1}$ . The power-spectral exponent of a time series and its Hausdorff measure are related by  $\beta = 2Ha + 1$  (MT, Eq. 62). For the random-walk model,  $\beta = 2$ ,  $Ha = 1/2$ , and the sedimentation rate is then  $R \propto T^{-1/2}$ . For the stochastic diffusion model,  $\beta = 3/2$ ,  $Ha = 1/4$ , and  $R \propto T^{-3/4}$ , in agreement with the numerical results.

The dependence of sedimentation rate on time span continues up to time scales of the Wilson cycle. On time scales of  $10^5$ – $10^8$  years, transgressive and regressive events give rise to alternating periods of deposition and erosion as mentioned previously. Korvin (1992) found, using the SEDPAK simulation package, that alternating periods of deposition and erosion resulting from sea-level change, combined with the diffusive parameterization of sediment transport of SEDPAK, resulted in a decreasing sedimentation rate with increasing time span in the same way that channel avulsion and diffusive sediment transport results in episodic sedimentation rates on smaller time scales.

### 3.5. Bed Thicknesses

Working from our preserved-thickness history of Fig. 32, we will define a bed as any consecutive sequence of time units at different depths. Con-

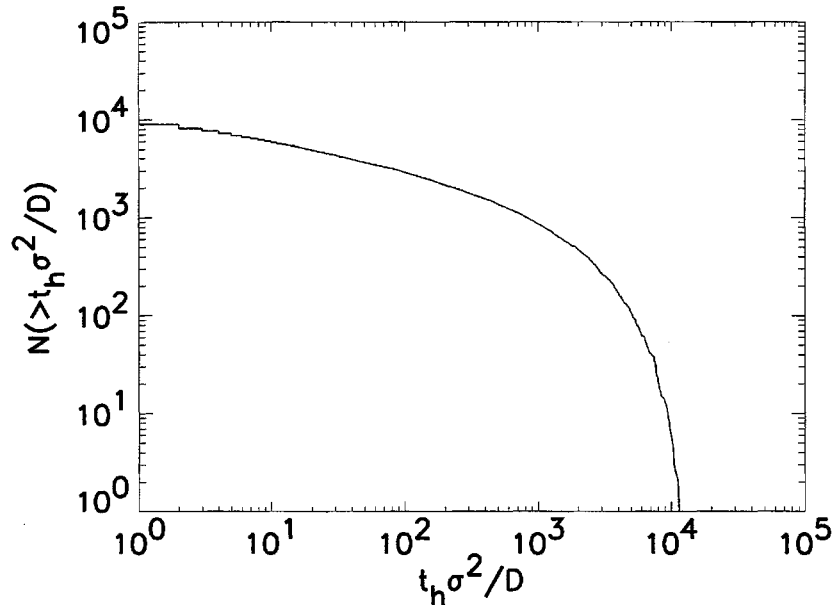


FIG. 36. Cumulative frequency-length distribution of hiatuses, the number of hiatuses longer than nondimensional hiatus length  $t_h \sigma^2/D$ , for synthetic sequences produced with the stochastic diffusion model.

versely, a hiatus is any consecutive sequence of time units with the same depth. In this section we will present bed-thickness and hiatus-length distributions and compare them with observations and with other models.

Plotnick (1986) presented the model for discontinuous sedimentation based on a fractal distribution of hiatus lengths illustrated in Fig. 33. The cumulative distribution of hiatus lengths, the number of hiatuses greater than or equal to a length of time,  $T$ , produced by our model is plotted in Fig. 36. In order to obtain an accurate curve, we generated 100 synthetic preserved-thickness histories and accumulated the hiatus distributions in order to obtain Fig. 36. The distribution is not fractal. This was at first surprising since a fractal distribution of hiatuses was used to illustrate how a power-law dependence of sedimentation rate on time span can occur. However, in the model of Fig. 33 each bed had the same thickness. In contrast, as we will show, the stochastic diffusion model of sedimentation results in bed thicknesses with an exponential distribution. Therefore, our observation of a scale-invariant sedimentation rate without a scale-invariant distribution of hiatuses is not inconsistent with the model of Fig. 33 since they result in different bed-thickness distributions.

The cumulative distribution of bed thicknesses generated by our model is plotted in Fig. 37 for the four different values of  $\sigma/\bar{\eta}$  indicated next to each distribution. For synthetic depositional histories with a relatively large  $\sigma/\bar{\eta}$ , such as 0.1, no deposition occurs during most of the history.

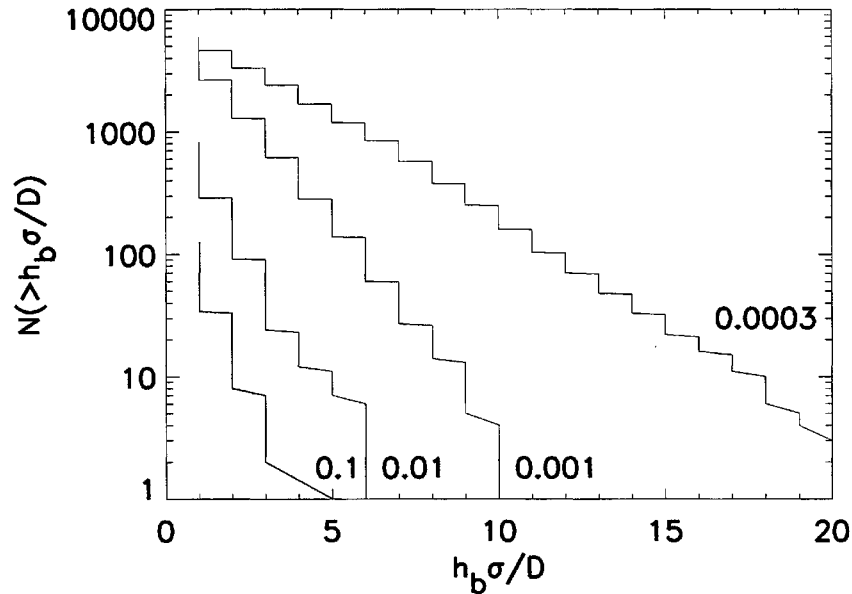


FIG. 37. Cumulative frequency–thickness distribution of nondimensional bed thicknesses for synthetic sediment columns with  $\sigma/\bar{\eta} = 0.1, 0.01, 0.001,$  and  $0.0003$ . The distributions are exponential.

The result is a small number of beds with a very skewed distribution. For smaller ratios, more thick beds appear in the record. The straight-line trends of the distributions on a log-linear axis indicate that the cumulative bed-thickness distributions are exponential. The noncumulative distribution is also exponential since the cumulative distribution is the integral of the noncumulative distribution. Exponential bed-thickness distributions are common in stochastic models of sedimentation (Dacey, 1979). Despite reported conclusions that stochastic models of sedimentation, including those that generate exponential bed-thickness distributions, accurately predict observed bed-thickness distributions (Mizutani and Hattori, 1972), we are not aware of any model which predicts the commonly observed log-normal distribution. This may not be a fundamental weakness of the bed formation models that have been proposed to date. Another possibility has been suggested by Drummond and Wilkinson (1996). They have argued that the observation of log-normal distributions is an artifact resulting from unrecognized or unrecorded small strata. They propose that exponential distributions are consistent with the data if the data for the frequencies of the smallest strata are considered incomplete and not considered in the distribution fitting. This is consistent with the conclusion of Muto (1995) who has presented the cumulative frequency–thickness distribution of four large turbidite data sets from Japan. He found that an exponential distribution best fit the data. However, power-law distributions

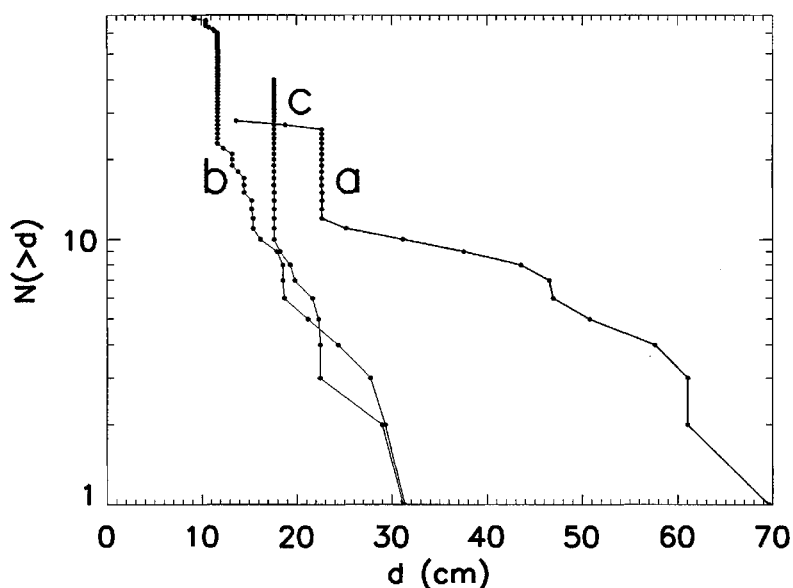


FIG. 38. Cumulative frequency–thickness distribution of bed thicknesses of deep-sea sequences from (a) Ra Stua, (b) Castagne, and (c) Cismon Valley, Italy published in Claps and Masetti (1994). The coefficients in the exponential distributions determined by a least-squares fit of the logarithm of the bed number to the bed thickness for the largest forty beds were  $-0.052$ ,  $-0.166$ , and  $-0.252$ , showing an increasing trend with sedimentation rate consistent with the model behavior.

have also been persuasively argued for the distribution of turbidite beds (Rothman *et al.*, 1993).

In Fig. 37, synthetic sedimentation histories with larger values of sedimentation rate,  $\sigma/\bar{\eta}$ , have a more skewed distribution or a steeper slope on a log-linear scale. This is consistent with the dependence of skew on sedimentation rate observed in deep-sea sequences in Italy by Claps and Masetti (1994). These authors published bed-thickness data from three formations in Italy: Ra Stua, Castagne, and Cismon Valley. The sedimentation rates for a 1-Ma time scale have been estimated to be 2.5, 1.7, and 0.6 cm/kyr, respectively, for these sections. In Fig. 37 we found that basins which filled slowly had bed-thickness distributions that were more skewed than those in basins which filled more quickly. The cumulative bed-thickness distributions for these sections based on data that were digitally scanned from Claps and Masetti (1994) are presented in Fig. 38. The model prediction that the skew of the bed-thickness distributions increases from the (a) Ra Stua section to the (b) Castagne and (c) Cismon Valley sections is consistent with the data.

#### 4. VARIABILITY OF THE EARTH'S MAGNETIC FIELD

##### 4.1. Variations of the Dipole Moment

As our third and final example we consider the time series of the Earth's magnetic field. Paleomagnetic studies show clearly that the polarity of the magnetic field has been subject to reversals. Kono (1971) has compiled paleointensity measurements of the magnetic field from volcanic lavas for 0–10 Ma. He concluded that the distribution of paleointensity is well approximated by a symmetric binormal distribution with mean  $8.9 \times 10^{22} \text{ Am}^2$  and standard deviation  $3.4 \times 10^{22} \text{ A} \cdot \text{m}^2$ . One normal distribution is applicable to the field when it is in its normal polarity and the other is applicable when it is in its reversed polarity.

We have utilized three data sets for computing the power spectrum of the dipole moment of the Earth's magnetic field. They are archeomagnetic data for time scales of 100 yr to 8 kyr from Kovacheva (1980), marine sediment data from the Somali basin for time scales of 1 kyr to 140 kyr from Meynadier *et al.* (1992), and marine sediment data from the Pacific and Indian Oceans from time scales of 20 kyr to 4 Myr from Meynadier *et al.* (1994). The data were published in table form in Kovacheva (1980) and obtained from L. Meynadier (personal communication, 1995) for the marine sediment data in Meynadier *et al.* (1992) and Meynadier *et al.* (1994). Marine sediment data are accurate measures of relative paleointensity but give no information on absolute intensity. In order to calibrate marine sediment data, the data must be compared to absolute paleointensity measurements from volcanic lavas sampled from the same time period as the sedimentary record. Meynadier *et al.* (1994) have done this for the composite Pacific and Indian Ocean data set. They have calibrated the mean paleointensity in terms of the virtual axial dipole moment for 0–4 Ma as  $9 \times 10^{22} \text{ A} \cdot \text{m}^2$  (Valet and Meynadier, 1993). This value is consistent with that obtained by Kono (1971) for the longer time interval up to 10 Ma. Using this calibration, we calibrated the Somali data with the time interval 0–140 ka from the composite Pacific and Indian Ocean data set. The data from Meynadier *et al.* (1994) are plotted in Fig. 39 as a function of age in Ma. The last reversal at approximately 730 ka is clearly shown. We obtained the power spectrum of each of the time series using the Lomb periodogram (Press *et al.*, 1992). The resulting spectra are given in Fig. 40. The composite sediment record from the Pacific and Indian Oceans is plotted up to the frequency  $1/(25 \text{ kyr})$ . Above this time scale good synchronicity is observed in the Pacific and Indian Ocean data sets (Meynadier *et al.*, 1994). This suggests that nongeomagnetic effects such as variable sedimentation rate are not significant in these cores above this

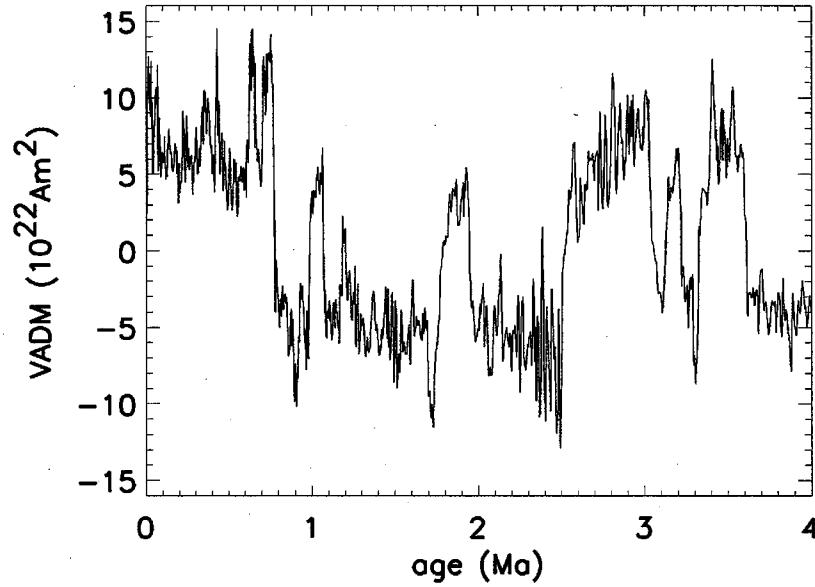


FIG. 39. Paleointensity of the virtual axial dipole moment (VADM) of the Earth's magnetic field (with reversed polarity data given by negative values) inferred from sediment cores for the past 4 Ma from Meynadier *et al.* (1994).

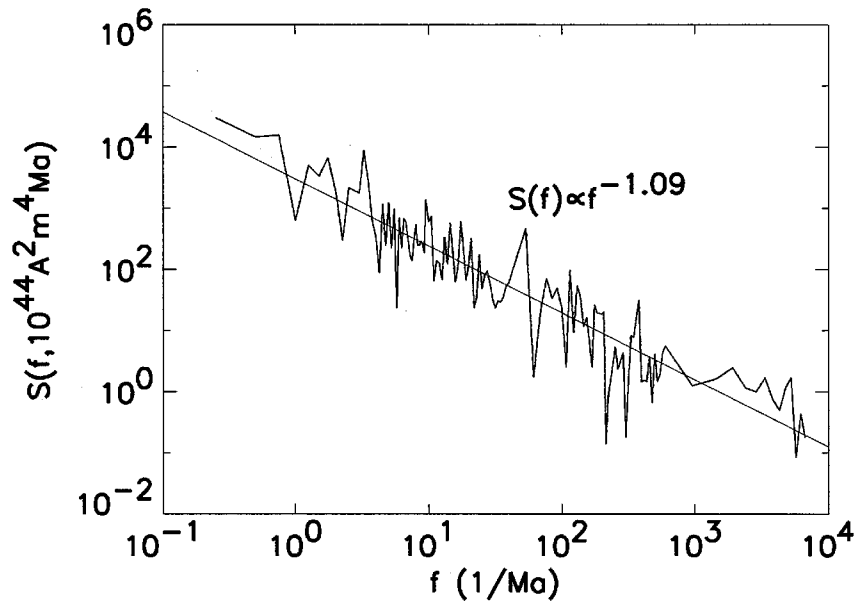


FIG. 40. Power-spectral density of the geomagnetic field intensity variations estimated from the Lomb periodogram of sediment cores from Meynadier *et al.* (1992) and Meynadier *et al.* (1994) and archeomagnetic data from Kovacheva (1980). The power-spectral density  $S$  is given as a function of frequency  $f$  for time scales of 100 yr to 4 Myr.

time scale. From frequencies of  $1/(25 \text{ kyr})$  to  $1/(1.6 \text{ kyr})$  we plot the power spectrum of the Somali data. For time scales of 1.6 kyr to the highest frequency we plot the power spectrum of the data of Kovacheva (1980). A least-squares linear regression to the data yields a slope of  $-1.09$  over 4.5 orders of magnitude. This indicates that the power spectrum is well approximated as  $1/f$  on these time scales.

The power spectrum of secular geomagnetic intensity variations has been determined to have a  $1/f^2$  power spectrum between time scales of 1 and 100 years (Currie, 1968; Barton, 1982; Courtillot and Le Mouel, 1988). This is consistent with the analysis of McLeod (1992), who found that the first difference of the annual means of geomagnetic field intensity is a white noise since the first difference of a random process with power spectrum  $1/f^2$  is a white noise. Our observation of  $1/f$  power-spectral behavior above time scales of approximately 100 years together with the results of Currie (1968) and Barton (1982) suggests that there is a crossover from  $1/f$  to  $1/f^2$  spectral behavior at a time scale of approximately 100 years.

#### 4.2. Reversal Record

We will now show that the statistics of the reversal record are consistent with those of a binormal  $1/f$  noise paleointensity record which reverses each time the intensity crosses the zero value. We will compare the polarity length distribution and the clustering of reversals between synthetic reversals produced with  $1/f$  noise intensity variations and the reversal history according to Harland *et al.* (1990) and Cande and Kent (1992a, 1995).

First we consider the polarity length distribution of the real reversal history. The polarity length distribution calculated from the chronology of Harland *et al.* (1990) is given as the solid line in Fig. 41. The polarity length distribution is the number of interval lengths longer than the length plotted on the horizontal axis. A reassessment of the magnetic anomaly data has been obtained by Cande and Kent (1992a, 1995). The polarity length distribution of their time scale normalized to the same length as the Harland *et al.* (1990) time scale, is presented as the dashed curve in Fig. 41. The two distributions are nearly identical. These plots suggest that the polarity length distribution is better fit by a power law for large polarity lengths than by an exponential distribution, as first suggested by Cox (1968). The same conclusion has been reached by Gaffin (1989) and Seki and Ito (1993).

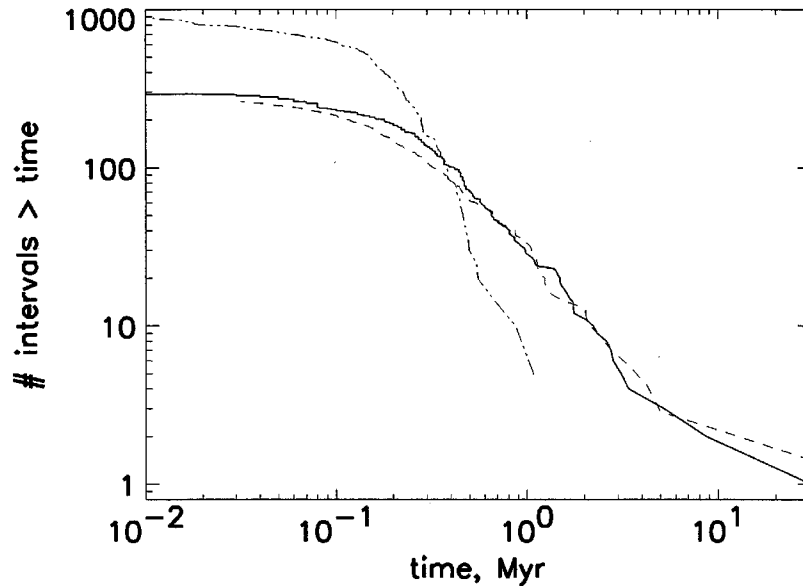


FIG. 41. Cumulative frequency-length distribution of the lengths of polarity intervals from the time scale of Harland *et al.* (1990) (solid curve), Cande and Kent (1992a, 1995) (dashed curve), and the Cande and Kent (1992a, 1995) time scale from C1 to C13 with cryptochrons included (dashed-dotted line).

The third curve, plotted with a dashed-dotted line, represents the polarity length distribution estimated from the magnetic time scale between C1 and C13 with “cryptochrons” included and scaled to the length of the Harland *et al.* (1990) time scale. Cryptochrons are small variations recorded in the magnetic anomaly data that may either represent variations in paleomagnetic intensity or short reversals (Blakely, 1974; Cande and Kent, 1992b). Cryptochrons occur with a time scale at the limit of temporal resolution of the reversal record from magnetic anomalies of the sea floor. The form of the polarity length distribution estimated from the record between C1 and C13 including cryptochrons is not representative of the entire reversal history because of the variable reversal rate which concentrates many short polarity intervals in this time period. However, this distribution enables us to estimate the temporal resolution of the reversal-record history. The distribution estimated from C1 to C13 has many more short polarity intervals than those of the full reversal history starting at a reversal length of 0.3 Myr. Above a time scale of 0.3 Myr the magnetic time scale is nearly complete. Below it many short polarity intervals may be unrecorded.

To show that this distribution is consistent with binormal  $1/f$  noise intensity variations, we have generated synthetic Gaussian noises with a power spectrum proportional to  $1/f$ , a mean value of  $8.9 \times 10^{22} \text{ A} \cdot \text{m}^2$ , and a standard deviation of  $3.4 \times 10^{22} \text{ A} \cdot \text{m}^2$  as obtained by Kono (1971),

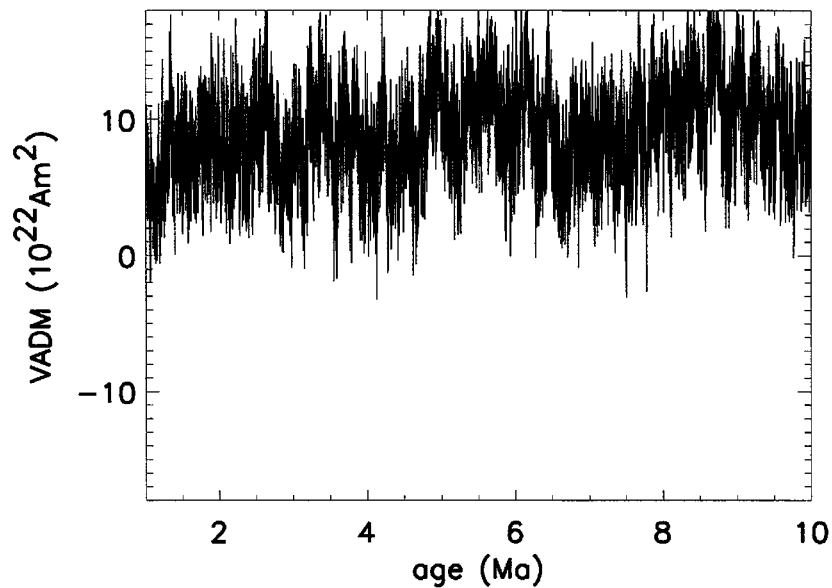


FIG. 42. A  $1/f$  noise with a normal distribution with mean of 8.9 and standard deviation of  $3.4 \times 10^{22} \text{ Am}^2$  representing the geomagnetic field intensity in one polarity state.

representative of the field intensity in one polarity state. These synthetic noises were generated using the Fourier-domain filtering technique discussed in MT, Section 3.2. An example is shown as Fig. 42. In order to construct a binormal intensity distribution from the synthetic normal distribution, we inverted every other polarity interval to the opposite polarity starting from its minimum value below the zero intensity axis and extending to its next minimum below the zero. The result of this procedure on the Gaussian,  $1/f$  noise of Fig. 42 is presented in Fig. 43. Its irregular polarity lengths are similar to those in the marine sediment data of Fig. 39.

The operation of reversing the paleomagnetic intensity when it crosses the zero intensity value is consistent with models of the geodynamo as a system with two symmetric attracting states of positive and negative polarity such as the Rikitake disk dynamo. Between reversals, the geomagnetic field fluctuates until a fluctuation large enough to cross the energy barrier into the other basin of attraction occurs. Kono (1987) has explored the statistical similarity between the Rikitake disk dynamo and the distribution of paleointensity. Our construction of the binormal  $1/f$  noise is consistent with his model.

We have computed the distributions of lengths between successive reversals for twenty synthetic noises scaled to length 169 Ma, the length of the reversal chronology, and have averaged the results in terms of the number of reversals. The results are plotted as the solid curve along with the Harland *et al.* (1990) time scale (dashed curve) in Fig. 44. The dots in

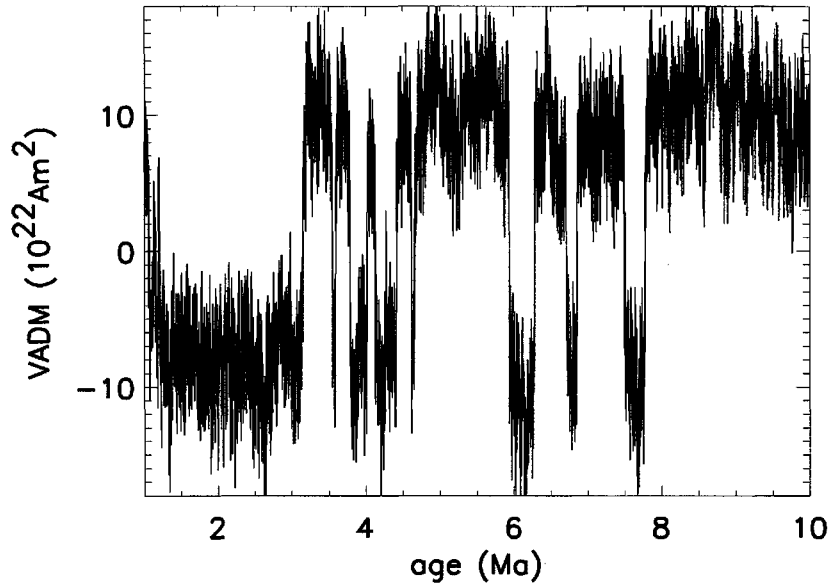


FIG. 43. Binormal  $1/f$  noise constructed from the normal  $1/f$  noise of Fig. 42 as described in the text.

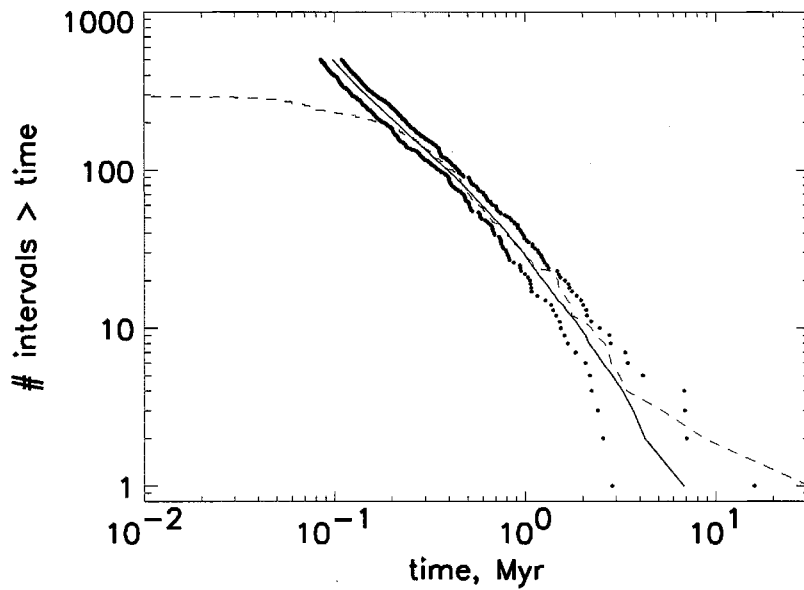


FIG. 44. Cumulative frequency-length polarity interval distributions from the Harland *et al.* (1990) time scale and that of the binormal  $1/f$  noise model of intensity variations. The distribution from the Harland *et al.* (1990) time scale is the dashed curve. The solid line is the average cumulative distribution from the  $1/f$  noise model. The dotted lines represent the minimum and maximum reversal-length distributions for 20 numerical experiments, thereby representing 95% confidence intervals.

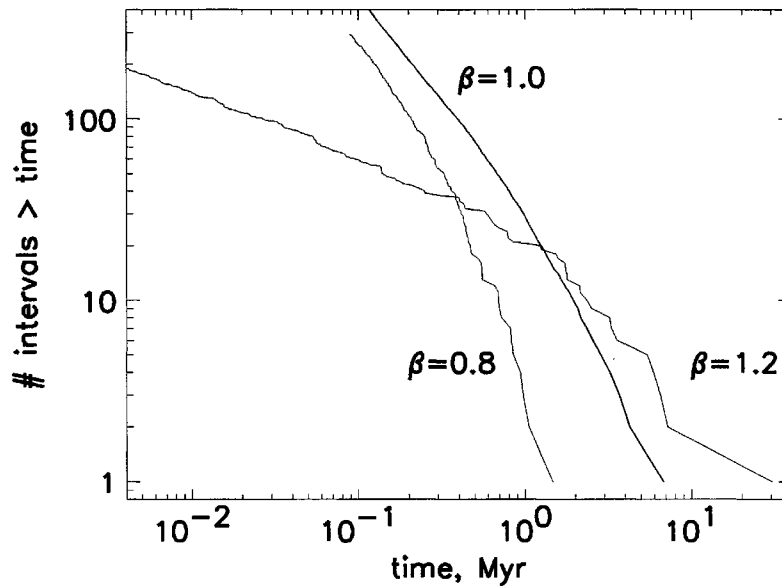


FIG. 45. Cumulative frequency-length polarity interval distributions for the  $1/f$  noise model of intensity variations (shown in the middle, the same as that in Fig. 44) and for intensity variations with power spectra proportional to  $f^{-0.8}$  and  $f^{-1.2}$ . This plot illustrates that the polarity length distribution is very sensitive to the form of the power spectrum, allowing us to conclude that the agreement between the model and the observed distribution in Fig. 43 is unique to  $1/f$  noise intensity variations.

Fig. 44 are the maximum and minimum values obtained in the twenty synthetic reversal chronologies for each reversal rank, thus representing 95% confidence intervals. The shape of the synthetic polarity length distribution is very similar to the Harland *et al.* (1990) time scale. The synthetic polarity length distribution matches the Harland *et al.* (1990) time scale within the 95% confidence interval over all time scales plotted except for the Cretaceous superchron, which lies slightly outside of the 95% confidence interval, and reversals separated by less than about 0.3 Myr. The overprediction of very short reversals could be a limitation of the model or a result of the incompleteness of the reversal record for short polarity intervals. As mentioned, the temporal resolution of the magnetic time scale inferred from magnetic anomalies is approximately 0.3 Myr. We conclude that the polarity length distribution produced from binormal  $1/f$  intensity variations is consistent with the observed polarity length distribution for all time scales for which the reversal record is complete.

We next consider whether the agreement illustrated in Fig. 44 is unique to  $1/f$  noise. We have computed polarity length distributions using binormal intensity variations with power spectra  $f^{-0.8}$  and  $f^{-1.2}$ . These results, along with the  $1/f$  result from Fig. 44, are given in Fig. 45. The shape of the polarity length distribution is very sensitive to the exponent of the

power spectrum. A slight increase in the magnitude of the exponent results in many more long polarity intervals than with  $1/f$  noise. We conclude that the agreement in Fig. 44 between the synthetic reversal distribution and the true reversal history is unique to  $1/f$  noise and provides strong evidence that the dipole moment has  $1/f$  behavior up to time scales of 170 Myr.

A binormal,  $1/f$  noise geomagnetic field variation is consistent with the qualitative results of Pal and Roberts (1988), who found an anticorrelation between reversal frequency and paleointensity. This anticorrelation is evident in the synthetic  $1/f$  noise of Fig. 43. During the time intervals of greatest average paleointensity the reversal rate is lowest.

In addition to the broad distribution of polarity lengths, the reversal history is also characterized by a clustering of reversals. This behavior has been quantified with the reversal rate. The reversal rate has been relatively high from 0–20 Ma and has decreased gradually going back in history to the Cretaceous superchron. An alternative approach to quantifying the clustering of reversals is with the pair-correlation function. The pair-correlation function  $C(t)$  is the number of pairs of reversals whose separation is between  $t$  and  $t + \Delta t$ , per unit time (Vicsek, 1992). The pair-correlation function for a set of points can be compared to that for a Poisson process to detect nonrandom clustering. The pair-correlation function analysis is more appropriate for comparison of the reversal history to the synthetic reversal history generated by a stochastic model since a stochastic model cannot predict behavior in time, such as when the reversal rate is large or small. However, a stochastic model may accurately reflect the extent to which small polarity intervals are followed by small polarity intervals and long intervals by long intervals as quantified with the pair-correlation function.

The pair-correlation function of reversals according to the Harland *et al.* (1990) and Cande and Kent (1992a, 1995) reversal histories is shown in Fig. 46 as filled and unfilled circles, respectively. Also presented in Fig. 46 is the pair-correlation function for a synthetic reversal data set based on binormal  $1/f$  noise dipole moment variations (boxes) and for a Poisson process (triangles). The functions are offset so that they may be placed on the same graph. The Poisson process was constructed with 293 points, the same number of reversals as the Harland *et al.* (1990) time scale, positioned with uniform probability on the interval between 0 and 170 Ma. The Poisson process yields a correlation function independent of  $t$ . The real and synthetic reversal histories variations exhibit significant clustering with more pairs of points at small separation and fewer at large separations than for a Poisson process. Straight-line fits of the form  $C(t) \propto t^{-\alpha}$  were obtained. The purpose of this was to show that similar

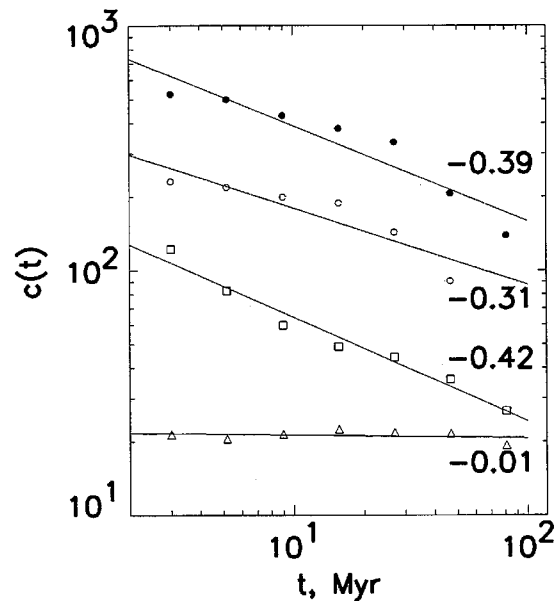


FIG. 46. Pair-correlation function of the reversal history according to the Harland *et al.* (1990) time scale (filled circles), Cande and Kent (1992a, 1995) (open circles), synthetic reversals produced from  $1/f$  noise model of intensity variations (boxes), and a Poisson process (triangles). The real and synthetic reversals exhibit similar nonrandom clustering. The data sets are offset.

clustering is observed in the real and synthetic reversals. The exponents of the Harland *et al.* (1990), Cande and Kent (1992a, 1995), and synthetic reversals are  $-0.39$ ,  $-0.31$ , and  $-0.42$ , respectively, indicating close agreement between the model and real reversals.

#### 4.3. Inclination and Declination Data

Power-spectral analyses of inclination and declination data have also been carried out. We obtained time-series data for inclination and declination from lake sediment cores in the Global Paleomagnetic Database (Lock and McElhinney, 1992). The core with the greatest number of data points was from Lac du Bouchet (Thouveny *et al.*, 1990). The inclination data from this data set are plotted in Fig. 47. The power spectra of the inclination and declination at Lac du Bouchet estimated with the Lomb Periodogram are presented in Fig. 48. We associate the spectra with a flat spectrum below a frequency of  $f \approx 1/(3 \text{ kyr})$  and a constant spectrum above a frequency of  $f \approx 1/(500 \text{ yr})$ . From frequencies of  $f \approx 1/(3 \text{ kyr})$  to  $f \approx 1/(500 \text{ yr})$  the inclination and declination are Brownian motions with  $S(f) \propto f^{-2}$ . Spectral analyses of inclination data from five other sediment cores were calculated. These spectra are presented in Fig. 49. The spectra

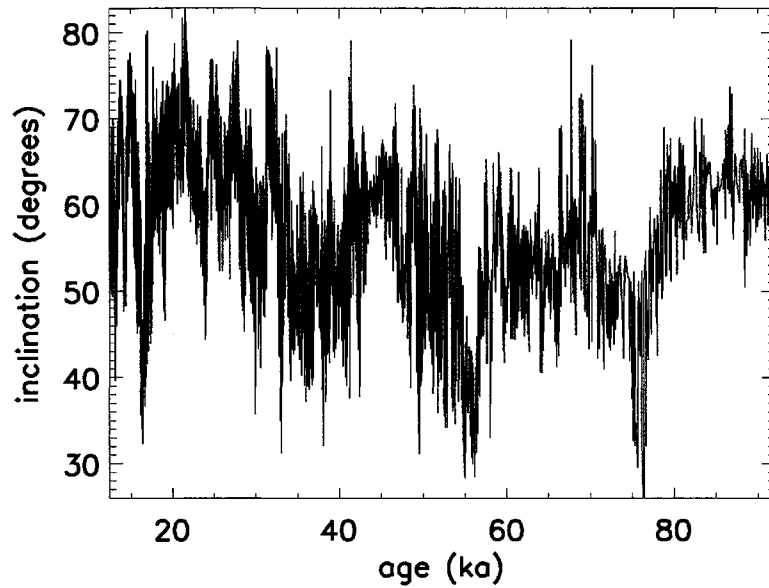


FIG. 47. Magnetic field inclination inferred from the Lac du Bouchet sediment core (Thouveny *et al.*, 1990).

correspond, from top to bottom, to cores from Anderson Pond (Lund and Banerjee, 1985), Bessette Creek (Turner *et al.*, 1982), Fish Lake (Verosub *et al.*, 1986), Lake Bullenmerri (Turner and Thompson, 1981), and Lake Keilambete (Barton and McElhinny, 1981). Since the data sets have fewer points, there is more uncertainty in the spectra and they are characterized

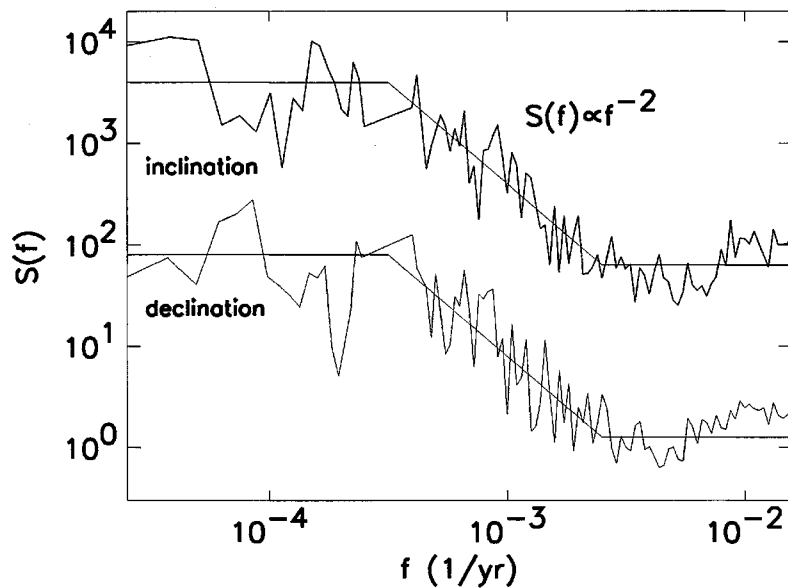


FIG. 48. Power spectra of inclination and declination from the Lac du Bouchet sediment core. The declination spectrum is offset from the inclination spectrum so that they may be placed on the same graph.

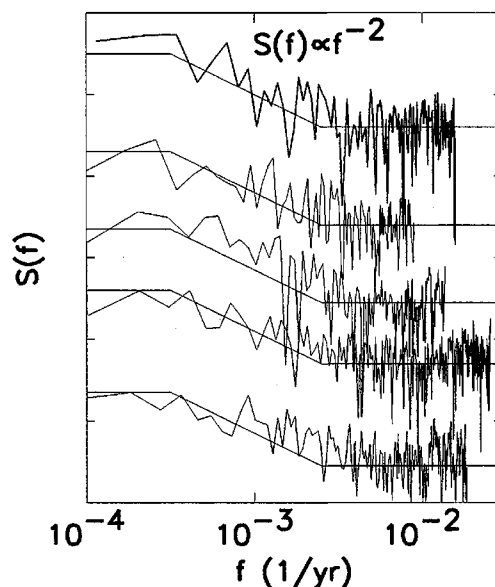


FIG. 49. Power spectra of inclination from the following locations, top to bottom: (1) Anderson Pond, (2) Bessette Creek, (3) Fish Lake, (4) Lake Bullenmerri, and (5) Lake Keilambete. The spectra are offset to place them on the same graph.

by greater variability between adjacent frequencies. The spectra have the same form, within the uncertainty of the spectra, as that associated with the spectra from Lac du Bouchet. These results suggest that 3 kyr and 500 yr are characteristic time scales of geodynamo behavior. Variations in inclination and declination are associated with changes in the nondipole components of the field. Therefore, the autocorrelation or decay time of the quadrupole moment is the maximum time scale for correlated fluctuations of inclination and declination to occur. The autocorrelation time of the quadrupole moment has been estimated by McLeod (1996) to be 1.6 kyr. This is within a factor of 2 of the 3-kyr time scale above which variations in inclination and declination are observed to be uncorrelated in the spectra of Figs. 48 and 49.

Many analyses of variations in paleointensity of the Earth's magnetic field concentrate on identifying characteristic time scales of variation. Many such characteristic time scales have been identified. Valet and Meynadier (1993) suggested, based on the same sediment core data analyzed in this paper, that the Earth's magnetic field regenerates following a reversal on a time scale of a few thousand years and then decays slowly on a time scale of 0.5 Myr before the next reversal. They termed this an "asymmetric saw-tooth" pattern. More recent data have shown that the "asymmetric saw-tooth" is not a robust pattern. Longer cores show a slow

decay preceding a reversal to be rare (Tauxe and Hartl, 1997). Moreover, Laj *et al.* (1996) have shown that the magnetic field does not always regenerate quickly after a reversal. Thibal *et al.* (1995) have quantified the rate of decrease in field intensity preceding a reversal and found it to be inversely proportional to the length of the polarity interval. The authors concluded from this that the length of the reversal was predetermined. Such behavior is not indicative of a predetermined polarity length. This can be concluded by considering the null hypothesis that variations in the field are characterized by any stationary random process. By definition, a stationary time series has a variance which is independent of the length of the series. The average rate of change of the time series over a time interval will then be a constant value divided by the interval of time, i.e., inversely proportional to time interval. Therefore, any stationary random function satisfies the relationship that Thibal *et al.* (1995) observed.

In the power-spectral analyses of geomagnetic variations inferred from sediment cores performed by Lund *et al.* (1988), Meynadier *et al.* (1992), Lehman *et al.* (1996), and Tauxe and Hartl (1997), dominant periodicities in the record were identified and proposed as characteristic time scales of geodynamo behavior. However, it must be emphasized that any finite length record will exhibit peaks in its power spectrum even if the underlying process is random such as a  $1/f$  noise. Periodicity tests such as those developed by Lees and Park (1995) need to be applied to data in order to assess the probability that a peak in a spectrum is statistically significant. The periodicity tests developed by Lees and Park (1995) are especially valuable because they do not depend on a particular model of the stochastic portion of the spectrum. Some of the periodicity tests that have been used in the geomagnetism literature assume forms for the stochastic portion of the spectrum that are not compatible with the  $1/f$  process we have identified. See Mann and Lees (1996) for an application of these techniques to climatic time series.

It is generally believed that secular geomagnetic variations are the result of internal dynamics while longer time-scale phenomena such as variations in the reversal rate are controlled by variations in boundary conditions at the core–mantle boundary (CMB) (McFadden and Merrill, 1995). However, our observation of continuous  $1/f$  spectral behavior for time scales of 100 yr to 170 Myr suggests that a single process controls variations in geomagnetic intensity over this range of time scales. In Section 4.4 we consider a model for geodynamo behavior which reproduces the  $1/f$  dipole moment variations over a wide range of time scales and exhibits many of the other features of geomagnetic variability we have identified.

#### 4.4. Model for Geomagnetic Variations

There has been great interest in  $1/f$  noise processes in the physics literature for many years (Weissman, 1988). One model of  $1/f$  noise is a stochastic process composed of a superposition of modes with exponential decay characterized by different time constants. The time constant for a stochastic process is defined through its autocorrelation function  $a(\tau)$ . For a stochastic process with a single time constant  $\tau_0$ , the autocorrelation function is given by  $a(\tau) = e^{-\tau/\tau_0}$ . The power spectrum of such a process is, by the Wiener–Khinchine theorem, the Fourier transform of the autocorrelation function:

$$S(f) \propto \frac{\tau_0}{1 + (2\pi f)^2}. \quad (42)$$

This is a Lorentzian spectrum with a Brownian-motion behavior ( $S(f) \propto f^{-2}$ ) for time scales small compared to  $\tau_0$  and white-noise behavior ( $S(f) = \text{constant}$ ) above the characteristic time constant. If the stochastic process is composed of a superposition of modes with time constants following a distribution  $D(\tau_0) \propto \tau_0^{-1}$ , where the  $D(\tau_0)\Delta\tau_0$  is the net variance contributed by modes between  $\tau_0$  and  $\tau_0 + \Delta\tau_0$ , then a  $1/f$  spectrum results over a range of frequencies (van der Ziel, 1950; Weissman, 1988). Such a distribution of exponential time constants has been documented for the Earth's magnetic field by McLeod (1996).

McLeod (1996) calculated the autocorrelation of each degree of the geomagnetic field during the last 80 years. The autocorrelation functions that he computed had an exponential dependence on time with degree-dependent time constants  $\tau_0 \propto n^{-2}$ . This behavior is consistent with a diffusion process. McLeod (1996) attributed this autocorrelation structure to a simple model of the geomagnetic field in which the field was stochastically generated with a balance between field regeneration and diffusive decay across a magnetic boundary layer. One way to model such a stochastic diffusion process is with a two-dimensional diffusion equation driven by random noise:

$$\frac{\partial B_z}{\partial t} = D\nabla^2 B_z + \eta(x, y, t), \quad (43)$$

where  $B_z$  is the axial component of the magnetic field at a point inside the core and  $\eta(x, y, t)$  is a Gaussian white noise representing random amplification and destruction of the field locally by dynamo action. To this

equation we add a term equal to  $c(p - B_{z,tot})$ :

$$\frac{\partial B_z}{\partial t} = D\nabla^2 B_z + \eta(x, y, t) + c(p - B_{z,tot}), \quad (44)$$

where  $c$  is a constant,  $B_{z,tot}$  is the dipole moment integrated over all space, and  $p$  is  $+1$  if the dipole moment of the field outside the core–mantle boundary is positive and  $-1$  if the dipole moment outside the core–mantle boundary is negative. The effect of this term is to create two basins of attraction (polarity states) within which the dipole field fluctuates around an intensity of  $+1$  or  $-1$  until a fluctuation large enough occurs to cross the barrier to the other basin of attraction. This term could be the result of a conservation of magnetic energy for the combination of the poloidal and toroidal fields such that when the poloidal dipole field intensity is low the toroidal field intensity, which is unobservable outside the core and not explicitly modeled in Eq. (44), is high and dynamo action is intensified, repelling the poloidal field away from a state of low dipole intensity.

In our model the core is modeled as a two-dimensional circular region of uniform diffusivity (the fluid outer core) surrounded by an infinite region with small but finite diffusivity and the boundary condition that  $B_z$  approach zero as  $r$  approaches zero, where  $r$  is the radial distance from the center of the earth. The diameter of the inner circular region is the diameter of the core–mantle boundary.

This model has been simulated by computer using finite differencing of the model equation on a two-dimensional lattice. It has been studied in terms of the distribution of values and power spectrum of the dipole moment and the power spectrum of the angular deviation from the dipole field. The dipole field from the simulation is plotted in Fig. 50. The field clearly undergoes reversals with a broad distribution of polarity interval lengths. Fig. 51 represents the dipole distribution of 10 simulations (solid curve) along with the fit to a binormal distribution (dashed curve). A binormal distribution fits the data well. The slight asymmetry is the result of this particular model run spending slightly more time in the negative polarity state than in the positive polarity state. Model outputs were generated which showed asymmetry in the other direction.

The average power spectrum of time series of the dipole field from 25 simulations is presented in Fig. 52. The spectrum has a low-frequency spectrum  $S(f) \propto f^{-1}$  and a high-frequency spectrum  $S(f) \propto f^{-2}$ . This is identical to the spectrum observed in sediment cores and historical data discussed earlier in the chapter. The crossover time scale is the diffusion time across the diameter of the core, estimated to be between  $10^3$  yr

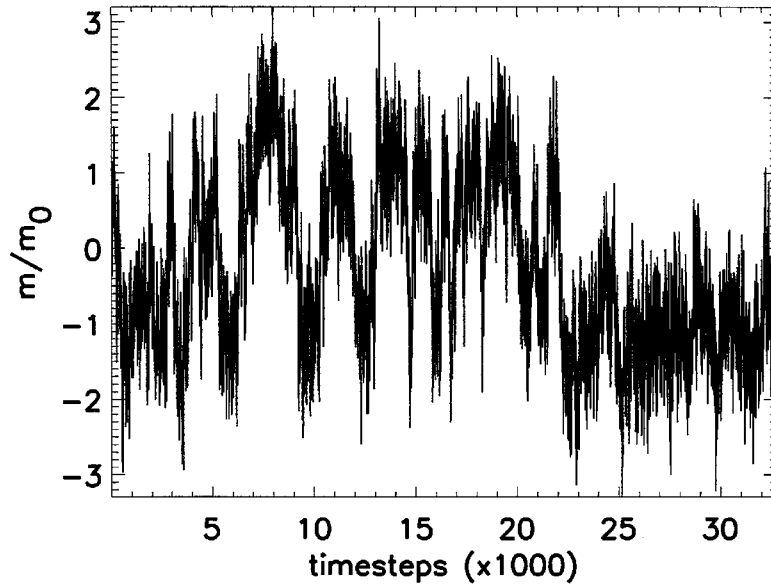


FIG. 50. Dipole moment produced by the model for geomagnetic variations normalized to the average dipole moment, set to be 1. The field exhibits reversals with a broad distribution of polarity interval lengths and a variable reversal rate decreasing at later times in the simulation.

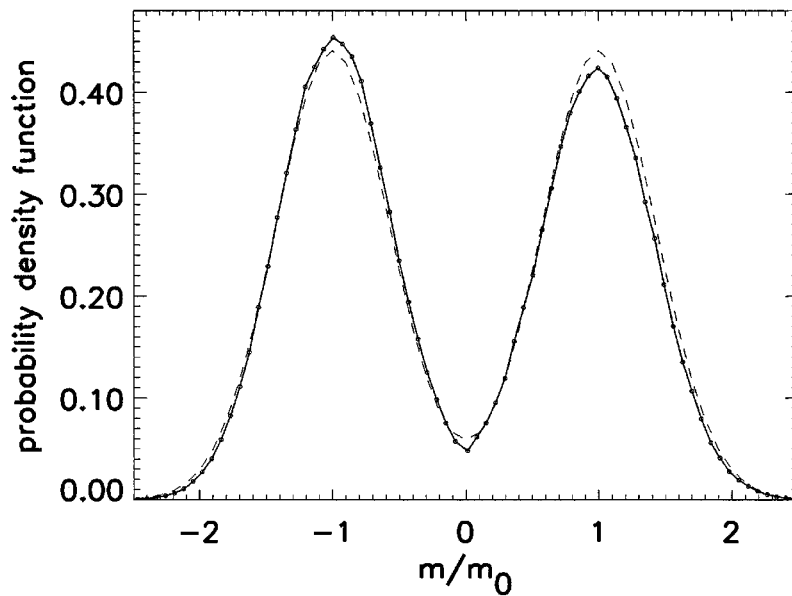


FIG. 51. Distribution of magnetic field according to ten simulations of the model (solid curve) and a binormal distribution fit to the data (dashed line). The binormal distribution fits the data well.

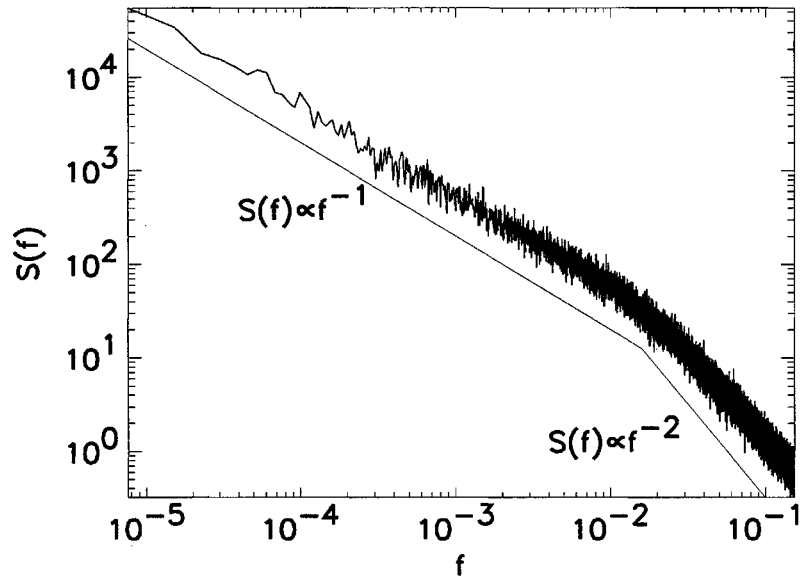


FIG. 52. Average power spectrum of the mean value of the magnetic field (dipole field) from 25 simulations. The spectrum has a low-frequency portion with  $S(f) \propto f^{-1}$  and a high-frequency region  $S(f) \propto f^{-2}$ . The same spectrum is observed in geomagnetic intensity from sediment cores and historical data.

(Harrison and Huang, 1990) and  $10^4$  yr (McLeod, 1996). These values are somewhat higher than the time scale of  $10^2$  yr identified as the crossover in the sediment core and historical data.

Figure 53 shows the average power spectrum of the angular displacement from the dipole from 25 simulations. The spectrum has a high-frequency region  $S(f) \propto f^{-2}$  which slowly flattens out to a flat spectrum at low frequencies. This is nearly consistent with the spectra of inclination and declination from lake sediment time series shown in Figs. 48 and 49. The measured value of the crossover from white-noise to Brownian-motion behavior in the lake sediment power spectra is 3 kyr. This value is consistent with estimates of  $10^3$  to  $10^4$  years for the diffusion time across the core from Harrison and Huang (1990) and McLeod (1996). A major discrepancy between the model and the observed spectrum is the absence of a flattening out of the spectrum of angular displacement at high frequencies in the model calculation.

## 5. OTHER APPLICATIONS

Self-affine time series occur in many other areas of earth science. For example, topographic profiles are Brownian motions (Turcotte, 1987). Pelletier (1999c) has shown that a model of topography governed by the

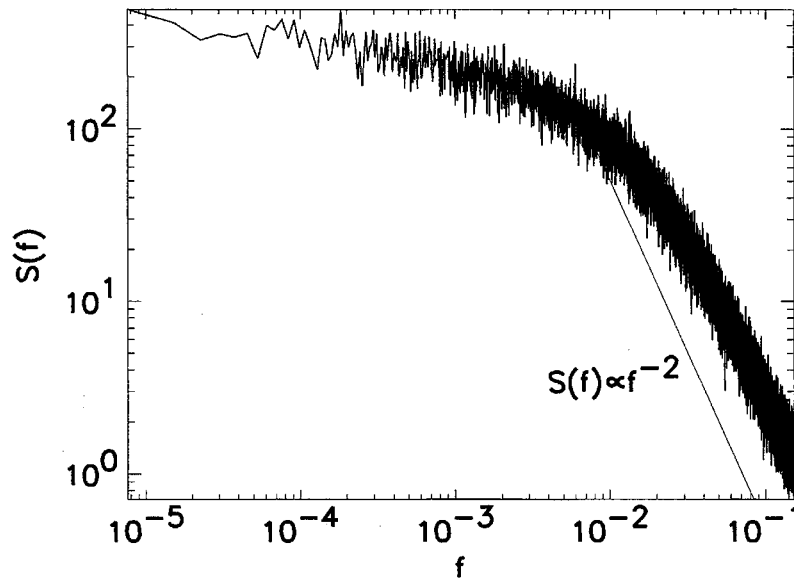


FIG. 53. Average power spectrum of the angular deviation from a dipole field from 25 simulations. The spectrum is  $S(f) \propto f^{-2}$  for high frequencies and gradually flattens out to a constant spectrum at low frequencies.

diffusion equation with the diffusivity a function of discharge predicts both the Brownian motion variations and the log-normal distribution of topography. Branching river networks with statistics identical to those of real river networks were also obtained. Gravity fields also exhibit power-law power spectra (Turcotte, 1987; Passier and Sneider, 1995). These power spectra have been interpreted as resulting from random density anomalies in the mantle (Lambeck, 1976). A related problem to the fractal structure of topography which may also exhibit self-affinity is sediment loads in rivers. Plotnick and Prestegard (1993) have obtained time-series data for sediment loads in rivers on time scales of minutes to days. They applied both the rescaled-range technique and power-spectral analysis to show that the time series are approximately self-affine.

Tjemkes and Visser (1994) have performed power-spectral analyses on the horizontal variability of temperature, humidity, and cloud water in the atmosphere. They found that different power-law behaviors were applicable over well-defined wave number ranges. These results are important for understanding the variability of the atmosphere and for improved characterization of these fields for inputs into large-scale models of the climate system (IPCC, 1995). The TOPEX/POSEIDON project has provided data on sea-surface height with global coverage with a 10-day sampling interval. Wunsch and Stammer (1995) have shown that sea-surface height has self-affine behavior in both space and time with three different values of  $\beta$  characterizing the variability over different wave number ranges. Variabil-

ity in sea-surface height has been modeled using the potential vorticity equation with stochastic forcing to represent variable wind conditions (Muller, 1996). These techniques are very similar to the stochastic partial differential equations discussed in this article, Sections 2–4. Hsui *et al.* (1993) have shown that sea-level variations are a self-affine time series on time scales of  $10^4$  to  $10^8$  yr. Since sea-level variations determine the major unconformities of the stratigraphic record, the record of the earth's history is determined by self-affine behavior.

Self-affine time series have applications in other fields. It has long been recognized that spatial variations in plankton abundance in the oceans are self-affine. This has been determined by performing power-spectral analysis on remotely sensed data for plankton along one-dimensional transects (Platt and Denman, 1975). Plankton variability has been modeled using stochastic diffusion equations similar to those presented in this paper (Fasham, 1978). Diffusion is used to model ocean mixing and stochastic terms are introduced to model the effects of local environmental variations that affect the population growth rate, such as variations in light intensity and nutrient concentration. Power-spectral analyses have also been performed on vegetation densities (Palmer, 1988). The time series were observed to have power-law power spectra. Sugihara and May (1990) and McKinney and Frederick (1992) have applied the self-affinity of population abundance in time to assessments of the probability of extinction. They argued that populations with stronger correlations in variability, characterized by larger values of  $\beta$  or  $Hu$ , have greater fluctuations in population size and have a higher probability of extinction.

Self-affine time series with  $\beta \approx 1$  are also observed in traffic flows (Musha and Higuchi, 1976). This behavior is reproduced in lattice gas models which move cars around on a lattice according to simple interaction rules that prevent cars from occupying the same space and that are driven by a random input of cars into the lattice (Takayasu and Takayasu, 1993).  $1/f$  noise has also been observed in the density of Internet traffic. This observation may have important implications for the design and testing of network software and services.

## 6. CONCLUSIONS

We have considered a variety of time series in this paper. As is the case for many other data sets, time series include both deterministic and stochastic components. We have concentrated our attention on the stochastic components. Our principal objective has been to show that the stochastic component of time series associated with complex phenom-

ena can have considerable order and, in particular, exhibit self-affine behavior. In order to do this we have considered three examples in some detail.

The first example we have considered is the natural variability of climate. On short time scales, atmospheric temperature observations exhibit deterministic daily and yearly periodicities. These have been removed from our considerations. On long time scales, periodicities of 100, 41, 23, and 19 kyr are observed. These four periodicities are Milankovitch cycles and are associated with tilt and precession. Again, we do not consider these in detail because the focus of our attention is on the stochastic variability. At frequencies below about  $1/(40 \text{ kyr})$ , the noise spectrum is flat (white). Radiative transfer from the atmosphere is balanced against the solar input. At frequencies between about  $1/(40 \text{ kyr})$  and  $1/(2 \text{ kyr})$ , the global temperature drifts and is a Brownian motion ( $\beta = 2$ ). The oceans and atmosphere act as a single thermal bath which is not buffered by radiative losses to infinity. At frequencies between about  $1/(2 \text{ kyr})$  and  $1/(1 \text{ month})$ , the atmospheric temperature is stationary and is well approximated by a self-affine behavior with  $\beta = 0.5$ . In this frequency range, the atmospheric temperature is buffered by heat exchange with the oceans, which act as a near-isothermal bath. At frequencies between about  $1/(1 \text{ month})$  and  $1/(1 \text{ day})$ , the temperatures at continental stations again drift, and are well approximated by a nonstationary self-affine behavior with  $\beta = 1.5$ , whereas maritime stations remain proportional to  $\beta = 0.5$ . The maritime stations are buffered by the oceanic heat sink, whereas the continental stations are not.

It is also shown that river-discharge and tree-ring time series exhibit stationary  $\beta = 0.5$  spectra. This is consistent with a Hurst exponent  $Hu \approx 0.7$ . This weakly persistent behavior was found to be widely applicable to natural time series by Hurst *et al.* (1965).

These studies of the stochastic variability of climate are important in a variety of ways. They provide an important test of the validity of global circulation models (GCMs). Manabe and Stouffer (1996) have carried out a spectral study of their GCM, and the agreement with the results given here is rather poor. Also, the fact that global temperature obeys a  $\beta \approx 0.5$  spectral behavior in the frequency range  $1/(100 \text{ yr})$  to  $1/(10 \text{ yr})$  can be used to compare the natural variability of climate to fluctuations that are attributed to global warming. Monte Carlo simulations with time series exhibiting a  $\beta = 0.5$  behavior can be used to obtain the probability that a specific change in global temperature can be attributed to natural variability.

We have also shown that variations in solar luminosity exhibit the same transitions as the climate data: from  $\beta \approx 0$  to  $\beta \approx 2$  to  $\beta \approx 0.5$ . Thus the

physics of the radiating layer of the sun must strongly resemble the physics of the Earth.

The second major example we considered is the variability of porosity in sedimentary basins. It is shown that the horizontal variations are well approximated by a Brownian motion ( $\beta = 2$ ) and the vertical variations by a fractional Brownian motion with  $\beta = 1.5$ . In order to explain these results we introduced the stochastic diffusion model. This model combines a white-noise deposition with the horizontal diffusion (Culling) model for material transport. This model reproduces the observed self-affine behavior.

We have also applied the stochastic diffusion model in order to explain the completeness of the sedimentary record. According to this model, the mean rate of deposition over a period  $T$ ,  $R(T)$ , depends on  $T$  according to  $R \propto T^{-3/4}$ . The observed dependence is  $R \propto T^{-0.76}$ .

The third example we considered is the temporal variability of the Earth's magnetic field. By combining a variety of paleointensity measurements, we are able to obtain the power spectrum of the dipole moment of the field over the frequency range  $1/(4 \text{ Myr})$  to  $1/(100 \text{ yr})$ . Over this entire range, the power spectrum is well approximated by a  $1/f$  ( $\beta = 1$ ) self-affine time series.

As a further test of this result we considered the field's reversal record. We produce synthetic  $1/f$  time series with the observed mean and variance of the Earth's magnetic field. Each time a synthetic field reaches zero field intensity, we assume that the polarity of the field is changed. We then compare the number-length statistics of the synthetic fields with the observed statistics. Good agreement is found.

Even though the dynamo driving the Earth's magnetic field is extremely complex, the statistical behavior of the resulting magnetic-field time series is quite simple. This simplicity must be one of the primary tests for the validity of new dynamo theories.

An important question that we have addressed in each of our applications is the cause of the observed self-affine behavior. We have shown that a variety of self-affine signals can result from transport phenomena in which there is a random element and a diffusion element. Which value of  $\beta$  that results, and over what frequency or wave number domain, depends on the dimensionality of the phenomena, the boundary conditions, and how the random element enters into the equation (whether as a noise in the mass or energy or in the flux of mass or energy). We have included other examples of self-affine phenomena in this section to stimulate researchers in those fields to apply techniques in this paper to their problems, if appropriate. If a differential equation could be developed to model self-affine behavior in other phenomena, researchers might come to

better understand the relative role of deterministic versus stochastic processes in those problems and have a null model against which to test for the presence of external forcings on the system or other phenomena.

#### ACKNOWLEDGMENTS

We wish to thank Bruce D. Malamud for helpful conversations and a critical review of the manuscript. This work was supported in part by NASA Grant NAGW-4702.

#### REFERENCES

- Agterberg, F. P. (1982). Recent developments in geomathematics. *Geoprocessing* 2, 1–32.
- Alexander, L. L. (1995). Geologic evolution and stratigraphic controls on fluid flow of the Eugene Island Block 330 Mini Basin, offshore Louisiana, Ph.D. dissertation, Cornell Univ., Ithaca, NY.
- Allen, P. A., and Allen, J. R. (1990). "Basin Analysis: Principles and Applications." Blackwell Science, Cambridge, Massachusetts.
- Arking, A., and Ziskin, D. (1994). Relationship between clouds and sea surface temperatures in the western tropical Pacific. *J. Clim.* 7, 988.
- Barnett, T. P., Del Genio, A. D., and Ruedy, R. A. (1992). Unforced decadal fluctuations in a coupled model of the atmosphere and ocean mixed layer. *J. Geophys. Res.* 97, 7341–7354.
- Barton, C. C., and Scholz, C. H. (1995). The fractal size and spatial distribution of hydrocarbon accumulations: implications for resource assessment and exploration strategy. In "Fractals in Petroleum Geology and Earth Sciences" (C. C. Barton and P. R. LaPointe, eds.), Plenum, New York, pp. 13–34.
- Barton, C. E. (1982). Spectral analysis of palaeomagnetic time series and the geomagnetic spectrum. *Philos. Trans. Roy. Soc. London Ser. A* 306, 203–209.
- Barton, C. E., and McElhinny, M. W. (1981). A 10,000 yr geomagnetic secular variation record from three Australian maars. *Geophys. J. Roy. Astron. Soc.* 67, 465–485.
- Berg, R. R. (1968). Point bar origin of Fall River sandstone reservoirs, northeast Wyoming. *Am. Assoc. Pet. Geol. Bull.* 52, 2116–2122.
- Blakely, R. J. (1974). Geomagnetic reversals and crustal spreading rates during the Miocene. *J. Geophys. Res.* 79, 2979–2985.
- Booy, C., and Lye, L. M. (1989). A new look at flood risk determination. *Water Resour. Bull.* 25, 933–943.
- Bras, R. L., and Rodriguez-Iturbe, I. (1985). "Random Functions and Hydrology." Addison-Wesley, Reading, MA.
- Cande, S. C., and Kent, D. V. (1992a). A new geomagnetic polarity time scale for the Late Cretaceous and Cenozoic. *J. Geophys. Res.* 97, 13917–13951.
- Cande, S. C., and Kent, D. V. (1992b). Ultrahigh resolution marine magnetic anomaly profiles: a record of continuous paleointensity variations? *J. Geophys. Res.* 97, 15075–15083.
- Cande, S. C., and Kent, D. V. (1995). Revised calibration of the geomagnetic polarity timescale for the Late Cretaceous and Cenozoic. *J. Geophys. Res.* 100, 6093–6095.

- Claps, M., and Masetti, D. (1994). Milankovitch periodicities recorded in Cretaceous sequences from the Southern Alps (Northern Italy). In "Orbital Forcing and Cyclic Sequences" (P. L. DeBoer and D. L. Smith, eds.), Blackwell Science, Cambridge, MA, pp. 99–107.
- Coleman, J. M., and Prior, D. B. (1982). Deltaic environments of deposition. *AAPG Mem.* **31**, 139–178.
- Courtillot, V., and Le Mouel, J. L. (1988). Time variations of the earth's magnetic field: From daily to secular. *Ann. Rev. Earth Plan. Sci.* **16**, 389–476.
- Cox, A. (1968). Lengths of geomagnetic polarity intervals. *J. Geophys. Res.* **73**, 3247–3260.
- Currie, R. G. (1968). Geomagnetic spectrum of internal origin and lower mantle conductivity. *J. Geophys. Res.* **73**, 2768–2779.
- Curry, W. H., and Curry III, W. H. (1972). South Glennock oil field, Wyoming: A pre-discovery thinking and post-discovery description. *Mem. Am. Assoc. Pet. Geol.* **15**, 415–427.
- Dacey, M. F. (1979). Models of bed formation. *Math. Geol.* **11**, 655–668.
- Deshpande, A., Flemings, P. B., and Huang, J. (1997). Quantifying lateral heterogeneities in fluvio-deltaic sediments using 3-D reflection seismic data. *J. Geophys. Res.* **102**, 15385–15401.
- Dolan, S. S., Bean, C. J., and Riollet, B. The broad-band fractal nature of heterogeneity in the upper crust from petrophysical logs. *Geophysical J. Int.* **132**, 489–507.
- Drummond, C. N., and Wilkinson, B. H. (1996). Stratal thickness frequencies and the prevalence of orderedness in stratigraphic sequences. *J. Geol.* **104**, 1–18.
- Dunne, T., Whipple, K. X., and Aubry, B. F. (1995). Microtopography of hillslopes and initiation of channels by Horton overland flow. In "Natural and Anthropogenic Influences in Fluvial Geomorphology: The Wolman Volume" (J. E. Costa *et al.*, eds.), *Geophysical Monograph 89*, American Geophysical Union, Washington, D.C., pp. 27–44.
- Family, F. (1986). Scaling of rough surfaces: effects of surface diffusion. *J. Phys. A Math. Gen.* **19**, L441–L446.
- Fasham, M. J. R. (1978). The statistical and mathematical analysis of plankton patchiness. *Oceanogr. Mar. Biol. Ann. Rev.* **16**, 43–79.
- Gaffin, S. (1989). Analysis of scaling in the geomagnetic polarity reversal record. *Phys. Earth Plan. Inter.* **57**, 284–290.
- Garcia, R. (1981). Depositional systems and their relation to gas accumulation in Sacramento Valley, California. *AAPG Bull.* **65**, 653–674.
- Garrett, A. E. (1984). Vertical eddy diffusivity in the ocean interior. *J. Mar. Res.* **42**, 359–393.
- Ghil, M. (1983). Theoretical climate dynamics: An introduction. In "Turbulence and Predictability in Geophysical Fluid Dynamics and Climate Dynamics" (M. Ghil, ed.), North Holland, Amsterdam.
- Gomes da Silva, L. M., and Turcotte, D. L. (1994). A comparison between Hurst and Hausdorff measures derived from fractional time series. *Chaos, Solitons & Fractals* **4**, 2181–2192.
- Harbaugh, J. W., Doveton, J. H., and Davis, J. C. (1977). "Probability Methods in Oil Exploration." John Wiley & Sons, New York.
- Harland, W. B., Cox, A., Llewellyn, P. G., Pickton, C. A. G., Smith, A. G., and Walters, R. (1990). "A Geologic Time Scale 1989." Cambridge Univ. Press, Cambridge.
- Harrison, C. G. A., and Huang, Q. (1990). Rates of change of the Earth's magnetic field measured by recent analyses. *J. Geomag. Geoelectr.* **42**, 897–928.
- Harvey, L. D. D., and Schneider, S. H. (1985). Transient climate response to external forcing on  $10^0$ – $10^4$  year time scales, Part I: Experiments with globally averaged, coupled, atmosphere and ocean energy balance models. *J. Geophys. Res.* **90**, 2191–2205.

- Hays, J. D., Imbrie, J., and Shackleton, N. J. (1976). Variations in the earth's orbit: pacemaker of the ice ages. *Science* **194**, 1121–1132.
- Hewett, T. A. (1986). Fractal distribution of reservoir heterogeneity and their influence of fluid transport. SPE Prof. Pap. 15386. Society of Petroleum Engineers, Richardson, TX.
- Hoffert, M. I., Callegari, A. J., and Hsieh, C.-T. (1980). The role of deep sea heat storage in the secular response to climatic forcing. *J. Geophys. Res.* **85**, 6667–6679.
- Hofmann, D. J., and Rosen, J. M. (1987). On the prolonged lifetime of the El Chichon sulfuric acid aerosol cloud. *J. Geophys. Res.* **92**, 9825–9830.
- Holliger, K. (1996). Upper-crustal seismic velocity heterogeneity as derived from a variety of P-wave sonic logs. *Geophys. J. Int.* **125**, 813–829.
- Hooke, R. L., and Rohrer, W. L. (1979). Geometry of alluvial fans: effects of discharge and sediment size. *Earth Surf. Process.* **4**, 147–166.
- Hsui, A. T., Rust, K. A., and Klein, G. D. (1993). A fractal analysis of Quaternary, Cenozoic–Mesozoic, and late Pennsylvania sea-level changes. *J. Geophys. Res.* **98**, 21963–21967.
- Hurst, H. E., Black, R. P., and Simaika, Y. M. (1965). “Long-term Storage: An Experimental Study.” Constable, London.
- Intergovernmental Panel on Climate Change, (1995). “Climate Change, The IPCC Scientific Assessment” (J. T. Houghton and B. A. Callendar, eds.), Cambridge Univ. Press, New York.
- Janosi, I. M., and Vattay, G. (1992). Soft turbulent state of the atmospheric boundary layer. *Phys. Rev. A* **46**, 6386–6389.
- Jouzel, J., Lorius, C., Petit, J. R., Genthon, C., Barkov, N. I., and Kotlyakov, V. M. (1987). Vostok ice-core: A continuous isotope temperature record over the last climatic cycle (160,000 years). *Nature* **329**, 403–407.
- Jouzel, J., and Merlivat, D. (1984). Deuterium and oxygen 18 in precipitation: Modeling of the isotopic effects during snow formation. *J. Geophys. Res.* **89**, 11,749–11,757.
- Kagan, Y. Y., and Knopoff, L. (1980). Spatial distribution of earthquakes: The two-point correlation function. *Geophys. J. Roy. Astron. Soc.* **62**, 303–320.
- Kendall, D. R., and Dracup, J. A. (1991). A comparison of index-sequential and AR(1) generated hydrologic sequences. *J. Hydrol.* **122**, 335–352.
- Kerr, R. A. (1978). Climate control: How large a role for orbital variations? *Science* **201**, 144–146.
- Kolmogorov, A. N. (1951). Solution of a problem in probability theory connected with the problem of the mechanism of stratification. *Trans. Am. Math. Soc.* **53**, 171–177.
- Kondev, J., and Henley, C. L. (1995). Geometrical exponents of contour loops on random Gaussian surfaces. *Phys. Rev. Lett.* **74**, 4580–4583.
- Kono, M. (1971). Intensity of the earth's magnetic field during the Pliocene and Pleistocene in relation to the amplitude of mid-ocean ridge magnetic anomalies. *Earth Planet. Sci. Lett.* **11**, 10–17.
- Kono, M. (1987). Rikitake two-disk dynamo and paleomagnetism. *Geophys. Res. Lett.* **14**, 21–24.
- Korvin, G. (1992). “Fractal Models in the Earth Sciences.” Elsevier, Amsterdam.
- Kovacheva, M. (1980). Summarized results of the archeomagnetic investigation of the geomagnetic field variation for the last 8000 yr in south-eastern Europe. *Geophys. J. Roy. Astron. Soc.* **61**, 57–64.
- Laj, C., Kissel, C., and Lefevre, I. (1996). Relative geomagnetic field intensity and reversals from Upper Miocene sections in Crete. *Earth Planet. Sci. Lett.* **141**, 67–78.
- Lambeck, K. (1976). Lateral density anomalies in the upper mantle. *J. Geophys. Res.* **81**, 6333–6340.

- Landwehr, J. M., and Matalas, N. C. (1986). On the nature of persistence in dendrochronologic records with implications for hydrology. *J. Hydrol.* **86**, 239–277.
- Lees, J. M., and Park, J. (1995). Multiple-taper spectral analysis: A stand-alone C-subroutine. *Comp. Geol.* **21**, 199–236.
- Lehman, B., Laj, C., Kissel, C., Mazaud, A., Paterne, M., and Labeyrie, L. (1996). Relative changes of the geomagnetic field intensity during the last 280 kyear from piston cores in the Acores area. *Phys. Earth Planet. Int.* **93**, 269–284.
- Lock, J., and McElhinney, M. W. (1992). The Global Paleomagnetic Database: Design, installation, and use with ORACLE. *Surv. Geophys.* **12**, 317–506.
- Lund, S. P., and Banerjee, S. K. (1985). The paleomagnetic record of Late Quaternary secular variation from Anderson Pond, Tennessee. *Earth Planet. Sci. Lett.* **72**, 219–237.
- Lund, S. P., Liddicoat, J. C., Lajoie, K. R., Henyey, T. L., and Robinson, S. W. (1988). Paleomagnetic evidence for long-term ( $10^4$  year) memory and periodic behavior in the earth's core dynamo process. *Geophys. Res. Lett.* **15**, 1101–1104.
- Malamud, B. D., and Turcotte, D. L. (1999). Self-affine time series: I Techniques of analysis, In "Advances in Geophysics" (R. Dmowska and B. Saltzman, eds.), Vol. 40, Academic Press, San Diego, pp. 1–89.
- Manabe, S., and Stouffer, R. J. (1996). Low-frequency variability of surface air temperature in a 1000-year integration of a coupled atmosphere-ocean-land surface model. *J. Climate* **9**, 376–393.
- Manley, G. (1974). Central England temperatures: Monthly means 1659–1973. *Quat. J. Roy. Met. Soc.* **100**, 389–405.
- Mann, M. E., and Lees, J. M. (1996). Robust estimation of background noise and signal detection in climatic time series. *Climatic Change* **33**, 409–445.
- Matteucci, G. (1990). Analysis of the probability distribution of the late Pleistocene climatic record: Implications for model validation. *Clim. Dyn.* **5**, 35–52.
- McFadden, P. L., and Merrill, R. T. (1995). History of the Earth's magnetic field and possible connections to core-mantle boundary processes. *J. Geophys. Res.* **100**, 307–316.
- McKinney, M. L., and Frederick, D. (1992). Extinction and population dynamics: New methods and evidence from Paleogene foraminifera. *Geology* **20**, 343–346.
- McLeod, M. G. (1992). Signals and noise in magnetic observatory annual means: Mantle conductivity and jerks. *J. Geophys. Res.* **97**, 17,261–17,290.
- McLeod, M. G. (1996). Spatial and temporal power spectra of the geomagnetic field. *J. Geophys. Res.* **101**, 2745–2763.
- McShea, D. W., and Raup, D. M. (1986). Completeness of the geologic record. *J. Geol.* **94**, 569–574.
- Meynadier, L., Valet, J.-P., Bassonot, F. C., Shackleton, N. J., and Guyodo, Y. (1994). Asymmetrical saw-tooth pattern of the geomagnetic field intensity from equatorial sediments in the Pacific and Indian oceans. *Earth Planet. Sci. Lett.* **126**, 109–127.
- Meynadier, L., Valet, J.-P., Weeks, R., Shackleton, N. J., and Hagee, V. L. (1992). Relative geomagnetic intensity of the field during the last 140 ka. *Earth Planet. Sci. Lett.* **114**, 39–57.
- Mitchell Jr., J. M. (1976). An overview of climatic variability and its causal mechanisms. *Quat. Res.* **6**, 481–493.
- Mizutani, S., and Hattori, I. (1972). Stochastic analysis of bed-thickness distribution of sediments. *Math. Geol.* **4**, 123–146.
- Molz, F. J., and Boman, G. K. (1993). A fractal-based stochastic interpolation scheme in subsurface hydrology. *Water Resour. Res.* **29**, 3769–3774.

- Muller, P. (1996). Stochastic forcing of quasi-geostrophic eddies. In "Stochastic Modelling in Physical Oceanography" (R. J. Adler, P. Muller, and B. Rozovskii, eds.), Birkhauser, Boston, pp. 381–395.
- Musha, T., and Higuchi, H. (1976). The  $1/f$  fluctuation of a traffic current of an expressway. *Jap. J. Appl. Phys.* **15**, 1271–1275.
- Muto, T. (1995). The Kolmogorov model of bed thickness distribution: An assessment based on numerical simulation and field-data analysis. *Terra Nova* **7**, 408–416.
- National Climatic Data Center (1994). "Global Daily Summary: Temperature and Precipitation 1977–1991," Version 1.0.
- National Geophysical Data Center (1995). "Global Paleomagnetic Database," Version 3.1. National Oceanographic and Atmospheric Administration.
- Noakes, D. J., Hipel, K. W., McLeod, A. I., Jimenez, C., and Yakowitz, S. (1988). Forecasting annual geophysical time series. *Int. J. Forecasting* **4**, 103–115.
- North, G. R., and Cahalan, R. F. (1981). Predictability in a solvable stochastic climate model. *J. Atmos. Sci.* **38**, 504–513.
- Novikov, E. A. (1963). Random force method in turbulence theory. *Soviet Phys., J.E.T.P.* **17**, 1449–1454.
- Pal, P. C., and Roberts, P. H. (1988). Long-term polarity stability and strength of the geomagnetic dipole. *Nature* **331**, 702–705.
- Palmer, M. W. (1988). Fractal geometry: A tool for describing spatial patterns of plant communities. *Vegetatio* **75**, 91–102.
- Passier, M. L., and Sneider, R. K. (1995). On the presence of intermediate-scale heterogeneity in the upper mantle. *Geophys. J. Int.* **123**, 817–837.
- Peixoto, J. P., and Oort, A. H. (1992). "Physics of Climate." American Institute of Physics, New York.
- Pelletier, J. D. (1996). Variations in solar luminosity from time scales of minutes to months. *Astrophys. J.* **463**, L41–L45.
- Pelletier, J. D. (1997a). Analysis and modeling of the natural variability of climate. *J. Climate* **10**, 1331–1342.
- Pelletier, J. D. (1997b). Kardar–Parisi–Zhang scaling of the convective boundary layer and the fractal structure of cumulus cloud fields. *Phys. Rev. Lett.* **78**, 2672–2675.
- Pelletier, J. D. (1999). Self-organization and scaling relationships of evolving river networks, *J. Geophys. Res.*, in press.
- Pelletier, J. D., and Turcotte, D. L. (1996). Scale-invariant topography and porosity variations in sedimentary basins. *J. Geophys. Res.* **101**, 28,165–28,175.
- Pilkington, M., and Todoeschuck, J. P. (1990). Stochastic inversion for scaling geology. *Geophys. J. Int.* **102**, 205–217.
- Platt, T., and Denman, K. L. (1975). Spectral analysis in ecology. *Ann. Rev. Ecol. Syst.* **6**, 189–210.
- Pleune, R. (1990). Vertical diffusion in the stable atmosphere. *Atmos. Env. A* **24**, 2547–2555.
- Plotnick, R. E. (1986). A fractal model for the distribution of stratigraphic hiatuses. *J. Geol.* **94**, 885–890.
- Plotnick, R. E., and Prestegard, K. (1993). Fractal analysis of geologic time series. In "Fractals in Geography" (L. De Cola and S. Lam, eds.), Prentice-Hall, Englewood Cliffs, NJ, pp. 193–210.
- Press, W. H., Teukolsky, S. A., Vetterling, W. T., and Flannery, B. P. (1992). "Numerical Recipes in C: The Art of Scientific Computing," 2nd ed. Cambridge Univ. Press, New York.

- Rosen, J. M., Kjome, N. T., McKenzie, R. T., and Liley, J. B. (1994). Decay of Mount Pinatubo aerosols at midlatitudes in the northern and southern hemispheres. *J. Geophys. Res.* **99**, 25,733–25,739.
- Rothman, D. H., Grotzinger, J., and Flemings, P. (1993). Scaling in turbidite deposition. *J. Sed. Res. A* **64**, 59–67.
- Sadler, P. M. (1981). Sediment accumulation rates and the completeness of stratigraphic sections. *J. Geol.* **89**, 569–584.
- Sadler, P. M., and Strauss, D. J. (1990). Estimation of completeness of stratigraphical sections using empirical data and theoretical methods. *J. Geol. Soc. London* **147**, 471–485.
- Santer, B. D., Taylor, K. E., Wigley, T. M. L., Penner, J. E., Jones, P. D., and Cubasch, U. Towards the detection and attribution of an anthropogenic effect on climate. *Clim. Dyn.* **12**, 77–100.
- Schwarzacher, W. (1975). "Sedimentation Models and Quantitative Stratigraphy." Elsevier, Amsterdam.
- Seinfeld, J. H. (1986). "Atmospheric Chemistry and Physics of Air Pollution." John Wiley & Sons, New York.
- Seki, M., and Ito, K. (1993). A phase-transition model for geomagnetic polarity reversals. *J. Geomag. Geoelectr.* **45**, 79–88.
- Shiomi, K., Sato, H., and Ohtake, M. (1997). Broad-band power-law spectra of well-log data in Japan. *Geophys. J. Int.* **130**, 57–64.
- Slack, J. R., and Landwehr, J. M. (1992). Hydro-climatic data network: A U.S. Geological Survey streamflow data set for the United States for the study of climatic variations: 1874–1988. *U.S. Geol. Surv. Open-File Rep.* 92–129.
- Stevenson, D. J. (1983). Planetary magnetic fields. *Rep. Prog. Phys.* **46**, 555–620.
- Strauss, D. J., and Sadler, P. M. (1989). Stochastic models for the completeness of stratigraphic sections. *Math. Geol.* **21**, 37–59.
- Sugihara, G., and May, R. M. (1990). Applications of fractals in ecology. *Trends in Ecol. Evol.* **5**, 79–86.
- Takayasu, M., and Takayasu, H. (1993).  $1/f$  noise in a traffic model. *Fractals* **1**, 860–866.
- Tarboton, D. G. (1994). The source hydrology of severe sustained drought in the Southwestern United States. *J. Hydrol.* **161**, 31–69.
- Tauxe, L., and Hartl, P. (1997). 11 million years of Oligocene geomagnetic field behavior. *Geophys. J. Int.* **128**, 217–229.
- Thibault, J., Pozzi, J.-P., Barthes, V., and Dubuisson, G. (1995). Continuous record of geomagnetic field intensity between 4.7 and 2.7 Ma from downhole measurements. *Earth Planet. Sci. Lett.* **136**, 541–550.
- Thomson, D. J. (1990). Quadratic-inverse spectrum estimates: Applications to palaeoclimatology. *Philos. Trans. Roy. Soc. London A* **332**, 539–597.
- Thouveny, N., Creer, K. M., and Blunk, I. (1990). Extension of the Lac du Bouchet palaeomagnetic record over the last 120,000 years. *Earth Planet. Sci. Lett.* **97**, 140–161.
- Tipper, J. C. (1983). Rates of sedimentation, and stratigraphical completeness. *Nature* **21**, 296–298.
- Tjemkes, S. A., and Visser, M. (1994). Horizontal variability of temperature, specific humidity, and cloud liquid water as derived from spaceborne observations. *J. Geophys. Res.* **99**, 23,089–23,105.
- Todoeschuck, J. P., Jensen, O. G., and Labonte, S. (1990). Gaussian scaling noise model of seismic reflection sequences: Evidence from well logs. *Geophysics* **55**, 480–484.
- Tubman, K. M., and Crane, S. D. (1995). Vertical versus horizontal well log variability and application to fractal reservoir modeling. In "Fractals in Petroleum Geology and Earth Sciences" (C. C. Barton and P. R. LaPointe, eds.), Plenum, New York, pp. 279–294.

- Turcotte, D. L. (1987). A fractal interpretation of topography and geoid spectra on the Earth, Moon, Venus, and Mars. *J. Geophys. Res.* **92**, 597–601.
- Turcotte, D. L. (1997). “Fractals and Chaos in Geology and Geophysics.” 2nd ed. Cambridge Univ. Press, Cambridge.
- Turner, G. M., Evans, M. E., and Hussin, I. B. (1982). A geomagnetic secular variation study (31,000–19,500 BP) in western Canada. *Geophys. J. Roy. Astron. Soc.* **71**, 159–171.
- Turner, G. M., and Thompson, R. (1981). Lake sediment record of the geomagnetic secular variation in Britain during Holocene times. *Geophys. J. Roy. Astron. Soc.* **65**, 703–725.
- Valet, J.-P., and Meynadier, L. (1993). Geomagnetic field intensity and reversals during the past four million years. *Nature* **366**, 234–238.
- van der Ziel, A. (1950). On the noise spectra of semiconductor noise and of flicker effect. *Physica* **16**, 359–375.
- Van Kampen, N. G. (1981). “Stochastic Processes in Physics and Chemistry.” North-Holland, Amsterdam.
- Van Vliet, K. M., van der Ziel, A., and Schmidt, R. R. (1980). Temperature-fluctuation noise of thin films supported by a substrate. *J. Appl. Phys.* **51**, 2947–2956.
- Verosub, K. L., Mehringer, P. J., and Waterstraat, P. (1986). Holocene secular variation in western North America: Paleomagnetic record from Fish Lake, Harney County, Oregon. *J. Geophys. Res.* **91**, 3609–3623.
- Vicsek, T. (1992). “Fractal Growth Phenomena.” World Science, River Edge, NJ.
- Vistelius, A. B., and Feigel’son, T. S. (1965). On the theory of bed formation. *Dokl. Akad. Nauk. SSSR* **164**, 158–160.
- Voorhies, C. V., and Conrad, J. (1996). Accurate predictions of mean geomagnetic dipole excursion and reversal frequencies, mean paleomagnetic field intensity, and the radius of the Earth’s core using McLeod’s rule. *NASA Technical Memorandum 104634*.
- Vose, R. S., Schmoyer, R. L., Stewer, P. M., Peterson, T. C., Heim, R., Karl, T. R., and Eischeid, J. K. (1992). The global historical climatology network: long-term monthly temperature, precipitation, sea-level pressure, and station pressure data. *Environ. Sci. Div. Pub. No. 392*, Oak Ridge National Laboratory, Oak Ridge, TN.
- Voss, R. F., and Clarke, J. (1976). Flicker ( $1/f$ ) noise: Equilibrium temperature and resistance fluctuations. *Phys. Rev. B* **13**, 556–573.
- Walden, A. T., and Hosken, J. W. J. (1985). An investigation of the spectral properties of primary reflection coefficients. *Geophys. Prospect.* **33**, 400–435.
- Wallis, J. R., Lettenmaier, D. P., and Wood, E. F. (1991). A daily hydroclimatological data set for the continental U.S. *Water Resour. Res.* **27**, 1657–1663.
- Weissman, M. B. (1988).  $1/f$  noise and other slow, nonexponential kinetics in condensed matter. *Rev. Mod. Phys.* **60**, 537–571.
- Wilde, P., Normark, W. R., and Chase, T. E. (1978). Channel sands and petroleum potential of Monterey deep-sea fan, California. *Am. Assoc. Petrol. Geol. Bull.* **62**, 967–983.
- Wunsch, C., and Stammer, D. (1995). The global frequency-wavenumber spectrum of oceanic variability estimated from TOPEX/POSEIDON altimetric measurements. *J. Geophys. Res.* **100**, 24,895–24,910.
- Yevjevich, V. M. (1967). An objective approach to definitions and investigations of continental hydrologic droughts. *Hydrol. Pap.* **23**, Colorado State Univ., Fort Collins, CO.
- Yiou, P., Jouzel, J., Johnsen, S., and Rognvaldsson, O. E. (1995). Rapid oscillations in Vostok and GRIP ice cores. *Geophys. Res. Lett.* **22**, 2179–2182.

# INDEX

## A

- Abbreviations and symbols, 83–87
- Aliasing, 22
- Antipersistence, *see* Persistence and antipersistence
- Atmosphere–ocean model, 102–113, 158
- Atmosphere–ocean–land surface model, 112–113
- Atmospheric temperature, 91–98, 100, 156
- Autocorrelation function
  - applied to
    - geomagnetic fields, 150, 152
    - synthetic time series, 9
  - autocovariance function, 6–7, 9, 50
  - continuous, 6
  - discrete, 7
  - Fourier analysis, *see* Fourier analysis
  - persistence and antipersistence, 6–7
  - relation to
    - power-spectral density, 7, 27
    - semivariograms, 8–9
    - variance of time series, 27–28
  - Weiner–Khinchine theorem, 152
  - white noise, 7
- Autocovariance function, 6–7, 9, 50
- Autoregressive (AR) model, 6, 115
- Average extreme-value analysis
  - applied to
    - Gaussian noises and motions, 66–69
    - log-normal noises and motions, 69–71
  - description, 64–66
  - rescaled-range, compared to, 67–68, 71
  - summary of strengths and weaknesses, 82

## B

- Bed thickness distributions, 131, 136–139
- Blackbody radiation, 93, 107
- Brownian motions
  - analyses using
    - average extreme-value analysis, 67–68
    - power-spectral analysis, 23–25, 40
    - rescaled-range analysis, 62–63
    - semivariogram analysis, 49–50
    - wavelet variance analysis, 73–74, 76–77
  - construction
    - Fourier filtering technique, 35–37
    - successive random additions, 43–47
    - white noise, running sum, 14–15
  - examples in nature
    - geomagnetic variations, 148–150, 152–156

- sediment deposition, 132–136
- temperature, 93–94, 98
- topography, 4, 11, 121, 126, 129–130, 155–156
- examples of synthetic, 12, 14–15, 17, 25, 29, 38, 46, 48, 74, 120
- fractional, *see* Fractional Gaussian noises and motions; Fractional log-normal noises and motions
- rescaling, 28–30
- standard deviation, 14–15
- successive random additions, 43–47
- variance, 14–15
- white noise, relation to, 14–15, 23–26

## C

- Cantor set, 133–134
- Climate variability
  - atmosphere–ocean model, 102–113, 158
  - deuterium, Vostok ice core, 91, 93–94, 98, 109–110
  - droughts, 53, 59, 115–117
  - Milankovitch cycles, 158
  - precipitation, 99–100
  - river discharge, 4–5, 59, 98–100, 115–117, 158
  - solar luminosity, 114, 158–159
  - stochastic diffusion model
    - one-dimensional, 100–107
    - two-layer, 107–114
  - summary, 158–159
  - temperature, 91–98, 100, 156
  - tree-ring widths, 98–100, 158
- Clouds, 130
- Coastlines, 1, 10–11, 130
- Coefficient of variation, 51–53
- Colorado river, 116–117
- Complex numbers, 21–22
- Composite long-memory processes, 79
- Conservation of energy, 102
- Continuous time series, 2–5
- Convolution, 73
- Correlation, pair, *see* Pair correlation
- Correlations in time series, *see* Persistence and antipersistence
- Correlogram, 7, *see also* Semivariogram analysis
- Cretaceous superchron, 146–147
- Cryptochrons, 143
- Culling model, 159

## D

- Delta function, 52
- Density, power-spectral, *see* Power-spectral density
- Denver basin hydrocarbons, 126–129
- Deposition, *see* Sediments
- Deterministic self-affine fractal, 11–12
- Detrending, 34–35, 95
- Deuterium, Vostok ice core, 91, 93–94, 98, 109–110
- Deviation, standard, *see* Variance
- Devil's staircase, 134
- Differencing self-affine time series, 14–15, 25–27, 37–39, 61
- Diffusion equation, 100, 102, 106, 123
- Dimensions, *see* Euclidean dimensions; Extreme-value exponent,  $H_e$ ; Fractal dimension,  $D$ ; Hausdorff exponent,  $H_a$ ; Hurst exponent,  $H_u$ ; Power-spectral density exponent,  $\beta$ ; Wavelet variance exponent,  $H_w$
- Dipole moment variability, 140–142, 153–155
- Discharge, river, 4–5, 59, 98–100, 115–117, 158
- Discontinuous sedimentation, 134, 137
- Discontinuous time series, 2–5
- Discrete Fourier transform, 21–22, *see also* Fourier analysis
- Discrete time series, 2–5
- Dispersional analysis, 79
- Distributions
  - bed-thickness, 131, 137–139
  - binormal, magnetic field as, 154
  - exponential, 131, 138–139, 142
  - families of, 3, 5
  - fractal, 10, 91
  - frequency-size, 10, 51, 91, 130, 137–139, 143, 146
  - Gaussian, *see* Gaussian distributions
  - log-normal, *see* Log-normal distributions
  - normal, *see* Gaussian distributions
  - power-law, 10, 91
- Droughts, 53, 59, 115–117

## E

- Earth's geodynamo, *see* Geomagnetic field
- Earth's magnetic field, *see* Geomagnetic field
- Earthquakes, 4–5, 128
- Elevation, *see* Topography
- Erosion, *see* Sediments
- Euclidean dimensions, 13
- Exponents, *see* Extreme-value exponent,  $H_e$ ; Hausdorff exponent,  $H_a$ ; Hurst exponent,  $H_u$ ; Power-spectral density exponent,  $\beta$ ; Wavelet variance exponent,  $H_w$

- Extended fractional Gaussian noises and motions, 39–40, *see also* Fractional Gaussian noises and motions
- Extreme-value exponent,  $H_e$ 
  - see also* Average extreme-value analysis
  - defined, 66
  - dependence on  $\beta$  for
    - Gaussian noises and motions, 66–68
    - log-normal noises and motions, 70–71
  - relation to  $H_u$ , 67–68

## F

- Fading, *see* Windowing
- Floods, 53, 59
- Fluvial sedimentation rates, 135, 156
- Fourier analysis
  - aliasing, 22
  - coefficients, 21–22, 35–37
  - coefficients after windowing, 34
  - description, 19–22
  - discrete Fourier transform, 21–22
  - filtering technique, 35–37
  - inverse Fourier transform, 20–21
  - leakage, 32–34, *see also* Windowing
  - nonperiodic continuous time series, 20–21
  - nonperiodic discrete time series, 21–22
  - Parseval's theorem, 27–28
  - periodic continuous time series, 19–20
  - prewhitening, 33
  - problems using, 32–35, 71
  - spectral variance, 32–33
  - spectrum, 20, *see also* Power-spectral analysis
  - units of, 21
  - transform, 19–22
  - Weiner-Khinchine theorem, 152
  - windowing, *see* Windowing
- Fourier's law of heat transport, 102
- Fractals
  - see also* Fractal dimension,  $D$ ; Self-affine fractals, Self-similar fractals
  - Cantor set, 133–134
  - devil's staircase, 134
  - statistical concept, 1, 10
- Fractal dimension,  $D$ 
  - definition, 10
  - derivation of relation between
    - $D$  and  $\beta$ , 28–30
    - $D$  and  $H_a$ , 16–18
  - methods for deriving
    - box-counting method, 10–11, 13, 126–127
    - ruler method, 30
  - time series, 18
- Fractional autoregressive integrated moving average (FARIMA) model, 79

- Fractional Brownian motions, *see* Fractional Gaussian noises and motions
- Fractional Gaussian noises and motions  
analyses using  
  average extreme-value analysis, 66–69  
  power-spectral analysis, 35–37, 44–45  
  rescaled-range analysis, 62–64  
  semivariogram analysis, 47, 49–51  
  wavelet variance analysis, 72–77  
construction  
  Fourier filtering technique, 35–37  
  successive random additions, 43–47  
  summing and differencing, 25–27  
  Weierstrass–Mandelbrot functions, 47  
examples in nature  
  geomagnetic field variations, 141, 149, 154  
  porosity variations, 124  
  temperature, 93–98  
examples of synthetic, 37–39, 41, 43, 47–48, 74, 120, 144  
Fourier filtering technique, 35–37  
persistence, *see* Persistence and antipersistence  
successive random additions, 43–47  
symbols used in analyses, 40  
two-dimensional, 129
- Fractional log-normal noises and motions  
analyses using  
  average extreme-value analysis, 69–71  
  power-spectral analysis, 55–56  
  rescaled-range analysis, 64–65  
  semivariogram analysis, 9, 56–58  
  wavelet variance analysis, 75, 77–78, 80–81  
conversion from fractional Gaussian noises and motions, 53  
discussion, 51–56  
drought analysis, 115  
examples of synthetic and in nature, 4, 54, 78, 101–102  
Joseph and Noah effect, 53  
persistence, *see* Persistence and antipersistence  
symbols used in analyses, 55
- Frequency domain, 19–20, 37–39
- Frequency-size distributions, 10, 51, 91, 130, 137–139, 143, 146
- G**
- Gaussian distributions  
  binormal distribution, magnetic field, 154  
  earthquakes, 4–5  
  fractional noises and motions, *see* Fractional Gaussian noises and motions  
  random, *see* White noise  
  relation to log-normal distributions, 51, 53, 55  
  stochastic diffusion model results as, 112, 126  
  successive random additions, 43–46  
  temperature fluctuations as, 112  
  topographic elevations, 127
- GCM, *see* General circulation models
- Geodynamo, Earth's, *see* Geomagnetic field
- General circulation models, 93, 112–113, 158
- Geomagnetic field  
  archeomagnetic data, 140–142  
  cryptochrons, 143  
  declination data, 148–151  
  dipole moment variability, 140–142  
  geomagnetic variations model, 152–155  
  global paleomagnetic database, 148–150  
  inclination data, 148–151  
  marine sediment data, 140–142  
  polarity reversals, 142–148  
  Rikitake disk dynamo, 144  
  summary, 159
- Global paleomagnetic database, 148–150
- Gravity fields, 156
- Green's function, 107–108
- Groundwater migration, 118
- Gulf of Mexico, well logs, 124–126
- H**
- Hadley circulation, 105, 110
- Hann window, 34
- Harr wavelet, 72
- Hausdorff exponent, *Ha*  
  *see also* Semivariogram analysis  
  box counting, 11, 16–18  
  dependence on  $\beta$  for  
    Gaussian noises and motions, 49–50  
    log-normal noises and motions, 57–58  
  derivation of relation between  
    *Ha* and  $\beta$ , 28–30  
    *Ha* and *D*, 16–18  
  Gaussian surfaces, 130  
  sedimentation rates, related to, 136  
  self-affine fractal definition, 11  
  self-affine time series definition, 14, 18  
  successive random additions, 45–47  
  variance, relation to, 14
- Heat diffusion, metallic film, 92–93, 103–105
- Heat transport, Fourier's law, 102
- Heavyside function, 123
- Hiatuses, sedimentary, 131, 133, 137
- Hurst exponent, *Hu*  
  *see also* Rescaled-range analysis  
  defined, 60–61  
  dependence on  $\beta$  for  
    Gaussian noises and motions, 63–64  
    log-normal noises and motions, 64, 66

- relation to *Ha*, 61
  - relation to *He*, 67–68
  - Hurst, Harold, 58–60, 100
  - Hydrocarbons, 126–130
  - Hydro-Climatic Data Network, 98–99
  - Hydrology
    - Colorado river, 116–117
    - droughts, 53, 59, 115–117
    - fluvial sedimentation rates, 135, 156
    - groundwater migration, 118
    - Hurst, Harold, 58–60, 100
    - Joseph and Noah effect, 53
    - Nile river, 59
    - precipitation, 99–100
    - rescaled-range analysis, 58–61
    - river discharges, 4–5, 59, 98–100, 115–117, 158
    - sediment loads in rivers, 135, 156
    - short-range persistence models, 6, 115
    - tree-ring widths, 99–100, 158
- I**
- Ice cores, 91, 93–94, 98, 109–110
  - Invariance, scale, 1, 10
  - Inverse Fourier transform, 20–21, *see also* Fourier analysis
- J**
- Joseph effect, 53
- L**
- Leakage, 33, *see also* Windowing
  - Lloydminster oil field, 130
  - Log-normal distributions
    - coefficient of variation, 51–53
    - discussion, 51–56
    - drought analysis, 115
    - examples of, 4–5, 52–54, 101–102
    - fractional noises and motions, *see* Fractional log-normal noises and motions
    - relation to Gaussian distributions, 51, 53, 55
  - Log-normal noises and motions, *see* Fractional log-normal noises and motions
  - Lomb periodogram, 93
  - Long memory, *see* Persistence and antipersistence
  - Long-range correlations, *see* Persistence and antipersistence

Lorentzian spectrum, 109, 111, 152

**M**

- Magnetic field, *see* Geomagnetic field
- Mandelbrot, Benoit, 1, 35
- Maximum likelihood estimators, 79
- McLeod–Hipel Time Series Datasets Collection, 60
- Memory, *see* Persistence and antipersistence
- Metallic film heat diffusion, 92–93, 103–105
- Mexican hat wavelet, 72–73
- Milankovitch cycles, 158
- Models
  - atmosphere–ocean, 102–113
  - atmosphere–ocean–land surface, 112–113
  - autoregressive (AR), 6, 115
  - Culling, 159
  - fractional autoregressive integrated moving average (FARIMA), 79
  - general circulation, 93, 112–113, 158
  - geomagnetic, 153–155
  - long-range persistence, *see* Average extreme-event analysis; Dispersional analysis; Maximum likelihood estimators; Power-spectral analysis; Rescaled-range analysis; Roughness–length method; Semivariogram analysis; Wavelet variance analysis
  - moving-average (MA), 6
  - random-walk, 122–124, 131–132
  - Sadler and Strauss, 131, 135
  - sedimentary bed formation, 131
  - stochastic diffusion, *see* Stochastic diffusion models
  - stratigraphic, Plotnick, 131, 133, 137
- Modulus, complex number, 22
- Mother wavelet, 71–72
- Motions, *see* Brownian motions; Fractional log-normal noises and motions
- Moving-average (MA) model, 6

**N**

- Nile river, 59
- Noah effect, 53
- Noises, *see* Brownian motions; Fractional Gaussian noises and motions; Fractional log-normal noises and motions; White noise; Persistence and antipersistence
- Nonperiodic time series, 20–22
- Nonstationary, *see* Stationary
- Normal distribution, *see* Gaussian distributions

## O

Ocean, models with atmosphere, 102–113  
 Oil wells, 126–130

## P

Pair-correlation technique

applied to  
 earthquakes, 128  
 geomagnetic reversals, 147–148  
 hydrocarbons, 127–129  
 synthetic hydrocarbon reservoirs, 129–130  
 description, 127–128, 147

Paleointensity, *see* Geomagnetic field

Paleomagnetism, *see* Geomagnetic field

Parseval's theorem, 27–28

Periodicity, tests for, 151

Periodogram, *see* Power-spectral analysis;  
 Power-spectral density

Persistence and antipersistence

description, 1–2, 5–6, 38–39  
 fractional noises and motions, *see*  
 Fractional Gaussian noises and  
 motions; Fractional log-normal noises  
 and motions

long-range, 5–6, 39, 79, *see also*  
 Autocorrelation function; Average  
 extreme-value analysis; Power-  
 spectral analysis; Rescaled-range  
 analysis; Semivariogram analysis;  
 Wavelet variance analysis

measures of, *see* Exponents  
 short-range, 5–6, 39, 115, *see also*  
 Autocorrelation function  
 stationarity, related to, 31–32  
 strength, 5–7, 19, 31–32, 39, *see also*  
 Exponents  
 uncorrelated time series, *see* White noise  
 weak vs strong, 5–7, 31–32, 39

Petroleum, spatial distribution of, 126–130

Plankton studies, 157

Poisson process, 147

Polarity, magnetic field, *see* Geomagnetic  
 field

Porosity in sedimentary basins, 92, 118, 124–  
 130, 159

Powder River basin hydrocarbons, 126–129

Power-law distributions, 10, 91

Power-law regimes, 91

Power-spectral analysis

*see also* Power-spectral density; Power-  
 spectral density exponent,  $\beta$

applied to  
 atmospheric temperature, 93–98, 156  
 Brownian motion, 23, 25  
 declination data, 148–150

deuterium, Vostok ice core, 93–94, 98  
 dipole moment variations, 140–142  
 Gaussian noises and motions, 35–37, 40–  
 45

geomagnetic field, 140–142, 148–151  
 geomagnetic model results, 153–155  
 gravity fields, 156  
 inclination data, 148–150  
 log-normal noises and motions, 55–56  
 plankton variability, 157  
 porosity variations, 118, 124–127  
 river discharges, 98–100  
 sea-surface heights, 156–157  
 sediment loads in rivers, 156  
 sedimentation rates, 136  
 solar luminosity, 114  
 stochastic diffusion model results, 100–  
 113, 120–122  
 temperature variability, 93–98, 156  
 topography, 118, 124, 126  
 tree-ring widths, 98–100  
 vegetation densities, 157  
 Vostok ice core, 93–94, 98  
 well logs, 118, 124–127  
 white noise, 23–24, 35–37  
 windowed time series, 39–44

binning data, 23  
 description, 19–26  
 Lomb periodogram, 93  
 overview of applications, 91–92  
 summary of strengths and weaknesses, 82  
 windowing, *see* Windowing

Power-spectral density

*see also* Power-spectral analysis; Power-  
 spectral density exponent,  $\beta$

continuous, 22  
 description, 22–28  
 discrete, 23  
 relation to

autocorrelation function, 27  
 variance, 27–28

units of, 22

windowing effects, 34, 39–44

Power-spectral density exponent,  $\beta$

*see also* Power-spectral analysis; Power-  
 spectral density

definition, 22

derivation of relation between  $\beta$ ,  $H_a$  and  $D$ ,  
 28–30

differenced time series, 25–27, 37–39

Fourier filtering technique, 35–37

fractional Gaussian noises and motions,  
 dependence on  $\beta$  for  $\beta_{PS}$ , 40, 45;  $H_a$ ,  
 49–50;  $H_e$ , 66–68;  $H_u$ , 63–64;  $H_w$ , 75,  
 77

fractional log-normal noises and motions,  
 dependence on  $\beta$  for  $\beta_{PS}$ , 55–56;  $H_a$ ,  
 57–58;  $H_e$ , 70–71;  $H_u$ , 64–66;  $H_w$ , 75,  
 81

summed time series, 25–27, 37–39  
 weak vs strong persistence, cross-over, 31–32  
 Power-spectral filtering, 35–37  
 Precipitation, 99–100  
 Prewhitening, 33

## R

Radiation, blackbody, 93, 107  
 Radiative damping, 111–112  
 Random additions, successive, 43–47  
 Random-walk model, 122–124, 131–132  
 Rescaled-range analysis  
 applied to  
 climatological time series, 100, 115, 158  
 Gaussian noises and motions, 62–64  
 log-normal noises and motions, 63–64  
 sediment loads in rivers, 156  
 average extreme-value analysis, compared to, 67–68, 71  
 continuous, 59–60  
 description, 58–61  
 discontinuous, 60–61  
 Hurst, Harold 58–60, 100  
 running sum, and, 61  
 summary of strengths and weaknesses, 82  
 Reservoir storage, 59  
 Reversals, magnetic field, *see* Geomagnetic field  
 Rikitake disk dynamo, 144  
 River discharges, 4–5, 59, 98–100, 115–117, 158  
 Roughness–length method, 79  
 Ruler method, 30  
 Running sum, 14–15, 25–27, 37–39, 61

## S

Scale invariance, 1, 10  
 Sea-surface heights, 156–157  
 Sedimentary basins, porosity variations in, 92, 118, 124–130, 159  
 Sedimentation, *see* Sediments  
 Sediments  
 bed thickness distributions, 131, 136–139  
 completeness, stratigraphic 131–136  
 deposition, 122–124, 131–139  
 erosion, 122–124, 131–139  
 hiatuses, 131, 133, 137  
 models for sedimentation and porosity  
 Culling, 159  
 overview, 118  
 random-walk, 122–124, 131–132  
 Sadler and Strauss, 131, 135  
 stochastic diffusion, 118–124

stratigraphic model of Plotnick, 131, 133, 137  
 porosity observations, 124–130  
 sedimentation, 117–139, 159  
 sedimentation variations, overview, 117–118  
 SEDPAK, 136  
 summary, 159  
 unconformities, 133–135, *see also* Hiatuses  
 Self affine, definition, 1  
 Self-affine fractals  
 box-counting method for, 11, 13  
 concept, 10–13  
 construction, deterministic, 11–12  
 definition, 11, 22  
 deterministic, 11–12  
 dimensions, 11, 13, 22, *see also* Exponents  
 self-affine time series, relation to, 16–18  
 standard deviation, 16–18  
 statistical, 11–13  
 topography as, 11–12  
 Self-affine time series  
 box-counting method for, 16–18  
 definition, 1  
 deriving relation between  
 $\beta$ ,  $H_a$  and  $D$ , 28–30  
 $H_a$  and  $D$ , 16–18  
 differencing, results on  $\beta$ , 25–27  
 first derivative, 26–27  
 power-law regimes, 91  
 rescaling, 28–30  
 self-affine fractals, relation to 16–18  
 standard deviation, 16–18  
 summing, results on  $\beta$ , 25–27, 37–39  
 Self-similar fractals  
 extension to time series, 16–18  
 fractal dimension,  $D$ , 10  
 statistical, 1, 10–11  
 Semivariogram analysis  
 applied to  
 Gaussian noises and motions, 9, 47, 49–51  
 log-normal noises and motions, 9, 56–58  
 autocorrelation function, relation to, 8–9  
 continuous, 8–9, 18  
 discrete, 8–9, 18  
 discussion, 8–9, 18–19, 50–51  
 summary of strengths and weaknesses, 82  
 variograms, 8  
 Shading, *see* Windowing  
 Short memory, 5–6, 39, 115, *see also* Persistence and antipersistence  
 Solar luminosity, 114, 158–159  
 Spectral analysis, *see* Autocorrelation function; Fourier analysis; Power-spectral analysis  
 Spectral filtering, 35–37  
 Spectral variance, 32–33  
 Staircase, devil's, 134  
 Standard deviation, *see* Variance

Stationarity  
 description, 8, 13–14, 50–51, 112, 151  
 persistence strength, relation to, 31–32  
 weak, 8

Stefan–Boltzmann law, 107

Stochastic component of time series, 1, 3

Stochastic diffusion model  
 for climate variability  
 one-dimensional, 100–107  
 two-layer, 107–114  
 for sedimentation and porosity, 118–124,  
 159  
 other studies using, 157

Storage, reservoir, 59

Stratigraphic completeness, 131–136

Stratigraphy, *see* Sediments

Streamflow, 4–5, 59, 98–100, 115–117, 158

Strong persistence, 5–7, 31–32, *see also*  
 Persistence and antipersistence

Successive random additions, 43–47

Summing self-affine time series, 14–15, 25–  
 27, 37–39, 61

Superchron, Cretaceous, 146

Symbols  
 appendix, 83–87  
 Gaussian noise and motion analyses, 40  
 log-normal noise and motion analyses, 55

Synthetic time series  
*see also* Fractional Gaussian noises and  
 motions; Fractional log-normal noises  
 and motions

construction  
 Fourier filtering, 35–37  
 running sum, 14–15, 25–27, 37–39  
 successive random additions, 43–47  
 Weierstrass–Mandelbrot functions, 47

**T**

Tapering, *see* Windowing

Temperature, atmospheric, 91–98, 100, 156

Time series  
 antipersistence, *see* Persistence and  
 antipersistence  
 average, 6–7  
 binning data, 23  
 characterization of, 3, 5–6  
 component  
 periodic, 3, 20, 95–96, 151  
 stochastic, 1, 3  
 trend, 3, 34–35, 95  
 continuous, 2–5  
 correlations in, *see* Persistence and  
 antipersistence  
 definition, 2–3  
 detrending, 34–35, 95  
 discontinuous, 2–5  
 discrete, 2–5

distributions, families of, 3, 5, *see also*  
 Distributions  
 lag, 6–7  
 mean, 6–7  
 moments, 8  
 periodicity, tests for, 151  
 persistence, *see* Persistence and  
 antipersistence  
 quantification, 3–6  
 running sum, 14–15, 25–27, 37–39, 61  
 standard deviation, 14  
 stationarity, 8, *see also* Stationarity  
 synthetic, *see* Synthetic time series  
 trend, 34–35, 95  
 variance, 6–8, 14

TOPEX/POSEIDON, 156–157

Topography  
 examples, 3–5, 11, 121, 126–127, 155–156  
 random-walk model, 122–124  
 stochastic diffusion model, 118–124

Traffic flow, 157

Transforms  
 Fourier, 19–21  
 wavelet, 71–79

Tree-ring widths, 98–100

Trend, 34–35, 95

**U**

Unconformities, 133–135, *see also* Hiatuses

Uncorrelated time series, 4–5, 7, *see also*  
 White noise

**V**

Variables, appendix, 83–87

Variance  
 Brownian motion, 14  
 coefficient of variation, 51–53  
 relation to  
 autocovariance function, 6–7  
 persistence strength, 31–32  
 power-spectral density, 27–28  
 self-affine time series, 14, 18  
 semivariograms, 8, 50–51  
 rescaled-range, standard deviation, 60  
 stationarity, *see* Stationarity  
 wavelets, *see* Wavelet variance analysis

Variograms, 8, *see also* Semivariogram  
 analysis

Vegetation densities, 157

Vostok ice core, 91, 93–94, 98, 109–110

## W

- Walker circulation, 105, 110
- Wavelet variance analysis  
 applied to  
   Gaussian noises and motions, 72–77  
   log-normal noises and motions, 75, 77–78, 80–81  
 description, 71–73  
 Mexican hat, 72–73  
 summary of strengths and weaknesses, 82–83  
 transform examples, 74–75, 78–79
- Wavelet variance exponent,  $H_w$   
*see also* Wavelet variance analysis  
 defined, 75  
 dependence on  $\beta$  for  
   Gaussian noises and motions, 75, 77, 81  
   log-normal noises and motions, 70
- Weak persistence, 5–7, 31–32, *see also*  
 Persistence and antipersistence
- Weak stationarity, 8
- Weierstrass–Mandelbrot functions, 47
- Weighting, *see* Windowing
- Weiner–Khinchine theorem, 152
- Welch window, 34
- Well logs, 118, 124–126
- Wells, oil, 126–130
- White noise  
 analyses on Gaussian white noises using  
   average extreme-value analysis, 67–68  
   Fourier analysis, 20  
   power-spectral analysis, 23–25, 35–36  
   rescaled-range analysis, 62–63  
   semivariogram analysis, 49–50  
   wavelet variance analysis, 73–74, 76–77
- Brownian motion, relation to, 14–15  
 description, 13–14  
 examples in nature  
   earthquakes, number per month, 4–5  
   geomagnetic variations, 148–150  
   temperature, 93–94, 98  
 examples of synthetic, 14, 37–38, 47–48, 74  
 Fourier filtering technique, 35–37  
 geomagnetic field modeling, 152–153  
 running sum, 14–15, 37–38  
 standard deviation, 14  
 successive random additions, 43–47  
 variance, 14
- Wilson cycle, 136
- Windowing  
 description, 33–34  
 effects, 39–44  
 Hann window, 34  
 Welch window, 34, 39–41, 43